

UNIVERSITY OF MIAMI

DYNAMICS OF SEA TEMPERATURE VARIABILITY  
ON FLORIDA'S REEF TRACT

By

Lewis J. Gramer

A DISSERTATION

Submitted to the Faculty  
of the University of Miami  
in partial fulfillment of the requirements for  
the degree of Doctor of Philosophy

Coral Gables, Florida

August 2013

©2013  
Lewis J. Gramer  
All Rights Reserved

UNIVERSITY OF MIAMI

A dissertation submitted in partial fulfillment of  
the requirements for the degree of  
Doctor of Philosophy

DYNAMICS OF SEA TEMPERATURE VARIABILITY  
ON FLORIDA'S REEF TRACT

Lewis J. Gramer

Approved:

---

Arthur J. Mariano, Ph.D.  
Professor of Meteorology and  
Physical Oceanography

---

M. Brian Blake, Ph.D.  
Dean of the Graduate School

---

Brian K. Haus, Ph.D.  
Associate Professor and Chair of  
Applied Marine Physics

---

Kevin D. Leaman, Ph.D.  
Professor of Meteorology and  
Physical Oceanography

---

Elizabeth M. Johns, Ph.D.  
Oceanographer  
U.S. National Oceanic and  
Atmospheric Administration  
Miami, Florida

GRAMER, LEWIS J.

(Ph.D., Meteorology and Physical Oceanography)

Dynamics of Sea Temperature Variability  
on Florida's Reef Tract.

(August 2013)

Abstract of a dissertation at the University of Miami.

Dissertation supervised by Professor Arthur J. Mariano.

No. of pages in text. (207)

Variability in 5- to 25-year records of hourly mean *in situ* sea temperature, ocean currents, and meteorology at diverse shallow-water habitats in the Florida reef tract (FRT) is analyzed. Tidal, diurnal, and annual periodicities generally dominate sea temperature variability, with strong variability apparent in the “weather band” of 3-42 d at one reef-flat site, and at the local inertial period at one offshore site near the shelf break. A statistically significant interannual warming trend is also observed at this one offshore site only. Significant covariability between sea temperature and coincident air temperature, wind speed, sea-surface temperature (SST) gradients, and incident radiation (light) is also found. However, this covariability itself varies with an annual period, and differs between sites with similar depths, apparently due to differences in seafloor slope.

A coastal ocean reef heat budget is estimated from the hourly mean *in situ* sea temperature, meteorology, satellite SST, and reanalysis data for each site, together with a model of insolation absorption in the water column and heat exchange at the seafloor. A term for smaller-scale heat advection, the so-called horizontal convection (HC) or *thermal siphon*, previously observed at coral reefs elsewhere in the world, balances the heat budget. At six of the eight sites analyzed, the budget matches the long-term annual

climatology of observed *in situ* sea temperature variability within estimated uncertainty, and matches full seasons at the two other sites. Budget results also match the observed daily sea temperature variability, with  $R^2 > 0.3$ , root mean squared error  $< 0.1$  K, and bias  $< 10$  mK at most sites. Results are most sensitive to the scaling chosen for the horizontal convection parameterization, to assumed rates of insolation absorption, and to uncertainties in estimated surface currents and sea temperature gradients. However, estimates for horizontal heat exchange, cross-shore gradients, and insolation absorption rates in the water-column are found to compare well with direct *in situ* and satellite measurements. The heat budget is also shown to produce reliable results when using only remotely sensed and reanalysis data, providing a mechanism for more reliable monitoring of thermal stress on coral reefs where long *in situ* records are not available.

Finally, modes of sea-temperature variability, particularly for periods when variability is large or poorly explained by the heat budget, are analyzed in the context of other meteorological and oceanographic data using the techniques of heuristic ecological forecasting, Principal Component Analysis (PCA), and an artificial neural network called a Self-Organizing Map (SOM). Anomalous patterns of meteorological and circulation variability are identified from the *in situ* and satellite record, that are associated with periods when observed sea temperature variability is not well-explained by the heat budget. A combination of these methods is shown to improve the understanding of past reef ecological impacts related to thermal stress, such as coral bleaching. Applications of the present research for improved understanding of coastal physical oceanography and coral reef ecology in the FRT are briefly discussed.

## **Dedication**

This work is dedicated to Jeff Drake, for helping me see that this was possible in the first place; to Jim Hendee and Arthur Mariano, for helping me to make it so; and especially to my loving and beautiful wife, Karen, who never let me forget it was.

## **Acknowledgments**

The author acknowledges support during preparation of this dissertation from the NOAA Coral Reef Conservation Program (CRCP Program IDs #535, #789, #881, #889) and NOAA High-Performance Computing and Communication program (HPCC), under the supervision of Dr. J. C. Hendee of the Coral Health and Monitoring Program (CHAMP) at AOML. Partial funding was also received through two grants from the National Oceanographic Partnership Program (Multi-sensor Improved Sea-Surface Temperature (MISST) for GODAE, 2008; and MISST, 2011-2016), both under Dr. C. Gentemann. Moored ADCP and CTD, and ship TSG data from the NOAA SFP program were provided courtesy of Dr. E. M. Johns and R. H. Smith, NOAA AOML. NCORE data were provided by E. Williams and K. Shulzitski, with permission of T. Lee and S. Sponaugle of RSMAS. FRRP data were courtesy of Dr. D. Lirman (TNC-FRRP), RSMAS rooftop station data courtesy of Dr. P. Minnett, and wave data courtesy of Dr. B. Haus, all of RSMAS. Satellite imagery and products were courtesy of Dr. C. Gentemann of Remote Sensing Systems, and Drs. C. Hu and F. Muller-Karger of USF. This work is solely the opinion of the author and does not constitute a statement of policy, decision, or position on behalf of RSMAS, University of Miami, NOAA, or the U.S. Government.

I wish to personally acknowledge the unfailing guidance and encouragement of my major advisor, Prof. Arthur J. Mariano, as well as my Committee, Profs. Brian Haus and Kevin Leaman of RSMAS and Dr. Libby Johns (the ever-positive) of NOAA AOML. My thanks go also to Profs. Don Olson and Bill Johns, for their inspiration. I must particularly acknowledge my boss, Dr. Jim Hendee of NOAA AOML, for his long

support and forbearance, as well as Dr. Chelle Gentemann for her support, and Dr. Molly Baringer, Derrick Snowden, Mike Jankulak, Michael Shoemaker, Louis Florit, Jon Fajans, Dr. Dwight Gledhill, Dr. Derek Manzello, Nelson Melo, Ryan Smith, Dr. Chuanmin Hu, Dr. Scott Heron, Dr. Alberto Mestas-Nuñez, both Drs. Stephen Monismith and J. Leichter (for a few important words each), and members of the NOAA FACE team – Dr. Tom Carsey, Jack Stamates, and Paul Dammann (whom I often miss), for all of their help along the way. At RSMAS, I must thank a long list of teachers and guides – Profs. Albrecht, Ault, Bakun, Clement, Ginsburg, Grosell, Hansell, Hitchcock, Iskandarani, Kourafalou, Langdon, Lee, Lirman, Minnett, Mooers, Nolan, Olascoaga, Ortner, Özgökmen, Peters, Reniers, Romeiser, Shay, Sponaugle, Zhang – as well as current and former classmates, especially Dr. Pedro Di Nezio, now of the University of Hawai'i. This work would never have been completed without the able help over the years of all the Librarians at RSMAS (especially Annie Campbell), and at NOAA AOML (Linda, Gloria, and Christie), the staff of the GSO (Cary, Veronica, Kris), and the MPO Administrative Assistants (Sandrine and her predecessors): thanks.

Thank you, Mary Ann Gramer; I think of you every day. And thank you to my supportive family – my wife, my sister, brother-in-law, brother, sister-in-law, and my three nephews and niece, all of whom made me want them to be proud of me. Thank you, Anthony, Barry, and Iuval. Last but not least, thank you to all of those – still living or not – who were willing to be there for me when I needed fatherly guidance, advice, or an example to look up to: Maj. Marcus Miller (USAF), William Ray Cain, Webster Fluharty, Howard A. Gramer, Sr., Eddie Estesson, Norman W. McLeod III, James Ford, Hector Hirigoyen, Zhou Junwen (laoshi), and most recently, Michael Coppola.

## TABLE OF CONTENTS

	Page
LIST OF FIGURES .....	vii
LIST OF TABLES .....	xxi
LIST OF ABBREVIATIONS .....	xxiii
Chapter	
1 INTRODUCTION .....	1
1. Geographical Context .....	2
2. Near-shore Oceanography .....	6
3. Offshore Oceanography .....	7
4. Reef-crest Oceanography .....	10
5. Research Questions .....	14
2 ANALYSIS OF VARIABILITY AND COVARIABILITY .....	17
1. Data and Methods .....	20
2. Results .....	32
3. Summary .....	54
3 REEF HEAT BUDGET .....	58
1. Additional Data .....	60
2. Methods .....	65
3. Results .....	89
4. Summary .....	107
4 ANALYSES OF ANOMALOUS VARIABILITY .....	111
1. Additional Data .....	111
2. Methods .....	115
3. Results .....	124
4. Summary .....	151
5 CONCLUSIONS AND RECOMMENDATIONS .....	153
1. Conclusions .....	153
2. Significance of the Research .....	161
3. Recommendations for Future Research .....	170
APPENDICES .....	181
BIBLIOGRAPHY .....	190

## List of Figures

Figure 1-1: Map showing boundaries of alongshore sub-regions and cross-shore reef zones within the FRT described in the text. Maps are used with permission of The Nature Conservancy – Florida Reef Resilience Program (FRRP): colors represent incidence of diver-observed coral bleaching and paling during summer 2007. Inset is northern region of the FRT, showing narrow cross-shore zones. .... 4

Figure 1-2: Representative cross-shore sections of seafloor topography from the Middle and Upper Florida Keys, illustrating the zones (i) through (iv) described in text – from the shore outward, to the upper section of the fore-reef slope (30 m isobath). Cross-shore distance (m) is shown on the x-axis, seafloor depth along the y-axis. Derived from Lidz et al. (2006), their Fig. 13; used with permission. .... 6

Figure 1-3: A pair of distinct cyclonic vortices interacting in the Straits of Florida (SF) in 2006. Vortices have similar horizontal scales ( $L \sim 30$  km), but different translational velocities. Chlorophyll *a* 1 km-resolution product derived from MODIS ocean color (USF 2012); clouds are gray, land black. .... 8

Figure 1-4: (a) EnviSat Advanced Synthetic Aperture Radar (ASAR) alternating polarization image of southern Straits of Florida from 2006-06-14 03:16 GMT, showing an energetic field of IWs exhibiting refraction, attenuation, and reflection related to mean-current shear and topography (ESA 2009). (b) USF MODIS true color image from 2010-04-28 16:11:39 GMT, showing IW trains similar to that in Fig. 1-4a, propagating east-west along the SF. IWs show up in this image against the background of sun-glint on the ocean in the Straits. .... 9

Figure 1-5: Schematic of upper-ocean processes driving sea temperature variability in the open ocean (courtesy of R. Weller, WHOI, <http://uop.whoi.edu>, used with permission). However, as noted in the text, additional processes not shown here will also operate over shallow, sloping seafloor topography like that in the FRT, e.g., seafloor reflection, benthic heat exchange, varying light attenuation within the water-column, and *horizontal convection* (see Ch. 3). ..... 13

Figure 2-1: Map of southern portions of Florida and the Florida Shelf, showing position of SEAKEYS and SFP automated monitoring stations along the FRT (stars). Stations are indicated by 5-letter code as described in the text and in Table 2-1. Coastline is in black, outlines of the 2, 10, 30, 80, 150, 300, and 700 m isobaths from NGDC 3” CRM bathymetry (see text) are shown in gray. .... 19

Figure 2-2: Histograms of (a,b,c) cross-shore and (d,e,f) alongshore ocean currents [m/s], from (a,d) *in situ* daily mean of ADCP profiles at LOOE1 bin-averaged over the water column, and coincident near-surface data from (b,e) GoM and (c,f) FKEYS HYCOM hydrodynamic models. Note difference in horizontal (velocity) scales between top ( $-0.25$  to  $+0.25$   $\text{ms}^{-1}$ ) and bottom ( $-1$  to  $+1$   $\text{ms}^{-1}$ ) panels. .... 28

Figure 2-3: Spectra of sea-temperature anomaly ( $\text{K}^2/\text{cpd}$ , log-log scale; abscissa shows period in d) for stations (a) FWYF1, (b) MLRF1, (c) SMKF1, and (d) LONF1; and for SFP station “LOOE1” at (e) 5 m and (f) 22 m. Periods of interest are indicated, including semi- diurnal tides and land-sea breeze ( $\approx 0.5$  d), diurnal tides and insolation ( $\approx 1$  d), local inertial period (“IP”= $26.5$  to  $27.6$  h), eddy / meander-passage and “weather” bands (4-42 d), semi-annual (tropical, 183 d), and annual cycles. The two LOOE1 spectra (e,f) constitute only a six-year record with intermittent gaps, obscuring the

relative power of the annual period there. Long-term mean was subtracted prior to analysis..... 35

Figure 2-4: Spectra at selected sites: (a) Wind speed (kts<sup>2</sup>/cpd) at instrument height for FWYF1, (b) LONF1, and (c) SANF1. (d) Air temperature anomaly (K<sup>2</sup>/cpd) at instrument height for MLRF1, and (e) SMKF1. (f) Specific humidity ((kg/kg)<sup>2</sup>/cpd) at instrument height for SMKF1. (g) Barometric pressure (hPa<sup>2</sup>/cpd) at instrument height for SMKF1, (h) tide height (feet<sup>2</sup>/cpd) for SMKF1, and (i) LONF1. Ocean currents for LOOE1 ((m/s)<sup>2</sup>/cpd): (j) alongshore and (k) cross-shore depth-averaged current vector components, and (l) near-surface speed, for a 1,173 d continuous record from 2005 Mar 25 to 2008 Jun 11. Long-term mean was subtracted from all time-series analyzed..... 39

Figure 2-5: Box-and-whisker plots for monthly distributions, showing monthly median (centerline, notch width indicates two standard errors), 25th and 75th percentiles (rectangular box), extremes twice the inter-quartile range from the median (whiskers), and outliers beyond the extremes (“x’s”). Panels: (a,b,c) Hourly mean sea temperature in °C at (a) MLRF1, (d) LONF1, (c) DRYF1; (d,e,f) air temperature at these same stations; (g,h,i) wind speed, cross-shore (west-to-east), and alongshore (south-to-north) wind components in knots at FWYF1; (j) wind speed at LONF1, (k,l) cross-shore (roughly north-to-south) and alongshore (roughly west-to-east) winds at SANF1..... 41

Figure 2-6: Hourly climatology of sea temperature – mean hourly values , as a function of year-day (0-365) and hour, across 20 years of available data at each site, in °C – for (a) Sombrero Key Reef station SMKF1, and (b) Long Key station LONF1. .... 42

Figure 2-7: All complete years of hourly mean NDBC sea temperature in °C, at (a) Sombrero Key Reef station SMKF1, 1990-2007, and (b) Long Key station LONF1,

1993-2009, plotted vs. year-day-hour; color indicates year. Years missing more than 45 d of data were excluded from each plot. .... 45

Figure 2-8: Analysis of variance: annual mean sea temperature (circles, °C) and 95% confidence intervals (line segments) at each of (a) FWYF1, (b) MLRF1, (c) LONF1, and (d) SMKF1, using the more restrictive of Tukey-Kramer and Dunn-Sidák significance tests in each case. Only years missing fewer than 45 d worth of data were used for annual averages at each site. .... 46

Figure 2-9: NDBC time series of hourly mean sea temperature (gray, °C), and robust least squares trend line (black) at SMKF1 (gray), showing a +1.4 °C temperature trend over 20 years. Analyzing most-current records for the present study, no robust trend is observed in any other multi-year sea-temperature time series from the FRT..... 47

Figure 2-10: NDBC time series of hourly mean tide level above MLLW at SMKF1 (in feet, gray): robust linear regression trend (black) shows a 3 inch increase in tide level over a nine year record. .... 48

Figure 2-11: Time-dependent, Morlet wavelet coherence analysis between *in situ* air and sea temperatures, at a range of periodicities from 40 h to 365 d (y-axis), for the years 2001-2011 (x-axis) at two sites: (a) MLRF1 and (b) LONF1. Heavy contours indicate statistical significance at the 95% confidence level, right-pointing arrows indicate in-phase variability, and arrows with a downward orientation indicate a degree of quadrature, i.e., air temperature variability at that periodicity precedes corresponding sea temperature. .... 53

Figure 3-1: (a) Map of southern Florida and the Florida Shelf, showing position of SEAKEYS and SFP automated monitoring stations along the FRT (stars). Stations

indicated by 5-letter code and arrow are described in the text and in Table 3-1 above. Outlines of the 2, 10, 30, 80, 150, 300, and 700 m isobaths from NGDC 3” CRM bathymetry (see text) are shown in gray. (b, c, inset d) Close-ups showing the NGDC isobaths in a 15x15 km grid surrounding stations (black star), at 2 m depth and every 10 m from 10-100 m (solid), and from 5-95 m (dashed). Maps are shown for (b) Sombrero Key Reef, (c) Long Key, and (inset d) Dry Tortugas. (e) Map and (f) bathymetry side-view showing NCORE monitoring moorings for sea temperature (TL1-4) and sea temperature and ocean currents (“A”, “B”, “C”), 2000-2002 (panels e and f both courtesy of Liz Williams)..... 62

Figure 3-2: (a) Spectrum using boxcar-windowed periodogram method, of quality-controlled hourly above-surface photosynthetically active radiation (PAR, 400-700 nm) for November 2008 – November 2011 at Molasses Reef. (b) Monthly boxplot of daily dose for above-surface insolation ( $\text{MJ}\cdot\text{m}^{-2}\cdot\text{d}^{-1}$ ) at MLRF1. (c) Monthly boxplot of daily dose for available insolation near the seafloor ( $\text{MJ}\cdot\text{m}^{-2}\cdot\text{d}^{-1}$ ) as measured at 1 m on MLRF1 (black), and as estimated for the heat budget (gray) from above-water PAR, surface albedo, and in-water absorption climatology, for a mean site depth of 3.55 m. (d) Weekly (\*) and monthly (■) median post-cleaning light-attenuation coefficient for PAR ( $K_d^{\text{PAR}}, \text{m}^{-1}$ ) as estimated from *in situ* post-cleaning surface and underwater hourly PAR. .... 70

Figure 3-3: Predicted horizontal convective warming ( $\text{K}\cdot\text{d}^{-1}$ , vertical axis) as a function of sea-surface cooling rate ( $\text{W}\cdot\text{m}^{-2}$ , axis into page) and seafloor slope  $\beta$  (breadth-wise axis) under various momentum and thermal balances (UU, SU, US, SS; see Eq. 3-3c). .... 81

Figure 3-4: Histograms of hourly representation error (x axes,  $W \cdot m^{-2}$ ) at FWYF1, calculated using methods of Fairall et al. (2003) for (a) latent and (b) sensible heat flux; and using propagation of error (see text and Appendices) for (c) net shortwave and (d) net longwave radiative fluxes. .... 87

Figure 3-5: (a) Cross-shore baroclinic ocean currents (top panel Hovmöller,  $ms^{-1}$ ), cumulative daily net heat flux (middle panel dashed line,  $K \cdot d^{-1}$ ) and wind stress (dotted,  $dyn \cdot cm^{-2}$ ) at MLRF1, and vertical temperature differences (solid gray) at LOOE1, during a month with periods of both daily warming and persistent cooling (see labels, middle panel). Box-and-whisker plots at current-measurement sites (b) LOOE1 and (c) NCORK, comparing observed (upper) vs. modeled (lower boxes) heat exchange . Observed is from vertical current shear and vertical sea temperature difference, modeled is from horizontal convection parameterizations (see Eq. 3-3c, Eq. 3-4). .... 90

Figure 3-6: Monthly climatology of net sea-surface heat flux estimates ( $Q_0$ ) from present study (dashed line with squares) for (a) Molasses Reef and (b) Long Key, compared with monthly mean ERAI and NARR reanalyses (circles), and several published climatologies (triangles). The heavy solid line with squares (“Actual”) is observed sea temperature variability, expressed in [ $W \cdot m^{-2}$ ] using estimated density, heat capacity, and depth of seawater at each site. Means were limited to months with valid estimates for at least 75% of the hours in that month, and to data for years 1993-2006. . 91

Figure 3-7: Year-day (a,c) and yearly (b,d) climatologies of combined terms from the present heat budget (solid lines with squares,  $W \cdot m^{-2}$ ) for the years 1993-2009. The plots show the present heat budget total radiative ( $Q_{SW}+Q_{LW}$ ,  $>0$ ) and turbulent ( $Q_{LH}+Q_{SH}$ ,  $<0$ ) surface heat fluxes, at two sites: (a,b) FWYF1 and (c,d) LONF1. Also

shown for comparison, ISCCP  $Q_{SW}+Q_{LW}$  and OAFflux  $1^\circ Q_{LH}+Q_{SH}$  published daily climatologies (dashed lines, circles), and estimates from the present study of *absorbed* radiative flux ( $\gamma Q_{SW}+Q_{LW}$ , triangle) and benthic heat flux into the ocean ( $Q_b$ , plus-sign).

..... 92

Figure 3-8: Daily climatology of observed sea temperature (thick line, °C) and cumulative net heat fluxes predicted by the heat budget (lighter lines, °C) bracketed by  $\pm$  one standard error (dashed lines), for: (a) Fowey Rocks (1993-2011), (b) Molasses Reef (1993-2011), (c) Long Key (1993-2011), (d) Sombrero Key Reef (1993-2008), (e) Looe Key Reef 5 m sensor (2005-2010), (f) Looe Key 22 m sensor (2005-2010), (g) Sand Key Reef (1993-2005), and (h) Dry Tortugas (1993-2005), showing results for three distinct annual  $K_d$  climatologies (see text). Daily means were computed using bootstrap procedure, with  $N=300$  random resampling with replacement..... 94

Figure 3-9: Monthly box-and-whisker plots of daily net heat budget terms [ $K \cdot d^{-1}$ ] at distinct sites, for all complete days during the years 1993-2012, at (a-f) MLRF1, and (g-l) LONF1: (a,g) change in observed daily mean sea temperature,  $\Delta_{1d}T_s$ ; and estimated from (b,h) cumulative total heat budget,  $\Sigma_{1d}\partial_t T_s$ ; (c,i) total heat budget excluding horizontal convection,  $\Sigma_{1d} u \cdot \nabla T_s + K \nabla^2 T_s + (Q_0(\gamma) + Q_b) / \rho C_p h$ ; (d,j) net vertical (surface and seafloor) heat flux,  $\Sigma_{1d}(Q_0(\gamma) + Q_b) / \rho C_p h$ ; (e,k) net heat flux into the sea-surface,  $\Sigma_{1d} Q_0 / \rho C_p h$ ; (f,l) latent sea-surface heat flux,  $\Sigma_{1d} Q_{LH} / \rho C_p h$ ..... 98

Figure 3-10: Results of applying the heat budget to a gridded 9 km-resolution “foundation” sea temperature product (MISST) and ERAI rather than *in situ* data. Plotted are observed *in situ* sea temperature (black), MISST daily sea temperature interpolated to each site (red), and heat budget model result (blue). (a) Florida Reef Resilience

Partnership site in the Upper Florida Keys during 2010 winter cold snap (see Lirman et al. 2010); (b) Molasses Reef during several summers (June-August) between 2002-2009.

..... 103

Figure 3-11: Climatological result for heat budget at MLRF1 (gray) based solely on MISST 9 km daily foundation sea temperature product and ERAI forcing, together with associated representation error bars (dotted lines), compared to observed sea temperature (black), and to the heat budget result produced with *in situ* data from Fig. 3-8 (red)..... 104

Figure 3-12: Histogram of hourly, time-varying sub-grid scale heat diffusion rate,  $K_{h,SGS}$ , calculated based on the output of the total heat budget at MLRF1 vs. observed sea temperature variability, and using the  $T_s$  Laplacian calculated from weekly composite AVHRR SST..... 106

Figure 4-1: Synoptic 1 km AVHRR SST for Florida and Eastern Gulf of Mexico from USF IMaRS, 2009-April-02 10:39 UT. Gray pixels are clouds. Inset is a blow-up of this image, showing smaller-scale internal structure of an apparent cyclonic vortex (probable mesoscale eddy) offshore of the Middle Keys. Plumes of warmer water appear to have originated at the 7-Mile and Long Key Bridge Channels inshore and been entrained by the vortex. There is a ribbon of cool water stretching along the coast to Broward County – possibly a result of the vortex interacting with the “wall” of the FRT.

..... 113

Figure 4-2: Synoptic 1 km AVHRR SST product from a daytime overpass 12 h prior to Fig. 4-1. Note marked differences in apparent extent of the WFS "cold tongue"

as well as in structure of both the eddy feature over Pourtalès Terrace, and the cyclonic front of the Loop Current (lower center). ..... 114

Figure 4-3: Complete time-series records of quality-controlled NDBC *in situ* data from Molasses Reef SEAKEYS station, together with representative variability metrics calculated from those data, from top to bottom: sea temperature, sea temperature variability ( $\Theta$ ), air temperature, air temperature variability ( $\mu_{3d}\sigma_{1d}T_a$ ), wind vector components  $W_U$  and  $W_V$ , 3 d SMA wind speed ( $\mu_{3d}U_{10}$ ), and wind vector variability ( $\sigma_{7d}(W_U+\sigma_{7d}W_V)$ ). ..... 125

Figure 4-4: Alternate variability metrics for *in situ* sea temperature from SMKF1: (a) whole record and (b) detail of summer 2001. Hourly sea temperature (black), 3 d SMA of 1 d standard deviation  $\Theta$  (red), 3 d SMA  $\mu_{3d}T_s$  (green), and an alternative variability metric (see text), the anomaly between 3 d SMA and 1 d minimum hourly value  $anom_{3d}^{min}T_s$  (blue). ..... 126

Figure 4-5: Time series of (from top to bottom) sea temperature  $T_s$ , (black),  $T_s$  variability metric  $\Theta$  (blue), cumulative total (green) and net sea-surface (red) heat budgets, air temperature variability  $\mu_{3d}\sigma_{1d}T_a$  (gray), and wind variability  $\sigma_{7d}U_{10}^x + \sigma_{7d}U_{10}^y$  (magenta) for May-September 2006. Two anomalous sea temperature variability events occurred in June, the first around June 4th (arrow) coincided with light winds, and passage of a vortex visible in satellite imagery offshore (Fig. 1-3). ..... 128

Figure 4-6: Sea temperature and wind variability metrics for SMKF1 during 2005. See text and Fig. 4-7 for further discussion. ..... 130

Figure 4-7: Chlorophyll *a* images of the Florida Keys, coincident with days of “non-wind related” anomalous sea temperature variability at SMKF1 in 2005. Images

are from USF IMaRS site, with contrast and sharpness enhanced to show subtle features: high chlorophyll a concentration estimates are denoted by red, while dark blue denotes very low concentration; clouds are shown in gray. Year-days 83 (March 24<sup>th</sup>) and 307 (November 3<sup>rd</sup>) are enlarged both to show the position of SMKF1 relative to the images, and to illustrate the detail available in the images. .... 131

Figure 4-8: Stimulus/Response Index (S/RI) for the "onshore flux" ecoforecast, evaluated in near real-time based on variability metric criteria calculated from SEAKEYS data broadcast hourly. Alerts are frequently seen during cold-front passages (November-April) but produce low S/RI (<60, light color); alerts during warmer months are not as frequent, but show higher S/RI (60-120, darker color) due to higher observed sea-temperature variability according to the metrics, to coincident peaks in satellite-derived chlorophyll *a*, and to the *lack* of coincident atmospheric variability..... 132

Figure 4-9: Dominant EOFs for un-normalized hourly sea temperature at Sombrero Key SEAKEYS station, arranged arbitrarily into 14 d (336 h) "frames" for analysis. This figure illustrates the importance of first attempting to normalize data prior to PCA..... 134

Figure 4-10: Dominant EOFs of detrended SMKF1 sea temperature. (a) Hourly time series: the first two modes represent the dominant frequencies of variability less than 14 d period; similar results were seen at most other sites analyzed in the FRT. (b) Daily mean: the dominant modes each again represent a dominant frequency of variability between 1 and 14 d period; this result varied somewhat by site, however, depending on the importance of "weather-band" (synoptic atmospheric) variability at each site. (c) Hourly time series with 24 h frame, highlighting diurnal variability. .... 135

Figure 4-11: Dominant EOFs of 14 d frames of variability metrics for: (a) sea temperature,  $\Theta$ ; (b) air temperature,  $\mu_{3d}\sigma_{1d}T_a$ ; (c) winds,  $\sigma_{7d}U_{10}^x + \sigma_{7d}U_{10}^y$ ; (d) net heat flux,  $\Sigma_{3d}(Q_0/\rho C_p h)$ . Dominant EOFs of 24 h (diurnal) frames for the variability metrics of (e) sea and (f) air temperature. .... 137

Figure 4-12: Extended PCA at SMKF1, showing dominant patterns of covariability between variability metrics for sea temperature (light blue) and air temperature (red), wind vector variability (green), and 3 d SMA wind speed (dark blue). Note the zero-line position is consistent across panels but varies by time series: sea temperature origin is at plot center, the others slightly above center. .... 138

Figure 4-13: Dominant extended EOFs as for Fig. 4-12, but only during those 14 d frames when anomalous sea temperature variability was observed. Note again multiple origins in multi-plots..... 139

Figure 4-14: Dominant EOF from spatial PCA of synoptic AVHRR SST anomaly, ie., with long-term field mean removed, for SMKF1 (all good images). Color scale is not shown, but range in image is from dark blue (-3 K) to dark red (+3 K)..... 140

Figure 4-15: Extended SOM performed on vectors that are the result of concatenating 14 d frames from time series of 3 d sea (light blue) and air temperature variability (red), 3 d SMA of wind speed (dark blue), and 3 d wind vector-component variability (green). Measurements from SMKF1, and frames are restricted to periods of anomalously high sea temperature variability (>95<sup>th</sup> percentile). Data were de-normalized following analysis: Note varying scale of individual plots within each panel. .... 142

Figure 4-16: Extended SOM of all 14 d frames lying in summer months (JAS) for variability metrics at SMK F1, regardless of sea temperature variability. Shown are sea (light blue) and air temperature variability (red), 3 d SMA wind speed (dark blue), and 3 d wind vector- variability (green). Note varying scales of plots within each panel (see above)..... 143

Figure 4-17: Extended SOM for summer months like that in Fig. 4-16, but for Sand Key SEAKEYS station (SAN F1). Some features are more prevalent in this SOM than at other reef-crest sites, e.g., patterns where sea temperature variability lags atmospheric forcing by several days..... 144

Figure 4-18: Spatial SOM on all good AVHRR SST anomaly images, i.e., with per-image mean removed, surrounding Fowey Rocks SEAKEYS station (FWYF1) for 2005. Biscayne Bay just to the west of the center in each unit is a potential source of cooler water in warm months (top units), and warmer water in winter (bottom). Color bar is not shown, but SST anomaly values correspond to a range of -3 (dark blue) to +3 K (dark red). The number “N” and percentage shown above each unit in the map refer to the number of useable synoptic images from 2005 that best matched that pattern. All axes show distance in km from the image origin at 25.22° N, 080.42° W..... 145

Figure 4-19: Spatial SOM of FWYF1 similar to Fig. 4-18, but for the year 2006. SST anomaly values shown in color range from -3 (dark blue) to +3 K (dark red). Number “N” and percentage refer to the number of useable synoptic images from 2006 that best matched that unit. All axes show distance in km from the image origin at 25.22° N, 080.42° W..... 146

Figure 4-20: SOM of SST anomaly surrounding FWYF1 during spring months (April-June) of 2005, totaling 186 useable SST images. Note the spurious feature in units at lower right of the map, highlighting the need for rigorous quality control of SST fields prior to SOM or PCA analysis. Manual removal of these features was necessary to produce the results shown in, e.g., Fig. 4-18. .... 147

Figure 4-21: Anomaly analyses for SMKF1: sea temperature,  $T_s$ ; its variability metric,  $\Theta$ ; S/RI for the “mass-coral-stress” ecoforecast (see text); the two dominant PCs from each of sea temperature PCA (Fig. 4-9) and extended PCA of  $\Theta$  and other variability metrics (Fig. 4-13); BMU from extended SOM of  $\Theta$  and other variability metrics (Fig. 4-15); and PC1 and PC2 of the equivalent  $T_s$  PCA on MLRF1. Highlighted periods are mass-bleaching summers of 1997 and 1998, bleaching event in 2005 that was moderated by hurricanes, and severe cold-snap mortality event of January 2010. .... 149

Figure 5-1: Increasingly magnified satellite SST image of the Gulf of Mexico, south Florida waters, and the Upper Keys portion of the FRT, highlighting limitations of the best available larger-scale data sets, in understanding the complex environment of the FRT. These images are 1 km resolution and are available multiple times daily subject to cloud cover. Understanding the impact on coral reefs of climate-scale variability using models with horizontal resolutions  $\sim 10^2$  km and time resolutions  $\sim 10^1$  d represents a still greater challenge. .... 166

Figure 5-2: Monthly mean sea/land-surface fields from the NOAA Climate Forecast System Reanalysis and Reforecast project (CFSRR) for December 2010. Panels include: insolation and longwave radiation, latent and sensible heat flux, net surface heat flux, and forecast SST. The Climate Forecast System and its reanalysis may provide near

real-time forcing data necessary for operational daily heat budget models utilizing the methods of the present research. .... 173

Figure 5-3: RSMAS HF WERA data field for the Straits of Florida offshore of FWYF1 (black star), April 12<sup>th</sup> 2005 18:00 local time: (a) quality-controlled surface current speed (color) and direction (arrows); (b) curl of this velocity field; (c) Okubo-Weiss Parameter (Parks, 2008) for this field. .... 176

## List of Tables

Table 2-1: Monitoring station locations, depths, and dates for which hourly <i>in situ</i> data – meteorology and sea temperature, respectively – are available. Along-shelf orientation is the assumed angle between local isobaths and True north. See also the accompanying map. ....	18
Table 2-2: Nominal measurement or modeling errors for sea temperature and other variables. ....	31
Table 2-3: Arithmetic mean and standard deviation of whole hourly records for NDBC sea temperature ( $T_s$ , °C) and CT salinity (S, PSU) at each site. ....	33
Table 2-4: Covariability: linear regression $R^2$ for change in daily mean sea temperature vs. meteorological and ocean forcing variables. ....	50
Table 3-1: Monitoring station locations as well as features of local bathymetry and benthic type, for sites where hourly <i>in situ</i> meteorological and sea temperature data are available. See also the map in Fig. 3-1, as well as information in Table 2-1 and Figure 2-1 above. ....	61
Table 3-2: Nominal measurement or modeling errors for heat budget inputs not described in Ch. 2. ....	85
Table 3-3: Numerical values of representation errors for each major term in the heat budget, estimated for site MLRF1. ....	86
Table 3-4: Results of robust regression between daily cumulative budget terms and change in daily mean sea temperature. Each field of the table gives a Scatter Index (SI%), the RMSE normalized by the standard deviation of $\Delta_{1d}T_s$ , and a bias in $K \cdot d^{-1}$ , for	

the linear regression. All daily regressions had p-statistic  $\ll 0.01$ ; however, regression results with  $R^2 < 0.20$  are shown in *gray italics*. ..... 96

Table 3-5: Sensitivity of the heat budget residual vs. observed daily variability at Molasses Reef, to changes in model parameters. .... 100

Table 3-6: Sensitivity of the heat budget residual vs. observed daily variability at Long Key, to changes in model parameters. .... 100

Table 4-1: Events of anomalous sea-temperature variability at three FRT sites for the years 2005-2008, summarized by probable forcing type (see text). ..... 129

Table A-1: Online sources for data and codes used in this work. .... 181

Table A-2: Results of robust linear regressions between data products used in the heat budget and *in situ* comparison data (see Chs. 2 and 3). Numbers shown are, in order, *bias, slope, RMSE*. ERAI for RSMAS radiative comparisons was interpolated to FWYF1, 1 km weekly composite AVHRR data for  $T_s$  gradient comparisons were interpolated to MLRF1, all other data are for station indicated. .... 182

Table A-3: Long-term seasonal and overall *median* (first value in each cell) and *interquartile range* (second value) for data products used in heat budget, interpolated to individual stations as indicated. Statistics for *in situ* depth-averaged currents from Looe Key ADCP are shown in bold; statistics for other *in situ* data not shown here are described in detail in Ch. 2. .... 183

## List of Abbreviations

$\Theta$  – sea-temperature variability metric defined as  $\mu_{3d}\sigma_{1d}T_s$  (see below)

$\alpha$  – thermal expansion coefficient

$\beta$  – maximum seafloor slope ( $\Delta z/\Delta x$ )

$\gamma$  – total insolation absorption rate

$\partial_t$  – time rate of change (per hour)

$\Delta_{1d}$  – change in daily mean

$\Delta V$  – vertical cross-shore current shear

$\nabla_h T_s$  – horizontal (x-y) gradient in  $T_s$

$\nabla_h^2 T_s$  – horizontal Laplacian:  $\nabla \cdot \nabla_h T_s$

$\varepsilon_b$  – longwave emissivity of the seafloor

$\varepsilon_w$  – longwave emissivity of sea surface

$\theta$  – hourly local solar zenith angle

$\mu_{1d}$  – daily mean of hourly value

$\rho$  – density of seawater

$\rho_b$  – mean density of seafloor substrate

$\sigma$  – estimation error (slope, bias, RMSE)

$\sigma_{1d}$  – std. deviation of 24 hourly values

$\sigma_b$  – Stefan-Boltzmann constant

$\Sigma_{1d}$  – daily sum of hourly values

$\tau$  – absorption rate of downward  $Q_{sw}$

A – broadband sea surface albedo

$A_b$  – seafloor albedo in PAR and NUV

AVHRR – Advanced Very High Resolution Radiometer aboard NOAA polar-orbiting environmental satellites

$B_0$  – sea-surface buoyancy flux /  $m^2$

C – total cloud cover [0-1]

$C_{bd}$  – benthic coefficient of drag

$C_{bh}$  – benthic heat flux coefficient

CHAMP – NOAA Coral Health and Monitoring Program at AOML

$C_p$  – specific heat capacity of seawater

$C_{pb}$  – specific heat capacity of substrate

CRM – NOAA NGDC Coastal Relief (3”-resolution bathymetry) Model

CT – conductivity-temperature sensor

CTD – conductivity-temp.-depth sensor

DRYF1 – Dry Tortugas SEAKEYS stn.

EOF – empirical orthogonal function (see PCA)

EFS – East Florida (continental) Shelf

ERA-Interim – ECMWF Reanalysis - Interim

FC – Florida Current

FIO – Florida Institute of Oceanography

FKNMS – Florida Keys National Marine Sanctuary (NOAA)

$F_q$  – varying  $\nabla_h$ SST “quality” weight  
 FRT – Florida reef tract  
 FWYF1 – Fowey Rocks SEAKEYS stn.  
 $g$  – acceleration due to gravity  
 GoM – Gulf of Mexico (model)  
 GS – Gulf Stream (system of currents)  
 $h$  – water depth experienced by a water parcel during a daily tidal excursion  
 $h_b$  – depth of thermally active substrate  
 $h_{base}$  – depth of constant substrate temp.  
 ICON – NOAA CHAMP Integrated Coral Observing Network  
 IW – internal wave  
 $K_b$  – substrate thermal conductivity  
 $K_d$  – attenuation coefficient, PAR+NUV  
 $K_h$  – Fickian heat diffusion coefficient  
 LC – Loop Current (Gulf of Mexico)  
 LONF1 – Long Key SEAKEYS stn.  
 LOOE1 – Looe Key Reef SFP buoy  
 $lp$  – low-pass (Butterworth) filtered  
 MISST – Multi-sensor Improved SST  
 MLLW – mean low-low water tide  
 MLRF1 – Molasses Reef SEAKEYS stn  
 MODIS – Moderate Resolution Imaging Spectroradiometer on Terra, Aqua sats.  
 NARR – NCEP North American Regional (atmospheric) Reanalysis  
 NCORC – NCORE site “C”  
 NCORE – National Center for Coral Reef Research (RSMAS)  
 NCORK – NCORE Key Largo site  
 NDBC – NOAA National Data Buoy Ctr  
 NGDC – NOAA National. Geodetic Data Center  
 NIR – near-infrared  
 NUV – near-ultraviolet  
 PAR – photosynthetic active radiation  
 PC – principal component  
 PCA – principal component analysis  
 $P_{PAR}, P_{NUV}, P_{pen}$  – fraction of sea-surface insolation in PAR, near UV, PAR+NUV  
 $Pr$  – total hourly precipitation  
 $q_a$  – hourly mean air specific humidity  
 $q_s$  – hourly saturated specific humidity  
 $Q_0$  – hourly net sea-surface heat flux (ex. absorption and benthic exchange)  
 $Q_b$  – net seafloor heat flux  
 $Q_{bcd}^I, Q_{bcd}^O$  – conduction in/out seabed  
 $Q_{bLW}$  – seafloor longwave flux  
 $Q_{bSH}$  – seafloor turbulent heat flux  
 $Q_{bSW}$  – seafloor shortwave heat flux  
 $Q_{LH}$  – latent (evaporative) heat flux  
 $Q_{LW}, Q_{LW}^I, Q_{LW}^O$  – longwave sea-surface heat flux (net, in, out)

$Q_{RH}$  – rain heat flux into ocean  
 $Q_{SH}$  – sensible heat flux into ocean  
 $Q_{SW}, Q_{SW}^I, Q_{SW}^O$  – shortwave sea-surface heat flux (net, in, out)  
 $R$  – convective energy dissipation rate  
 $RH$  – relative humidity  
 $RMSE$  – root mean squared error  
 $RSMAS$  – Rosenstiel School (U. Miami)  
 $S$  – salinity (PSU)  
 $SANF1$  – Sand Key SEAKEYS stn.  
 $SAR$  – synthetic-aperture radar  
 $SEAKEYS$  – FIO/NDBC program for sustained ecological research and monitoring related to management of the Florida Keys seascape  
 $SF$  – Straits of Florida  
 $SFP$  – NOAA South Florida Ecosystem Research and Monitoring Project  
 $SMA$  – simple moving average  
 $SMKF1$  – Sombrero Key SEAKEYS stn  
 $SOM$  – self-organizing (Kohonen) map  
 $SST$  – sea-surface (satellite) temperature  
 $T_a$  – hourly mean air temperature  
 $T_b$  – sea-floor substrate temperature  
 $T_{base}$  – invariant deep substrate temp.  
 $T_{cold}$  – “cool-skin” sea surface temp.  
 $T_{dew}$  – hourly dew-point temperature  
 $T_f$  – dominant periodicity of forcing  
 $T_s$  – sea temperature at sensor depth  
 $TOGA-COARE$  – Tropical Ocean Global Atmosphere – Coupled Ocean Atmosphere Response Experiment  
 $TSG$  – thermosalinograph  
 $\mathbf{u}$ , – ocean current velocity vector  
 $\mathbf{u}_{hc}$  – horizontal convection current  
 $\mathbf{u}_{sfc}$  – ocean near-surface current vector  
 $\mathbf{u}_{tide}$  – barotropic tidal current vector  
 $u_f$  – convection characteristic velocity  
 $u_{xs}, u_{ls}$  – (local) cross- and longshore ocean current vector components  
 $U_{10}, U^x_{10}, U^y_{10}$  – wind at 10 m  
 $U^{xs}_{10}, U^{ls}_{10}$  – cross- and longshore winds  
 $USF$  – University of South Florida  
 $WFS$  – West Florida (continental) Shelf  
 $w_h$  – dominant sea-surface wave height  
 $w_p$  – mean wave period [s]

## Chapter 1. Introduction

The research described herein derives from work carried out since 2006 under the Integrated Coral Observing Network (ICON) project, a part of the Coral Health and Monitoring Program (CHAMP) at the National Oceanic and Atmospheric Administration (NOAA) Atlantic Oceanographic and Meteorological Laboratory (AOML). A goal of the ICON project is to deploy autonomous scientific instrumentation, and gather additional scientific data from collaborators, in order to monitor and assess the ecological impact of physical (meteorological and oceanographic) conditions on sensitive coral reefs around the world. A physical variable with wide-ranging impact on coral reef ecology is sea temperature, and extreme variability in sea temperature in particular is known to be a significant biological stressor on corals (Baker et al. 2008).

As part of the NOAA ICON project, data transmitted in near real-time by autonomous reef monitoring stations in Florida waters and elsewhere are archived, and those archived data are processed and analyzed. Hourly *in situ* sea temperature data from stations in the Florida Keys shows intermittent events of unusually high periodic variability, having periods between 12 and approximately 30 h, and lasting from three to more than 14 d. Furthermore, examining high-resolution satellite (ocean temperature and color) imagery of the Straits of Florida (SF), signatures can often be observed of apparent cyclonic circulation offshore of these Florida Keys monitoring sites. In a systematic analysis, Gramer and colleagues (Gramer et al. 2009; see also Chapter 4 below) found that a substantial fraction of events of high sea-temperature variability at these Keys sites coincide with satellite imagery suggesting cyclonic vortices immediately offshore. A

more rigorous analysis of sea temperature variability on the Florida reefs was suggested by these findings, resulting in the present research.

A further motivation for this work is to refine a system of automated alerts for thermal variability on coral reefs, as well as the potential exchange of nutrients and reproductive material between the reef and offshore waters which can be correlated with such variability. These automated *ecological forecast* alerts have been provided by email and the Web to scientific researchers, public resource management authorities, and commercial interests as part of ICON's funded mandate since the 1990s. Results of the analysis described here have been synthesized into a set of "expert-system rules" to automatically match patterns in near real-time data for FRT autonomous monitoring sites. Such rule-based ecological forecast models (Guimaraes et al. 2001; Hendee et al. 2001; Hendee et al. 2007; Gramer et al. 2009) are an integral part of the ICON project.

## **1. Geographical Context**

The Florida reef tract (FRT) is a narrow barrier and patch reef system that is less than 10 km offshore of southeastern Florida and the Florida Keys. The structures of the FRT consist of both paleoreefs and living corals, in either of barrier-reef or patch-reef configurations, as well as hard-bottom, sand, and seagrass bed habitats. The FRT extends almost 500 km from the Dry Tortugas west of Key West, to Martin County north of Palm Beach. The ecological and economic importance of the FRT is considerable. Studies of human uses of the FRT and associated ecosystems indicate that this fragile marine environment may contribute as much as US \$6 billion per annum to the regional economy (Causey 2002; Johns et al. 2004; Johns et al. 2001). The FRT may also represent a critical *refugium* for corals and associated organisms of the Caribbean and

Gulf of Mexico, under scenarios of rapid climatic change (Manzello et al. 2012; Riegl et al. 2009). Effective management of the reefs and related ecosystems within Florida Keys National Marine Sanctuary (FKNMS) and the other parts of the Marine Protected Area (MPA) network associated with the FRT will depend critically on a detailed, quantitative understanding of the physical environment (Keller et al. 2009). Thermal and photo-thermal stresses are major factors influencing the health and management of coral reef ecosystems. Observations of and physical insights into sea temperature variability are needed for natural-resources managers in the FRT to identify reef areas that are less prone to temperature extremes and associated ecological impacts (Baker et al. 2008; Baskett et al. 2010; Graham et al. 2008; Hoegh-Guldberg et al. 2005; Lirman et al. 2011; Maynard et al. 2010; Yee et al. 2008).

Coastal ocean physical regimes in the FRT vary strongly with both the distance from shore, and with relative position alongshore on the tract. The marine geography of the FRT can be separated roughly into six alongshore sub-regions – please refer to Fig. 1-1. These sub-regions are distinguished by differences in the size of land masses inshore (Burpee 1979; Peng et al. 1999; Haus et al. 2004), the volume of transport through water channels that cut through those landmasses (Smith 1998; Lee and Smith 2002; Smith 2002; Smith and Lee 2003), the orientation of the coastline relative to dominant seasonal wind direction (Lee and Williams 1999), the relative breadth and depth of offshore topography, and the relationship between that topography and the Florida Current (FC), a component of the Western Boundary Current system of the northern sub-tropical Atlantic gyre (ibid.). These distinct cross-shore sub-regions are: (1) the Dry Tortugas and “Quick-sands”, (2) the Lower, (3) Middle, and (4) Upper Florida Keys, (5) Biscayne Bay and

waters off of the coast of mainland Monroe and Miami-Dade counties, and (6) the narrow stretch of the East Florida Shelf (EFS) off of Broward, Palm Beach and Martin counties.

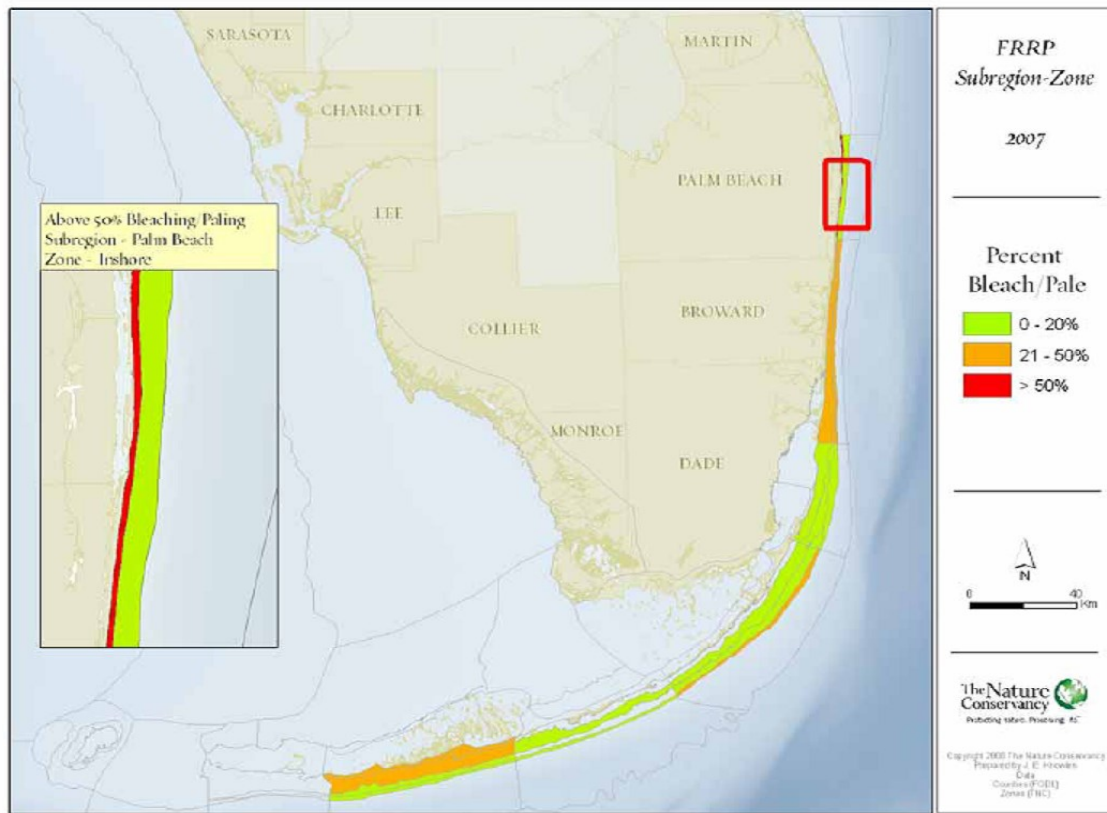


**Figure 1-1: Map showing boundaries of alongshore sub-regions and cross-shore reef zones within the FRT described in the text. Maps are used with permission of The Nature Conservancy – Florida Reef Resilience Program (FRRP); colors represent incidence of diver-observed coral bleaching and paling during summer 2007. Inset is northern region of the FRT, showing narrow cross-shore zones.**

Apart from alongshore distinctions, the FRT can also be divided into five narrow cross-shore zones, based on bottom topography, geomorphology, and benthic habitat type (Lidz et al. 2006; Finkl and Andrews 2008; Walker et al. 2008; Smith et al. 2011). For the discussion that follows, please refer to Fig. 1-1 and Fig. 1-2, as well as to Table 2-1 and Table 3-1 and their accompanying maps below. These five cross-shore zones lie, respectively:

- i) Near-shore, within 2 km or less of shore: Bands of mangrove and sea grass habitat, interrupted by developed land (especially in the northern FRT) and by tidal

channels and broader “bridge channels” (especially in the Tortugas, Lower and Middle Keys);

ii) Mid-shelf, from 1 to more than 6 km offshore: The mid-shelf consists of Hawk Channel and other shallow (5 to 15 m depth) channels overlaying hard and sandy bottom, interspersed with patch reefs and sea grass beds – in the north this represents a very narrow zone of gently sloping bottom behind the outer reefs;

iii) Reef-crest, approximately 8 km offshore in the Florida Keys, but as close as 2 km to shore in the northern FRT: A narrow “outer shelf” in many places only a few hundred meters wide, formed by the crest of the barrier reef (or elongated patch reefs in the northern FRT), reaching a minimum depth of between 2 and 20 m;

iv) Reef-slope, approximately 9 km offshore in the lower FRT, just 3-4 km offshore in the north: A steeply inclined, topographically complex fore-reef or “continental” slope, where the “shelf-break” may be identified with the 30 m isobath;

v) Finally, anywhere from 4 to 10 km offshore: A group of deeper (150 to 300 m) stepped marine terraces, such as Pourtalès Terrace off the Middle and Upper Florida Keys (Lee et al. 1992), Miami Terrace offshore of Miami, or the complex of unnamed terraces offshore of the other mainland counties (Finkl and Andrews 2008).

Offshore in the SF, a cyclonically-bending channel, the ~100 km wide FC periodically meanders over the slopes and terraces of zones (iv) and (v). Beneath the FC is the cold and relatively fresh (salinity < 34 PSU) Antarctic Intermediate Water (AAIW) from the Southern Ocean (Schmitz 1996). The AAIW may be a source watermass to the terraces of zone (v) and even waters further inshore, during periods of extreme upwelling.

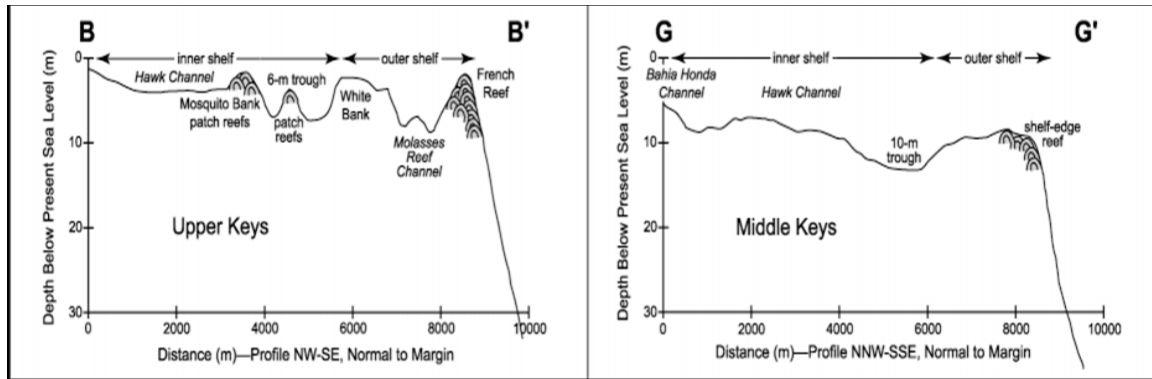


**Figure 1-2: Representative cross-shore sections of seafloor topography from the Middle and Upper Florida Keys, illustrating the zones (i) through (iv) described in text – from the shore outward, to the upper section of the fore-reef slope (30 m isobath). Cross-shore distance (m) is shown on the x-axis, seafloor depth along the y-axis. Derived from Lidz et al. (2006), their Fig. 13; used with permission.**

## 2. Near-shore Oceanography

In zones (i) and (ii), the near-shore and mid-shelf, studies (Lee and Williams 1999; Haus et al. 2004; Fiechter et al. 2008) find strong correlations between local wind forcing and coastal ocean circulation at weekly to annual periods. The forcing mechanisms underlying such correlations include Stokes drift (surface-wave residual transport), and wind-driven transport consistent with an Ekman layer over shallow water (Graber et al. 1997; Haus et al. 2004; Mao and Heron 2008). Tides and direct air-sea fluxes play a role in the oceanographic variability of these zones as well. Katsaros et al. (2005) find significant horizontal gradients in diurnal variability of air-sea flux and wind-driven mixing over the inner and middle shelf of the FRT. In a study of the West Florida Shelf (WFS), Virmani and Weisberg (2005) also find small scales of air-sea flux variability there.

Pitts (2002) observed strong tidal flows near shore and in mid-shelf channels of the Lower Keys and reefs to their west. Other studies have shown the importance of tidal

forcing in Biscayne Bay (Wang and Vandekreeke 1986), and the mid-shelf zones in the Middle (Shay et al. 1998) and Upper Keys (Haus et al. 2000). Tidal currents also enhance mixing in the near-shore environment (Wang et al. 2003). Other influences on the near-shore environment include surface-wave breaking, and groundwater discharge through the porous substrate (Caccia and Boyer 2007; Lirman et al. 2008). A recent study by Stalker et al. (2009) finds that groundwater may account for 10% of the freshwater input into Biscayne Bay overall. Finally, in the northern FRT, surface wave breaking near-shore is likely to force flows, mixing, and sediment transport among nearby patch reefs.

### **3. Offshore Oceanography**

Offshore of the reef crest in cross-shore zones (iv) and (v), oceanographic variability is strongly influenced by the FC, its cross-isobath meanders (Smith 1983; Lee et al. 1995; Peters et al. 2002; Davis et al. 2008), and smaller dynamical features associated with the cyclonic FC front such as mesoscale eddies (Lee 1975; Lee et al. 1994; Fratantoni et al. 1998; Hitchcock et al. 2005), and smaller-scale (length ~ 1-10 km) vortices (Haus et al. 2000; Yeung et al. 2001; Shay et al. 2003; Sponaugle et al. 2005; Criales et al. 2007; Richardson 2007). These dynamical features can frequently be tracked via satellite through the SF by their transport of anomalously warm or cool water, and of particulates and biomass (ocean color observations, e.g., Fig. 1-3). The cyclonic front of the FC is defined by an area of strong current shear, cyclonic vorticity, and steeply sloping isopycnals along the edge of the FC nearest the U.S. continental shelf.

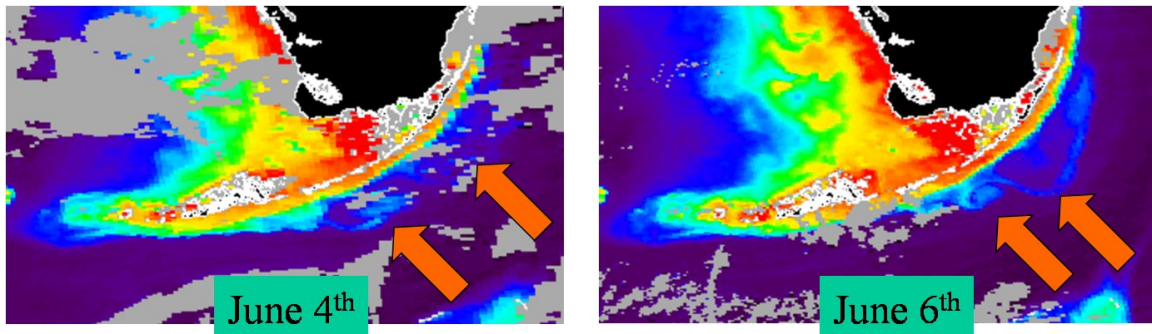


**Figure 1-3: A pair of distinct cyclonic vortices interacting in the Straits of Florida (SF) in 2006. Vortices have similar horizontal scales ( $L \sim 30$  km), but different translational velocities. Chlorophyll *a* 1 km-resolution product derived from MODIS ocean color (USF 2012); clouds are gray, land black.**

In the area between the FC front and the reefs, vortices may exhibit complex interactions with one another (Fig. 1-3), and with the complex, rapidly sloping, corrugated bottom topography of the FRT (Fig. 1-2). An example of such a non-linear process that may be a direct result of interaction between vortices and FRT topography are so-called “bleeding eddies” – coast-hugging bands of water with cool surface temperatures and positive vorticity, that may stretch from a mesoscale eddy off the Keys 100 km or more “downstream” (i.e., eastward and northward) along a substantial portion of the entire length of the FRT. These cool water bands may in fact be a common occurrence in the FRT (see Chapter 4).

At still smaller spatial scales (length  $\sim 100$  m to 1 km), near-inertial and other internal waves (IWs) have been observed over the reef slope and over more exposed areas just inshore of it (Shay et al. 1998; Soloviev et al. 2003; Parks 2008). IWs are observed to break on the steeply shoaling topography of zone (iv), dominating thermal variability at certain times of the year (Leichter et al. 1996; Leichter et al. 1998; Leichter and Miller 1999; Leichter et al. 2005; Davis et al. 2008). Breaking IWs are observed at depths from 20 to below 80 m, with periodicities from near-inertial ( $<30$  h) to less than 5 h. Leichter et al. (2005) and Soloviev et al. (2003) both find the prevalence of internal

oscillations in the FRT to be correlated with seasonal patterns of density stratification in the deeper waters of zones (iv) and (v) offshore. Breaking IWs have also been implicated as a significant forcing mechanism for cross-shelf transport in the Lower Keys and Dry Tortugas (Crales et al. 2007).

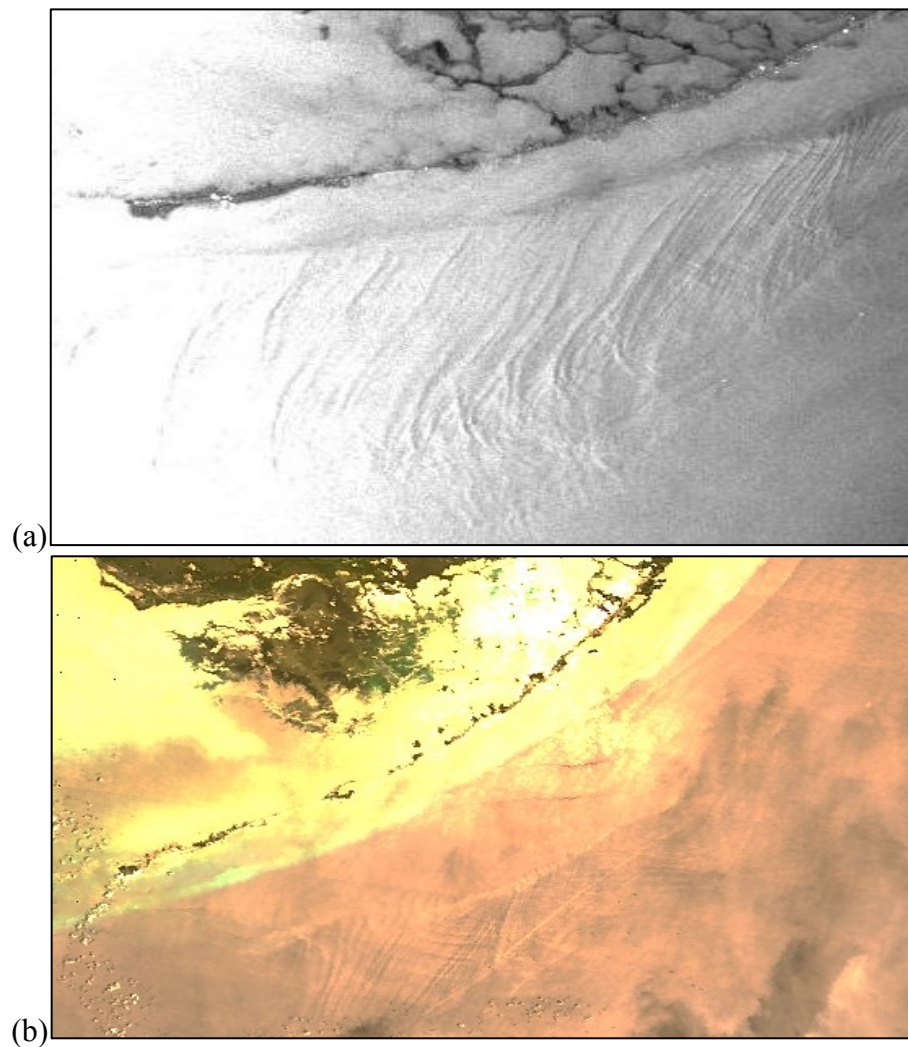


**Figure 1-4: (a) EnviSat Advanced Synthetic Aperture Radar (ASAR) alternating polarization image of southern Straits of Florida from 2006-06-14 03:16 GMT, showing an energetic field of IWs exhibiting refraction, attenuation, and reflection related to mean-current shear and topography (ESA 2009). (b) USF MODIS true color image from 2010-04-28 16:11:39 GMT, showing IW trains similar to that in Fig. 1-4a, propagating east-west along the SF. IWs show up in this image against the background of sun-glint on the ocean in the Straits.**

In satellite-derived imagery like Fig. 1-4, trains of IWs are observable in the SF, e.g., during periods when tropical cyclones pass through the Gulf of Mexico. IW patterns in radar and sun-glint images are the result of small-scale surface waves being attenuated by surface convergence/divergence resulting from IW propagation – i.e., sub-surface IW motion modifying sea-surface roughness (Alpers 1985). Note that such IW trains moving over the sloping seafloor will tend to refract toward the crest-line of the FRT, as in Fig. 1-4. Furthermore, research (Davis et al. 2008; Xu et al. 2008) suggests that the interaction of oceanic eddies with both seafloor topography and strongly-sheared mean currents may excite packets of internal waves in the coastal environment. Vortices and IWs both represent important mid-scale connections, linking regional- and larger-scale circulation with smaller, “reef-scale” oceanographic variability at the reef-slope and reef-crest.

#### **4. Reef-crest Oceanography**

The “outer shelf” or reef-crest, zone (iii), is where most of the automated ocean monitoring stations in the FRT are situated. Local forcing such as surface wave setup, air-sea flux, and Stokes drift may frequently dominate circulation on the reef-crest (Hearn 2008). The effect of sea-surface insolation at shallow sites such as reefs may also depend on attenuation of radiation in the water column, and reflectivity and scatter at the seabed.

Over most of the length of the FRT, the crest itself is too shallow to admit direct lateral passage of vortices, internal waves, or Ekman transport from offshore. However, in some stretches of the FRT, the reef-crest may be too deep to cause breaking of long surface waves (swell). There, internal waves incident at very shallow angles may

propagate further inshore, and the sea-level setup or set-down associated with offshore eddies may directly impact circulation within the shelf.

Upwelling can occur near the reef-crest due to a variety of mechanisms (Hu et al. 2009). Besides coastal Ekman divergence and internal wave breaking, numerical experiments and observations demonstrate that both mesoscale-eddy dynamics (McGillicuddy et al. 1998; Xu et al. 2008), and interaction between a sheared mean flow like the FC and a shoaling, corrugated sea bottom (MacCready and Pawlak 2001; Legg 2004), may cause upwelling, as well as vertical mixing. Conditions on the reef slope of the FRT may be conducive to all of these dynamic processes.

In summary, potential forcing regimes at the reef-crest of the FRT (Fig. 1-5 illustrates some of these) are, from smallest to largest spatial scale:

- Heating/cooling of the water column from below by seafloor heat exchanges, including reflected insolation and ground-water discharge;
- Heating/cooling of water column by air-sea heat fluxes and direct insolation;
- Variations in the absorption and scatter profile of insolation within the water column – recent research at USF (Barnes et al. 2013; Zhao et al. 2013) using 1 km-resolution satellite ocean color data shows distinct patterns of annual and geographic variability in light attenuation throughout the FRT, yet no research has been published to date relating this sub-surface light attenuation to oceanographic variability;
- Cross-shore Stokes (wave-forced) drift, and potentially Langmuir circulation where water depths allow Langmuir cells to fully develop;

- Swell breaking at the reef crest, with associated pressure setup and cross-shelf transport (Wolanski 1986; Jago et al. 2007; Hench et al. 2008), as well as enhanced vertical mixing (Skirving et al. 2004; Heron et al. 2008);
- Ekman (wind stress-forced) transport cross-shore, with associated upwelling, downwelling, and horizontal advection of sea-temperature and other gradients – such events may also enhance horizontal mixing over the slope;
- Barotropic tidal forcing (Pitts 1997) resulting in residual transports of heat, nutrients, and particulates near the bottom boundary layer – this residual tidal flow may combine with wind-driven transport from other alongshore sub-regions and cross-shore zones, e.g., including inter-island channels;
- Shoaling and breaking on the reef-slope of internal waves, forced by winds, barotropic or baroclinic tides – shoaling may both refract internal waves onto the shelf break just below the reef crest itself, and increase wave periodicities as a result of wave-breaking at the critical slope on the topography;
- Forcing by cyclonic eddies interacting with the reef slope, causing mixing, and generation of smaller anti-cyclones and internal waves, e.g., along corrugations in the reef-slope topography;
- Forcing by FC meanders interacting with the terraces and the reef slope, causing mixing, vortex shedding, and internal wave generation on the topography as well as direct transport;
- Transport of anomalous (warm, cool, saline, fresh or eutrophic) water from regions upstream of the FRT. Such episodic events can include: WFS water flowing through Dry Tortugas and Marquesas; translation of larger eddies into the SF (Fratantoni

et al. 1998); LC “short-circuiting” from the Yucatan channel to the SF in the wake of LC ring-shedding events (ibid.; EM Johns pers. comm. based on drifter data only; DB Olson pers. comm.); or transport of Mississippi or Atchafalaya River water into the SF (Ortner et al. 1995; Gilbert et al. 1996; Hu et al. 2005a).

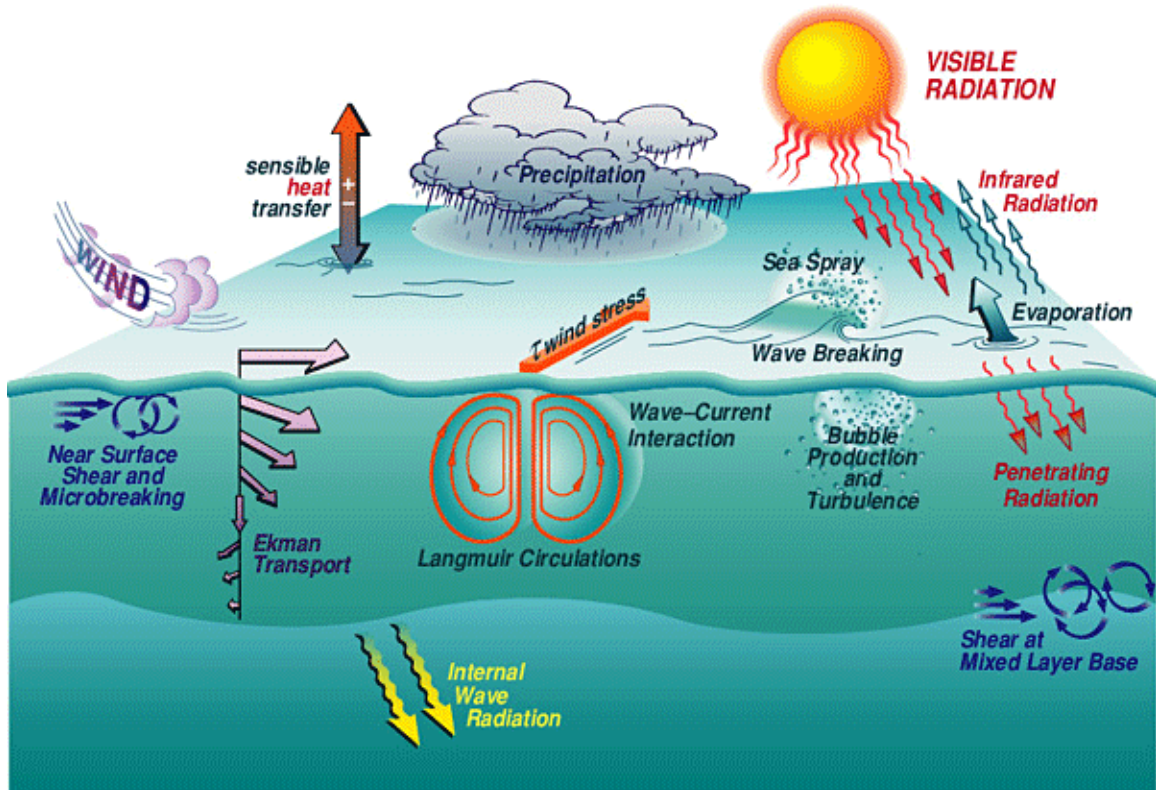


Figure 1-5: Schematic of upper-ocean processes driving sea temperature variability in the open ocean (courtesy of R. Weller, WHOI, <http://uop.who.edu>, used with permission). However, as noted in the text, additional processes not shown here will also operate over shallow, sloping seafloor topography like that in the FRT, e.g., seafloor reflection, benthic heat exchange, varying light attenuation within the water-column, and *horizontal convection* (see Ch. 3).

## 5. Research Questions

The research described here does not seek to characterize in detail the complex hydrodynamic processes outlined above. Rather, it first quantifies the other important forcing mechanisms for sea-temperature variability near the reef crest and elsewhere, including vertical heat fluxes, and larger-scale heat advection and heat diffusion. As a final step in that research, however, the frequency of events of sea-temperature variability not adequately explained by such other mechanisms are examined, and available satellite and model products are used to characterize the patterns of near-surface sea temperature, ocean color, and circulation coincident with these events.

The goals of the present research are to document and explain the dominant frequencies and modes of ocean thermal variability at distinct sites within the FRT, to identify extreme events in that variability, and to characterize those features of variability using a combination of satellite, model, reanalysis, and *in situ* data. In particular, the covariability between observed sea temperature and estimated effects from various forcing mechanisms are directly investigated using available observations.

In detail, the following questions are answered by the present research:

- 1) What is the spectrum of sea temperature at monitored coral-reef sites in and around the FRT? What are the dominant temporal modes and most common temporal patterns in this thermal variability, at each of super- and near-inertial, weather-band, annual, and interannual periodicities, respectively? How do the dominant modes and patterns in each passband differ at different sites along the reef crest, and how do they differ from patterns of variability at similar frequencies for locations inshore of the FRT (Hawk Channel and Florida Bay)?

2) What are the dominant patterns of variability in wind stress and air-sea heat flux at each of these reef monitoring sites? Show that sufficient data (*in situ*, model, reanalysis, and satellite) are available from multiple monitoring sites, to calculate climatology time series of each of the air-sea forcing terms (short- and longwave, sensible, and latent heat flux terms) in the reef heat budget for those sites. What portion of the thermal variability at each site, in each of the frequency bands in question (Question 1), can be explained by these individual heat budget forcing terms?

3) Kilometer-resolution satellite SST data are currently available for the FRT. Do these data correlate significantly with data from collocated benthic and mid-water sea temperature sensors? What spatiotemporal filtering methodologies yield the best correlation between these satellite and bulk sea temperatures? How does the filtering method or the quality of the best fit vary, between the reef crest and other monitored sites inshore of the FRT? Are horizontal gradients calculated from the filtered satellite data at sites analyzed in question (2), sufficient to calculate a climatology of the heat mixing and advection terms in the heat budget for those sites? What data are available that will allow near-surface currents and transports to be estimated at these sites, and what is the reliability of such estimates? What portion of thermal variability at longer periods for each site can be explained by these advection and mixing terms?

4) Does the net heat budget estimate from questions (2) and (3) “close”, within the estimated error bands? In other words, does an annual climatology of this total heat budget produce a net heating and cooling whose sum within the estimated error is equivalent to zero (or to the observed interannual trend, if one exists)? Furthermore, does the amplitude and phase of this estimated heat budget climatology match amplitude and

phase for the observed sea temperature at each site? Based on previous research at other shallow-water sites (Evans et al. 1998; Nihei et al. 2002; Monismith et al. 2006; Cardenas and Wilson 2007), it is expected that air-sea fluxes and larger-scale advection and mixing alone cannot balance the heat budget. Thus, the impact of smaller-scale processes on the heat balance must be quantified, including a model of heat exchange with the seafloor, and a horizontal-convection process termed the "thermal siphon" (Monismith et al. *ibid.*).

5) Events of extreme sea temperature variability are apparent from *in situ* data at the reef crest (Ch. 3, Ch. 4). What portion of such extreme variability can be explained by terms in the heat budget calculated in questions (2)-(4)? When events of extreme *in situ* sea temperature variability are not well explained by the heat budget, can available *in situ*, satellite, and model data distinguish patterns of vertical mixing (mixed-layer deepening), upwelling, or other physical processes that explain such variability?

An overriding question which the research described here addresses is whether existing observational systems (*in situ*, remote sensing) and hydrodynamic modeling provide a reliable, spatially coherent, and sufficiently high-resolution picture of dominant forcing mechanisms for sea-temperature variability and thermal stress on Florida reefs? The answer relies on the inherent time and spatial scales of forcing found by the present research to be significant to sea-temperature variability at different sites. The models and codes to answer these questions furthermore provide a fresh starting point from which to analyze thermal variability at other shallow-water coral reefs near continental margins, e.g., Gulf of Mexico, western Caribbean, Australia (Great Barrier Reef, Ningaloo). Such geographic expansion offers a promising direction for future research based on this work.

## Chapter 2. Analysis of Variability and Covariability

Variability in 5- to 25-year records of hourly mean *in situ* sea temperature from a network of monitoring stations at diverse shallow-water habitats in the FRT is analyzed. Tidal, diurnal, and annual periodicities generally dominate, with “weather band” (3-42 d) variability most apparent at one site near shore, and inertial-period variability apparent at one offshore site near the shelf break. A statistically significant interannual warming trend is also observed at this one offshore site only. Data for estimating atmospheric forcing, incident sea-surface radiation, water depth, ocean currents, and sea-surface temperature gradients are then evaluated and analyzed from *in situ* measurements and other data sources. Significant covariability between sea temperature and some of these other variables is found, but this covariability itself varies with an annual period, and differs between topographically distinct sites. Differences in dominant physical forcing mechanisms are hypothesized to explain these differences in covariability between seasons and between sites.

SEAKEYS is a network of autonomous Coastal Marine Automated Network (C-MAN) stations that have been jointly maintained by the Florida Institute of Oceanography (FIO; Ogden et al. 1994) and the U.S. National Oceanic and Atmospheric Administration (NOAA) National Data Buoy Center (NDBC). Hourly mean wind speed and direction, barometric pressure, air and sea temperature, and in some cases dew-point temperature and tide height, at shallow sites both near shore and on the reef crest of the FRT, were measured and transmitted via satellite from 1987 to 2012. Hourly mean data from independent additional conductivity-temperature (CT) and light sensors deployed at

SEAKEYS sites have also been quality-controlled and archived since 2001 by the Coral Health and Monitoring Program / Integrated Coral Observing Network (CHAMP/ICON) at NOAA Atlantic Oceanographic and Meteorological Labs (AOML). The NOAA/AOML South Florida Ecosystem Research and Monitoring Project (SFP) carried out bimonthly shipboard surveys of the coastal physical oceanography, chemistry, and microbiology of the FRT from 1995 to 2012. In addition, the SFP has maintained oceanographic monitoring stations at several sites within the FRT, recording hourly ocean current profiles, sea temperature, and other variables. Table 2-1 and the accompanying map summarize the locations and available *in situ* data for the specific SEAKEYS/AOML and SFP autonomous monitoring stations discussed in this text.

**Table 2-1: Monitoring station locations, depths, and dates for which hourly *in situ* data – meteorology and sea temperature, respectively – are available. Along-shelf orientation is the assumed angle between local isobaths and True north. See also the accompanying map.**

<i>Station code</i>	<i>Name, type of installation</i>	<i>Latitude, Longitude °</i>	<i>Along-shelf orientation °T</i>	<i>Sea temperature sensor depth</i>	<i>Data dates: sea temp., meteorology</i>	<i>Other sensors</i>
FWYF1	Fowey Rocks, reef crest light.	25.590, -80.097	2	2.0 m	1991- 2013, 1991- 2013	CT
MLRF1	Molasses Reef, reef crest light.	25.010, -80.380	54	2.7 m	1987- 2013, 1987- 2013	Light (PAR, NUV), CT
LONF1	Long Key, Bay-side day marker	24.840, -80.860	(0)	1.3 m	1992- 2013, 1992- 2011	CT, tide, dew point
SMKF1	Sombrero Key, reef crest light.	24.628, -81.111	65	2.0 m	1988-2008, 1988-2012	CT, tide, dew point
LOOE1	Looe Key Reef, fore-reef slope buoy	24.543, -81.402	73	5.0 m, 22.0 m	2005-2010, –	CTD, ocean currents
SANF1	Sand Key, reef crest light.	24.460, -81.880	82	1.0 m	1991-2005, 1991-2012	CT
DRYF1	Dry Tortugas, reef shallows.	24.638, -82.862	(58)	1.0 m	1992-2005, 1992-2005	CT

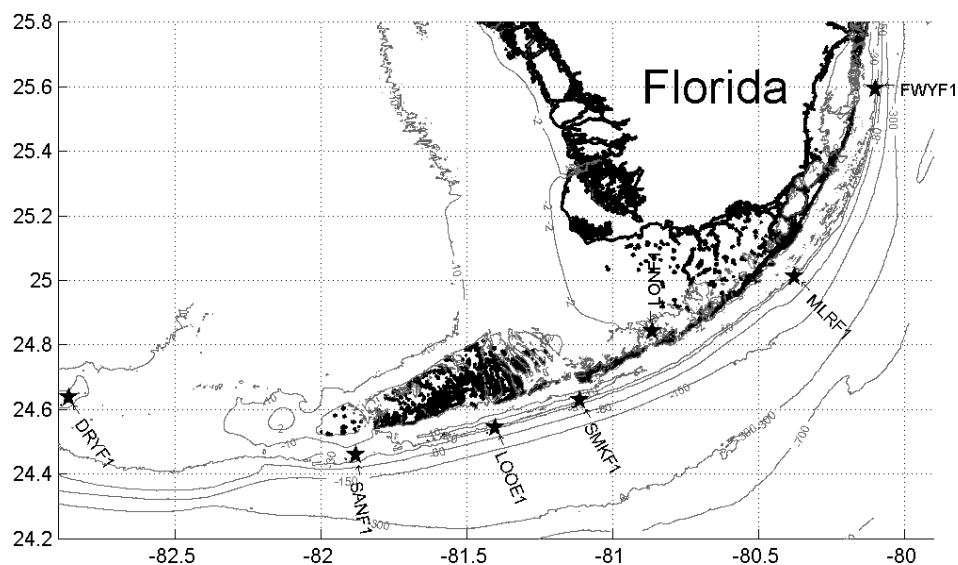


**Figure 2-1: Map of southern portions of Florida and the Florida Shelf, showing position of SEAKEYS and SFP automated monitoring stations along the FRT (stars). Stations are indicated by 5-letter code as described in the text and in Table 2-1. Coastline is in black, outlines of the 2, 10, 30, 80, 150, 300, and 700 m isobaths from NGDC 3" CRM bathymetry (see text) are shown in gray.**

These *in situ* measurements were integrated with data derived from atmospheric reanalyses, a high spatial-resolution satellite sea-surface temperature (SST) product, moderate-resolution coastal bathymetry model, an ocean tidal solution, and operational models of ocean surface waves. Integrated data were used to estimate radiative fluxes at the sea surface, sea state and albedo, near-surface ocean currents, and sea-temperature gradients surrounding the *in situ* monitoring sites. For comparison, data were also analyzed from a moderate resolution assimilating ocean model for the Gulf of Mexico and Florida, and a higher-resolution non-assimilating model for the Florida Keys. A guiding aim of these analyses has been to produce a budget of ocean heating, capable of explaining the observed sea temperature variability (see Chapter 3 of this work, referred to hereafter as “Ch. 3”, and Gramer and Mariano in prep., hereafter “GM2”).

## 1. Data and Methods

### *In situ Sensors*

For SEAKEYS stations, whose site depths range from 1.5 to 3 m, data already quality-controlled by NDBC were used (Gilhousen 1988,1998), with additional removal of suspect data for the present study. Sea temperature at SEAKEYS sites was measured by two sensors: one, a conductivity-temperature (CT) instrument from Falmouth Scientific, Inc. (now Teledyne-RDI), calibrated biannually with nominal accuracy 0.005 °C, reported hourly mean temperatures to 0.01 °C precision. Secondly, a thermistor was deployed suspended in thermally conductive fluid, nearly filling a metal canister that extends through ~1 m of the shallow water column, with nominal accuracy 0.08 °C and temperatures reported to 0.1 °C. The latter “NDBC sea temperature sensors” provided a longer, more complete record than CT; these data were used in the present study. SEAKEYS CT sea temperatures were used only as an independent check on NDBC temperatures, e.g., in the error analysis below; CT salinity values were also analyzed.

Two sea-temperature measurement records were analyzed from the SFP station in ~23 m of water off of Looe Key (“LOOE1”), from a Sea-Bird SBE 37-SM MicroCAT with <0.01 °C accuracy at 5 m depth, and from a thermistor with nominal precision 0.4 °C incorporated into the bottom-mounted Teledyne RDI 600 KHz acoustic Doppler current profiler (ADCP) at 22 m. The ADCP also provided hourly ocean current profiles in 0.75 m bins from 2.1 to approximately 22 m above bottom (1–2 m below the sea surface), for the period 2004 Nov 05 to 2010 Feb 10; near-surface and near-bottom six-bin (4.5 m) averages and whole-water column means were examined. Similar to other sites (see below), a cross- and along-shelf (isobath) reference frame was used by rotating all *in situ*

current vectors 73 °T (Lee and Williams 1999). Quality control of these SFP temperature and currents data were applied for the present study by incorporating procedures recommended by Ryan H. Smith (pers. comm.), including removal from ensemble average currents of bins with “percentage good” return less than 50%, and of “surface” and side-lobe contaminated bins based on echo-amplitude and current-profile spikes. In addition, a subset of 1-minute data gathered by thermosalinograph (TSG) aboard R/V Calanus and R/V F. G. Walton Smith during SFP’s bimonthly cruises in 1995-2010 were used, to validate satellite-derived cross-shore sea-temperature gradients near each site (see Appendices).

Approximately seven years of *in situ* data (2004-2011) from the University of Miami’s Rosenstiel School of Marine and Atmospheric Science (RSMAS) were analyzed for precipitation and downward short- and longwave radiative flux. These data, recorded once each two minutes by a monitoring station at RSMAS 17 km inshore of the FRT, were courtesy of Dr. P. Minnett (pers. comm.). Approximately two months of hourly *in situ* wave data from March to May 2005 at three RSMAS monitoring sites off Biscayne Bay courtesy of Dr. B. Haus were also analyzed (Wang 2008; Haus et al. 2010, their Fig. 3b, sites TAB-N, TAB-S, and WADP). Additional quality-control procedures were applied to both of the above RSMAS datasets for the present study. These RSMAS data were used to estimate empirical adjustments and verify error estimates for reanalysis and wave model data (see Appendices).

### *Other Data Sources*

Other large-scale gridded data products were used and evaluated in the present study to replace *in situ* measurements that were either not available or had significant time gaps; it was also hoped these products would prove useful in understanding sea temperature variability at other sites where meteorological monitoring has not been done. Six-hourly atmospheric forecast and radiative analysis fields from the European Centre for Medium-range Weather Forecasting (ECMWF) Reanalysis – Interim ("ERA-Interim", Berrisford et al. 2009; Dee and Uppala 2009; Dee et al. 2011) were extracted for the following variables: 10 m winds, surface (2 m) air temperature, downward shortwave radiative flux (insolation), downward longwave radiative flux, specific humidity, barometric pressure, total cloud cover, and atmospheric planetary boundary layer height. Although hourly barometric pressure was measured at SEAKEYS sites, there were sufficient time gaps in those quality-controlled time series that surface atmospheric pressure from ERA-Interim was used for this study. A 1.5x1.5°-subsamped grid of the ERA-Interim was subset for a 10° radius around southern Florida for 1989-2011, and downscaled to individual reef sites by bilinear spatial interpolation. These four-times-daily cumulative-sum time series were then interpolated to hourly values using a cubic spline fit.

Net short- and longwave sea-surface fluxes ( $Q_{SW}$  and  $Q_{LW}$ , respectively) are the sum of components into (downward) and out (upward) of the ocean:  $Q_{SW} = Q_{SW}^I - Q_{SW}^O$ ,  $Q_{LW} = Q_{LW}^I - Q_{LW}^O$ . Downward fluxes into the ocean  $Q_{SW}^I$  and  $Q_{LW}^I$  were extracted directly from ERA-Interim. In order to improve their application in understanding sea temperature variability, a linear correction was applied to both short- and longwave downward fluxes from ERA-Interim for all sites (Gramer in prep.), based on robust linear regressions of these reanalysis data against hourly averages from quality-controlled direct

insolation and longwave measurements in the RSMAS rooftop dataset. The slope of the best ERAI-*in situ* fit was found to vary by time of year (op. cit.). This variation may be related to seasonal differences in errors for the mean altitude and prevalence of daytime cloud cover (significant factors affecting downward radiative fluxes) in southern Florida. In particular during the warmest months of July-September (JAS), the large slope correction and negative bias in uncorrected reanalysis  $Q_{LW}^I$  may be because it significantly underestimates cloud-cover related to the marine layer and atmospheric convection, e.g., from thunderstorms forming over mainland Florida and the Straits of Florida. This is also supported by the analysis of insolation and visible light data (op. cit.), where a summer-time drop in measured *in situ* light is not well represented by reanalysis data.

Upward longwave flux  $Q_{LW}^O$  was not estimated at this stage of the research, as its calculation requires an estimate of the “cool-skin” effect (see Ch. 3). Insolation reflected by the sea-surface was calculated assuming a simple time-varying shortwave sea-surface albedo  $A$ , as  $Q_{SW}^O = A \cdot Q_{SW}^I$ . Albedo  $A$  was estimated from ERAI significant wave height and total cloud cover, and time of day, using the empirical relationship described in Jin et al. (2011). Summer-time mid-day mean  $A$  at all sites varied from 4% to 8%, while estimates from other sources including those from ERAI vary between 4% and 8%. Uncertainty in  $A$  was thus set at a constant factor of 4% of  $Q_{SW}^I$ . Unlike in other studies (e.g., MacKellar et al. 2012), this albedo  $A$  is not intended to account for reflection or scatter of sunlight below the upper ~1 m of the water-column. Such total reflectivity is estimated in Ch. 3, for comparison with MacKellar et al. (op. cit.) and other studies.

A significant concern in the present analysis was the quality of the meteorological and other data interpolated from ERAI due to its low spatial-resolution (1.5°). The six-hourly North American Regional Reanalysis (NARR; Mesinger et al. 2006) from the NOAA National Centers for Environmental Prediction (NCEP) is a regional reanalysis product at higher horizontal resolution (32 km) than ERAI. Significant biases have been found in cloud-cover and radiance data from both the ERAI (Betts et al. 2009; Dee and Uppala 2009; Markovic et al. 2009; Dee et al. 2011) and NARR (Derber and Wu 1998; McNally et al. 2000; Markovic et al. 2009). However, Markovic et al. (2009) find significantly smaller bias and scatter vs. *in situ* data in ERA40 (a long-term reanalysis covering 1957-2002, which is now being continued forward to the present in the form of the ERAI), as compared to NARR for the same comparison years (1996-2001). For the present study, regression RMSE vs. *in situ* data for insolation, downward longwave flux, and various meteorological variables from NARR were also found to be significantly larger at all sites than those from ERAI (see Appendices). ERAI downward radiative fluxes for this region also compared favorably with the International Satellite Cloud Climatology Project (ISCCP) of Zhang et al. (2004).

The atmospheric reanalyses analyzed in the present study incorporate land-based measurements. A study by Virmani and Weisberg (2005) found that the use of land-based measurements to estimate specific humidity over marine coastal areas may introduce significant biases. Their study examined sites on the West Florida Shelf, but the results highlight the possibility of similar issues with estimating specific humidity from reanalysis for sites in the FRT. In the measurement errors analysis below, a limited record of SEAKEYS *in situ* dew point temperatures were used to estimate the effect of

this possible bias. In fact, both reanalysis-based air temperature and specific humidity showed significant bias and scatter relative to *in situ* measurements during the warmer months of the year at these sites (see Appendices). However, in the case of specific humidity, the record of dew-point temperature measurements at SEAKEYS sites has been very incomplete, with reliable records at only two sites and more than a decade of data at only one (SMKF1). ERAI specific humidity data for these sites therefore represent a necessary supplement to the *in situ* record in order to quantify, for example, the role of latent heat fluxes in sea temperature variability (Ch. 3).

Overall, regressing ERAI vs. *in situ* sea-level specific humidity at SMKF1 and barometric pressure everywhere showed little scatter. ERAI air temperature regressed with *in situ* data well at all sites, except during summer months. ERAI wind speed during frequent winter cold front passage shows a significant positive bias (Gramer in prep.). In a previous heat budget study (Gramer et al. 2012), these respective errors in ERAI air temperature and wind speed partially compensated for one another. A heat budget is described in Ch. 3, however, which is constructed using *in situ* air temperature and winds, eliminating these sources of estimation error.

Hourly water-height variation and tidal-currents time series for this study were derived from Oregon State University's TPXO 7.2 tidal solution (Egbert and Erofeeva 2002; Egbert et al. 2010). Tide solutions were extracted using the tide model driver (TMD) software of Padman, Howard, and Erofeeva (see Appendices) implemented in MATLAB<sup>®</sup>. NOAA's National Geodetic Data Center (NGDC) 3-arcsecond horizontal-resolution Coastal Relief Model (3" CRM; Divins and Metzger 2008) was used to estimate cross-shore angle to True north using a seven-point sample of the 3" CRM 20 m

isobath contour at each site. In this way, at reef-crest sites, the positive x-direction for all fields (hereafter referred to as “offshore”) was chosen so as to correspond with the maximum local bathymetric gradient. Finally, approximately six years of total cloud cover observations from three airports in the Florida Keys and Homestead, Florida, were extracted from NOAA National Climatic Data Center (NCDC) archives, for comparison with reanalysis estimates.

For sea temperature, relatively smooth estimates of horizontal gradients and Laplacians were calculated using a centered 5-point finite difference scheme on a weekly-composite, 1 km-resolution SST dataset produced by the University of South Florida (USF) from the Advanced Very-High Resolution Radiometers flown on NOAA polar-orbiting satellites (AVHRR SST from Muller-Karger and Hu, e.g., Hu et al. 2009). For purposes of comparison, near-surface ocean currents and sea temperature fields also were extracted around each site from six-hourly-mean outputs of the 900 m horizontal-resolution Florida Keys embedded non-assimilative HYbrid-Coordinate Ocean Model of Kourafalou and Kang (FKEYS HYCOM, see, e.g., Kourafalou et al. 2009) for years 2004-2008. FKEYS HYCOM was forced by the Fleet Numerical Meteorology and Oceanography Center’s Navy Operational Global Atmospheric Prediction System (NOGAPS, Rosmond et al. 2002). Similarly, daily mean outputs were derived for comparison during years 2003-2011 from an experimental analysis using the 4 km horizontal-resolution, 20 vertical-layer Gulf of Mexico (GoM) HYCOM model forced by NOGAPS (e.g., Prasad and Hogan 2007; Zamudio and Hogan 2008; Gierach et al. 2009), which assimilates observations using the Navy Coupled Ocean Data Assimilation system (NCODA, Cummings 2005; Chassignet et al. 2009). Due to land masking, sites SANF1

and DRYF1 (see Table 2-1) used nearest-neighbor data from the gridded ocean data sets; these data were bilinearly interpolated for other sites. For gradients from GoM HYCOM, 3-point finite differencing was used. A cubic spline fit was done to all product/model time series to produce hourly data.

Analysis of ocean-current vector-components from *in situ* data at LOOE1 (Fig. 2-2) shows that hourly mean cross-shore currents near the reef crest are much smaller than alongshore, often similar to the estimation error for the deployed instrument. Shallow-water barrier reef systems with high “linear” (long-shore) reef density similar to the FRT can provide an effective barrier against low-frequency variability in cross-shore currents (Wolanski and Spagnol 2000). This difference was pronounced at LOOE1 throughout the year. By contrast, horizontal gradients in sea temperature were dominated by cross-shore variability at the reef crest, and were negligible at inshore sites (see Appendices). Data from the SFP TSG dataset verified the sign and magnitude of these seasonal satellite SST gradients using underway measurements at points 0.9 to 1.1 km in- and offshore of the reef-crest, respectively. Kilometer- and larger-scale advection of temperature gradients is thus expected to be small throughout the study domain.

The *in situ* TSG data also (see Appendices) confirm findings by numerous previous studies that AVHRR may significantly underestimate horizontal SST gradients during warm months, due to persistent cloud cover, low winds, and other factors (Sturges and Leben 2000; Katsaros and Soloviev 2004; Katsaros et al. 2005). In addition, a significant number of AVHRR weekly composites could not be used due to issues with cloud pixel filtering. This SST dataset provides a long record (1993-present) of high

spatial-resolution data, but relatively little reliable information on horizontal gradients during the warmest months.

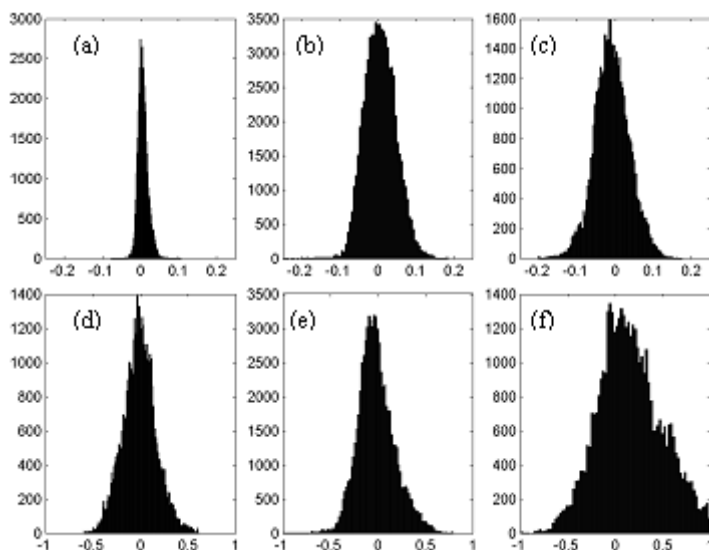


**Figure 2-2: Histograms of (a,b,c) cross-shore and (d,e,f) alongshore ocean currents [m/s], from (a,d) *in situ* daily mean of ADCP profiles at LOOE1 bin-averaged over the water column, and coincident near-surface data from (b,e) GoM and (c,f) FKEYS HYCOM hydrodynamic models. Note difference in horizontal (velocity) scales between top ( $-0.25$  to  $+0.25$   $\text{ms}^{-1}$ ) and bottom ( $-1$  to  $+1$   $\text{ms}^{-1}$ ) panels.**

Statistical comparisons were performed between *in situ* ocean current measurements from the LOOE1 mooring and both HYCOM models, and between sea temperature gradients estimated from AVHRR weekly SST and these models: for detailed analysis, see the Appendices. Of particular note, both ocean models predict cross-shore currents much larger than those observed at LOOE1 (Fig. 2-2). This disparity between observed alongshore currents and much smaller cross-shore currents is consistent with previous studies in the Keys as well (Haus et al. 2000, their Fig. 8; Davis et al. 2008, their Fig. 6). Large scatter is also found in regressions between alongshore sea temperature gradients based on these models and those from the AVHRR SST dataset. However, weekly median cross-shore gradients from the 4 km GOM HYCOM

do compare well with 1 km weekly AVHRR (see Appendices). Limitations in the bathymetry used by the two hydrodynamic models are a likely source of the differences in cross-shore currents and temperature gradients between the models and satellite data.

Wave measurements were not available for these sites. This study assessed three methods for estimating peak wave period and significant wave height: peak wave period and significant wave height based on wind speed, due to Pierson-Moskowitz and Huang, respectively, both as described in Bourassa et al. (2001); output of the NOAA operational multi-grid Wave Watch III model (WW3; Tolman 2008); and sea state estimates from ERA-Interim reanalysis (ERA-Interim; Dee et al. 2011; Semedo et al. 2011). WW3 was improved in early 2005 with a higher (4-arcminute mean) resolution multi-mesh grid: prior to that (1999-2005), a moderate 0.25°-resolution fixed grid was used. *In situ* data from three RSMAS study sites for March-May 2005 (Haus et al. 2010) were regressed against outputs from all three of these sources. The simple parameterization significantly overestimated significant wave height at all three sites, with low predictive power ( $R^2 < 0.2$ ). The WW3 significant wave height and peak wave period provided the best fit to the *in situ* data analyzed. However, after empirical corrections were applied to ERA-Interim (see Appendices), regression of both ERA-Interim and WW3 with *in situ* data showed similar root-mean-squared error (RMSE), slope, and bias. ERA-Interim provides self-consistent wave forecast data for the full period of *in situ* data at SEAKEYS stations (1987-present).

### *Summary of Error Estimates*

Published estimates of slope and residual measurement error for all directly measured and reanalysis quantities were used as a starting point in the error analysis that follows. Nominal measurement errors in quality-controlled *in situ* data from SEAKEYS sites were first derived from NDBC estimates. Data from redundant sensors were then used to verify or modify published error estimates at specific sites, specifically CT sea temperature (five sites) and secondary wind sensor (four sites).

Table 2-2 summarizes the median measurement errors (RMSE) estimated as described above, showing in each case the largest median error across all sites analyzed. Where comparison data were available, slope error is the magnitude of the difference between unity and the slope found by robust least-squares linear regression vs. that comparison data,  $B$ , expressed as a percentage, i.e., slope error  $\equiv |1-B| \times 100\%$ . Representation errors for derived terms were calculated using the methods of propagation of uncertainty (Emery and Thomson 2001).

Table 2-2: Nominal measurement or modeling errors for sea temperature and other variables.

<i>Name</i>	<i>Variable</i>	<i>Slope error ± RMSE</i>	<i>Error source or estimation method</i>
Sea temperature	$T_s$	0% ±0.11 [°C]	NDBC (2009); regression vs. redundant <i>in situ</i> sensors
Air temperature	$T_a$	±0.10 [°C]	NDBC (2009)
Dew-point temperature	$T_{dew}$	0% ±0.31 [°C]	Betts et al. (2009); regression vs. <i>in situ</i> sensors NDBC (2009)
Zonal, meridional, cross-shore, alongshore wind velocities at 10 m	$U_{10}^x, U_{10}^y, U_{10}^{xs}, U_{10}^{ls}$	3% ±0.55 [ $ms^{-1}$ ]	NDBC (2009); regression vs. redundant <i>in situ</i> sensors
Salinity	S	±0.5 PSU	Range of natural variability
Tide height variation	h	30% ±0.1 [m]	Regression vs. <i>in situ</i> (SMKF1, LONF1); Erofeeva pers. comm., Egbert et al. (2010)
Relative Humidity	RH	0% ±5 [%]	Calculated from $T_a, errT_a, T_{dew}, errT_{dew}$ ; Betts et al. (2009)
Air specific humidity	$q_a$	0% ±0.0005 [kg/kg]	Calculated from $T_a, errT_a, RH, errRH$ ; Betts et al. (2009)
Saturated specific humidity	$q_s$	0% ±0.0001 [kg/kg]	Calculated from $T_s, errT_s$
Precipitation	Pr	0% ±0.03 [mm/hr]	Betts et al. (2009); regression vs. <i>in situ</i> data
Barometric pressure	$P_a$	<1% ±1 [hPa]	Betts et al. (2009); regression vs. <i>in situ</i> sensors NDBC (2009)
Total cloud cover	C	±10 [%]	Markovic et al. (2009); Betts et al. (2009); regression vs. airport data (NCDC)
Downward insolation (ex empirical adj.)	$Q_{sw}^1$	3% ±35 [ $Wm^{-2}$ ]	Markovic et al. (2009); Betts et al. (2009); regression vs. RSMAS $Q_{sw}^1$
Downward longwave flux (adj.)	$Q_{LW}^1$	1% ±3 [ $Wm^{-2}$ ]	Markovic et al. (2009); Betts et al. (2009); regression vs. RSMAS $Q_{LW}^1$
Tidal current	$u_{tide}$	30% ±0.1 [ $ms^{-1}$ ]	Erofeeva pers. comm., regression vs. high-pass filtered <i>in situ</i> ADCP data
Significant wave height	$w_h$	35% ±0.2 [m] (13%)	Regression vs. <i>in situ</i> data at inshore stations (Lee et al. 2009; Rascle and Ardhuin 2009; Ardhuin et al. 2010; Haus et al. 2010)
Horizontal near-surface sea temperature gradient	$\nabla_h T_s$	3% ±0.3 [ $K \cdot km^{-2}$ ]	Regressed horizontal gradients in 1 km composite satellite SST and ship-based TSG, $\partial_x SST_{AVHRR}$ vs. $\partial_x T_{TSG}$
Horizontal sea temperature Laplacian	$\nabla_h^2 T_s$	3% ±0.04 [ $K \cdot km^{-2}$ ]	Regression $\partial_{xx} SST_{AVHRR}$ vs. $\partial_{xx} T_{TSG}$

## 2. Results

Analysis of variability for periods between 3 h and interannual is given below, for long-term hourly *in situ* records of sea temperature, air temperature, barometric pressure, wind speed, and wind vector components, as well as more limited multi-year records of specific humidity and tide height where available. See previous statistical analyses of *in situ* SEAKEYS data (e.g., Peng et al. 1999; Moulin 2005) for comparison with the results that follow. For LOOE1, variability is analyzed for six-year records (between 2004 and 2010) of hourly sea temperature both at 5 m and near bottom (22 m), and of ocean current velocities (see above). At all sites, whole-record and time-limited covariability between sea temperature and other variables is then analyzed at multi-day to interannual frequencies.

### *Sea Temperature Mean and Spectra*

As summarized in Table 2-3, whole-record mean and standard deviations of hourly mean sea temperature at all sites were similar, with shallower sites generally slightly cooler. Sample size of the hourly data that went into these statistics varied from  $\approx 200,000$  at MLRF1 to  $\approx 70,000$  at DRYF1. Salinity data from CT (CTD in the case of LOOE1) were also quality-controlled to calculate long-term mean and standard deviation, Table 2-3. The narrow salinity variations at LOOE1 (5 m) and DRYF1 are probably due to short records there (four and one years, respectively).

**Table 2-3: Arithmetic mean and standard deviation of whole hourly records for NDBC sea temperature ( $T_S$ , °C) and CT salinity (S, PSU) at each site.**

<i>Site</i>	<i>Mean <math>T_S</math> (°C)</i>	<i>Std. dev. <math>T_S</math> (°C)</i>	<i>Mean S (PSU)</i>	<i>Std. dev. S (PSU)</i>
<i>FWYF1</i>	26.4	2.6	35.5	1.5
<i>MLRF1</i>	26.7	2.6	35.4	1.5
<i>LONF1</i>	26.2	4.1	35.7	2.6
<i>SMKF1</i>	26.9	2.8	35.4	2.1
<i>LOOE1 5 m</i>	26.7	2.8	36.2	0.3
<i>LOOE1 22 m</i>	26.5	2.6	–	–
<i>SANF1</i>	26.5	2.8	36.1	1.3
<i>DRYF1</i>	25.8	3.2	36.0	0.2

Analysis of power spectral density estimates for sea temperature from SEAKEYS and SFP sites allows some immediate conclusions (Fig. 2-3). Unless otherwise specified, all power spectral densities in this work were estimated using the Thomson multi-taper method with long-term mean removed: Higher-frequency sea-temperature variability is generally dominated by some combination of diurnal insolation, tides, and the land-sea breeze cycle, while the dominant low-frequency variability at all sites is annual (365 d period), with semi-annual (183 d) variability either subtle (LONF1, Fig. 2-3d) or absent (elsewhere). Sea temperature from Sombrero Key Reef station SMKF1 offshore in the Middle Keys (Fig. 2-3c) is representative of reef-crest sites, showing the dominant semidiurnal, diurnal, and annual periods over its entire 20-year record. SMKF1 is also the only site showing interannual sea-temperature variability in its spectrum, at period greater than 1,000 d. Note however, the longest contiguous record (gaps < 120 d) at SMKF1 is less than 5,500 d.

Narrow, low peaks are apparent at periodicities of 3-7 d, consistent with the passage of mesoscale oceanic features offshore (Lee and Smith 2002), at three reef-crest sites: (a) FWYF1, (b) MLRF1, and (c) SMKF1. This is distinguished from the broader range of periodicities (3-42 d) characteristic of synoptic atmospheric variability, which is

only clearly apparent at LONF1. The relative weakness of the signal for propagation of mesoscale features offshore in the spectra from the reef-crest suggests that mesoscale variability is intermittent at best for most sites – a conclusion also borne out by time-limited, wavelet spectral analysis (Gramer in prep.). Energy at 14 d period (MF or MSF tidal constituents), only suggested elsewhere, is clearly apparent at two sites in the western Keys, SANF1 and DRYF1 (figures not shown).

At the site with the shallowest, flattest topography, Long Key station “LONF1” (Fig. 2-3d), there is a broad range of periods between those for mesoscale propagation and annual variability which have significant energy. This suggests that a direct response to synoptic variability in atmospheric forcing, e.g., cold fronts or easterly waves (the “weather” band), may play a more significant role in sea temperature at this site than it does at sites on the reef-crest. Interestingly, a slight enhancement in the “weather” band is also seen in one other temperature record – that located near-bottom at LOOE1. This suggests a dynamical connection between atmospheric variability and conditions near the seafloor at this site on the reef slope of the FRT. A physical mechanism is suggested to explain this apparent connection in GM2, and the chapters which follow in this work.

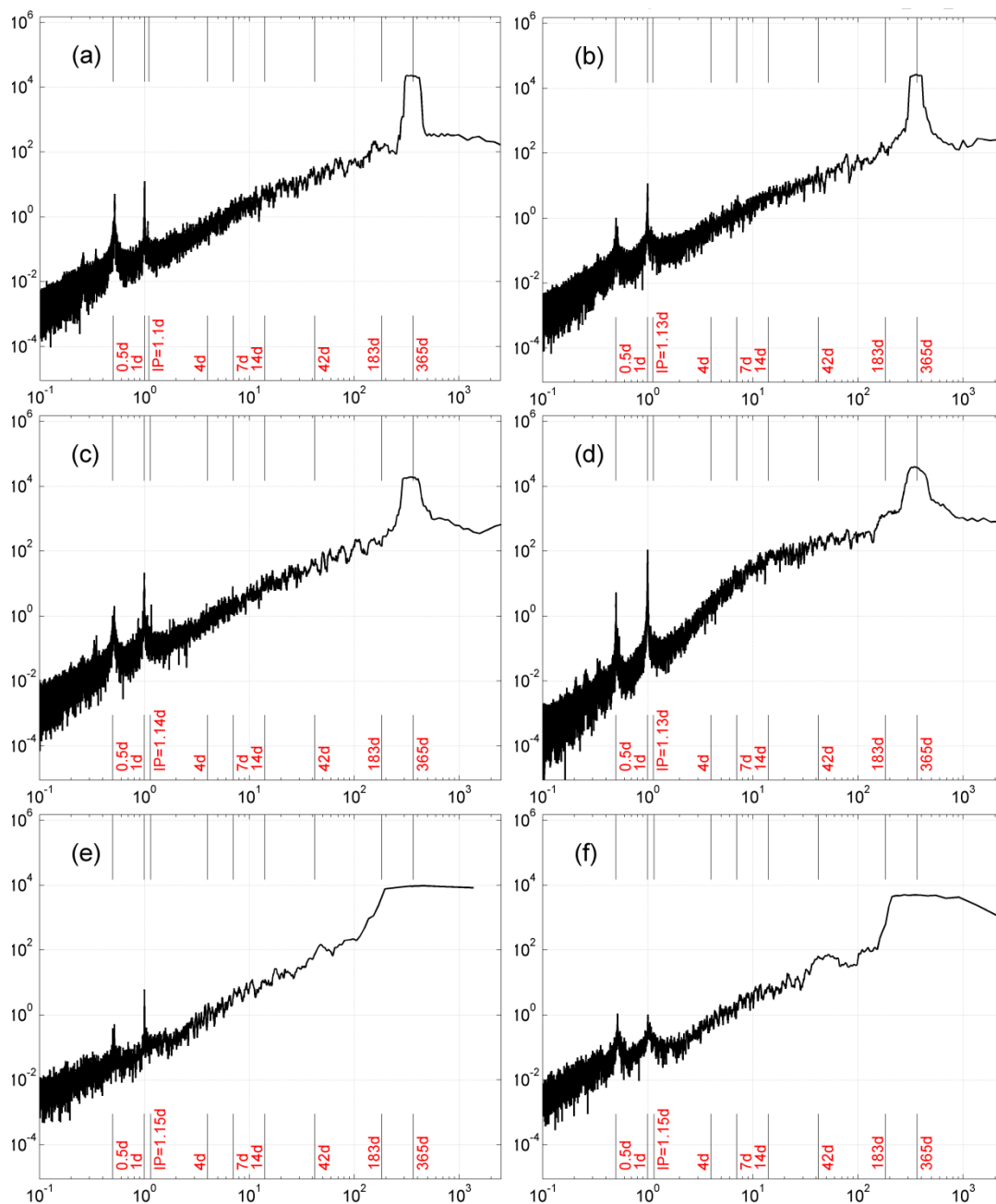


**Figure 2-3: Spectra of sea-temperature anomaly ( $K^2/cpd$ , log-log scale; abscissa shows period in d) for stations (a) FWYF1, (b) MLRF1, (c) SMKF1, and (d) LONF1; and for SFP station “LOOE1” at (e) 5 m and (f) 22 m. Periods of interest are indicated, including semi-diurnal tides and land-sea breeze ( $\approx 0.5$  d), diurnal tides and insolation ( $\approx 1$  d), local inertial period (“IP”=26.5 to 27.6 h), eddy / meander-passage and “weather” bands (4-42 d), semi-annual (tropical, 183 d), and annual cycles. The two LOOE1 spectra (e,f) constitute only a six-year record with intermittent gaps, obscuring the relative power of the annual period there. Long-term mean was subtracted prior to analysis.**

At higher frequencies, semi-diurnal tidal/land-sea breeze effects on sea temperature variability are energetic at all sites, with an enhanced effect at FWYF1 (Fig. 2-3a); significant energy at near-inertial frequencies (27.4 h period), however, is seen only at SMKF1 (Fig. 2-3c). Some variability at shorter periods (6-8 h, not indicated) is also evident at several sites (Fig. 2-3a-d). Distinct peaks for the two diurnal tide periods ( $K1 \approx 23.9$  and  $O1 \approx 25.8$  h) can be discerned at some sites (Fig. 2-3a-c). In general, diurnal variability at 23.9 h dominates the higher frequencies everywhere except FWYF1 (Fig. 2-3a), and at the near-bottom depth (22 m) at LOOE1 (Fig. 2-3f). Diurnal energy at depth at LOOE1 is similar to the energy at 12 h period; at that depth, it would likely be primarily due to tidal forcing rather than diurnal warming.

At FWYF1, the energy of diurnal variability is similar to that at the other shallow, high-slope reef crest sites; however, the semi-diurnal signal here appears to be enhanced relative to other sites, which lie further south and west. One possible explanation for this enhancement lies in the differences between the relative amplitudes of diurnal and semidiurnal tidal constituents at this Atlantic-coast site, vs. other sites nearer to the Gulf of Mexico. But the two semidiurnal tidal constituents (12 and 12.4 h) do not show distinct peaks at FWYF1 as they do for other shallow sites. This fact suggests the enhancement could be attributable to a stronger land-sea breeze cycle at this site off mainland Florida, relative to other sites further from the mainland in the Keys. However, *in situ* tide height data were not available from FWYF1 to assist in distinguishing between these two possibilities.

### *Spectra of Other Variables*

Analysis of variability in other *in situ* variables (Fig. 2-4) shows relatively little geographic variation across the FRT. For brevity, power spectral density estimates are shown only for sites that demonstrate distinctive features. Wind speed (Fig. 2-4a-c), air temperature (Fig. 2-4d-e), and specific humidity (Fig. 2-4f) all show strong variability at annual, diurnal, and “weather band” (3-42 d) periodicities; wind speed also shows semi-annual (“tropical”) variability, especially at sites further south and west (Fig. 2-4b, c). Semi-diurnal variability in air temperature and humidity is prominent, but while present is much weaker in wind speed, except at one offshore site (Fig. 2-4c).

*In situ* barometric pressure spectra were similar at all sites, represented here by the longest, most continuous record at SMK1 (Fig. 2-4g); energy is seen at diurnal and semi-diurnal (land-sea breeze) periods, with enhancement within the weather band (actually 4-6 d) and subtle jumps at 40-100 d period at all sites. The latter encompasses the long-mode period (65-70 d) of the Madden-Julian oscillation (e.g., Kiranmayi and Bhat 2009). However, this variability is not apparent in any other atmospheric variable analyzed (albeit it may be obscured by the weather band), with the exception of *in situ* light at MLRF1, analyzed in Ch. 3.

*In situ* tidal height at two sites with long records, SMK1 and LONF1 (Fig. 2-4h,i) shows power as expected at the main tidal constituent periods: compound M4=6.2 h, S2=12.0 h, M2=12.4 h, K1=23.9 h, O1=25.8 h, MF=13.7 d, MM=27.5 d, SSA=183 d, SA=1 yr). As suggested by the sea temperature data (Fig. 2-3), the relative power of the semi-diurnal tide is significantly greater at the offshore site (SMK1) than in Florida Bay (LONF1). An additional weak mode at  $\approx 36$  d (possibly a beat between two other modes)

also appears at both sites, while co-tidal oscillations (8.38, 8.17, 4.93, 4.14, 3.53, and 3.08 h) are clearly apparent at just one site – LONF1, on the geographically constrained Bay side of the Keys, and lying less than 5 km from a large inter-island channel.

Finally, spectra of a continuous record of ocean currents at one site, LOOE1 (Fig. 2-4j-l) consistently show variability at only one periodicity, ~12 h. Cross-shore currents averaged over the water-column showed much lower variability at all frequencies than alongshore currents (Fig. 2-4j,k). Diurnal variability in cross-shore currents was almost absent, while in alongshore currents peaks were apparent at multiple near-diurnal and near-inertial frequencies. Examining spectra of seasonal time-series of cross-shore currents for multiple years, however (figures not shown), revealed two distinct features: depth-averaged cross-shore currents showed somewhat enhanced diurnal power in warmer months, especially Jul-Aug-Sep, while an average of six near-bottom bins (from ~2 to 6 m above the seafloor) showed significant enhancement in cooler months, especially Dec-Jan-Feb. An average of six near-surface bins (4.5 m below the height of peak intensity and side-lobe contamination) showed less pronounced tidal peaks over all seasons, with broader variability between 8 and 30 h (Fig. 2-4l). Near-surface currents also featured broadly enhanced energy in the “weather” band, suggesting a strong contribution from atmospheric forcing. Interestingly, all currents time series (surface, bottom, depth-averaged, cross- and alongshore) also showed a subtle, narrow peak near frequencies associated with the passage of oceanic mesoscale features (e.g., eddies) offshore of the Keys (4-7 d).

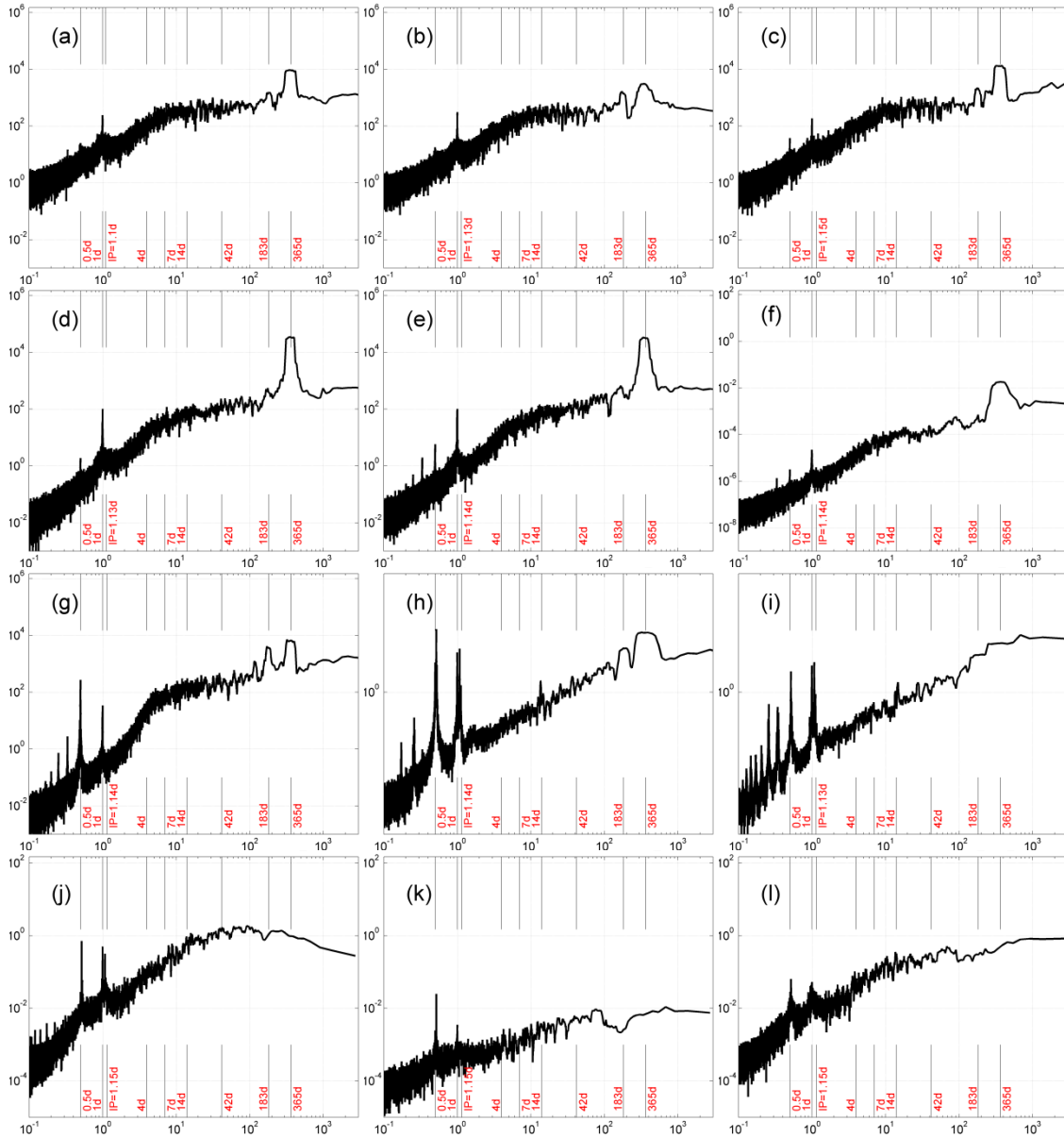


**Figure 2-4: Spectra at selected sites: (a) Wind speed (kts<sup>2</sup>/cpd) at instrument height for FWYF1, (b) LONF1, and (c) SANF1. (d) Air temperature anomaly (K<sup>2</sup>/cpd) at instrument height for MLRF1, and (e) SMKF1. (f) Specific humidity ((kg/kg)<sup>2</sup>/cpd) at instrument height for SMKF1. (g) Barometric pressure (hPa<sup>2</sup>/cpd) at instrument height for SMKF1, (h) tide height (feet<sup>2</sup>/cpd) for SMKF1, and (i) LONF1. Ocean currents for LOOE1 ((m/s)<sup>2</sup>/cpd): (j) alongshore and (k) cross-shore depth-averaged current vector components, and (l) near-surface speed, for a 1,173 d continuous record from 2005 Mar 25 to 2008 Jun 11. Long-term mean was subtracted from all time-series analyzed.**

### *Annual Variability*

#### **Sea Temperature and Meteorology**

Monthly distributions of *in situ* sea and air temperature, wind speed, and cross- and alongshore components of wind velocity for the whole record at representative SEAKEYS sites are shown in Fig. 2-5. Geographically, air temperatures (Fig. 2-5d-f) vary little throughout the FRT except that, in winter, sites farther to the west (and farther from the influences of land and Biscayne or Florida Bays) experience fewer extreme cold temperatures (Fig. 2-5f). Similarly, monthly median wind speed varies little between a northern site (FWYF1, Fig. 2-5g) and a far western site (DRYF1) site (figure not shown), both of which are well offshore; however, for the sole site within Florida Bay (LONF1, Fig. 2-5j) both the median and interquartile range of wind speed are somewhat less in winter months than at other sites. All sites are subject to occasional extreme outlier wind speeds during tropical weather events, especially in Aug-Sep. Differences in cross- (Fig. 2-5h,k) and alongshore (Fig. 2-5i,l) winds between FWYF1 to the north (Fig. 2-5h,i) and SANF in the west (Fig. 2-5k,l) are attributable to the change in topographic orientation relative to prevailing easterly winds, although some differences in zonal (west-to-east) wind variance between the two are also apparent in cooler months, especially in Dec-Jan-Feb, likely due to the influence of the land-sea breezes cycle at FWYF1.

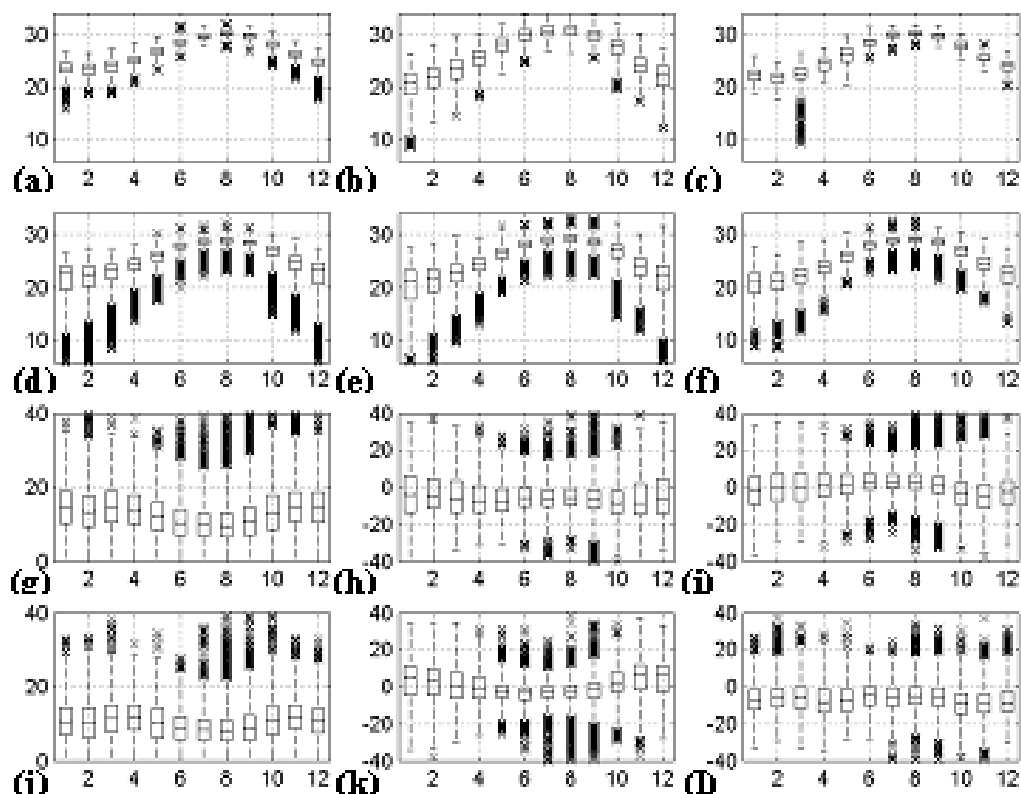


**Figure 2-5: Box-and-whisker plots for monthly distributions, showing monthly median (centerline, notch width indicates two standard errors), 25th and 75th percentiles (rectangular box), extremes twice the inter-quartile range from the median (whiskers), and outliers beyond the extremes (“x’s”). Panels: (a,b,c) Hourly mean sea temperature in °C at (a) MLRF1, (d) LONF1, (e) DRYF1; (d,e,f) air temperature at these same stations; (g,h,i) wind speed, cross-shore (west-to-east), and alongshore (south-to-north) wind components in knots at FWYF1; (j) wind speed at LONF1, (k,l) cross-shore (roughly north-to-south) and alongshore (roughly west-to-east) winds at SANF1.**

Fig. 2-6 shows a mean year of hourly sea temperature for two sites, SMKF1 and LONF1, separated by only 28 km in the Middle Keys. Climatological peak sea temperature at SMKF1 (Fig. 2-6a) occurs at 17:00 local time on year-day 221 (early August, 31.1 °C) and low temperature at 06:00 LT on year-day 35 (early February, 22.3 °C), with a mean annual amplitude of 8 K. Variation in median diurnal amplitude with year-day is also observed at SMKF1, with a minimum of 0.7 K·d<sup>-1</sup> in October and a peak above 1.4 K·d<sup>-1</sup> in January. Other reef-crest sites FWYF1, MLRF1, and SANF1 experienced similar, slightly less extreme annual amplitudes of 7 K, and similar

seasonality in median diurnal range, with minimum  $0.5 \text{ K}\cdot\text{d}^{-1}$  in September-November and peaks above  $1.2 \text{ K}\cdot\text{d}^{-1}$  in January. One shallow, flat site lying just 20 km from the continental slope, DRYF1, has a more moderate seasonality in median diurnal range than any other site ( $0.2$  in November up to  $0.8 \text{ K}\cdot\text{d}^{-1}$  in March-April), but by contrast has an annual cycle with amplitude 10 K. The other shallow, flat site, LONF1 on the Bay side (Fig. 2-6b) experiences minimum median diurnal amplitude of  $1.1 \text{ K}\cdot\text{d}^{-1}$  in December and a peak in April above  $1.7 \text{ K}\cdot\text{d}^{-1}$ , with a 12 K mean annual amplitude having peak  $31.9^\circ\text{C}$  on year-day 227, and minimum  $9.5^\circ\text{C}$  early in the morning on year-day 10. Thus, DRYF1 is an outlier in annual range, and LONF1 an outlier in both diurnal and annual (seasonal) ranges. Some diurnal extremes are observed, with sites in all regions experiencing  $>3 \text{ K}$  diurnal ranges during 40 to as many as 100 d of their 20-year records, predominantly in winter.

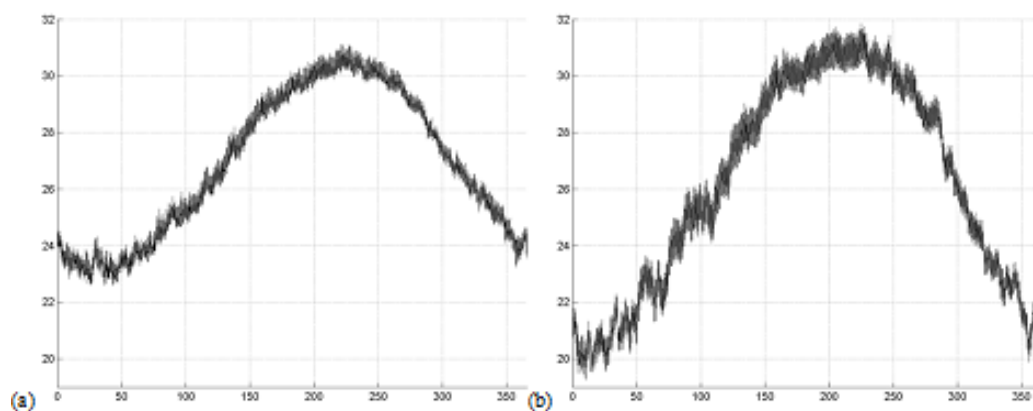


**Figure 2-6: Hourly climatology of sea temperature – mean hourly values, as a function of year-day (0-365) and hour, across 20 years of available data at each site, in  $^\circ\text{C}$  – for (a) Sombrero Key Reef station SMKF1, and (b) Long Key station LONF1.**

### Air-Sea Gradients

At LONF1, the climatological weekly median of air-sea temperature difference  $T_a - T_s$  reaches a minimum (most extreme difference) of  $-2.0$  K in mid-June, and a maximum of  $+0.1$  K in early January. This is the opposite of other SEAKEYS sites, where minimum weekly median  $T_a - T_s$  of  $-2.7$  to  $-1.6$  K occurs in November-December-January while maxima between  $-0.9$  and  $-0.5$  K occur in June. Differences between  $T_a - T_s$  at LONF1 and other *in situ* sites are even more marked in terms of diurnal variability: in boreal winter at LONF1, weekly median  $T_a - T_s$  taken only during mid-day hours may exceed  $+0.5$  K, a circumstance that does not occur for any significant subset of data from the other *in situ* records. DRYF1 shows a somewhat distinct seasonal pattern from other sites, with peak median  $T_a - T_s$  of  $-1.0$  to  $+0.3$  K occurring in March-April, and a minimum  $-1.7$  to  $-2.4$  K in December-January. Finally, for brief periods (individual daily medians), *in situ*  $T_a - T_s$  at all SEAKEYS sites may range from  $-16$  to  $+8$  K.

In terms of atmospheric water content over the Florida Keys, ERAI displays a weak annual cycle in weekly median difference between atmospheric and saturated specific humidity,  $q_a - q_s$ , of  $-0.008$  to  $-0.005$  kg/kg between August and January, respectively. This pattern matches at 95% confidence the weekly median *in situ*  $q_a - q_s$  at the one reef-crest site with dew temperature data, SMKF1 – except in August-September, when *in situ* is greater than ERAI by only  $\sim 0.001$  kg/kg. At LONF1 however, where dew point temperature was recorded from 2004 to 2010, phase in the annual cycle is similar but annual amplitude is greater: weekly median *in situ*  $q_a - q_s$  at LONF1 reaches a minimum (lowest extreme) of  $-0.011$  in August, and a maximum of  $-0.002$  kg/kg in

January, indicating that specific humidity for this site from reanalysis may overestimate cooling due to latent heat flux in cooler months, and underestimate it in warmer months.

### *Interannual Variability*

As described above, the amplitude of annual variability in sea temperature at these sub-tropical reef sites (~7 K) is significantly greater than their peak climatological diurnal cycle (<2 K). However, interannual variability in hourly sea temperature at these sites may in turn exceed the mean annual amplitude. Fig. 2-7 plots hourly sea temperature time-series from both SMKF1 and LONF1 superimposed by year-day. Variability between years of up to 10 K is apparent at SMKF1 (Fig. 2-7a), and up to 14 K at LONF1 (Fig. 2-7b) during all seasons except summer, when the range at both sites is more restricted (<6 K at SMKF1, <8 K at LONF1). Interannual variability at all other sites near the reef crest (including flat, shallow DRYF1, not shown) was somewhat more moderate than that at SMKF1 (~6-8 K). A much shorter record of sea temperatures is available from the SFP site “LOOE1” (2006-2010 at 5 m, 2004-2010 at 22 m, figures not shown): within year-day variability at 5 m never exceeded 5 K over approximately four years. Yet despite its short record, the 22 m sensor at LOOE1 showed a peak in year-day interannual variability of from 6 to 10 K in June-July, a period when all other sites show relatively less interannual variability. Examination of hourly records between years suggests that upwelling (e.g., by breaking internal waves, Leichter et al. 2005) is a key mechanism explaining this anomalous interannual summer variability at 22 m at LOOE1.

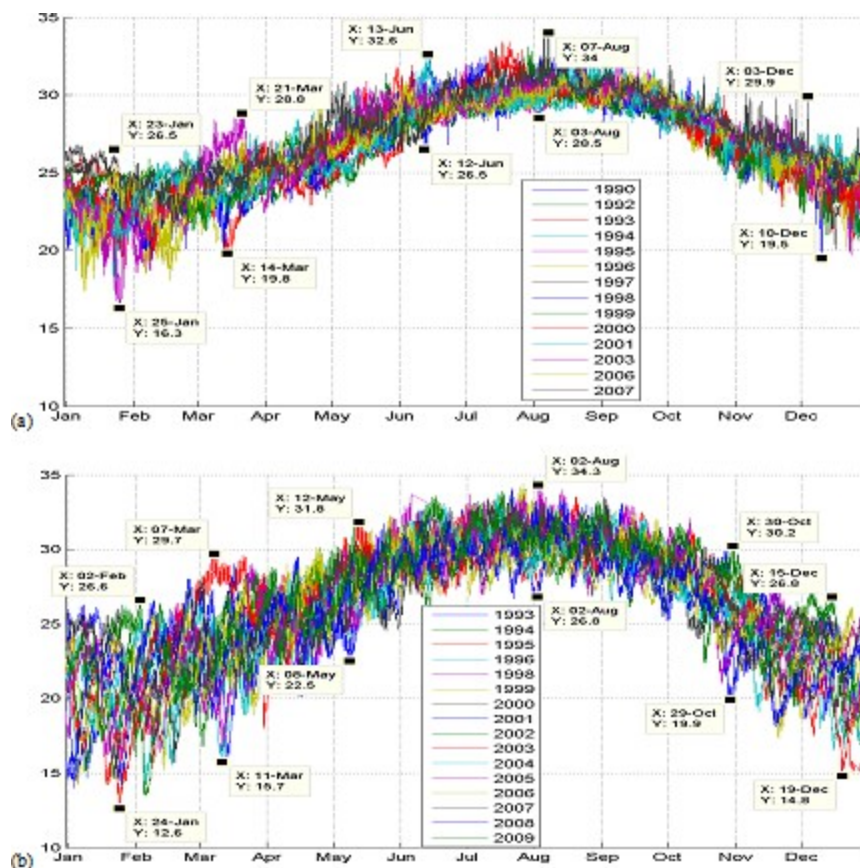


**Figure 2-7: All complete years of hourly mean NDBC sea temperature in °C, at (a) Sombbrero Key Reef station SMKF1, 1990-2007, and (b) Long Key station LONF1, 1993-2009, plotted vs. year-day-hour; color indicates year. Years missing more than 45 d of data were excluded from each plot.**

Fig. 2-8 shows annual mean sea temperatures for several sites with 95% confidence levels. Annual means show no trend at most of these reef sites, despite the fact that hourly sea temperature records at these sites include as many as 22 full years of data, spanning the years 1987 to 2011 (see Table 2-1). However, as Fig. 2-8d indicates, the annual mean does have a statistically significant long-term trend at one site, SMKF1. The quality-controlled sea temperature record at this site unfortunately ended in early 2008. However, the annual mean in 2007 here was  $>0.5$  K greater than in any prior year, capping a trend of steadily increasing annual mean temperature for most years since 1997-1998, when a massive Keys-wide coral bleaching event occurred (e.g., Manzello et

al. 2007a; Manzello et al. 2007b). No other site shows a persistent interannual trend, nor does any other site's annual mean sea temperature approach the peak reached at this site in 2007 of 27.7 °C.

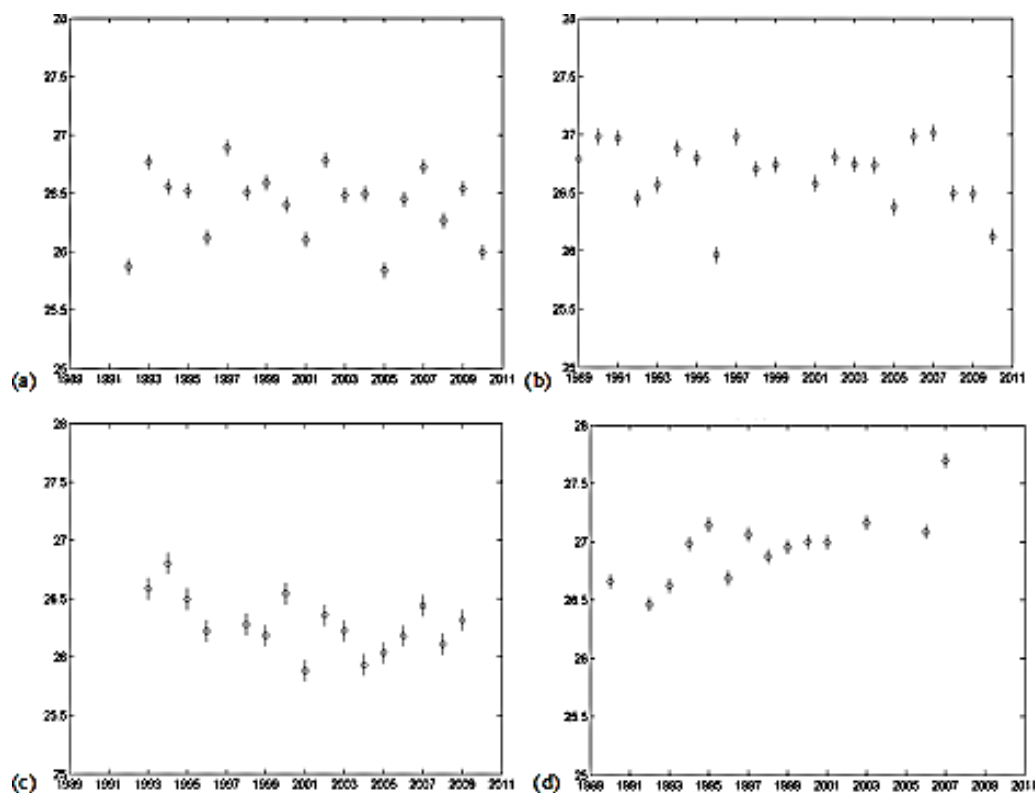


**Figure 2-8: Analysis of variance: annual mean sea temperature (circles, °C) and 95% confidence intervals (line segments) at each of (a) FWYF1, (b) MLRF1, (c) LONF1, and (d) SMKF1, using the more restrictive of Tukey-Kramer and Dunn-Sidák significance tests in each case. Only years missing fewer than 45 d worth of data were used for annual averages at each site.**

This warming trend at SMKF1, previously noted in a NOAA meeting report by Manzello (2004), is made more striking when the full quality-controlled, hourly sea temperature record is regressed against time (Fig. 2-9) using a robust iteratively reweighted least squares fit with a bi-square weighting function (Holland and Welsh 1977). Care must be taken in interpreting this trend, however, as the SMKF1 sea temperature sensor began providing data that NDBC flagged as anomalously high and overly variable in 2008. Furthermore, similar trends at the other SEAKEYS sites

described by Manzello (2004) were not reproduced when up-to-date sea temperature records for those sites were analyzed in the present study. To verify the robustness of the trend at SMKF1, a simple linear regression between yearly mean, including only the fourteen years with fewer than 45 d missing, and year from the start of the record (yearly mean  $\sim$  (year-1988)) was done (figure not shown): a slope of 0.05 K/year explained 60% of the variability in annual mean with standard error of 0.014 and a p-statistic  $<0.004$ . Even excluding the mean for the potentially problematic year of 2007, the resulting slope of 0.04 K/year still explains 50% of the variability in annual mean, with a p-statistic  $<0.01$ . Analysis of variance in yearly mean at all of the other SEAKEYS sites for the same period (1991-2006) did not show any warming trend with significance at 95% level.

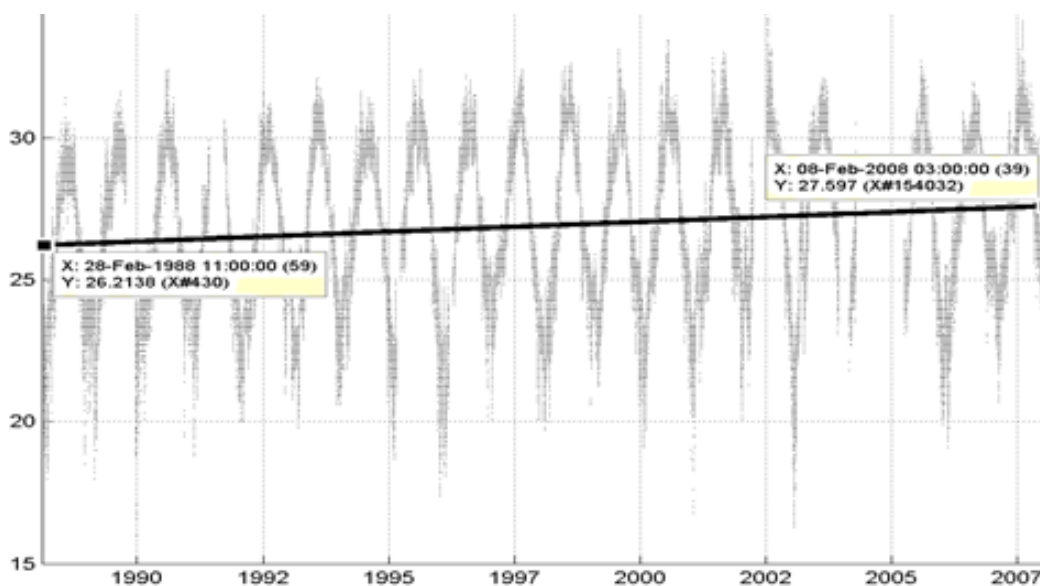


**Figure 2-9: NDBC time series of hourly mean sea temperature (gray, °C), and robust least squares trend line (black) at SMKF1 (gray), showing a +1.4 °C temperature trend over 20 years. Analyzing most-current records for the present study, no robust trend is observed in any other multi-year sea-temperature time series from the FRT.**

As an independent corroboration of this trend, simultaneous quality-controlled hourly relative tide height (in feet) at SMKF1 was also regressed against time (Fig. 2-10). Over a limited nine-year record (2001-2009), annual mean tide height showed an

increasing trend totaling approximately 3 inches ( $R^2 \approx 0.4$ ,  $p < 0.1$ ). With the assumption of a constant long-term mean in salinity, the calculation of simple thermosteric anomaly associated with a nine year temperature increase of  $0.04 \text{ K} \cdot \text{yr}^{-1}$  happens to agree closely with this linear trend in tidal height.

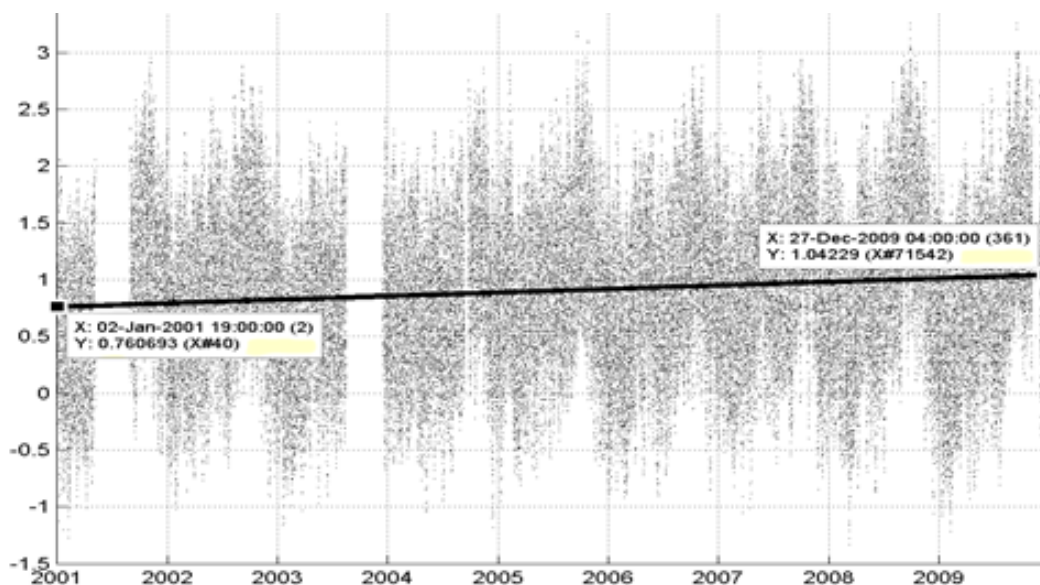


**Figure 2-10: NDBC time series of hourly mean tide level above MLLW at SMKF1 (in feet, gray): robust linear regression trend (black) shows a 3 inch increase in tide level over a nine year record.**

If the observed warming trend is not an instrumental or other artifact, some physical mechanisms suggest themselves to explain this geographically localized warming. Most obviously, SMKF1 is near a large cross-island channel (Moser) connecting the reef tract with the warmer summer waters of Florida Bay and the southern West Florida Shelf; yet Long Key station LONF1 on the Florida Bay side of the Keys shows no such increasing sea temperature trend despite a similarly long record. Interestingly, however, robust regression of both the hourly and annual mean LONF1 tidal record for 2001-2009 did show a positive slope totaling over 8 inches (figure not shown).

Another potential explanation for this apparent localized warming trend lies in horizontal advection and mixing between Sombrero Key Reef and the surface-waters of the southern Straits of Florida, including the Florida Current (FC). As noted in the discussion of Fig. 2-3c, SMK1 is the only site analyzed for this study which shows persistent sea temperature variability at the local inertial frequency. Waters inshore of SMK1 are shallow (<15 m); surface and bottom friction are likely to dissipate inertial motions there; therefore, this spectral peak suggests a dynamical interaction between SMK1 and deeper waters offshore. Furthermore, a prior study of episodic sea temperature variability at near-mesoscale frequencies (Gramer et al. 2009) found a significant enhancement in variability coincident with FC meanders and eddies offshore at SMK1, relative to other SEAKEYS sites. This suggests that waters offshore may play a greater role in explaining sea temperature variability at SMK1 than at other sites, and may also be related to the interannual warming trend confined to this one site on the FRT (Achberger et al. 2012; Chollett et al. 2012).

### *Covariability*

A primary goal of the research outlined in this and an ensuing study (Ch. 3) is to improve understanding of the physical mechanisms driving sub-surface sea temperature variability on coral reefs. Toward that end, coefficients of determination ( $R^2$ ) were calculated at each site, for day-to-day changes in daily mean *in situ* sea temperature ( $\Delta_{1d}T_s$ ), vs. the daily mean ( $\mu_{1d}$ ) or cumulative daily value ( $\Sigma_{1d}$ ), of the other physical variables analyzed in this study. Covariability analyses are summarized in Table 2-4.

Coefficients of determination were calculated from Pearson's correlation coefficient  $R$  as part of a robust least-squares linear regression with bi-square iterative

reweighting. Significance of each result was tested using exact F-statistic, with effective degrees of freedom reduced based on observed autocorrelation in each variable time-series: it should be noted that integral time scales for all daily-difference variables described here (including sea temperature change) was only one day, while integral time scales of daily-mean and daily-sum variables were found to vary from one to 10 days. Comparisons lacking significance at 95% confidence ( $p\text{-value} > 0.05$ ) are indicated by “\*\*\*”; however, all of these  $R^2$  values appear weak, and those values below 0.25 ( $|R| < 0.5$ ) may be considered to be suspect.

**Table 2-4: Covariability: linear regression  $R^2$  for change in daily mean sea temperature vs. meteorological and ocean forcing variables.**

<i>SITE</i>	<i>FWYFI</i>	<i>MLRFI</i>	<i>LONFI</i>	<i>SMKFI</i>	<i>LOOEI</i> <i>5 m</i>	<i>LOOEI</i> <i>22 m</i>	<i>SANFI</i>	<i>DRYFI</i>
<b><i>Predictor Variable</i></b>								
<i>In situ</i> $\Delta_{1d}T_a$	.16	.27	.27	.17	.22	.09	.24	.07
ERA1 $\Delta_{1d}T_a$	.14	.26	.20	.14	.21	.10	.22	.05
<i>In situ</i> $\Delta_{1d}Q_a$	–	–	.24	.06	–	–	–	–
ERA1 $\Delta_{1d}Q_a$	.12	.24	.27	.15	.19	.08	.22	.10
<i>In situ</i> $\mu_{1d}U_{10}^{xs}$	.04	.13	>0	.08	.13	.09	.11	.10
<i>In situ</i> $\mu_{1d}U_{10}^{ls}$	.03	.01	.20	>0	**	.03	.01	.03
<i>In situ</i> $\mu_{1d}Wind^2$	.05	.08	.28	.06	.06	.02	.08	.15
ERA1 $\mu_{1d}Wind^2$	.07	.08	.13	.06	.07	.02	.07	.11
Adj. ERA1 $\Sigma_{1d}Q_{sw}^1$	.02	.02	.01	.02	.04	.02	.03	.05
Adjusted ERA1 $\mu_{1d}H_s$	.05	.08	.15	.05	.07	.02	.05	.12
AVHRR $\Delta_{1d}SST$	.05	.04	.11	.06	.11	.03	.06	.18
$\mu_{1d}\hat{\rho}_{xs}SST$	.01	.01	**	.01	.02	.01	.01	**
$\mu_{1d}\hat{\rho}_{ls}SST$	**	**	**	**	**	**	**	**
$\mu_{1d}\hat{\rho}_h^2SST$	**	**	**	**	**	**	**	**
$\mu_{1d}Current_{xs}$	–	–	–	–	.01	**	–	–
$\mu_{1d}Current_{ls}$	–	–	–	–	.01	**	–	–

For each variable, covariability was calculated using all of the coincident days where both the variable and *in situ* sea temperature provided a complete day of quality-controlled data: at most SEAKEYS sites, other variables were found to have between 5,800 and 8,400 full days (16-23 years) of data coincident with that for sea temperature. Quality-controlled sea temperature records at DRYF1 and LOOE1 were shorter, with between 1,500 and 3,000 full days (4-8 years) of data for sea temperature coincident with other variables. Meteorological *in situ* data analyzed for LOOE1 were taken from nearby station SMKF1, lying 31 km to the north-northeast of LOOE1. These results also serve as a test of the usefulness of ERAI meteorological data relative to *in situ* data, in understanding sea-temperature variability.

For all sites, the variables showing greatest predictive value for  $\Delta_{1d}T_s$  were air temperature ( $\Delta_{1d}T_a$ ) and specific humidity ( $\Delta_{1d}q_a$ ), with mean-squared *in situ* wind speed also explaining significant variability at one site, LONF1. Of interest for the present study was whether predictability of sea-temperature change based on any of these other variables differed over time – either intermittently (see Fig. 2-11), or by time of the year, e.g., during the months of the Florida warm/rainy season May through October (MJJASO), or the Florida dry/cold-front season (NDJFMA). At all sites during MJJASO, mean sea-surface insolation explained a significantly larger portion of sea temperature variability ( $\Sigma_{1d}Q_{SW}^1 R^2 \approx 0.10$ ) than it did for whole-year or NDJFMA averages, while MJJASO *in situ* air temperature variability for warm months explained much less ( $\Delta_{1d}T_a R^2 < 0.10$ ) than whole-year averages did, at all sites analyzed except LONF1 ( $R^2 = 0.21$ ). This reflects a dominance of insolation over surface cooling during warming months; however, mean wind speed (both *in situ* and reanalysis) also showed

higher coefficients of determination vs. sea temperature during MJJASO vs. cooler months ( $\mu_{1d}Wind^2$ ,  $R^2 > 0.10$ ) at most sites. In addition, at FWYF1, cross-shore wind speed ( $\mu_{1d}U_{xs10}$ ) was less well-correlated with  $\Delta_{1d}T_s$  ( $R^2 \approx 0.04$ ) than at most other sites where the reef tract has a more east-west orientation. These observations suggest that mechanisms other than prevailing winds are significant in cross-shore heat exchange in the FRT especially during cooler months, e.g., heat advection or mixing forced by surface waves, or by other mechanisms that may be more prevalent in the northern vs. the western Straits of Florida.

Variability in ERAI data for air temperature and air specific humidity for MJJASO explained observed sea temperature variability still less than did direct measurements – in every case, less than half of the corresponding  $R^2$  for *in situ* data over the same months. Similarly, in all cases sea temperature gradients from AVHRR SST showed significantly lower predictive power during the warmer months than at other times. These summer results indicate that both ERAI meteorology and AVHRR SST are problematic for explaining annual cycles in sea temperature at these sites. For horizontal sea-temperature gradients, in particular, some source other than the AVHRR satellite data would be helpful to quantify warm-weather heat advection and mixing. It is of note that winter-time predictive power of AVHRR SST gradients (both cross- and alongshore) was similar between sites with topography oriented north-south (FWFY1) and those that are east-west (e.g., SANF1), indicating the strong influence of local topography and coastal geomorphology.

In order to further quantify periodicities in the covariability between *in situ*  $T_s$  and the other variables described above, a series of time-dependent coherence analyses with

95% confidence testing were performed using the continuous Morlet wavelet transform (Grinsted et al. 2004). A 40 h low-pass filter was applied to ten-year subsets 2001 – 2011, in order to focus on mesoscale, weather band, and longer period covariability. *In situ* and ERAI air temperature ( $T_a$ ) both showed significant coherence with sea temperature at all periodicities analyzed (analysis with *in situ* data shown in Fig. 2-11). At reef-crest sites (e.g., Fig. 2-11a), the relative unimportance of weather-band variability in air temperature for warmer months is confirmed by this analysis. At such sites, ERAI or *in situ* specific humidity ( $q_a$ , figures not shown) was found to be coherent with  $T_s$  only occasionally, in the wake of extreme cold fronts, occurring during winter approximately every two to three years and lasting for periods of a few days. At LONF1, by contrast,  $q_a$  often varied coherently with  $T_s$  in the weather-band throughout the cooler months of each year (Fig. 2-11b).

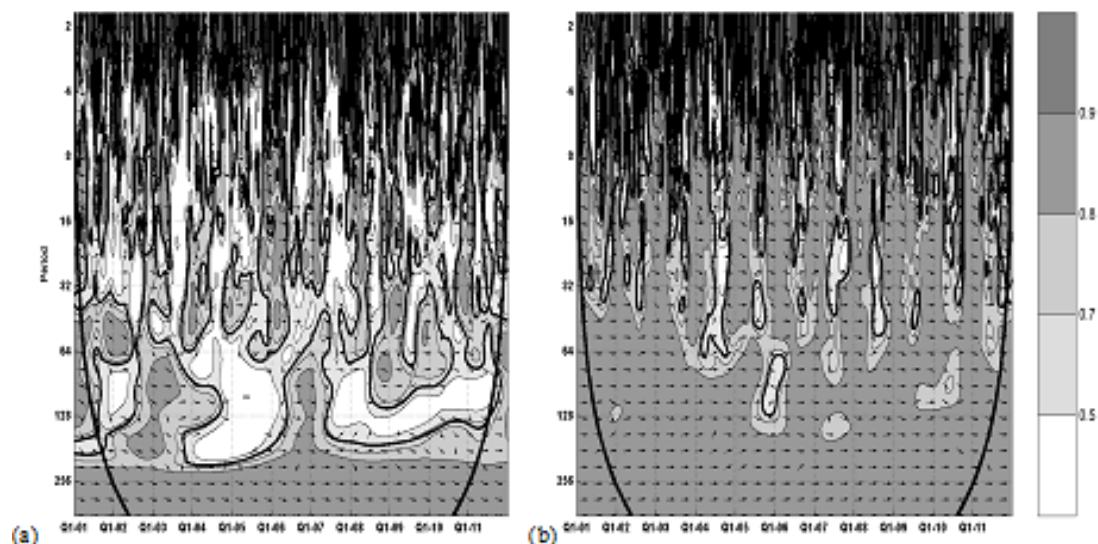


**Figure 2-11: Time-dependent, Morlet wavelet coherence analysis between *in situ* air and sea temperatures, at a range of periodicities from 40 h to 365 d (y-axis), for the years 2001-2011 (x-axis) at two sites: (a) MLRF1 and (b) LONF1. Heavy contours indicate statistical significance at the 95% confidence level, right-pointing arrows indicate in-phase variability, and arrows with a downward orientation indicate a degree of quadrature, i.e., air temperature variability at that periodicity precedes corresponding sea temperature.**

Also at LONF1, wind speed in the wavelet analysis showed significant anti-coherence with  $T_s$  at periods from 3 to 42 d (figure not shown) throughout the year. In particular, meridional (south-to-north) wind variability at LONF1 was positively coherent with sea temperature variability during winter months – in other words, winds turning northerly and blowing down from Florida Bay and the WFS during multiple days were associated with ocean cooling at this one site. At all other sites, significant wind speed anti-coherence with sea temperature was limited to the occasional passage of an easterly wave or tropical disturbance through the region in warmer months, and the alongshore component of the wind vector consistently showed less coherence than did absolute wind speed. At most reef-crest sites, however, with the notable exception of FWYF1, cross-shore winds varied coherently with sea temperature at weather-band periodicities during winter months. Cross-shore gradient in AVHRR SST at these same sites also varied coherently with sea temperature, but only at periods of 180 d or more (i.e., tropical and annual cycles). Both analyses, however, corroborate the significance of cross-shelf heat transport for sea temperature variability at such sites. The above were the only variables and times that showed any significant wavelet coherence with sea temperature at any site for periodicities between 40 h and annual.

### **3. Summary**

The variability of *in situ* hourly sea temperature and meteorological data over two decades was analyzed at diverse sites in the FRT. In addition, air temperature, winds, and barometric pressure at each site were interpolated from two reanalysis products, ERAI and NARR, in order to evaluate the ability of reanalyses to reproduce long-term

meteorological variability at such sites. To provide additional data germane to sea temperature variability, downward short- and longwave radiative fluxes, atmospheric specific humidity, significant wave height, and peak wave period and direction were also interpolated from ERAI, and these estimates were compared with limited records of *in situ* data, and with data from NARR and an operational surface-wave model. While comparisons for NARR data show significant scatter, statistical comparisons of ERAI with these independent sources show good agreement in most cases. Empirical adjustments to correct systematic slope and bias errors in ERAI-derived short- and longwave radiative fluxes and significant wave height were applied based on comparisons with *in situ* data.

Long-term mean and variability in sea temperature at all sites was presented. Whole-record averages of hourly mean sea temperature at all sites were between 25.8 (DRYF1) and 26.9 °C (SMKF1). Variability in hourly mean at very shallow sites near the outer reefs (SEAKEYS sites FWYF1, MLRF1, SMKF1, and SANF1) shows dominant diurnal and annual periods, with diurnal amplitude of order 0.5-1.4 K by season, and annual amplitude 7-8 K. Interannual (between year-day) variability at these sites is greater, at 10 K. The shorter record of sea temperatures at one deeper reef-slope site (SFP site “LOOE1”, 5 and 22 m, 2005-2010) show similar annual (8 K) cycles, but a much greater range of diurnal variability (0.8-3.0 K by season) likely due to upwelling and other oceanographic processes. Sea temperature at very shallow, flat sites (SEAKEYS sites LONF1 and DRYF1) is also dominated by diurnal and annual cycles but with somewhat greater amplitudes in both, 1-2 and 10-12 K, respectively. However, within year-day variability between years at DRYF1 is similar to that at reef-crest sites (8

K), while that at LONF1 is greater at up to 14 K. Significant variability at other periodicities is apparent at some sites, including strong response to dry season cold-front passage in the “weather band” (3-42 d period) at LONF1 on the Bay side, and variability at local inertial ( $\approx 27$  h) periods at SMK1.

Finally, only one site analyzed shows a robust interannual trend in its annual mean sea temperature: SMK1, a site that lies near both the reef crest, and near a large inter-island channel that connects the reef tract with Florida Bay. It is suggested that this long-term warming trend at SMK1 may be a result of greater cross-shore transport of heat at this site relative to other sites near the reef crest. Evidence in support of this hypothesis is seen in both the unusual near-inertial period variability at this site, and the relatively frequent occurrence at the site, previously noted by Gramer et al. (2009), of episodes of sea temperature variability that coincide with the presence of FC meanders and eddies just offshore of it. This may suggest that under scenarios of larger-scale, regional or climatic ocean warming, this area of the Middle Keys will be more susceptible to thermal stress than the other areas of the FRT.

It is well known that sea temperatures in sub-tropical and tropical coastal waters co-vary strongly with insolation, air-sea temperature differences, specific humidity, winds, and transport of horizontal sea-temperature gradients. In this study, covariability between changes in daily mean sea temperature and other variables, including insolation, longwave flux, air temperature change, winds, sea state, and horizontal sea-temperature gradients was evaluated using robust linear regression. Insolation was generally found to dominate during warmer months when wind-forced heat fluxes and circulation are likely to be at a minimum. Air-sea cooling on the other hand appears to play a more significant

role during extreme weather events, such as winter cold fronts, thunderstorms, or occasional easterly atmospheric waves. The prevalence of cold front passages in winter thus leads to a greater role for air-sea cooling during these months.

However, the analysis of covariability in the present study suggests that other forcing mechanisms for sea temperature variability may also be at work, mechanisms not directly related to the meteorological or radiative forcing analyzed above. A portion of unexplained variability on the reef crest may be related to sub-mesoscale and mesoscale oceanic variability – internal waves, eddies, and meanders of the FC. These processes are directly related to both upwelling and cross-shore flows over the reef slope (e.g., Lee et al. 1992; Leichter et al. 2006; Davis et al. 2008; Davis and Monismith 2011), and it has been suggested that these processes can modify sea temperature at the reef crest (Gramer et al. 2009). Yet the analysis also points out other differences, even between seemingly similar sites, in both the features of sea temperature variability and in its covariability with other variables. Such differences suggest forcing at relatively small spatial scales, depending, e.g., on details of geomorphology, geography, or seafloor topography: evidence for such smaller-scale forcing mechanisms is described in the following chapter.

## Chapter 3. Reef Heat Budget

An ocean heat budget is estimated from observational data, including hourly mean *in situ* sea temperature at several diverse, shallow-water reef sites in the Florida reef tract. Sea temperature data are combined with coincident meteorological data from *in situ* sensors and atmospheric reanalysis, estimates of heat advection and diffusion from satellite sea-surface temperature gradient fields, winds, and waves, and a model of heat exchange at the seafloor in order to estimate heat budget terms. Daily and climatological mean heating estimates from the budget are compared with observed sea temperature variability over four- to twenty-year records, with published surface heat-flux climatologies, and with outputs from two hydrodynamic ocean models for surface flux, advection, and diffusion of heat. Results of comparison with *in situ* sea temperature are sensitive to assumed rates of insolation absorption, and to uncertainties in estimated surface currents and sea temperature gradients; estimates for how much insolation is absorbed in the water-column at these reef sites are evaluated using *in situ* measurements. A term for smaller-scale heat advection, the so-called horizontal convection or thermal siphon previously observed at other coral reef systems, is needed to balance the heat budget and provide a close fit to observed sea temperature variability at most sites.

The Florida Reef Tract (FRT) and the coastal ocean that surround it represent a precious natural resource, in terms of biodiversity and beauty, and also because of the income to local economies associated with the commercial and tourism activities it supports (Johns et al. 2001). Furthermore, the living reef and high shelf break that it helps to maintain serve as a vital natural wave break for the storm-prone, heavily

populated south Florida coastline. Significant research has been done over the past 40 years to understand the coastal oceanography of the FRT (e.g., Porter and Porter 2002). Nevertheless, some critical questions remain concerning the role of atmospheric forcing and ocean dynamics in the thermal environment of FRT marine ecosystems. Answers to these questions will ultimately better inform marine protected area managers charged with stewardship of these resources (e.g., Keller et al. 2009).

In order to understand better the physical mechanisms driving sea temperature variability in the FRT, quality-controlled, hourly *in situ* data from seven autonomous reef-monitoring stations (see maps below) were integrated with an atmospheric reanalysis, a high spatial-resolution satellite sea-surface temperature product, an ocean tidal solution, and a high-resolution operational model of northern Atlantic Ocean surface waves. These data, together with estimates of measurement error and empirical corrections associated with them, were described in Chapter 2 above, hereafter “Ch. 2”, and in Gramer and Mariano (in review, hereafter “GM1”). The integrated data are used in the present study to estimate radiative and turbulent heat fluxes at the sea surface and seafloor, diurnal warm-layer evolution, and lateral (advective and diffusive) heat fluxes to produce a detailed heat budget for reef sites in the FRT. Results are also evaluated using a moderate-resolution, assimilating ocean model for the Gulf of Mexico, and a higher-resolution non-assimilating model for the Florida Keys.

A dynamical process, previously undocumented in the FRT, is found to close the heat budget at most sites, and in the process to explain a significant portion of observed sea temperature variability. This additional process is horizontal convection, also known as the thermal siphon (Monismith et al. 2006) – thermally induced exchange currents

between a shallow reef site and deeper waters nearby. Additional evidence for the action of the thermal siphon is presented based on simultaneous ocean currents and sea temperature data for multiple depths, at several monitoring stations in the FRT.

## **1. Additional Data**

### *In situ Data*

*In situ* data for this study were taken from the SEAKEYS network of autonomous C-MAN stations, jointly maintained by FIO (Ogden et al. 1994) and NDBC as described in Ch. 2; from the oceanographic monitoring station maintained by the NOAA South Florida Ecosystem Research and Monitoring Project (SFP) at NOAA AOML, also described above; and from multiple sites in the Upper Keys monitored during previous studies by the University of Miami ("NCORE", Sponaugle et al. 2003; Sponaugle et al. 2005; Sponaugle and Shulzitski pers. comm., see Fig. 3-1). Incident light, both above the water surface and near the seafloor, has also been measured at one former SEAKEYS site (Molasses Reef) since 2008 by the Coral Health and Monitoring Program / Integrated Coral Observing Network (CHAMP/ICON) at AOML. Table 3-1 and the accompanying map summarize the locations and other characteristics of these sites. NCORE data were gathered and processed as described in the references cited above. Methods for SEAKEYS and SFP data were summarized in Ch. 2; processing of CHAMP/ICON data is summarized below.

From 2008 to the present, hourly mean radiative flux data were gathered for the CHAMP/ICON project by two upward-facing Biospherical Instruments Inc. multichannel cosine irradiance profiling spectroradiometers (BICs) deployed at SEAKEYS station MLRF1 at Molasses Reef, one above surface (model # BIC2104R) and one at

approximately 2 m depth (BIC2104U). These BICs simultaneously measure whole-field light in the broad photosynthetically active radiation band (PAR, 400-700 nm,  $\mu\text{-mole quanta m}^{-2} \text{ s}^{-1}$ ), and in three narrow ultraviolet bands ( $380\pm 5$  nm,  $330\pm 5$  nm, and 305 nm variable bandwidth,  $\text{mW m}^{-2}\text{nm}^{-1}$ ). These BIC data have been quality controlled by the CHAMP/ICON program, and were used in the present study for validation and measurement-error estimation of reanalysis-derived insolation data (see below).

**Table 3-1: Monitoring station locations as well as features of local bathymetry and benthic type, for sites where hourly *in situ* meteorological and sea temperature data are available. See also the map in Fig. 3-1, as well as information in Table 2-1 and Figure 2-1 above.**

<i>Station Code</i>	<i>Name, type of installation</i>	<i>Latitude, Longitude</i> °	<i>Isobath orientation</i> °T	<i>Tidal average depth, h</i>	<i>T<sub>s</sub> sensor depth</i>	<i>Benthic reflectivity PAR+NUV</i>	<i>Mean cross-shelf slope</i>
FWYF1	Fowey Rocks, reef crest light.	25.590, -80.097	2	12 m	2.0 m	24%	4%
NCORC	NCORE Site C (2000-2002);	25.067, -80.319;	42;	23 m	4.0 m, 21 m;	20%	2%
NCORK	Key Largo Site (2007-2008)	25.031, -80.348	55	23 m	7.0 m, 23 m		
MLRF1	Molasses Reef reef-crest light.	25.010, -80.380	54	11 m	2.7 m	24%	3%
LONF1	Long Key, Bay-side day marker.	24.840, -80.860	(0)	2.0 m	1.3 m	17%	0.3%
SMKF1	Sombrero Key reef-crest light	24.628, -81.111	65	9.1 m	2.0 m	24%	2%
LOOE1	Looe Key reef-slope buoy.	24.543, -81.402	73	23 m	5.0 m, 22 m	20%	4%
SANF1	Sand Key reef crest light.	24.460, -81.880	82	20 m	1.0 m	20%	2%
DRYF1	Dry Tortugas reef shallows.	24.638, -82.862	(58)	2.5 m	1.0 m	24%	0.4%

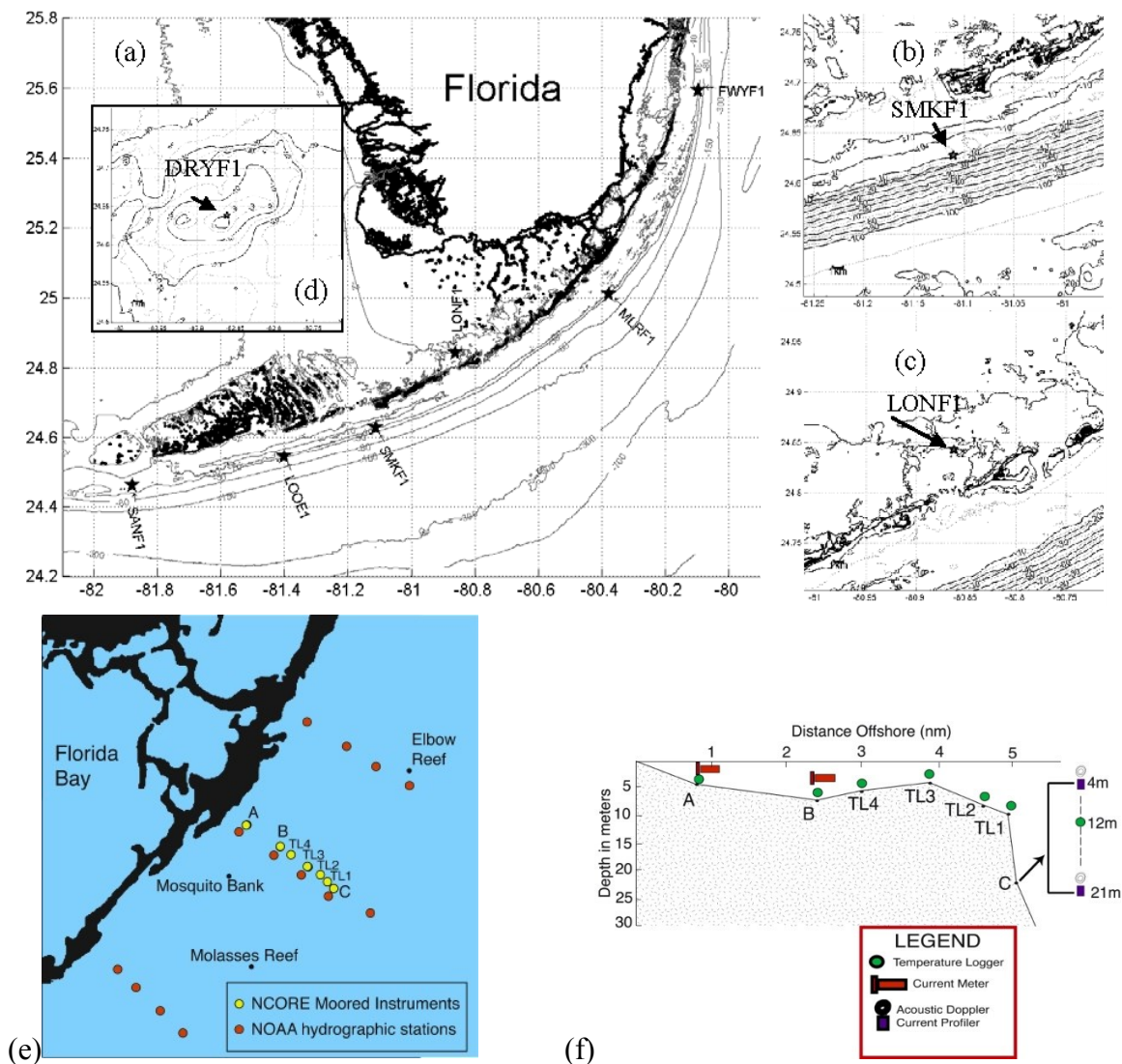


**Figure 3-1:** (a) Map of southern Florida and the Florida Shelf, showing position of SEAKEYS and SFP automated monitoring stations along the FRT (stars). Stations indicated by 5-letter code and arrow are described in the text and in Table 3-1 above. Outlines of the 2, 10, 30, 80, 150, 300, and 700 m isobaths from NGDC 3" CRM bathymetry (see text) are shown in gray. (b, c, inset d) Close-ups showing the NGDC isobaths in a 15x15 km grid surrounding stations (black star), at 2 m depth and every 10 m from 10-100 m (solid), and from 5-95 m (dashed). Maps are shown for (b) Sombrero Key Reef, (c) Long Key, and (inset d) Dry Tortugas. (e) Map and (f) bathymetry side-view showing NCORE monitoring moorings for sea temperature (TL1-4) and sea temperature and ocean currents ("A", "B", "C"), 2000-2002 (panels e and f both courtesy of Liz Williams).

In addition, approximately four years of *in situ* data (Jun 2000-Nov 2002 and Apr 2007-Oct 2008) from two previous RSMAS studies were used to validate parameters of the horizontal convection process. The NCORE project at RSMAS (e.g., Sponaugle et al.

2005, their Fig. 1, sites C and T1-T4) deployed two Sontek acoustic current meters moored at 4 and 21 m depth in 22 m of water (referred to herein as site “NCORC”), and four TKSA water temperature loggers (bottom-mounted in 4-12 m of water) along a 3.6 km cross-shelf section of the reef tract near 25.067°N, 80.317°W in 2000-2002. Quality-controlled data recorded once each 10 minutes from these sensors were provided by E. Williams of RSMAS, with permission of Drs. T. N. Lee and S. Sponaugle. Similarly, sensors were deployed at an NCORE site identified here as “NCORK” (Key Largo) on a mooring near the reef tract at 25.031°N, 80.348°W during 2007-2008, measuring ocean currents and sea temperature every 5 minutes at depths of 7 and 23 m. These respective sites lie within 9 and 5 km of MLRF1, to its northeast. These data were provided by K. Shulzitski and Drs. Lee and Sponaugle.

#### *Other Data Sources*

As described in Ch. 2, six-hourly atmospheric forecast and radiative analysis fields from the European Centre for Medium-range Weather Forecasting (ECMWF) Reanalysis – Interim (“ERA-Interim”, Berrisford et al. 2009; Dee et al. 2011) were used for downward shortwave radiative flux (insolation), downward longwave radiative flux, total cloud cover, specific humidity, barometric pressure, and atmospheric planetary boundary layer height. A 1.5x1.5°-subsamped grid of the ERA-Interim was downscaled to individual reef sites for the years 1989-2011 by bilinear interpolation, these time series were interpolated to hourly values using a cubic spline fit, and an empirical correction was then applied (see Ch. 2). Surface wave state was required in the present study to estimate both Stokes drift (residual surface transport forced by waves), and sea-surface roughness (affecting both turbulent heat flux rates and sea surface shortwave albedo). Wave measurements

were not available for these sites. Sea-state estimates from ERAI (Dee et al. 2011; Semedo et al. 2011) provided self-consistent wave forecast data for the full period of *in situ* data at SEAKEYS stations (1987-present), with empirical adjustments (Ch. 2).

A critical factor when comparing heat fluxes with changes in sea temperature (heat storage) is the depth of the water column. Sea temperature sensors at all sites, other than LOOE1 and the NCORE sites, were fixed to structures on very shallow promontories, with total water depths of less than 4 m. However, mean water column depth for this study was chosen to encompass a reasonable daily tidal excursion for a local water mass at each site, by taking the mean sea depth of the seven grid-points (~650x650 m) surrounding that site from the NGDC 3-arcsecond resolution Coastal Relief Model (Divins and Metzger 2008). Hourly water height was then varied using a tidal time series of Oregon State University's TPXO 7.2 tidal solution (e.g., Egbert and Erofeeva 2002; Egbert et al. 2010). The NGDC 3" CRM was also used to estimate maximum slope of the seafloor topography at each site using a seven-point finite-difference, and to choose cross-shore angle to True north as described previously (Ch. 2).

## 2. Methods

### *Total Heat Budget*

The overall reef heat budget consists of terms for storage rate, surface and seafloor vertical fluxes, and horizontal advection and diffusion of heat. It may be modeled by the following equation (Reed and Halpern 1975; Kraus and Businger 1994; Castellari et al. 1998; Fairall et al. 2003; Wilson-Diaz et al. 2009):

$$\partial_t T_s = + \frac{Q_0 + Q_b}{\rho C_p h} - \vec{u}_{sfc} \cdot F_q \nabla_h T_s - (1-R) \vec{u}_{hc} \cdot \nabla_h T_s (Q_0, h, \beta) + K_h \nabla_h^2 T_s \quad (3-1)$$

Here  $T_s$  is the sea temperature and  $\partial_t T_s$  is the Eulerian time rate of change in temperature.  $Q_0$  is net heat flux at the sea surface from all sources, while  $Q_b$  is net heat flux at the seafloor. Term  $h$  is the tidally varying, spatial-mean water-column depth of each site (see above), and  $\rho$  and  $C_p$  are the density and specific heat capacity of seawater, respectively, estimated from *in situ* data using the SEAWATER toolbox (Morgan 1994) for MATLAB<sup>®</sup>, based on UNESCO 1983 (Fofonoff and Millard 1983) with an assumed constant salinity for each site of between 35.5 and 36 PSU (see Ch. 2). Net sea-surface heat flux has terms, respectively, for absorbed shortwave SW and longwave LW radiative fluxes, sensible SH and latent LH turbulent heat fluxes, and flux due to rainfall, RH,

$$Q_0 = \gamma Q_{SW} + Q_{LW} + Q_{SH} + Q_{LH} + Q_{RH}.$$

Heat advection is represented by two sets of terms:  $\vec{u}_{sfc} \cdot F_q \nabla_h T_s$  represents advection of the kilometer-scale horizontal sea temperature gradient. This is derived from a gridded product whose accuracy may vary over the annual cycle – parameterized by the factor  $F_q$  (see below). An additional term for smaller-scale heat advection over a sloping seafloor,  $(1-R) \vec{u}_{hc} \cdot \nabla_h T_s (Q_0, h, \beta)$  is dependent on net surface heat flux, the local

site depth  $h$  and seafloor slope  $\beta = \Delta z / \Delta x$ , and the turbulent mixing efficiency  $R$ . This *horizontal convection* term is explained in detail below. Heat diffusion is assumed (e.g., Reed and Halpern 1975) to be the product of a lateral eddy diffusivity,  $K_h$ , and the Laplacian of the sea-surface temperature field,  $\nabla_h^2 T_s$ .

### *Radiative Fluxes*

Net sea-surface insolation is the sum of downward (I) and upward (O) components:  $Q_{SW} = Q_{SW}^I - Q_{SW}^O$ . Similarly, net longwave sea-surface flux is  $Q_{LW} = Q_{LW}^I - Q_{LW}^O$ . Downward radiative fluxes  $Q_{SW}^I$  and  $Q_{LW}^I$  were derived from ERAI with corrections (see Appendices).  $Q_{SW}^O$  was calculated assuming a simple time-varying shortwave sea-surface albedo  $A$ , as  $Q_{SW}^O = A \cdot Q_{SW}^I$ , and albedo  $A$  was estimated using the empirical relationship from Jin et al. (2011). Upward longwave flux was estimated as a gray-body function of hourly “cold-skin” temperature,

$$Q_{LW}^O = \epsilon_w \sigma_b (T_{cold} + 273.14)^4.$$

Here a constant sea-surface emissivity  $\epsilon_w = 0.97$  is assumed (Reed 1976),  $\sigma_b$  is the Stefan-Boltzmann constant, and  $T_{cold} = (T_s - \Delta T_{cold})$  is calculated according to Fairall et al. (2003), see below. As described below, a linear correction was applied to both short- and longwave downward fluxes from ERAI, based on robust linear regression of these reanalysis data against the RSMAS rooftop monitoring station data.

Absorbed net insolation,  $\gamma Q_{SW}$  [ $W \cdot m^{-2}$ ], was estimated as follows. A constant percentage of  $Q_{SW}$ ,  $P_{pen} = P_{PAR} + P_{NUV} = 54.9\%$ , was assumed to be within the visible photosynthetically active radiation (PAR) and near ultraviolet (NUV) bands (Papaioannou et al. 1993; Jacovides et al. 2003; Leal et al. 2011), with the remainder in

the near infrared (NIR). The entire NIR component of net insolation was assumed to be absorbed within the upper 1 m of water (Morel and Antoine 1994). Shortwave radiation reaching the benthos (see Fig. 3-2c below) was estimated using an exponential attenuation coefficient,  $K_d$ , to model absorption within the water column of the penetrative (PAR+NUV) insolation.  $K_d$  was assumed to be independent of solar incidence angle, while effective optical path-length in the water column was calculated based on time of day. The total attenuation rate of downward-directed insolation, where  $\theta$  is hourly local solar zenith angle, was thus calculated as (Morel and Antoine 1994; Ishizaki and Yamanaka 2010),

$$\tau = \exp(-K_d \cdot h \cdot \sec(\theta)).$$

Combined seafloor reflectivity and backscatter for PAR and NUV was estimated as a linear combination based on the mix of benthic habitat types at a site, assuming bottom reflectivity/scatter of  $A_b^{\text{sand}} = 0.40$  for sand and coral rubble, and  $A_b^{\text{other}} = 0.07$  for all other bottom types (Hochberg et al. 2003; Hochberg et al. 2004; E. Hochberg, pers. comm.). The mix of benthic habitat types within 100 m of each site was estimated from published studies (Lidz et al. 2006; Brock et al. 2008; Palandro et al. 2008; Walker et al. 2008; Bertelsen et al. 2009; Moses et al. 2009) – see Table 3-1. In lieu of a detailed radiative transfer model, specular reflection of light returned upward from the benthos, absorbed at the rate  $\tau$  (calculated above), was initially assumed. This original method indicated a median net loss of 8% or  $40 \pm 30 \text{ W} \cdot \text{m}^{-2}$  of net midday insolation at the shallowest site (LONF1), or of 4% or  $20 \pm 10 \text{ W} \cdot \text{m}^{-2}$  at all other sites. However, it is more realistic to assume significant backscatter from the rough seafloor at these sites, suggesting a mean  $45^\circ$  angle for all upward penetrative radiation throughout the day.

Total insolation absorption rate in the water column was thus estimated as,

$$\gamma = 1 - P_{\text{pen}} \cdot \tau [1 - A_b \cdot (1 - \exp[-K_d \cdot h \cdot \sec(45^\circ)])],$$

with the slope error for  $\gamma$  estimated according to the values above (8% at LONF1, 4% elsewhere). The resulting net loss of insolation upward through the sea surface was estimated to have a median midday value of  $25 \pm 15$  at the flat site LONF1, or  $28 \pm 15$   $\text{W} \cdot \text{m}^{-2}$  at a site near the reef-crest. This suggests a median net reflectivity at shallow reef sites, combining sea-surface albedo and upward insolation loss from the water column, of  $53 \pm 35$  or 11% for reef flats,  $58 \pm 30$   $\text{W} \cdot \text{m}^{-2}$  or 12% for reef-crest. Compare this to direct measurements at Heron Island, Great Barrier Reef, Australia of 11-15% or  $32$ - $42$   $\text{W} \cdot \text{m}^{-2}$  for reef-flat (1 m), and 4% or  $20$   $\text{W} \cdot \text{m}^{-2}$  for a deeper (11 m) site (MacKellar et al. 2012).

To validate corrections and error estimates for insolation, a three-year record of above-surface light data at station MLRF1 from 2008 Nov to 2011 Nov (visible light at 400-700 nm, ultraviolet at  $380 \pm 5$ ,  $330 \pm 5$ , and 305 nm variable bandwidth) was quality-controlled and analyzed (Fig. 3-2a and 3-2b). For insolation, best fit vs. the RSMAS measurements was found to be Adjusted ERAI  $Q_{\text{sw}}^1 = B(\text{ERAI } Q_{\text{sw}}^1)$ , where B was 0.88 in summer months July through August (JAS), and 0.93 for all other months. These linear corrections are validated by analysis of the *in situ* PAR data at MLRF1 (Fig. 3-2, Appendices); regression of corrected ERAI vs. insolation estimated from the MLRF1 showed a  $+0.8$   $\text{MJm}^{-2}\text{d}^{-1}$  bias, 5% slope error and RMSE of  $2.5$   $\text{MJ m}^{-2}\text{d}^{-1}$ .

Above-surface light data were then combined with a quality-controlled record of coincident underwater PAR and NUV from  $\sim 2$  m depth at the site, in order to estimate errors in the attenuation coefficient using the method of Kirk (1994). Due to rapid biofouling of underwater light sensors, care was taken to use only underwater light

measurements taken between 24 h and 14 d after a known instrument cleaning (Fig. 3-2c and 3-2d). This filtering left 4,030 coincident above- and underwater hourly data points across three years, including data for every month of the year except October. Daily dose ( $\text{MJ}\cdot\text{m}^{-2}\cdot\text{d}^{-1}$ ) was calculated from *in situ* data for both net surface insolation (Fig. 3-2b) and insolation reaching the benthos, and based on surface light and a climatological mean light attenuation coefficient (both Fig. 3-2c). A model of seabed-water heat exchange developed for these sites is described below, including absorption of radiation by the benthos, and absorption in the water column of radiation reflected and backscattered upward from the benthos.

In spectral analysis of hourly PAR at MLRF1 (Fig. 3-2a), strong signals at 12 h and higher frequencies are almost certainly an artifact of the lack of a signal during nighttime hours. However, slight peaks in both the 30 d and 60-70 d bands are also apparent in the spectrum; these lower-frequency signals may relate mean surface light to larger-scale atmospheric variability, e.g., the long-mode period of the Madden-Julian oscillation. Of interest in the monthly means of daily surface dose (Fig. 3-2b) is the significant mid-summer dip: this is consistent with persistent cloud cover caused by convective local weather processes during the rainy season.

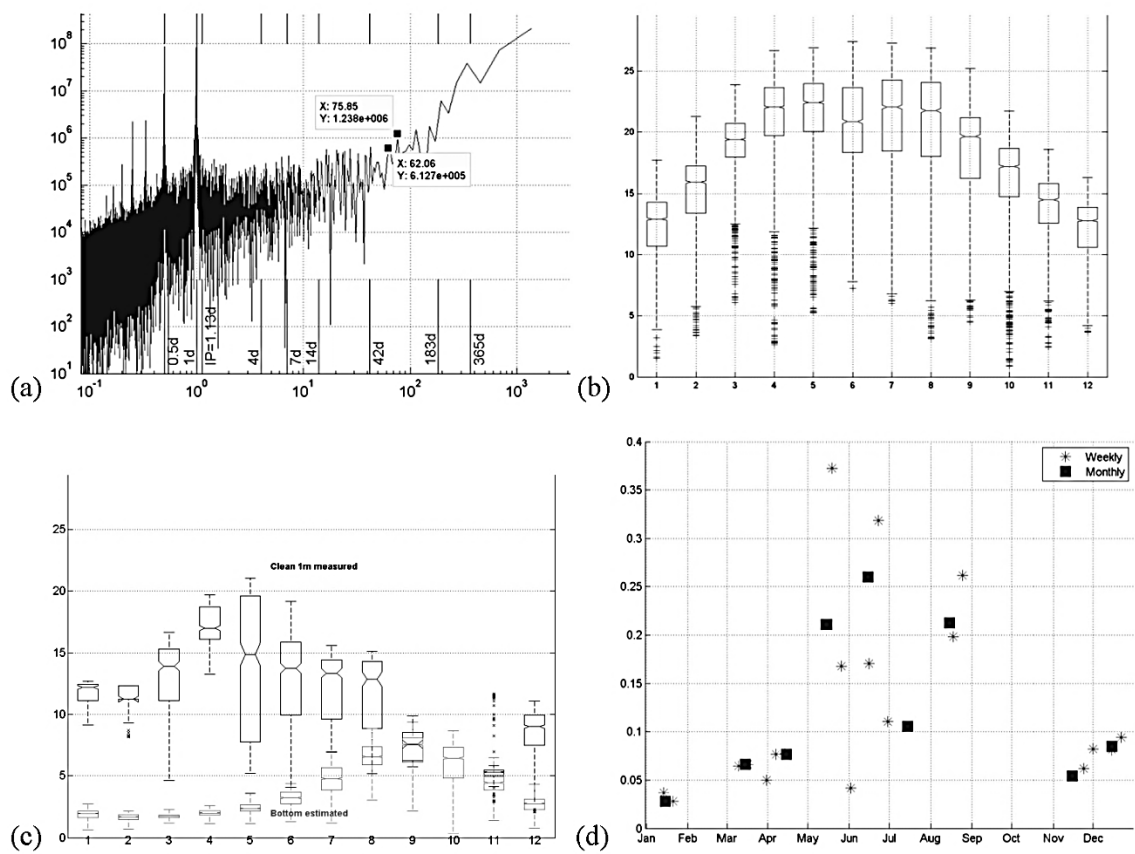


**Figure 3-2:** (a) Spectrum using boxcar-windowed periodogram method, of quality-controlled hourly above-surface photosynthetically active radiation (PAR, 400-700 nm) for November 2008 – November 2011 at Molasses Reef. (b) Monthly boxplot of daily dose for above-surface insolation ( $\text{MJ}\cdot\text{m}^{-2}\cdot\text{d}^{-1}$ ) at MLRF1. (c) Monthly boxplot of daily dose for available insolation near the seafloor ( $\text{MJ}\cdot\text{m}^{-2}\cdot\text{d}^{-1}$ ) as measured at 1 m on MLRF1 (black), and as estimated for the heat budget (gray) from above-water PAR, surface albedo, and in-water absorption climatology, for a mean site depth of 3.55 m. (d) Weekly (\*) and monthly (■) median post-cleaning light-attenuation coefficient for PAR ( $K_d^{\text{PAR}}$ ,  $\text{m}^{-1}$ ) as estimated from *in situ* post-cleaning surface and underwater hourly PAR.

Median attenuation coefficient for *in situ* PAR ( $K_d^{\text{PAR}}$ ) showed a consistent annual cycle across multiple years, ranging from 0.05 in January to 0.25  $\text{m}^{-1}$  May-June (Fig. 3-2d). This range of values is consistent with variations between coastal and deeper sites elsewhere in the ocean (e.g., Chen et al. 2007; Lewis et al. 2011). Median attenuation coefficients calculated from narrowband UV sensors ranged from  $K_d^{380\text{nm}}=0.05\text{-}0.20$  to  $K_d^{305\text{nm}}=0.25\text{-}0.45$   $\text{m}^{-1}$ , all with seasonal peaks at the same time as slightly early than that for  $K_d^{\text{PAR}}$  (figures not shown). The combined broadband

attenuation coefficient  $K_d$  for both PAR and narrow-band NUV at this site was thus found to vary annually from 0.05 to 0.25  $m^{-1}$ , with an annual peak between year-days 110 and 200.

These estimates also agree well with published attenuation for PAR and NUV based on *in situ* and remote sensing data at multiple sites in the FRT (e.g., Lesser et al. 2000; Palandro et al. 2004; Zepp et al. 2008), and with more recent studies of the reef tract based on high-resolution satellite ocean color data (Barnes et al. 2013; Zhao et al. 2013). For one very shallow site (LONF1), the satellite ocean color-derived estimates of  $K_d^{PAR}$  by Zhao et al. (op. cit.) were much higher, with mean  $K_d \approx 0.88$  and seasonal variability of  $\pm 0.40$ . The monthly data of Zhao et al. and Barnes et al. show seasonality which varies significantly between sites; in particular, their attenuation data most frequently show peaks between December and February at LONF1, between February and April at most reef crest sites (MLRF1, SMKF1, and SANF1), and between April and May at FWYF1.

Estimates of daily dose of insolation were calculated from PAR measured at MLRF1 at 1 m depth, and were also estimated near-bottom for a mean MLRF1 site depth of 3.55 m using measured above-surface PAR combined with empirical estimates of sea-surface reflectivity and climatological insolation attenuation/absorption as described above (Fig. 3-2c). Median near-bottom daily dose estimates for August of 8  $MJ \cdot m^{-2} \cdot d^{-1}$  are consistent with estimates from a prior field and remote-sensing study (Barron et al. 2009).

### *Turbulent Air-Sea Fluxes*

The algorithms of the Tropical Ocean Global Atmosphere Coupled Ocean Atmosphere Response Experiment (TOGA COARE 3.0a) were used to calculate latent, sensible, and precipitation heat fluxes (Clayson et al. 1996; Fairall et al. 2003) and their associated representation errors. Adjustments to latent and sensible heat fluxes are applied by the COARE 3.0a algorithms for the “effective” wind speed relative to sea-surface ocean currents, for wave-induced roughness, for atmospheric planetary boundary layer height, and for the ocean cool-skin effect (Fairall et al. 1996; Fairall et al. 2003; see also Error Analysis and Sources below).

Warm-layer adjustment is a further option of the 3.0a algorithms that adjusts diurnal warming to the depth where sea temperature measurements are made (Price et al. 1986). This adjustment was retained at sites that border deeper water offshore: FWYF1, MLRF1, LOOE1 (for both sensors), SMKF1, and SANF1. Turbulent fluxes for shallow, flat sites LONF1 and DRYF1 showed superior fit to observed variability when warm-layer adjustment was *not* applied. Maximum warm-layer depth is a parameter specifying the depth at which this warm-layer deepening is assumed to stop. At sites where the warm-layer adjustment was retained, that parameter was set to 0.5 m less than the mean hourly water depth, i.e., truncating development of the diurnal warm layer just above the bottom boundary layer.

### *Bottom Boundary-Layer Fluxes*

Heat fluxes between the seafloor and overlying ocean, the term  $Q_b$  in this heat budget, may be significant in the time evolution of temperature in very shallow water (Nadaoka et al. 2001; Uncles and Stephens 2001; Nihei et al. 2002; Wells et al. 2012). A

straightforward approach to modeling water-seafloor heat flux is taken here, using published methods (Comer and Grenney 1977; Webb and Zhang 1997; Evans et al. 1998) as follows. Benthic heat flux into the water column is estimated by simple hourly forward integration of a model for benthic substrate temperature,  $T_b$ , which includes terms respectively for shortwave radiation absorbed by the benthos  $Q_{bSW}$ , net longwave radiation into the benthos  $Q_{bLW}$ , heat conducted into the substrate  $Q_{bCD}^I$ , heat conducted from the seafloor upward  $Q_{bCD}^O$ , and heat convectively mixed into the bottom boundary layer from the water above,  $Q_{bSH}$ ,

$$\rho_b C_{pb} h_b \cdot \partial_t T_b = Q_{bSW} + Q_{bLW} + Q_{bCD}^I - Q_{bCD}^O + Q_{bSH}. \quad (3-2)$$

Shortwave radiation absorbed by the benthos is a function of seabed reflectivity,  $A_b$ , and of the downward shortwave net radiation not absorbed by the water column,

$$Q_{bSW} = P_{pen} \tau (1 - A_b) Q_{SW}$$

(see descriptions of  $P_{pen}$ ,  $\tau$ ,  $A_b$ , and  $Q_{SW}$  under Radiative Fluxes, above). Longwave flux into the seafloor  $Q_{bLW}^I$  is calculated as a gray-body function of *in situ* water temperature  $T_s$  (similar to the calculation of  $Q_{LW}^O$  using  $T_{cool}$  in Radiative Fluxes above). Upward longwave flux  $Q_{bLW}^O$  is a gray-body function of  $T_b$ , where seabed longwave emissivity  $\epsilon_b$  is estimated as an areal average of representative values for saturated marine sediment  $\epsilon_{sed}=0.82$  and for hard substrate  $\epsilon_{other}=0.98$ , based on the local mix of benthic habitat types (see above). Heat conducted from the substrate  $Q_{bCD}^I$ , is calculated assuming a time-invariant base substrate temperature  $T_{base}$  (set equal to long-term mean sea

temperature at each site), at a depth  $h_{\text{base}}$  meters below the seafloor (chosen arbitrarily as 2 m), and a constant rate of heat conduction through the benthos,  $K_b$ , according to,

$$Q_{\text{bCD}}^{\text{I}} = -K_b (T_b - T_{\text{base}})/h_{\text{base}}.$$

$K_b$  was estimated again as an areal average for each site, using end-point values  $K_{\text{b, sed}}=1$  for marine sediment (Nobes et al. 1986) and  $K_{\text{b, rock}}=2.8$  for porous water-submerged rock (Thomas et al. 1973). Heat conducted from the seafloor into the ocean,  $Q_{\text{bCD}}^{\text{O}}$ , is calculated using benthic and ocean temperatures, assuming a thermal boundary layer in the benthos of depth  $h_b=0.03$  m. Turbulent flux  $Q_{\text{bSH}}$  is calculated as a function of modeled hourly tide-current speeds at each site, using a coefficient of drag  $C_{\text{bd}}=0.017$  as estimated on a reef slope in the FRT by Davis and Monismith (2011), and a benthic heat flux coefficient  $C_{\text{bh}}=1.0 \times 10^{-2}$ ,

$$Q_{\text{bSH}} = \rho C_p u_{\text{tide}} C_{\text{bd}} C_{\text{bh}} (T_s - T_b).$$

Terms  $\rho$  and  $C_p$  in this equation refer to values calculated for seawater, while  $\rho_b$  and  $C_{\text{pb}}$  in Eq.3- 2 above refer to density and specific heat capacity for the benthic substrate, estimated at each site based on its benthic habitat type.

### *Heat Advection*

As shown in a previous analysis of ocean current components from *in situ* data at Looe Key spar (Ch. 2), cross-shore currents near the reef crest are considerably smaller than alongshore currents, often near the limit of measurement error for the deployed instruments. Analysis of currents at NCORE sites “NCORC” and “NCORK” also bears out this conclusion (figures not shown). Shallow-water barrier reef systems with high “linear” (long-shore) reef density can provide an effective barrier against intrusion of

low-frequency ocean currents (Wolanski and Spagnol 2000), a conclusion consistent with these observations. The dominant sea-surface temperature gradient at the reef crest is cross-shore (Ch. 2, and Appendices). Therefore, at sites near the reef crest/shelf-break, larger-scale advection of heat was expected to play only a small role in the overall heat budget. However, currents within 0-3 m of the surface forced by waves (Stokes drift) were calculated using an empirical relationship based on low frequency wind speed and surface-wave height, from Ardhuin et al (2009). For that calculation, the 10-meter *in situ* wind speed at each site was used with a two-way Butterworth 72-hour low-pass filter applied, significant wave height was derived from ERAI model output, and cutoff wave frequency was chosen as a simple function of peak wave period from model output,  $f_c=1/(0.5 \cdot w_p)$ . Other methods of estimating surface currents from wind were also evaluated, including simple linear relationships between surface current and low-frequency wind speed  $\mathbf{u}_{sfc} = \lambda \cdot \mathbf{U}_{10,lp}$  (see Sensitivity Analysis below), with  $\lambda$  ranging from 1.0 to 3.5% (Shay et al. 2007; Mao and Heron 2008; Ardhuin et al. 2009).

Advection and diffusion terms in the heat budget were calculated from horizontal gradients in the weekly composite Advanced Very High Resolution Radiometer Sea-Surface Temperature (AVHRR SST) as described in Ch. 2 and GM1. To estimate errors in heat advection and diffusion, thermosalinograph (TSG) data were analyzed (see Appendices) from bimonthly ship-based SFP transects across the reef (E. M. Johns, pers. comm.) for the period 2003-2010. Their results confirm other studies in the sub-tropics which find that both satellite and near-surface *in situ* SST may provide a misleading picture of horizontal gradients, particularly during periods of rapid warming (Sturges and Leben 2000; Katsaros and Soloviev 2004; Katsaros et al. 2005). A recent study by

Castillo and Lima (2010) further finds that benthic sea temperature on coral reefs can be poorly correlated with satellite-derived SST during rapid warming. In essence, the SST dataset chosen for this study, while providing consistent data at high spatial resolution over a long record (1993-2012), provides relatively little reliable information on horizontal gradients, particularly during the warmest months centered around year-day 228 (see Fig. 2-6). To account for this, a simple annual sinusoid-weighting factor  $F_q$  was applied to heat advection estimates using AVHRR SST, with full weight on year-day 45 and zero weight on year-day 228. Two exceptions were SANF1, where AVHRR SST gradients could not be used with empirical surface currents at all, and FWYF1, where extreme gradient estimates during months October-December forced a peak  $F_q$  around year-day 100 to be adopted.

#### *Horizontal Heat Diffusion*

The term  $\nabla^2 T_{km}$  was estimated directly from weekly composite AVHRR SST fields using a second-order, centered finite-difference scheme (with 5 points for most sites, 3 points for SANF1 and DRYF1). For comparison, in both the GoM and FKEYS HYCOM, horizontal heat diffusion is implemented with a constant effective lateral eddy heat diffusivity of  $K_{h,model}$  ( $20 [m^2 \cdot s^{-1}]$  in GoM, per A. Wallcraft and P. Hogan, pers. comm.;  $2.0 [m^2 \cdot s^{-1}]$  in FKEYS). However, direct estimates of lateral eddy heat diffusivity in the presence of both strong horizontal temperature gradients and steep topography (Park and Chu 2008), similar to conditions found in the FRT, have found significant variability in this parameter over km spatial scales and monthly time scales. In the present study, the annual sinusoidal weighting  $F_q$  used for heat advection was

applied to a constant eddy heat diffusivity of 20,  $K_h = F_q \cdot 20$ , to account for unreliability in gradients from AVHRR data in warmer months (see above). Such dispersion calculated with a slowly (seasonally) varying diffusivity  $K_h$  may be referred to as “pseudo-Fickian” diffusion. However, results were also evaluated using eddy heat diffusivity that varied as a function of wind speed  $K_{h,wind} = 20 \cdot \min[1, (U_{10}/35)^2]$  (see Sensitivity Analysis below). Finally, a sub-grid scale (sub-km) eddy diffusivity  $K_{h,SGS}$  was calculated as a function of AVHRR gradient and heat budget residual, with only positive diffusivities permitted: results using this smaller-scale enhancement to eddy diffusivity are described below.

#### *Horizontal Convection*

Finally, the addition of another term for small-scale heat advection was found to significantly improve *in situ* comparisons with the reef heat budget. This term arises when a horizontally invariant heat flux is applied to a shallow-water site with a gradient in bottom depth. Buoyancy-driven flows or “gravity currents” are induced, moderating sea-temperature variability near the top of the slope (Hughes and Griffiths 2008; Mao et al. 2010b; Mao et al. 2010a).

To understand this effect under different regimes, studies have examined uniform surface cooling (Sturman et al. 1999; Lei and Patterson 2005; Bednarz et al. 2008; Mao et al. 2010b), and periodic heating and cooling where all heat flux is directly absorbed in the water column (Farrow and Patterson 1993; Bednarz et al. 2009). The case where penetrative solar radiation is absorbed and re-radiated by the seafloor has also been considered by numerical, theoretical, and field studies (Mao et al. 2009; Chubarenko 2010; Mao et al. 2010a; Wells et al. 2012). Such thermal exchange currents over sloping

topography are referred to in literature as “horizontal convection” or the *thermal siphon* (Monismith et al. 1990).

Horizontal convection has been directly observed over coral reefs on the Gulf of Eilat in the Red Sea (Monismith et al. 2006) and near shore in Hawai’i (Wells et al. 2012), as well as elsewhere in the oceans and inland waters (Monismith et al. 1990; James and Barko 1991; Farrow and Patterson 1993; Shapiro et al. 2003). In the study by Monismith et al. (2006), bottom slope at their site was estimated at  $\beta \approx 0.20$  (20%), with extremes of persistent cooling on the order of  $-400 \text{ W}\cdot\text{m}^{-2}$ . In the sub-tropical marine environment of the FRT, net cooling and heating are often much less than this; however, during and after the passage of cold fronts, daily mean net surface heat flux in the FRT falls below  $-500 \text{ W}\cdot\text{m}^{-2}$ , while during summer doldrums hourly median net warming exceeds  $+500 \text{ W}\cdot\text{m}^{-2}$  (figures not shown).

The topographic slopes estimated for this study were derived from NGDC bathymetry as described above, and are summarized in Table 3-1. At one flat site, LONF1, slope was nearly negligible at 0.003. However, at sites near the reef-crest (FWYF1, MLRF1, SMKF1, and SANF1) and the reef-slope (LOOE1 and the NCORE current meter sites), slopes range from  $\beta \approx 0.02$  to 0.04. This is far less than the 0.20 slope reported in the Gulf of Eilat study. Yet Monismith et al. (2006) present scaling arguments which suggest that over bottom slopes in the range  $0.01 < \beta < 0.2$ , thermal siphon heat exchange rates (see below) are relatively insensitive to seafloor slope and peak cooling or heating rate; indeed for this range of slopes in the steady-state, heat exchange rates based on such scaling increase roughly as  $0.1/\ln(\beta)$  (Fig. 3-3).

Published studies offer a variety of methods for estimating the characteristic velocity, volumetric flow rate, and net heat exchange from horizontal convection. However, Monismith et al. (2006) is the first published study where scaling was directly applied to field data from a coral reef slope, to estimate horizontal convection based on a mathematical relationship with surface buoyancy flux, water depth, and seafloor slope. That paper offers six distinct scales for convective exchange currents (their Table 1 and Appendix): these respectively describe periods when horizontal convection is spinning up (unstable thermal balance), when it is quasi-stationary (stable thermal balance); and when buoyancy forcing is balanced in the cross-shore momentum equation by three distinct sets of terms – advective (steady) inertia, unsteady inertia, and dissipative stress. All six scales are based on a characteristic convective velocity scale  $u_f$ , defined as,

$$u_f = (h \cdot B_0)^{1/3}. \quad (3-3a)$$

Here  $h$  is water depth and  $B_0$  is buoyancy flux per unit area [ $m^2 s^{-3}$ ] as defined below. Based on field, lab, and theoretical estimates of spin-up lag time  $O(24 \text{ h})$  for stable, radiation-induced horizontal convection (Chubarenko 2010), the present study estimates buoyancy flux from a 24-hour simple moving average (24hSMA) of net surface heat flux. With  $\alpha$  the thermal expansion coefficient (Fofonoff and Millard 1983) and other terms as defined previously, the buoyancy flux per unit area of sea surface is then defined as,

$$B_0 = g\alpha Q_{24hSMA}/\rho C_p. \quad (3-3b)$$

At the beginning of each period of cooling or warming, lag times for onset of horizontal convective transport are calculated using the scaling in Chubarenko (op. cit.). The dominant thermal forcing periodicity,  $T_f$ , is estimated using short-time Fourier

analysis or a simple run-length encoding. The scaling relationships from Monismith et al. (op. cit.) are then used to estimate a cross-shore volume discharge rate per unit length of reef,  $Q_{hc}^V$  [ $m^2s^{-1}$ ]. For the inviscid case which this paper assumes to hold, the momentum equations (Monismith et al. 2006, their Appendices) are balanced between inertia and buoyancy forcing. The choice in the present study of whether the dominant momentum balance is steady- (periodic) or unsteady-inertial,  $Q_{hc,S}^V$  or  $Q_{hc,U}^V$ , is made on a site-by-site basis. On the other hand the choice between steady and unsteady thermal forcing,  $Q_{hc,*S}^V$  or  $Q_{hc,*U}^V$ , is time-dependent: during periods of balanced diurnal heating and cooling, estimates  $Q_{hc,*S}^V$  are used. During intermittent periods of persistent warming (rare) or cooling, scaling relations for unsteady thermal forcing,  $Q_{hc,*U}^V$ , are used,

$$\begin{aligned} Q_{hc,SS}^V &= A+B \cdot u_f \cdot \beta^{-1/3} \cdot h, & Q_{hc,US}^V &= A+B \cdot (u_f^3 \cdot T_f h)^{1/2}, \\ Q_{hc,SU}^V &= A+B \cdot \beta^{2/3} \cdot u_f (u_f T_f / h)^{3/2}, & Q_{hc,UU}^V &= A+B \cdot \beta \cdot u_f^3 \cdot T_f^2 / h. \end{aligned} \quad (3-3c)$$

The empirical constants A and B used for each scaling, were those found by Monismith et al. (op. cit., their Figs. 10a,c,d,f) to provide the best fit with observations from that study. For example, for unsteady inertial momentum balance and steady thermal forcing,  $Q_{hc,US}^V$ , the constants  $A=-0.026$ ,  $B=3.0$  were used. Under various thermal forcing conditions, these values were also found to provide acceptable fits with observed current shears at Looe Key and the NCORE sites (Fig. 3-5). For the range of slopes near the reef-crest ( $\beta=0.02-0.04$ ) and the range of depths offshore (1-40 m), estimates of  $Q_{hc}^V$  using these various values were also found to be in good agreement ( $\pm 20\%$ , figures not shown) with the depth dependence relationship for volumetric

exchange rates derived by Chubarenko (op. cit.). The term for contribution of the thermal siphon to the reef heat budget was then calculated using the relations,

$$\vec{u}_{hc} = \frac{Q^V_{hc}}{h}; \nabla_h T_{hc} = -Q_{24hSMA} \left( \frac{1}{h} - \frac{1}{(h + \beta x)} \right) / \rho C_p. \quad (3-4)$$

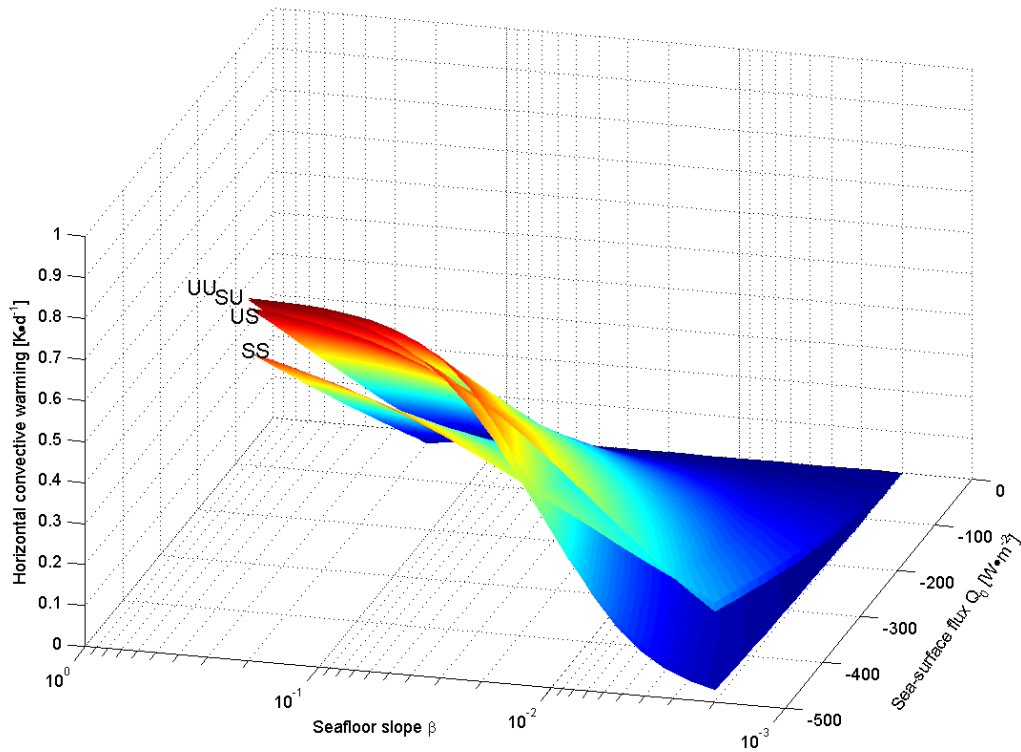


**Figure 3-3: Predicted horizontal convective warming (K·d<sup>-1</sup>, vertical axis) as a function of sea-surface cooling rate (Wm<sup>-2</sup>, axis into page) and seafloor slope β (breadth-wise axis) under various momentum and thermal balances (UU, SU, US, SS; see Eq. 3-3c).**

A further consideration was the relative strength of thermal siphon responses to warming and cooling, respectively. Lei and Patterson (2006) developed a numerical model of the thermal siphon under periodic forcing due to alternating surface cooling and radiative warming. Their results suggest that overturning during times of surface cooling produces a consistent convective response, while in the shallow-water case, development of instabilities during penetrative warming leads to a significantly weaker, intermittent

response. This result is found to be consistent with analysis of current shear in the present study also; it is modeled in the heat budget by scaling the total temperature moderation due to the thermal siphon during warming periods by 0.66, while cooling is scaled by 1.00 (op. cit., their Figs. 3 and 5).

Turbulent mixing also acts as a control on thermal exchange flows, resulting from the vertical current shear and from flow over an uneven seafloor. Common estimates of mixing efficiency (rate of transfer of kinetic energy to potential energy) from observation and experiment (e.g., Peltier and Caulfield 2003) are ~20%. However, tank experiments (Prastowo et al. 2009) find that over sloping, rough topography and in the presence of vertical hydraulic controls, as will be the case for example in spur-and-groove reef slope formations, this value may be as low as 8%. Net heat exchange was estimated assuming a combined constant rate of  $R=0.08$  due to mixing and entrainment (Spigel et al. 1986), consistent with published studies under similar conditions (Davis and Monismith 2011; Dunckley et al. 2012).

#### *Error Analysis and Sources*

Measurement errors for most directly measured and reanalysis quantities were estimated previously in Ch. 2 and in GM1. Representation errors for turbulent heat fluxes were estimated using the methods of Fairall et al. (2003), summarized together with the bulk formulae for calculating fluxes below in the Appendices.

Representation errors for absorbed insolation, large- and small-scale advection, and mixing terms were calculated directly using the method of propagation of uncertainty as described in Emery and Thomson (2001). A significant source of potential error in the

heat budget was the interpolation of low-resolution (1.5°) ERAI fields for downward shortwave and longwave radiative flux, total cloud cover, specific humidity, and barometric pressure (e.g., Berrisford et al. 2009; Dee and Uppala 2009). The six-hourly North American Regional Reanalysis (NARR; Mesinger et al. 2006) with 32 km spatial resolution was also evaluated for this purpose (Ch. 2). As described in Ch. 2, and in GM1 and studies cited therein, regression RMSE vs. *in situ* data for insolation, downward longwave flux, and various meteorological variables from NARR were much larger at all sites than those from the nominally lower resolution ERAI. Use of ERAI data in the present study was also found to result in significant reductions in heat budget residuals vs. observed sea temperature variability (see below). ERAI downward radiative fluxes also compared well with those from the International Satellite Cloud Climatology Project (ISCCP) climatology of Zhang et al. (2004).

To calculate estimation error for reanalysis  $Q_{SW}^1$ , data from ERAI and NARR were compared with quality-controlled *in situ* PAR cosine irradiance data for three years (2008-2011) at one site (MLRF1; see Fig. 3-2a, 3-2b). PAR irradiance (light in passband 400-700 nm) is reported from MLRF1 in units of  $\mu\text{mol quanta}\cdot\text{m}^{-2}\cdot\text{s}^{-1}$ ; PAR may be converted to radiative flux units ( $\text{W}\cdot\text{m}^{-2}$ ) by several methods (Payne 1972; Morel and Smith 1974; Godfrey et al. 1991; Papaioannou et al. 1993; Dye and Shibasaki 1995). The present study uses a conversion suggested by Dye (2004) of 0.2193 J per  $\mu\text{mol quanta}$ . A linear relationship between insolation and PAR in units of  $\text{W}\cdot\text{m}^{-2}$ ,  $Q_{SW}^1 = P_{PAR} \text{PAR}$ , has been investigated under a variety of conditions, e.g., by Papaioannou et al. (1993) and by Jacovides et al. (2003). These sources suggest  $P_{PAR}=0.501$ , used in the present study. Robust linear regression between 6-hourly adjusted ERAI and *in situ* above-surface

insolation calculated from PAR at MLRF1 (see above),  $df > 4000$ , shows a slope error of  $< 1\%$ , a bias of 4 and root mean-squared error (RMSE) of  $35 \text{ W}\cdot\text{m}^{-2}$ , with coefficient of determination  $R^2 \sim 0.9$ . Errors regressing daily dose ( $\text{MJ}\cdot\text{m}^{-2}\cdot\text{d}^{-1}$ ) between *in situ* and adjusted ERAI were of the same order. By contrast, regression of 6-hourly NARR with *in situ* insolation based on MLRF1 PAR showed slope error 30%, bias 20 and RMSE  $100 \text{ W}\cdot\text{m}^{-2}$ ,  $R^2 \sim 0.6$ .

As reported above in Ch. 2, a positive summer bias in ERAI air temperature vs. *in situ* data is accompanied by a negative winter bias in ERAI wind speed. In a previous heat budget study (Gramer et al. 2012) these respective biases complemented one another to produce apparently good matches to *in situ* sea temperature variability. ERAI fields for insolation, downward longwave radiative flux, barometric pressure, and specific humidity were used throughout the present study, but air temperature and winds were used from *in situ* measurements. For the Looe Key heat budget only, *in situ* air temperature and wind data from nearby Sombrero Key Reef station (SMKF1), 30 km ENE of Looe were used. For heat budget calculations at reef sites where *in situ* meteorological measurements are not available, work is now underway to evaluate alternate sources of gridded meteorological data.

One issue with bulk turbulent flux estimates such as those from the COARE algorithms presented here is that the *in situ* data upon which they are based are hourly mean values. As such they sample not just smaller-scale turbulent fluxes, co-variability on time scales of seconds to minutes, but also mesoscale atmospheric motions (Clayson et al. 1996; Vickers and Mahrt 2006). Another issue is that the dynamical basis of these

bulk parameterizations, Monin-Obukhov similarity theory, breaks down under spatially anisotropic conditions, e.g., those where a strong vertical or lateral gradient in sea temperature is present (ibid.). Data were not analyzed to estimate errors from either of these effects here. However, a proposed direction for future research would be to make use of *in situ* data with higher sampling frequencies (10 min or less) across a reef crest, to estimate errors introduced into the turbulent flux calculations by the use of hourly means.

Finally, for those terms in the budget which rely on horizontal gradients in the AVHRR SST field, the annual periodic weighting  $F_q$  for advection and diffusion was applied to their error estimates vs. SFP data as well. Table 3-2 summarizes measurement errors for inputs to the reef heat budget not previously reported in Ch. 2 and GM1. Slope error is as defined in Ch. 2 and GM1.

**Table 3-2: Nominal measurement or modeling errors for heat budget inputs not described in Ch. 2.**

<i>Name</i>	<i>Input Variable</i>	<i>Error <math>\sigma</math> (slope <math>\pm</math> RMSE)</i>	<i>Error Source or Method</i>
Depth experienced by a watermass throughout the tide cycle	$h$	30% $\pm$ 0.1 m	Regression vs. <i>in situ</i> (SMKF1, LONF1); Erofeeva pers. comm., (Egbert et al. 2010)
Net $Q_{SW}$ absorption	$\gamma$	7%	See text
Upward longwave flux	$Q_{LW}^0$	0% $\pm$ 4 $W \cdot m^{-2}$	Propagation of published uncertainty in cold-skin temp. (Fairall et al. 2003)
Surface storage rate	$3600/h\rho C_p$	Slope error $1 \times 10^{-5}$	Propagation of uncertainty in $T_s$ , $S$ , $h$
Benthic storage rate	$3600/h_b\rho_b C_{pb}$	Slope error $5 \times 10^{-5}$	Propagation of uncertainty in $h_b$ , benthic habitat classification
Wave-forced surface current	$u_{sfc}$	20%	(Ardhuin et al. 2009)
Horizontal near-surface sea temperature gradient	$F_q \nabla_h T_s$	5% $\pm$ 0.35 $K \cdot km^{-1}$	Ch. 2, and see text
Horizontal near-surface sea temperature Laplacian	$K_h \nabla_h^2 T_s$	5% $\pm$ 0.05 $K \cdot km^{-2}$	Ch. 2, and see text

Methods for estimating representation errors using propagation of errors from measured quantities are described in detail in the Appendices. Representation errors calculated for the individual budget terms and for the heat budget as a whole are summarized in Table 3-3 for one representative site.

**Table 3-3: Numerical values of representation errors for each major term in the heat budget, estimated for site MLRF1.**

Name	Term	Median error $\sigma$ [ $W \cdot m^{-2}$ ]	Scatter Index (error normalized by mean value)	Error variance ( $\frac{\max - \min}{6}$ )
Sensible heat flux	$Q_{SH}$	1	9%	6
Latent heat flux	$Q_{LH}$	10	9%	44
Precipitation heat flux	$Q_{RH}$	2	50%	1
Net surface longwave radiative flux	$Q_{LW}$	12	22%	0.5
Net surface shortwave radiative flux	$Q_{SW}$	23	12%	13
Absorbed shortwave flux	$\gamma Q_{SW}$	23	14%	17
Net surface heat flux	$Q_0(\gamma)$	29	35%	43
Net seabed heat flux	$Q_b$	1	7%	7
Net 1-D sea flux	$Q_0 + Q_b$	$30 W \cdot m^{-2}$ , $0.004 K \cdot hr^{-1}$	30%	$44 W \cdot m^{-2}$ , $0.005 K \cdot hr^{-1}$
Surface heat advection	$u_{sfc} \cdot F_q \nabla_h T_s$	40	100%	60
Horizontal heat diffusion	$K_h \nabla_h^2 T_s$	2	100%	1
Total kilometer-scale heat budget	$\partial_t T_{km}$	$65 W \cdot m^{-2}$ , $0.01 K \cdot hr^{-1}$	70%	$100 W \cdot m^{-2}$ , $0.02 K \cdot hr^{-1}$

Histograms of bulk representation error for latent and sensible heat flux at MLRF1 are shown in Fig. 3-4. While median errors are  $\approx 10 W \cdot m^{-2}$  for latent flux and  $\approx 1 W \cdot m^{-2}$  for sensible flux, a few outliers in these raw error estimates are very large. One reason for this is the lack of key *in situ* data: for example, reanalysis specific humidity may appear to be very close in value to saturated specific humidity calculated from an *in*

*situ* sea temperature, resulting in anomalous errors in air-sea flux algorithms. Similarly, extremes in AVHRR SST gradients and Laplacians not removed by quality control also introduce anomalous errors. Days containing an outlier in any of the error estimates summarized in Table 3-3 were removed in the results that follow, resulting in the elimination of several brief “events” or periods in the results where the total heat budget diverged sharply from observed sea temperature variability. Heat budget estimates were removed from all daily and other means below when any one hourly error estimate for any budget term exceeded an arbitrary cutoff of  $200 \text{ W}\cdot\text{m}^{-2}$  or  $0.5 \text{ K}\cdot\text{hr}^{-1}$ . This procedure removed from seven (7) to 75 d, from 0.3 to 1.1% of the complete record of heat budget estimates at each site, predominantly during the months of March, April, and May (~1% of all days in those months). These events may also coincide with extreme local convective weather, or breaking of internal waves or meanders and frontal eddies of the Florida Current offshore, and are investigated in Chapter 4.

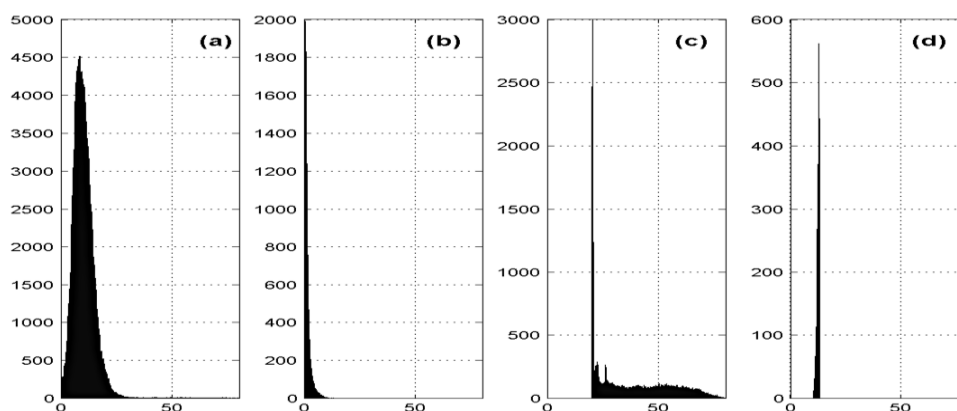


**Figure 3-4: Histograms of hourly representation error (x axes,  $\text{W}\cdot\text{m}^{-2}$ ) at FWYF1, calculated using methods of Fairall et al. (2003) for (a) latent and (b) sensible heat flux; and using propagation of error (see text and Appendices) for (c) net shortwave and (d) net longwave radiative fluxes.**

### Mixed-Layer Deepening

It is important to note that a key term of the open-ocean heat budget equation has been omitted in the present reef heat budget – that associated with entrainment of cool water due to wind-driven (i.e., non-diurnal) mixed layer deepening. Over the entire reef crest and waters inshore of it within the FRT, i.e., cross-shore zones (i) through (iii) described in Ch. 1, the seafloor depth is of order 30 m or less. Within the Florida Keys, the water column over these three zones (i.e., near-shore waters of the Keys, Hawk Channel, and at the outer reef) is generally less than 10 m deep. In the present results, therefore, main or seasonal mixed-layer deepening has been ignored as a direct forcing term for reef sea temperature variability. The AVHRR products provide an estimate of horizontal SST gradients at 1 km resolution, closing this gap in the reef heat budget.

Immediately offshore of the reef crest however, everywhere in the FRT, the outer reef slope closely adjoins waters that may be 100 m or deeper. An open question which future research may address is whether a model of mixed-layer deepening, together with estimates of horizontal *onshore* advection, can successfully explain some significant part of sea temperature variability on the fore-reef slope or the reef crest. A hydrodynamic model of sufficient spatiotemporal granularity could be used. Another approach would be to use sea-surface wind stress and heat flux estimates to perturb a published seasonal climatology of mixed-layer depth and sub-thermocline sea temperature profiles for the SF, to estimate mixed layer depth,  $h$ , and temperature jump at the base of the mixed layer,  $\Delta T$ . A mixed layer entrainment term,  $\Delta TW_e/h$ , based on these estimates could be added to the heat budget for (Kraus and Businger 1994; Wilson-Diaz et al. 2009) using:

$$W_e = -2 [m_1 u_*^3 - 1/2 h (\alpha g / \rho C_p) Q_0] / (\alpha g \Delta T h) \quad (3-5)$$

### 3. Results

#### *Horizontal Convection Parameters*

To validate the choice of horizontal convection parameterization and to estimate errors for the horizontal convection contribution to the overall heat budget, predicted horizontal convection estimates for stations MLRF1 and SMKF1 were compared with ocean cross-shore current shear and vertical temperature differences from three other sites. Data from approximately 2.8 years (1050 d) at LOOE1, 1.6 years (600 d) at NCORE site “NCORC”, and 330 d at NCORE site “NCORK” were analyzed, with depth-averaged currents removed. ADCP current profiles at LOOE1 (Fig. 3-5a) show near-bottom flows during horizontal convection mainly occupy a range of depths within 6 m of the seafloor.

This matches results from field and numerical studies (see references cited previously). In order to utilize current meter and sea temperature measurements taken at only two depths on a mooring line (sites NCORC and NCORK), near-bottom currents and vertical temperature deviation were extrapolated to occupy a water column 5 m in height. Heat transport resulting from measured current shear and near-bottom temperature deviation was then accumulated over all available months, and compared with coincident horizontal convection heat exchange rates from the heat budget at Molasses Reef (Eq. 3-3c, Eq. 3-4). The resulting monthly net heat exchanges show good agreement in months when cooling predominated (Fig 3-5b, 3-5c); during months when warming predominated, heat exchange was both weaker and more intermittent, as expected from previous studies, e.g., Lei and Patterson (2006). Near-bottom temperature

and currents in June-August also show variability related to brief upwelling events, as might be expected from internal wave breaking.

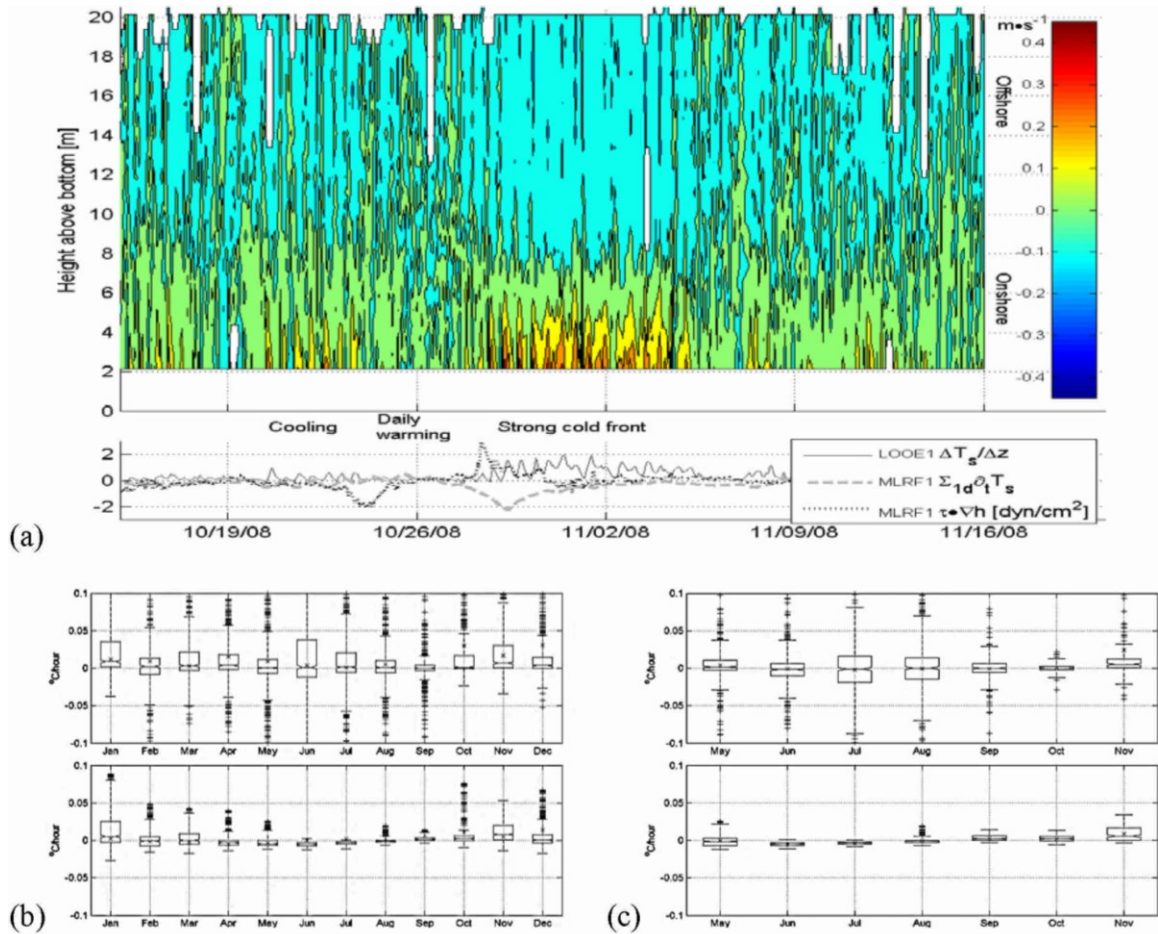
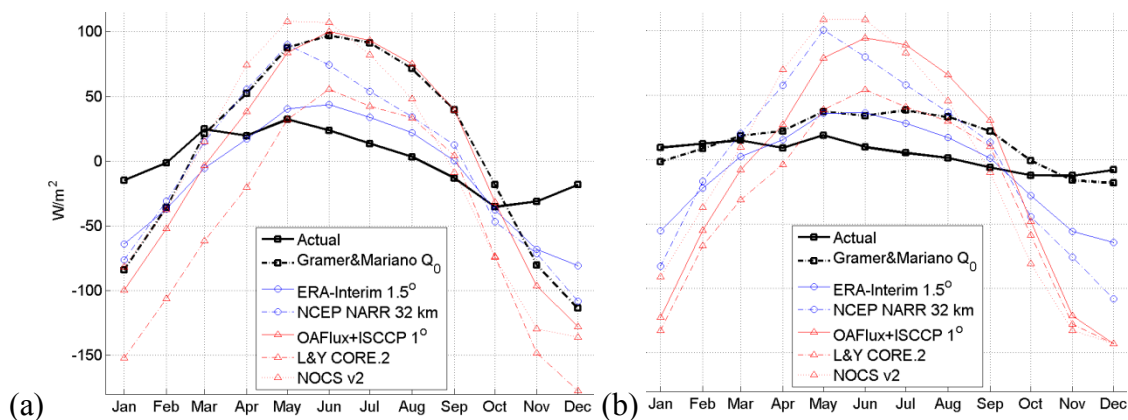


Figure 3-5: (a) Cross-shore baroclinic ocean currents (top panel Hovmöller,  $\text{ms}^{-1}$ ), cumulative daily net heat flux (middle panel dashed line,  $\text{K}\cdot\text{d}^{-1}$ ) and wind stress (dotted,  $\text{dyn}\cdot\text{cm}^{-2}$ ) at MLRF1, and vertical temperature differences (solid gray) at LOOE1, during a month with periods of both daily warming and persistent cooling (see labels, middle panel). Box-and-whisker plots at current-measurement sites (b) LOOE1 and (c) NCORK, comparing observed (upper) vs. modeled (lower boxes) heat exchange. Observed is from vertical current shear and vertical sea temperature difference, modeled is from horizontal convection parameterizations (see Eq. 3-3c, Eq. 3-4).

### *Climatological Comparisons*

Monthly (Fig. 3-6) and daily (Fig. 3-7) mean surface heat flux estimates from the present study were compared with flux estimates taken directly from the ERAI and NARR reanalyses, and with published global heat flux climatologies spatially

interpolated to each site: the National Oceanographic Centre at Southampton Version 2 (NOCS v2) monthly flux climatology of Berry and Kent (2009); the Common Ocean Reference Experiment Version 2 (CORE.2) monthly flux climatology of Large and Yeager (2009); the Objectively Analyzed Air-sea Fluxes Version 3 (OA Flux), a daily turbulent flux climatology of Yu and Weller (2007) at 1° resolution; and the International Satellite Cloud Climatology Project (ISCCP) three-hourly Global Surface and Atmospheric Radiative Fluxes of Zhang et al. (2004).



**Figure 3-6: Monthly climatology of net sea-surface heat flux estimates ( $Q_0$ ) from present study (dashed line with squares) for (a) Molasses Reef and (b) Long Key, compared with monthly mean ERAI and NARR reanalyses (circles), and several published climatologies (triangles). The heavy solid line with squares (“Actual”) is observed sea temperature variability, expressed in  $[W \cdot m^{-2}]$  using estimated density, heat capacity, and depth of seawater at each site. Means were limited to months with valid estimates for at least 75% of the hours in that month, and to data for years 1993-2006.**

Radiative and turbulent flux estimates from the present study agree well with published climatologies at all sites near the reef crest and the deeper ocean (Fig. 3-6a, 3-7a, 3-7b). At both the flat, shallow site on the Bay side of the Keys (LONF1; Fig. 3-6b, 3-7c, 3-7d) and the other flat, shallow site surrounded by deeper ocean (DRYF1), air-sea differences in temperature and specific humidity show seasonality markedly different from the reef-crest. This leads to a distinct annual cycle in sensible ( $Q_{SH}$ ) and latent ( $Q_{LH}$ ) heat fluxes, when compared with reef-crest sites and published climatologies.

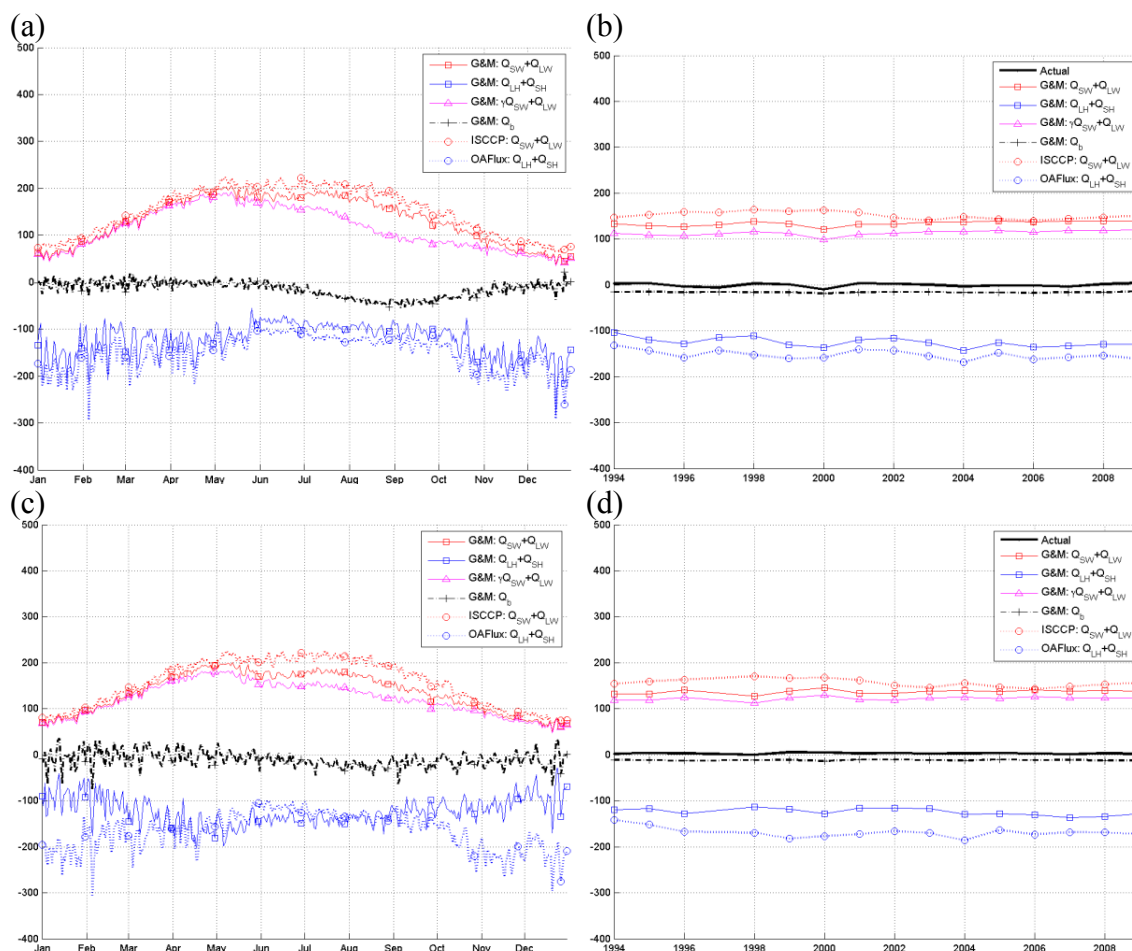


**Figure 3-7: Year-day (a,c) and yearly (b,d) climatologies of combined terms from the present heat budget (solid lines with squares,  $W \cdot m^{-2}$ ) for the years 1993-2009. The plots show the present heat budget total radiative ( $Q_{SW}+Q_{LW}$ ,  $>0$ ) and turbulent ( $Q_{LH}+Q_{SH}$ ,  $<0$ ) surface heat fluxes, at two sites: (a,b) FWYF1 and (c,d) LONF1. Also shown for comparison, ISCCP  $Q_{SW}+Q_{LW}$  and OAFflux  $1^\circ Q_{LH}+Q_{SH}$  published daily climatologies (dashed lines, circles), and estimates from the present study of absorbed radiative flux ( $\gamma Q_{SW}+Q_{LW}$ , triangle) and benthic heat flux into the ocean ( $Q_b$ , plus-sign).**

For all sites other than LONF1 and DRYF1, air-sea temperature difference is at a minimum in December and maximum in June. This seasonality matches that in OAFflux with 95% certainty from late April to early October, differing from OAFflux during October-April by only about  $-0.3$  K, with a peak difference of  $-2.5$  K in February. By contrast, weekly median air-sea temperature difference  $T_a-T_s$  at LONF1 reaches a minimum (most extreme difference) in June and a maximum in January. The resulting differences between daily mean  $Q_{SH}$  estimated by *in situ* data and those from OAFflux are

obvious in Fig. 3-7c, 3-7d, with similar differences for the monthly climatologies (Fig. 3-6b). DRYF1 shows a somewhat distinct pattern, with peak median  $T_a - T_s$  in March and April, but is otherwise similar to LONF1.

OAFflux displays a weak annual cycle in weekly median air-sea (saturated) specific humidity difference, matching with 95% confidence the pattern at the one reef-crest site with dew-point temperature data, SMKF1 – except in August-September, when *in situ* is greater than OAFflux by only  $\sim 0.001$  kg/kg. At LONF1 however, where dew point temperature was recorded from 2004 to 2010, phase in the annual cycle is similar but annual amplitude is stronger. This leads to markedly different estimates of  $Q_{LH}$  from *in situ* data at LONF1 (Fig. 3-6b, 3-7c, 3-7d), while  $Q_{LH}$  estimates at other sites match the published climatologies more closely (Fig. 3-6a, 3-7a, 3-7b).

#### *In situ Comparisons*

The ultimate test of the validity and usefulness of a reef heat budget is its ability to model the actual sea temperature experienced by organisms above and on the reef. A reliable integration requires reliable, accurate estimates with minimal bias. Eq. 3-1 provides an estimate of the rate of change in sea temperature in  $[K \cdot s^{-1}]$ , based on hourly mean data for forcing terms. Rates of change and error estimates were accumulated to units of  $[K \cdot d^{-1}]$ , and whole days with anomalous error estimates were removed (see Error Analysis and Source above). The resulting daily time series were used to build an annual climatology of temperature change, for direct comparison with the annual climatology of daily mean sea temperature at each site (Fig. 3-8).

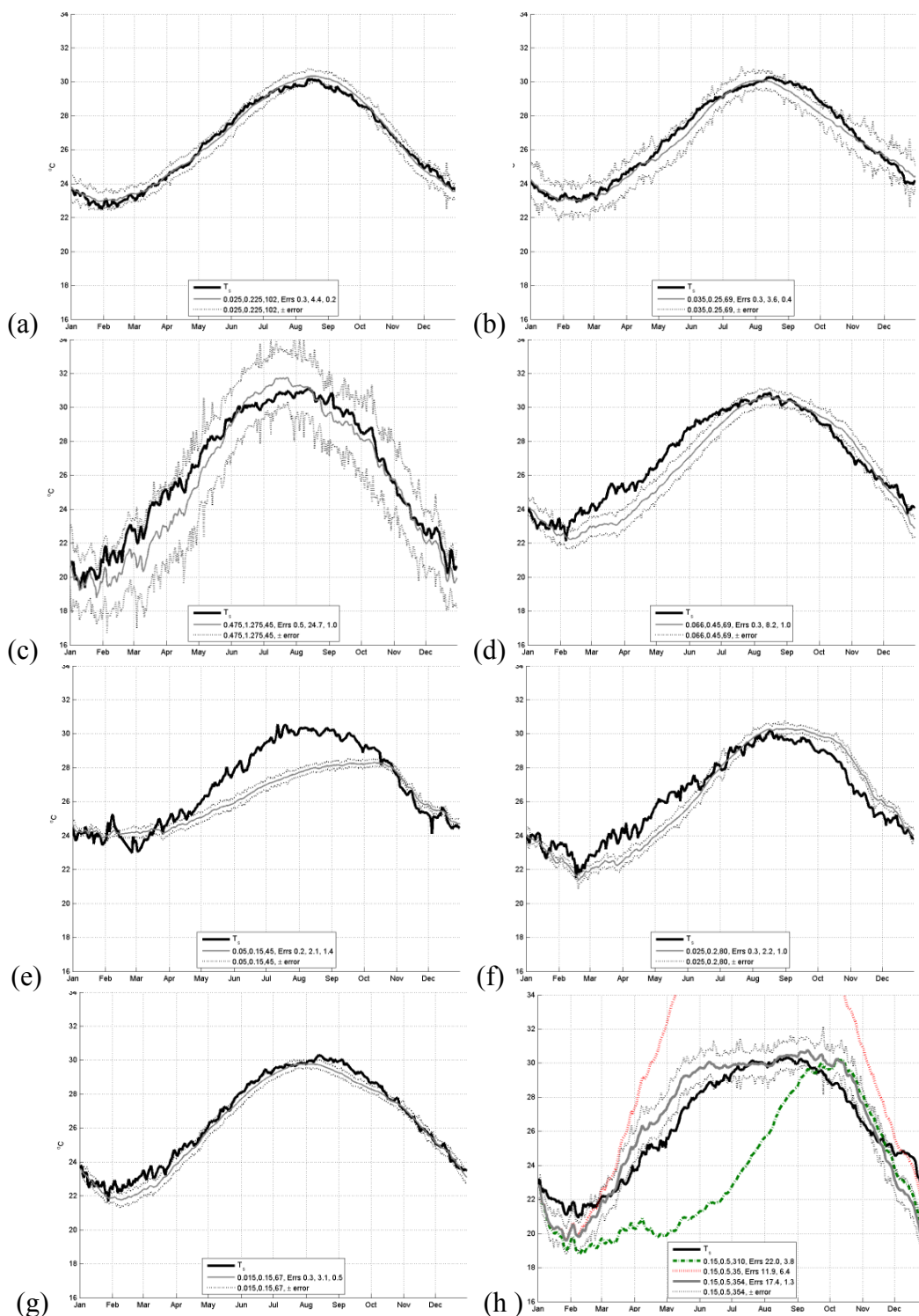


**Figure 3-8: Daily climatology of observed sea temperature (thick line, °C) and cumulative net heat fluxes predicted by the heat budget (lighter lines, °C) bracketed by  $\pm$  one standard error (dashed lines), for: (a) Fowey Rocks (1993-2011), (b) Molasses Reef (1993-2011), (c) Long Key (1993-2011), (d) Sombrero Key Reef (1993-2008), (e) Looe Key Reef 5 m sensor (2005-2010), (f) Looe Key 22 m sensor (2005-2010), (g) Sand Key Reef (1993-2005), and (h) Dry Tortugas (1993-2005), showing results for three distinct annual  $K_d$  climatologies (see text). Daily means were computed using bootstrap procedure, with  $N=300$  random resampling with replacement.**

Legends in Fig. 3-8 refer to the climatological absorption rate for penetrative insolation assumed at each site, attenuation coefficient  $K_d$ : FWYF1 – ranging from 0.025-0.225 peaking on year-day 102; MLRF1 – 0.035-0.250 day 69; LONF1 – 0.475-1.275 day 45; SMKF1 – 0.066-0.450 day 69; LOOE1 5 m – 0.050-0.150 day 45; LOOE1 22 m – 0.025-0.200 day 80; SANF1 – 0.015-0.150 day 67; DRYF1 – 0.15-0.500 day 310. Heat budget climatological means show agreement within the estimated representation error for much of the year, at all sites except the shallow LOOE1 sensor at 5 m (Fig. 3-8e), and DRYF1 in the far western FRT (Fig. 3-8h). It is likely that the shallow sensor at LOOE1 experienced significant larger-scale heat advection during warmer months, when this term was not well represented in the heat budget, and may also have experienced intermittent horizontal convective exchange during periods of rapid warming as well. DRYF1, on the other hand, lies 100 km from the nearest other site studied (SANF1), on a shallow flat (2-3 m depth); the global tide model (TPXO 7.2) chosen for tide heights and currents at all other sites predicted very low tidal currents at DRYF1: a higher-resolution tide model specific to the Gulf of Mexico produced currents and convective heat exchange rates with the seafloor associated with those currents, that significantly improved the overall balance. Finally, Fig. 3-8h shows the sensitivity of these results to  $K_d$ : differing results for small variations in the assumed annual cycle of  $K_d$  are shown – with peak year-days 310, 354, and 35, respectively.

#### *Dominant Thermal Forcing*

Relative contributions to sea-temperature variability from different forcing mechanisms in the heat budget were evaluated, by combining sub-collections of the terms in the overall budget (Eq. 3-1), including absorbed insolation  $\gamma Q_{SW}$ , latent surface heat

flux  $Q_{LH}$ , and advection and diffusion  $u \cdot \nabla T_s + K \nabla^2 T_s$ . The contribution of each set of terms was regressed against change in the daily mean sea temperature, using a robust algorithm with iteratively reweighted least squares. Scatter Index (RMSE expressed as a percentage of the long-term standard deviation of the daily mean sea-temperature change) and bias for those linear regressions are summarized in Table 3-4.

**Table 3-4: Results of robust regression between daily cumulative budget terms and change in daily mean sea temperature. Each field of the table gives a Scatter Index (SI%), the RMSE normalized by the standard deviation of  $\Delta_{1d}T_s$ , and a bias in  $K \cdot d^{-1}$ , for the linear regression. All daily regressions had p-statistic  $\ll 0.01$ ; however, regression results with  $R^2 < 0.20$  are shown in *gray italics*.**

Station, $T_s$ depth, sample N	2: $Q_{SW}$ (SI%, bias)	3: $\gamma Q_{SW}$	4: $Q_{LW}$	5: $Q_{LH}$	6: $Q_{SH}$	7: $Q_0$	8: $Q_0(\gamma) +$ $Q_b$	9: $Q +$ $u \cdot \nabla T_s +$ $K \nabla^2 T_s$	10: Total $\partial_t T_s$
FWYF1, 5312 d	<i>29%, +0.34</i>	<i>31%, +0.30</i>	<i>9%, -0.09</i>	<i>31%, -0.19</i>	<i>4%, -0.01</i>	<i>52%, +0.04</i>	<i>59%, -0.04</i>	<i>62%, -0.01</i>	<i>23%, 0.0</i>
MLRF1, 5480 d	<i>32%, +0.37</i>	<i>30%, +0.32</i>	<i>9%, -0.10</i>	<i>34%, -0.20</i>	<i>4%, -0.01</i>	<i>57%, +0.05</i>	<i>56%, -0.03</i>	<i>67%, -0.01</i>	<i>25%, +0.01</i>
LONF1, 5445 d	<i>73%, +2.05</i>	<i>63%, +1.89</i>	<i>21%, -0.58</i>	<i>63%, -1.21</i>	<i>12%, -0.08</i>	<i>58%, +0.17</i>	<i>80%, -0.11</i>	<i>82%, -0.11</i>	<i>32%, +0.04</i>
SMKF1, 3710 d	<i>31%, +0.45</i>	<i>29%, +0.41</i>	<i>9%, -0.12</i>	<i>33%, -0.25</i>	<i>5%, -0.02</i>	<i>55%, +0.05</i>	<i>55%, -0.01</i>	<i>60%, 0.00</i>	<i>25%, +0.01</i>
Looe 5 m, 1056d	<i>18%, +0.19</i>	<i>17%, +0.18</i>	<i>5%, -0.05</i>	<i>20%, -0.10</i>	<i>3%, -0.01</i>	<i>33%, +0.03</i>	<i>30%, +0.01</i>	<i>30%, +0.02</i>	<i>15%, +0.01</i>
Looe 22m, 1563 d	<i>15%, +0.18</i>	<i>14%, +0.17</i>	<i>5%, -0.05</i>	<i>19%, -0.09</i>	<i>3%, 0.00</i>	<i>33%, +0.03</i>	<i>33%, +0.01</i>	<i>36%, +0.02</i>	<i>25%, +0.01</i>
SANF1, 3551 d	<i>16%, +0.21</i>	<i>16%, +0.19</i>	<i>5%, -0.06</i>	<i>14%, -0.10</i>	<i>2%, -0.01</i>	<i>26%, +0.06</i>	<i>28%, 0.00</i>	<i>28%, 0.00</i>	<i>18%, +0.01</i>
DRYF1, 2196 d	<i>189%, +1.69</i>	<i>108%, +1.38</i>	<i>53%, -0.44</i>	<i>132%, -0.72</i>	<i>20%, -0.04</i>	<i>270%, +0.47</i>	<i>184%, -0.10</i>	<i>183%, -0.10</i>	<i>63%, 0.0</i>

The annual cycle of surface fluxes in this study agrees well with published climatologies, with the exception of latent heat flux estimates at the two flat, shallow sites noted above. However, the amplitude of annual temperature variability implied by the overall estimates (net flux/ $\rho C_p h$ ) is significantly greater than actually observed (Fig. 3-6; Table 3-4, column 7). At certain times and sites, even when terms for benthic flux and

“lost” insolation are considered, a simple one-dimensional “air-sea-seafloor” heat budget may overestimate variability by an order of magnitude (Fig. 3-6; Table 3-4, column 8, regression slopes as low as 0.19). And although they may improve the explanation of certain variability events, the addition of advection and diffusion terms does not improve statistical comparisons with daily variability at any site (Table 3-4, column 9, slopes as low as 0.18). Essentially, these terms are not closely correlated with air-sea fluxes, and including them in the budget still greatly overestimates the amplitude of diurnal, annual, and interannual variability. An additional heat-budget term anti-correlated with air-sea heat fluxes is needed to adequately explain the observed variability, particularly at sites near a sloping seafloor: horizontal convection (Table 3-4, column 10).

Based on the results summarized in Table 3-4, dominant forcing terms were identified at each site (Fig. 3-9). The monthly distributions of the cumulative heat budget without horizontal convection (Fig. 3-9c, 3-9i) share many of the features of the observed daily variability (Fig. 3-9a, 3-9g), while overestimating both the median, the interquartile range, and the range of extremes in variability for most months. The total heat budget (Fig. 3-9b, 3-9h) matches variability closely in the median at all sites, while particularly underestimating the range of daily variability at reef-crest sites.

The dominant heat balance therefore at reef-crest and fore-reef slope sites in the FRT during the warming months of February to August is between horizontal convection (Fig. 3-5b, Fig. 3-5c) and absorbed insolation. During reef-crest cooling months of September to February, the dominant term balancing horizontal convection shifts to latent surface heat flux. Over reef flats in the FRT, horizontal convection may still play a

smaller role, and benthic heat exchange is also important, although the dominant balance throughout the year here is between absorbed insolation and latent flux.

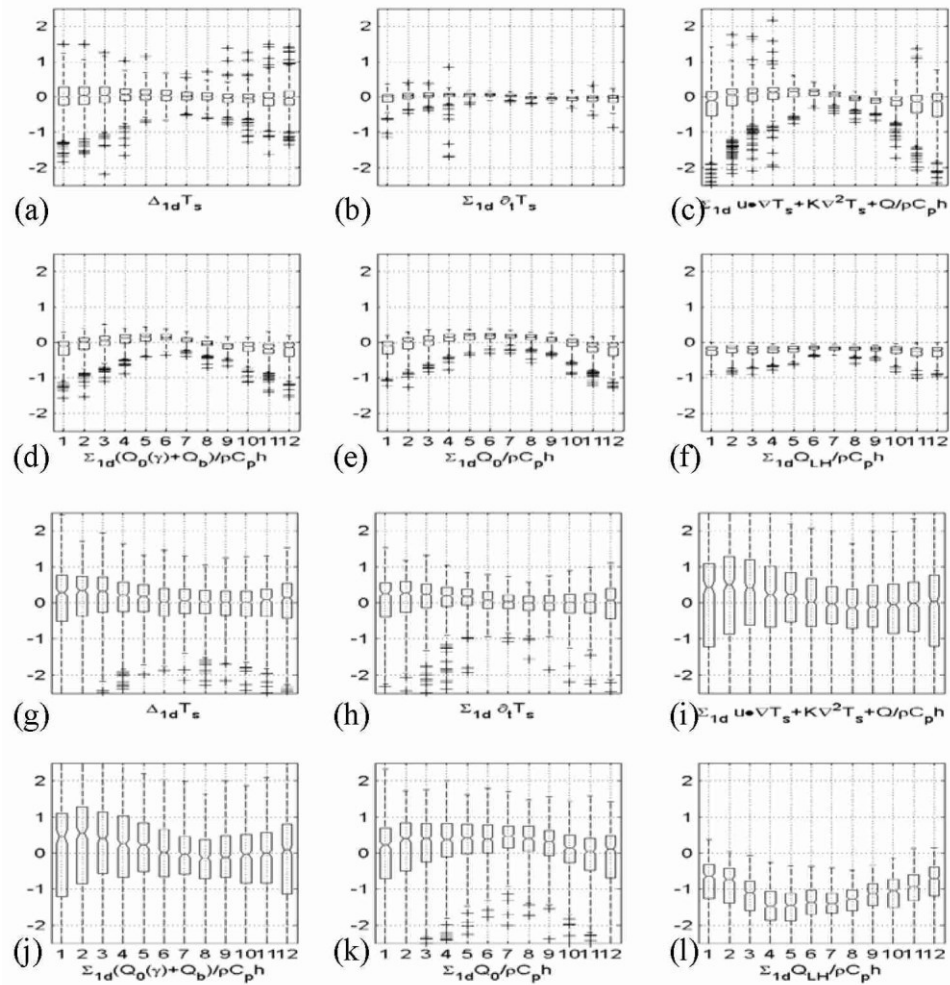


**Figure 3-9: Monthly box-and-whisker plots of daily net heat budget terms [ $\text{K}\cdot\text{d}^{-1}$ ] at distinct sites, for all complete days during the years 1993-2012, at (a-f) MLRF1, and (g-l) LONF1: (a,g) change in observed daily mean sea temperature,  $\Delta_{1d}T_s$ ; and estimated from (b,h) cumulative total heat budget,  $\Sigma_{1d}\partial_1T_s$ ; (c,i) total heat budget excluding horizontal convection,  $\Sigma_{1d}u\cdot\nabla T_s + Kv^2T_s + (Q_0(\gamma) + Q_b)/\rho C_p h$ ; (d,j) net vertical (surface and seafloor) heat flux,  $\Sigma_{1d}(Q_0(\gamma) + Q_b)/\rho C_p h$ ; (e,k) net heat flux into the sea-surface,  $\Sigma_{1d}Q_0/\rho C_p h$ ; (f,l) latent sea-surface heat flux,  $\Sigma_{1d}Q_{LH}/\rho C_p h$ .**

### *Sensitivity Analysis*

The preceding section quantified residuals between the overall heat budget and observed sea temperature variability. A number of parameters needed to be chosen in the construction of the heat budget. Here those parameters are briefly summarized, and the sensitivity of the budget residuals (RMSE) to them is analyzed. It should be noted that any biases are not averaged out and accumulate in the temporal integration, leading to large errors: Only parameters showing the greatest change in RMSE between daily mean variability and the cumulative heat budget are given in Tables 3-5 and 3-6.

Absorbed radiative fluxes were estimated based on shortwave ocean-surface albedo  $A$  (assumed value, reanalysis, or empirically estimated), broadband penetrative light attenuation coefficient  $K_d$  (peak day of the year, mean  $K_d$ , and annual range), seabed reflectivity  $A_b$ , and seawater longwave emissivity  $\epsilon_w$ . Turbulent fluxes were evaluated using the COARE 3.0a algorithms both with and without diurnal warm-layer adjustment, using either ERAI-only data or ERAI together with *in situ* meteorological data as inputs, or data from the NCEP NARR instead (see above), and finally based on differing choices of model for significant wave height  $w_h$  and peak wave period  $w_p$  inputs.

Larger scale advection and diffusion of heat were estimated based on those same wave models, combined with wind in an empirical relationship and coupled with fixed-resolution regional-scale weekly composite SST fields, and a range of choices for the multipliers  $F_q$  (for advection) and  $K_h$  (for diffusion). Horizontal convection depends on the choice of velocity scaling (combinations of both steady or unsteady thermal forcing, and one of steady, unsteady, or dissipative stress momentum balances), and upon mixing efficiency  $R$ . Finally, the conversion of heat fluxes into heat storage ( $\partial_t T$ ) depends on

water density  $\rho$  calculated based on a choice of constant salinity, and on a choice of estimates for the water depth experienced by a parcel of water during a daily tidal excursion  $h$ .

**Table 3-5: Sensitivity of the heat budget residual vs. observed daily variability at Molasses Reef, to changes in model parameters.**

<i>Parameter</i>	<i>Assumed Method</i>	<i>Variation #1</i>	<i>RMSE ↑ #1</i>	<i>Variation #2</i>	<i>RMSE ↑ #2</i>	<i>Variation #3</i>	<i>RMSE ↑ #3</i>
<i>Albedo</i>	Jin et al.	ERAI	600%	Const 4%	230%	Const 11%	260%
<i>K<sub>d</sub></i>	0.035-0.250 (yd 70)	0.035-0.250 (yd 115)	460%	0.035-0.200 (yd 70)	250%	Const 0.15	620%
<i>A<sub>b</sub></i>	24%	17%	150%	0%	360%	100%	980%
<i>Warm layer</i>	Yes	No	440%	--		--	--
<i>Meteorology</i>	<i>In situ</i> + ERAI	ERAI only	240%	<i>In situ</i> + NARR	730%	NARR only	730%
<i>F<sub>a</sub></i>	0-1 (yd 45)	Const 0	350%	Const 1	430%	0-1 (yd 91)	165%
<i>Advection + Diffusion data</i>	AVHRR, empirical wind+wave	GoM HYCOM	1000%	FKEYS HYCOM	2000%	Empirical + GoM	1000%
<i>HC momentum, thermal balance</i>	Steady, Unsteady	Steady, Steady	175%	Unsteady, Unsteady	860%	Unsteady, Steady	150%
<i>Water depth</i>	Tidally varying (TPXO)	Tidally varying (GoM)	4000%	Fixed depth of station (2.7 m)	15000%	Tidal = mean station depth (11 m)	105%

**Table 3-6: Sensitivity of the heat budget residual vs. observed daily variability at Long Key, to changes in model parameters.**

<i>Parameter</i>	<i>Assumed Method</i>	<i>Variation #1</i>	<i>RMSE ↑ #1</i>	<i>Variation #2</i>	<i>RMSE ↑ #2</i>	<i>Variation #3</i>	<i>RMSE ↑ #3</i>
<i>Albedo</i>	Jin et al.	ERAI	1430%	Const 4%	580%	Const 11%	540%
<i>K<sub>d</sub></i>	0.475-1.275 (yd 45)	0.475-1.275 (yd 91)	460%	0.475-1.375 (yd 45)	120%	Const 0.88	590%
<i>A<sub>b</sub></i>	17%	24%	156%	0%	400%	100%	1600%
<i>Warm layer</i>	No	Yes	1200%	--	--	--	--
<i>Meteorology</i>	<i>In situ</i> + ERAI	ERAI only	2300%	<i>In situ</i> + NARR	950%	NARR only	1400%
<i>Wave model</i>	ERAI	WW3	2000%	Bulk wind	210%	--	--
<i>Advection + Diffusion data</i>	Empirical wind+wave	GoM HYCOM	340%	FKEYS HYCOM	1000%	Empirical + GoM	340%
<i>Water depth</i>	Tidally varying (TPXO)	Tidally varying (GoM)	120%	Fixed depth of station (1.3 m)	1100%	Tidal mean = station depth (2.0 m)	140%

Comparing results at the reef-crest vs. the flats, the crest site (MLRF1, Table 3-5) shows a high sensitivity to parameters controlling advection, water depth, and horizontal convection, as well as moderate sensitivity to the assumed rate of light absorption in the water column, albedos, and use of reanalysis air temperature and winds. By contrast, the flats site (LONF1, Table 3-6) shows a high relative sensitivity to benthic heat exchange, meteorology, and sea-surface roughness, moderate sensitivity to light absorption parameters and adjustment for a diurnal warm-layer, and relatively low sensitivity to all other parameters. Thus, it is extremely important to ensure unbiased estimates for reliable estimation of the heat balance terms.

#### *Heat Budget from Foundation Sea Temperature and Reanalysis*

As a test of the broad regional applicability of the reef heat budget, periods of ecologically significant sea temperature variability on the FRT were modeled using remotely-sensed and reanalysis data as inputs. The 92 m horizontal-resolution NGDC CRM was used at each site to characterize bathymetry as above – i.e., cross-isobath orientation, seafloor depth, and maximum slope. ERAI was used for atmospheric and radiative forcing data as described above, but also for air temperature and winds (Dee et al. 2011). Sea temperature input to the heat budget was derived from a relatively low spatial-resolution (9 km), daily gridded global “foundation” sea temperature product, the Multi-sensor Improved Sea Surface Temperature (MISST; Gentemann et al. 2009). *In situ* sea temperatures were used solely for comparison with heat budget results. No corrections other than those described in the Methods above and Appendices below were applied to these reanalysis and remote-sensing data, to produce the results shown below.

A brief period of extreme cold weather, relative to historical Florida norms, occurred in January 2010. This event was observed by sea temperature recorders placed near the seafloor at sites of coral nurseries or naturally occurring live reefs throughout the Florida Keys, as part of the Florida Reef Resilience Program. This 2010 cold snap resulted in mass mortality of corals and other coastal ocean organisms in the FRT, and was only partially observable using available synoptic satellite SST and other remote sensing (Lirman et al. 2010); the severity of the cold snap was not reproduced in the MISST data itself. However, the heat budget proved able to reproduce the rapid cooling observed at each of these shallow-water sites, despite the use of relatively large-scale atmospheric and sea temperature products as inputs (Fig. 3-10a).

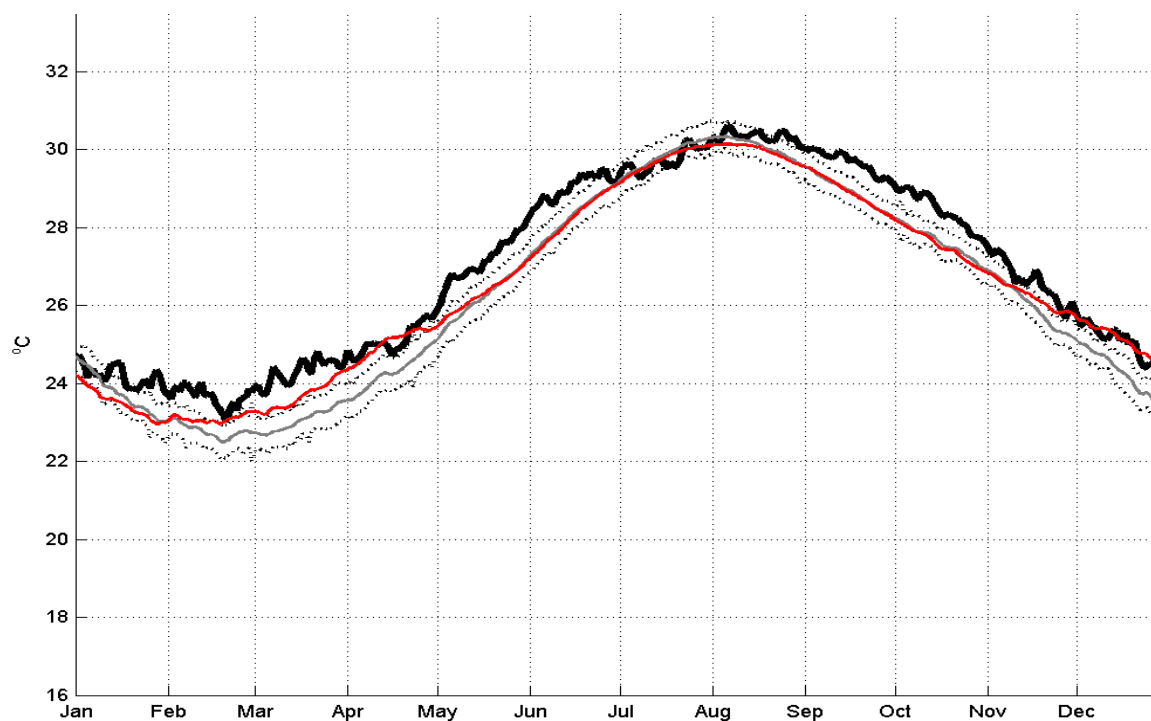
The relatively rapid warming which followed the cold snap was not reproduced well by the heat budget, likely due to the importance in that warming of horizontal mixing and advection that were not well represented from the weekly composite SST and empirical surface current estimates used in the heat budget. Corals are, however, also susceptible to reduced growth, bleaching, and mortality associated with extremes of warm sea temperature (e.g., Manzello et al. 2007a; Manzello et al. 2007b; Cantin et al. 2010) as well as cold temperatures. The heat budget was therefore applied to SEAKEYS sites across several years of gradual summer warming, based solely on MISST and ERAI. Results are plotted for one reef crest site, Molasses Reef, in Fig. 3-10b.



Figure 3-10: Results of applying the heat budget to a gridded 9 km-resolution “foundation” sea temperature product (MISST) and ERAI rather than *in situ* data. Plotted are observed *in situ* sea temperature (black), MISST daily sea temperature interpolated to each site (red), and heat budget model result (blue). (a) Florida Reef Resilience Partnership site in the Upper Florida Keys during 2010 winter cold snap (see Lirman et al. 2010); (b) Molasses Reef during several summers (June-August) between 2002-2009.

For the more gradual summer warming due to increasing insolation rates, especially during periods of low winds and minimal wind-driven reef circulation, the heat budget accounts well for both peaks and seasonal patterns of sea temperature variability

at these sites. This may be considered particularly significant for those summers when significant warm-water bleaching and mass mortality of corals were observed to occur, such as 2005 (Manzello et al. 2007a). The close match can also be seen in climatological annual results, shown for MLRF1 in Fig. 3-11. As this shows, a slight tendency for the MISST-based heat budget to overcool in January-March and November-December is offset by slight overwarming in May-June. However, this heat budget forced only by low-resolution global products (gray) shows remarkable agreement with observed *in situ* sea temperature variability (black) and with the heat budget result based on that (red). Planned future work will expand the reef heat budget using lower-resolution reanalysis and SST, to allow modeling of sea temperature variability in the wider Florida Keys National Marine Sanctuary and other, more remote coral reefs elsewhere (see Chapter 5).



**Figure 3-11: Climatological result for heat budget at MLRF1 (gray) based solely on MISST 9 km daily foundation sea temperature product and ERAI forcing, together with associated representation error bars (dotted lines), compared to observed sea temperature (black), and to the heat budget result produced with *in situ* data from Fig. 3-8 (red).**

### *Sub-Grid Scale Diffusion*

Heat diffusion was generally negligible in the heat budget at all sites, based on the weekly AVHRR SST and a seasonally varying diffusion coefficient. However, many of these are sites where tidal currents over the rough, rapidly sloping seafloor are likely to produce efficient mixing (Davis and Monismith 2011). The question thus arises as to the appropriateness of the heat diffusion model used in the present heat budget. Literature has suggested both condition-dependent diffusivity (Park and Chu 2008) and that a more direct approach to estimating horizontal turbulent fluxes may be useful (e.g., Jones et al. 2008, Monismith et al. 2009). Measurements, direct or indirect, of horizontal heat-dispersion were not available for the sites in this study, necessitating analysis via some other method to try to answer this question.

Assuming that pseudo-Fickian heat diffusion (see above) is an appropriate model for horizontal mixing over the FRT, both the time-varying rate of diffusion and the two-dimensional sea temperature fields used to calculate the Laplacian are parameters that may be examined. Limitations associated with the weekly composite AVHRR dataset used for the present heat budget are discussed elsewhere in this work (see above). However, the possibility must also be considered that a different seasonal pattern of time-varying heat diffusivity might improve the heat budget.

This possibility was evaluated by assuming that grid- and sub-grid-scale Fickian heat diffusion terms can be combined linearly. An additional "implied" sub-grid-scale thermal diffusivity was calculated. Implied diffusivity is the rate of diffusion of the weekly composite AVHRR SST which would be required to balance fully the heat budget relative to observed variability. To estimate this, budget-predicted hourly sea

temperature change was subtracted from observed change, and then divided by an hourly spline fit to the Laplacian of the AVHRR sea temperature field around each point.

The resulting “hourly sub-grid-scale diffusivity”,  $K_{h,SGS}$  is well modeled by a Weibull distribution with a broad peak at  $120 \text{ m}^2/\text{s}$ , but also another sharp anomalous peak at  $10 \text{ m}^2/\text{s}^{-1}$ . Fig. 3-12 shows a histogram of  $K_{h,SGS}$  at MLRF1 for the years 2004-2008. The eddy diffusion thus assumed to balance the heat budget has characteristic velocity  $u'$  between  $0.01$  and  $1.0 \text{ ms}^{-1}$ . These values are within previously published limits for time-varying diffusivity. However, multiply regressing these  $K_{h,SGS}$  values against wind speed, tidal currents, and their cross-shore components failed to show any statistically significant relationships (figures not shown).

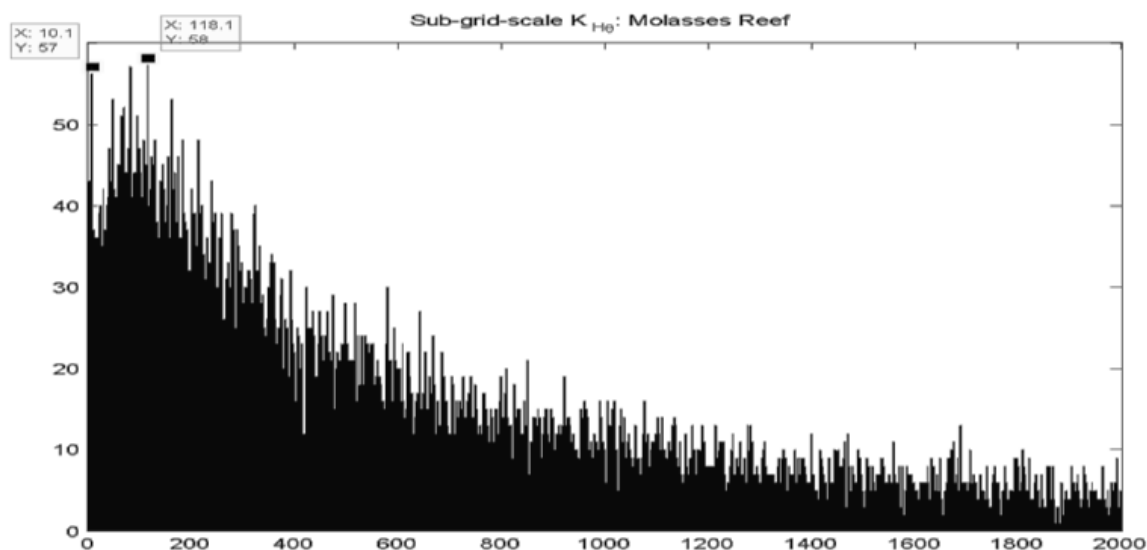


**Figure 3-12: Histogram of hourly, time-varying sub-grid scale heat diffusion rate,  $K_{h,SGS}$ , calculated based on the output of the total heat budget at MLRF1 vs. observed sea temperature variability, and using the  $T_s$  Laplacian calculated from weekly composite AVHRR SST.**

## 4. Summary

The Florida Reef Tract (FRT) is a coral reef ecosystem 3-8 km wide, fringing the south and east Florida Shelf. To manage this large, fragile ecosystem requires reliable information on thermal stress. To this end, *in situ* sea temperature and meteorological data have been gathered at reef sites in the FRT for over two decades, and a heat budget (e.g., Wilson-Diaz et al. 2009) has been developed to model near-bottom sea temperature using these data.

Downward short radiative fluxes for the heat budget were interpolated directly from reanalysis (Ch. 2). Upward radiative fluxes were estimated from *in situ* sea temperature and ERAI atmospheric and sea-state data, using published empirical relationships. ERAI data were used with empirical corrections applied as described above and in the Appendices below. Turbulent fluxes were estimated using the COARE 3.0a algorithms (Fairall et al. 2003), using *in situ* sea temperature and meteorological data from a combination of reanalysis and *in situ* measurements. In a prior publication (Gramer et al. 2012), a heat budget was presented using ERAI for all meteorological variables, including air temperature and wind speed. As described above, ERAI air temperature and wind speed show confounding seasonal biases relative to the *in situ* data in the FRT. The present study thus represents an important extension to the earlier result.

A simple ocean heat budget based on surface fluxes significantly overestimates sea temperature variability at reef sites. At many reef sites, the importance of diurnal warm layer evolution on lower-frequency sea temperature is seen (Table 3-5). Water over flat, shallow topography cannot absorb all the short-wave radiation entering the sea surface, and reflectivity and heat exchange at the seafloor at such sites is important for

sea temperature evolution there as well (Fig. 3-7, and Table 3-6). A sub-model of benthic heat exchange was needed to balance the heat budget (e.g., Evans et al. 1998; Nihei et al. 2002) at all sites, from shallowest (LONF1, DRYF1) to deepest (LOOE1).

The ultimate predictive success of the heat budget for all sites, and especially those with high topographic slope (rise/run  $\beta > 0.01$ ), depends largely on the sub-km scale process of the *thermal siphon* (Monismith et al. 2006), which exchanges heat between the reef and deeper water nearby, significantly moderating the response of the reef water to rapid surface warming or cooling. To the knowledge of the author, horizontal convection has not been previously reported in the coastal waters of the FRT. At higher relief sites, where topographic slopes exceed 0.5% for example, the sea temperature response to air-sea forcing is significantly moderated by horizontal convection, particularly during rapid air-sea cooling (Fig. 3-3, Fig. 3-5, Fig. 3-6, and Table 3-5).

Thus the heat balance at reef-crest and fore-reef slope sites is seen to be dominated by horizontal convection throughout the year, counter-balanced by absorbed insolation during warming months (MAMJA) and latent surface flux during cooling months (SONJF). Over reef flats in the FRT, horizontal convection plays a smaller role, with benthic heat exchange somewhat more significant. Here, however, the dominant balance throughout the year is between absorbed insolation and latent flux.

When high-resolution seafloor topography and bottom type are accounted for adequately, the reef heat budget accurately reproduces annual- and shorter-period sea-temperature variability on individual coral reefs. An important next step in this research is the application of the heat budget model, now optimized for a variety of sites where *in situ* data have been gathered, to the many sites where such data are not available. One

approach for this is to use remote sensing and reanalysis to estimate atmospheric forcing (e.g., Aquarius, ASCAT, or reanalyses that assimilate these sources), and daily-gridded “foundation” sea temperature (e.g., the 9 km-resolution MISST dataset; Gentemann et al. 2009). This provides researchers and resource managers with “now-casts” of sea-temperature variability at remote reef sites where seafloor characteristics and regional oceanography are known, but *in situ* data are lacking. That work is now underway, and some of the results are described above.

Finally, after all terms in the present heat budget have been accounted for, there are short periods of unusual sea-temperature variability in these records that are not adequately explained by the heat budget. A few of these events may be attributable to extreme atmospheric forcing that is not well modeled by existing methods for estimating air-sea flux, e.g., tropical weather events like those in 2005, or extreme cold weather like that in early 2010 (Fig. 3-7, Fig. 3-10). Some of these anomalous short-duration events may also be due to small-scale convective weather during the Florida rainy season, or to small-scale ocean heat advection and mixing, not adequately represented in the data and models available for this study. Future improvements in both atmospheric reanalysis and in the high-resolution ocean modeling of this region would clearly be of benefit in examining this possibility.

Other events of anomalous variability however are not coincident with any observed atmospheric extremes, and yet are more persistent than small-scale processes would suggest. These events are likely to be related to mesoscale and sub-mesoscale oceanic variability – internal waves, strong frontal gradients, eddies, and other instabilities in the Florida Current. Such processes may be related to both upwelling, and

to cross-shore flows over the fore-reef slope (e.g., Lee et al. 1992; Leichter et al. 2006; Davis et al. 2008; Davis and Monismith 2011), and have been shown to affect sea temperature at the reef crest (Gramer et al. 2009).

It should be noted that water advection and mixing at all scales, horizontal convection, and upwelling all may do more than merely condition the thermal environment of coral reefs. They can also change the availability of reproductive materials during spawning and settlement (e.g., Sponaugle et al. 2005; Criales et al. 2007), of nutrients for photosynthesis and respiration (James and Barko 1991; Hitchcock et al. 2005), and of prey for filter feeding by corals and other reef organisms (Monismith et al. 2010). Just as the overall heat budget provides a better understanding of the reef thermal environment, quantifying these smaller-scale dynamic processes can also improve estimates of loading by nutrients and organic or inorganic particulates (e.g., Leichter et al. 2003).

The results described in this Chapter will contribute to the more effective management of these fragile resources in the context of anthropogenic and other near- and far-field influences. However, the occasional events not well explained by this heat budget also show that further study is warranted, to characterize the incidence and influence of higher-frequency variability and “extreme processes” on the reef. The following Chapter of this work analyzes higher-frequency sea temperature variability on the Florida reef tract that is not well described by the current heat budget, and attempts to characterize the likely forcing mechanisms associated with that variability.

## Chapter 4. Analyses of Anomalous Variability

The heat budget of Chapter 3 explains many of the features of observed sea temperature variability on the FRT, at periods ranging from diurnal to interannual. Isolated events of anomalous variability are also observed in the *in situ* record, however, which are not well explained by the heat budget, nor do they appear to coincide with corresponding atmospheric variability. Furthermore, while generally isolated in time and space, certain of these events are either more persistent or more wide-spread than can be explained by small-scale oceanographic processes.

It is hypothesized that some of these events are related to mesoscale and sub-mesoscale oceanic variability, e.g., the breaking of internal waves, or the movement of strong frontal gradients, eddies, and other instabilities associated with the Florida Current. Such processes produce both upwelling (vertical motion of isopycnals), and cross-shore flows across the fore-reef slope and the reef crest (e.g., Lee et al. 1992; Leichter et al. 2006; Davis et al. 2008; Davis and Monismith 2011). Such events have been shown to coincide frequently with anomalous sea temperature variability at the reef crest in the FRT (Gramer et al. 2009).

### 1. Additional Data

Since August 1993, the University of South Florida's (USF) Institute for Marine Remote Sensing (IMaRS) has collected multi-band infrared irradiances for the waters of Florida and the eastern Gulf of Mexico, from AVHRR sensors aboard the fleet of NOAA polar-orbiting environmental satellites. These data are archived as geo-referenced, 1 km-resolution SST maps (Hu et al. 2009), accessible via the Web in near real-time, that is,

normally within 12 h of each satellite pass. Weekly and monthly composite and composite-anomaly SST fields summarizing these synoptic images are also available, as described in Chapters 2 and 3 above. Similarly, 1 km-resolution synoptic SST maps derived from the Aqua and Terra MODIS instrument are produced by USF in near real-time, from 2003 to the present. Finally, USF provides MODIS geo-referenced fields of two- and three-band ocean color data (true color, chlorophyll *a*, and other products; e.g., Hu et al. 2005b; Cannizzaro and Carder 2006) for 2003-2012 via the Web, across several regions of the world and at spatial resolutions ranging from 1 to 4 km square.

High-resolution satellite data for both SST and ocean color have been archived by USF for the SF, Florida Bay, and the shallow coastal waters of the Florida Shelf at 1 km resolution. See for example, Fig. 4-1 below. A bulge of cool water can be seen occupying the Pourtales Terrace offshore of the FKNMS. Also of note in the image is a coast-hugging ribbon of cooler water, stretching from the Upper Keys all the way up to the northern FRT (Broward County). Such “cool-water bands” are in fact frequently observed in high-resolution satellite SST and ocean color images of the FRT, when a mesoscale eddy or recirculation associated with an FC meander is present offshore of the Florida Keys.

It is hypothesized that these bands may be the result of interaction between cyclonic vortices and the “wall” of the FRT reef slope. Similar features have been predicted by Nof (1988; 1999) based on conservation of potential vorticity, and can be seen frequently when mesoscale vortices interact directly with zones (iii) and (iv) of the FRT (see, Fig. 1-3, Fig. 4-1, Fig. 4-7). Spatial subsets of the USF data are analyzed below, in order to characterize regimes and time and space scales of variability in the

waters surrounding the study sites, with particular emphasis on periods of anomalous *in situ* sea-temperature variability that are not well explained by the heat budget of Ch. 3.

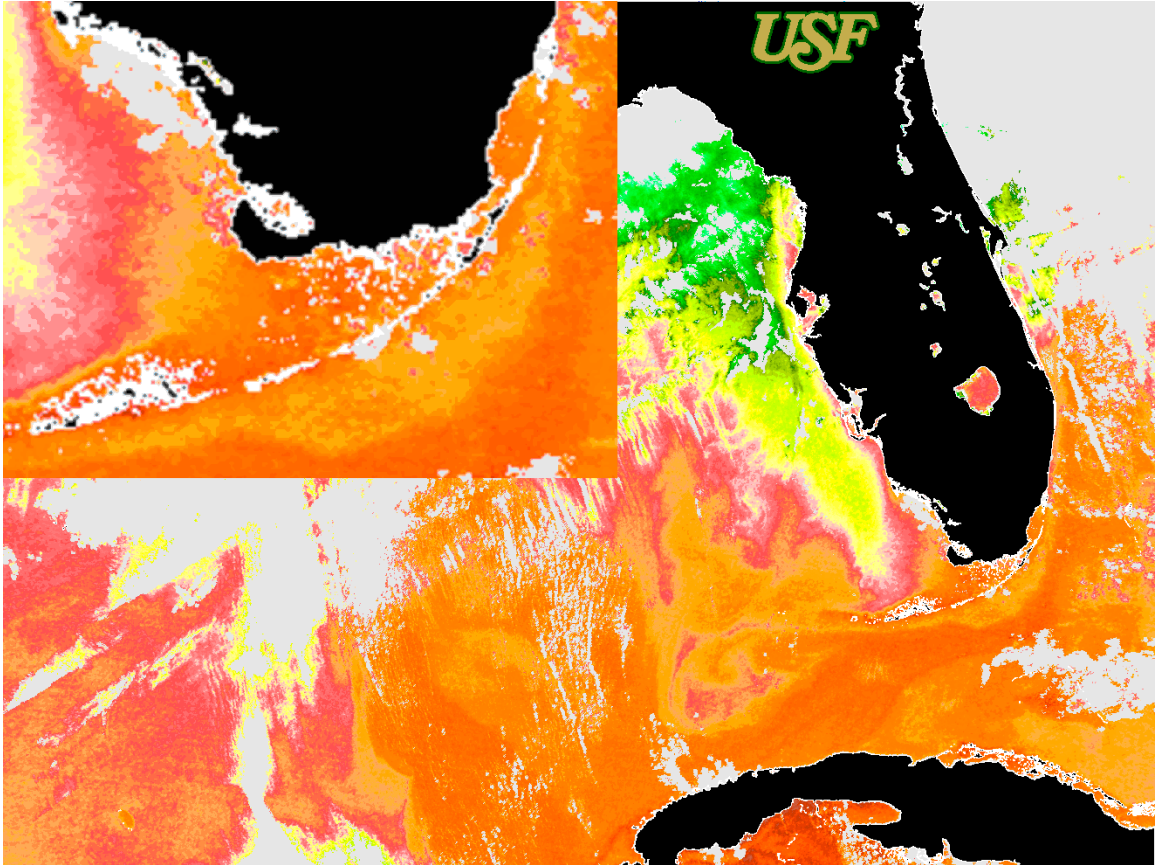


**Figure 4-1: Synoptic 1 km AVHRR SST for Florida and Eastern Gulf of Mexico from USF IMaRS, 2009-April-02 10:39 UT. Gray pixels are clouds. Inset is a blow-up of this image, showing smaller-scale internal structure of an apparent cyclonic vortex (probable mesoscale eddy) offshore of the Middle Keys. Plumes of warmer water appear to have originated at the 7-Mile and Long Key Bridge Channels inshore and been entrained by the vortex. There is a ribbon of cool water stretching along the coast to Broward County – possibly a result of the vortex interacting with the “wall” of the FRT.**

Some of the difficulties associated with using synoptic AVHRR-derived SST products for these sub-tropical sites are highlighted however by another image taken during daytime (Fig. 4-2), approximately 12 h prior to the one shown in Fig. 4-1. As discussed below and in Ch. 5, inevitable differences in cloud cover between images will

present problems for pattern analysis based on these images. More significantly for their use in understanding reef sea temperature variability, however, these two images taken close to one another in time show markedly different ocean surface thermal features. The apparent extent of the prominent feature known as the west Florida Shelf “cold tongue” (Liu et al. 2006b) varies between the two images by more than 50 km, while details in both the vortical structure over the Pourtalès Terrace and frontal eddies in the Loop Current upstream of the FRT show inconsistencies at similar and smaller spatial scales. The dynamics of the ocean within the bounds of the FRT are energetic at both high frequencies and large wavenumbers.

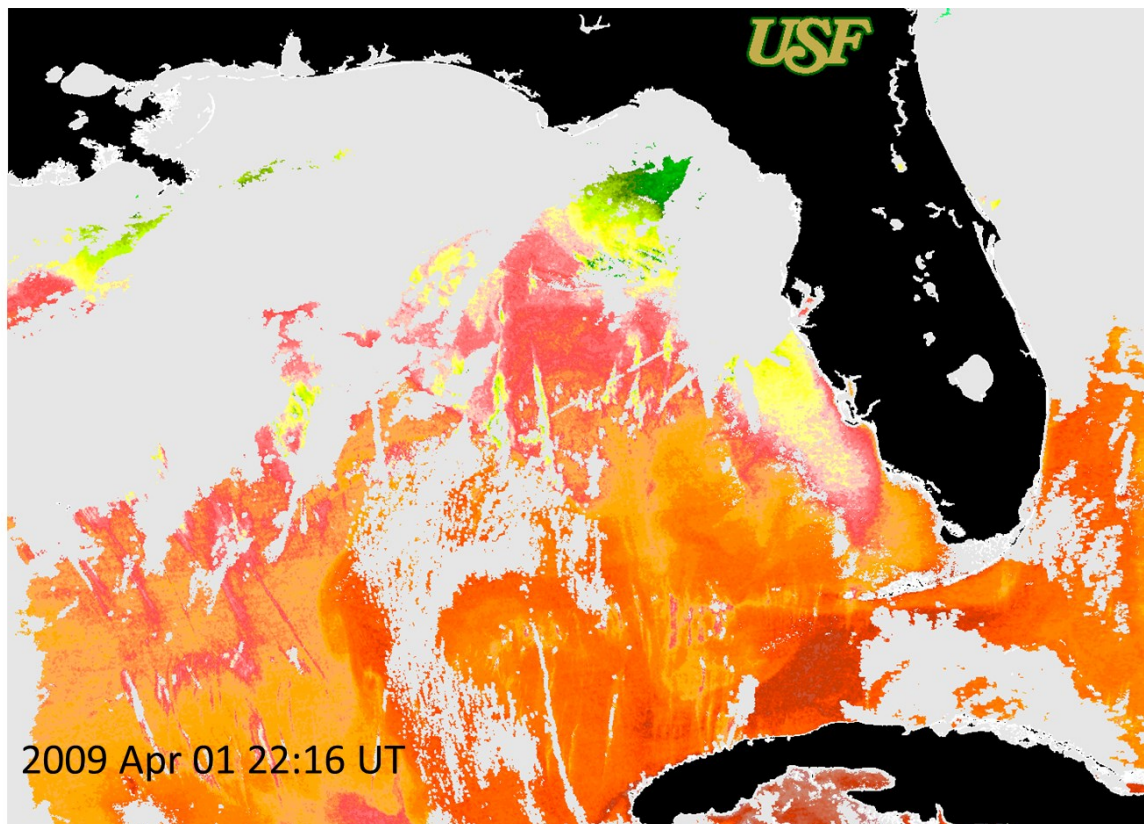


**Figure 4-2: Synoptic 1 km AVHRR SST product from a daytime overpass 12 h prior to Fig. 4-1. Note marked differences in apparent extent of the WFS "cold tongue" as well as in structure of both the eddy feature over Pourtalès Terrace, and the cyclonic front of the Loop Current (lower center).**

## 2. Methods

A number of methods are described here to summarize variability and co-variability, and to detect anomalous events in the data. These are variability metrics, heuristic ecological forecasts, principal component analysis, and self-organizing maps.

### *Variability Metrics and Events*

One approach to characterizing anomalous sea temperature variability in terms of other time series is the calculation of simple variability metrics. In addition to measured data (Ch. 2), and calculated heat fluxes (Ch. 3), time series metrics for higher-frequency *variability* of sea temperature and its forcing variables have also been derived. In the analysis for a previous study (Gramer et al. 2009, see also below), a useful tool for tracking time-dependent changes in hourly temperature variability was found in the sample standard deviation of a moving subsample window. These subsample standard deviations (Eq. 4-1) are calculated as of each hour of a record, using a “top-hat” (square wave) sliding time window of, for example, 24 h. The same analysis found that smoothing aided interpretation of these temperature variability metrics, and of the forcing time series. Smoothing was done either by a simple moving average (SMA; Eq. 4-1), the sample mean of a moving top-hat window, or by low-pass filters (LP) based on Fourier analysis (see below).

Smoothed time series and variability metrics calculated for the present study were: sea temperature and air temperature standard deviation over a 24 h window,  $\sigma_{1d}(T_s)$  and  $\sigma_{1d}(T_a)$ ; 3 d SMA smoothing of the 1 d standard deviation time series,

$$\Theta \equiv \mu_{3d}\sigma_{1d}T_s,$$

and  $\mu_{3d}\sigma_{1d}T_a$ ; 3 d mean wind speed,  $\mu_{3d}(W)$ ; and metrics for 3- and 7-day subsampled variability in wind speed and direction, using a sum of subsample standard deviations of  $W_U$  (eastward) and  $W_V$  (northward) wind velocity components for 3 or 7 d,  $\sigma_{3d}W_U + \sigma_{3d}W_V$  or  $\sigma_{7d}W_U + \sigma_{7d}W_V$ , respectively. Forcing variability metrics were also calculated based on components of the heat budget (Ch. 3):  $\mu_{3d}(Q_{LH}/\rho C_p h)$ ,  $\mu_{3d}(Q_0/\rho C_p h)$ ,  $\mu_{3d}([Q_0 + Q_b]/\rho C_p h)$ ,  $\mu_{3d}(F_q u \cdot \nabla_h T + K_h \nabla_h^2 T + [Q_0 + Q_b]/\rho C_p h)$ , and  $\mu_{3d}(\partial_t T_s)$ . Fig. 4-3 below shows whole records of quality-controlled sea and air temperature and winds at selected SEAKEYS sites, as well as some representative variability metrics there.

For all analyses referred to in this Chapter, smoothed data are exclusively the result of SMA. The rationale for this is first that SMA preserves within-day periodicities (higher frequencies) in the original data, and second that SMA is well implemented by expert systems platforms and real-time data feeds available to the ICON project – which Fourier analysis and LP filtering are not. A further advantage of SMA over LP in “now-cast” or forecast applications (see below) is that SMA is *realizable* – i.e., relying only on past data; for shorter-period means, that is a less significant concern. Note that many of these same analyses were also performed using both 40- and 72-hour LP filters; although some important details differed between the results, most of the features referred to in the figure captions, both above and below, were also present when LP-filtered time series were used in place of SMAs for similar cutoff periods.

The following equations (Eq. 4-1, Eq. 4-2) are used in the results which follow:

$$\begin{aligned}\mu_{N-days}(q)(hour_i) &= \frac{1}{24 \cdot N} \sum_{j=i-24 \cdot N}^i q(hour_{i-j}) \\ \sigma_{N-days}(q)(hour_i) &= \sqrt{\frac{1}{24 \cdot N - 1} \sum_{j=i-24 \cdot N}^i [q(hour_{i-j}) - \mu_{N-days}(q)(hour_i)]^2} \\ \mu_{N-days} \sigma_{M-days}(q)(hour_i) &= \frac{1}{24 \cdot N} \sum_{j=i-24 \cdot N}^i \sigma_{M-days}(q)(hour_{i-j})\end{aligned}\tag{4-1}$$

$$\begin{aligned}\min_{N-days}(q)(hour_i) &= \min_{j=i-24 \cdot N}^i (q(hour_{i-j})) \\ \max_{N-days}(q)(hour_i) &= \max_{j=i-24 \cdot N}^i (q(hour_{i-j})) \\ anom_{N-days}^{\max}(q)(hour_i) &= (\max_{1d} - \mu_{N-days})(q)(hour_i) \\ anom_{N-days}^{\min}(q)(hour_i) &= (\mu_{N-days} - \min_{1d})(q)(hour_i)\end{aligned}\tag{4-2}$$

Wind vector components were also smoothed with a 3 d SMA, and smoothed wind direction derived from them: a 3 d SMA wind direction that was predominantly on- or offshore was considered to be unfavorable to wind-driven upwelling. Periods of anomalously high sea temperature variability in the FRT were identified and classified as follows (Gramer et al. 2009):

*Recognition* of anomalous sea temperature variability was based on the metric for short-term variance in sea temperature,  $\Theta$ . Reef-crest *in situ* sea temperature variability exhibits tidal frequencies at ~12 and 24 h, as well as inertial variability at ~25 h (SMKF1). So standard deviation of  $T_s$  was estimated over a 1 d moving window.

However, the goal is to find *persistent* events, consistent with passage times for eddies or internal wave trains, for example; this suggested use of a 3 d SMA to smooth the metric.

*Classification* of individual events was based on their likely forcing. Is wind-driven circulation likely to be the primary forcing for this anomalous variability? If wind is persistently weak (low SMA) and/or wind direction is unfavorable for *upwelling* (see Ch. 1 and above), then upwelling driven by FC meanders, eddies, or internal waves becomes a more likely explanation for high sea-temperature variance.

*Validation* of recognized events and of their classifications was done by visual examination of coincident satellite imagery. Persistent nutrient pulses, for example, are likely to coincide with a signal for high chlorophyll *a* derived from the USF MODIS ocean color. Also, in particular, does visual examination of the satellite SST or ocean color (chlorophyll *a*) data show apparent cyclonic circulation near the site?

Instances when sea temperature exhibited anomalous variability but winds were light and/or not variable were labeled as “non-wind events”. One such event is shown in both Fig. 1-3 and Fig. 4-5. See the Results below for further details.

#### *Heuristic Ecological Forecasts*

On the basis of the variability metrics and event classifications described above, ecological forecast models (Murawski and Matlock 2006) also known as *ecoforecasts* were constructed. An ecoforecasts is a set of heuristic, “if-then” pattern-matching rules applied to a collection of environmental time series (Hendee et al. 2001; Hendee et al. 2009), in order to assess possible ecological impacts relating to those environmental stressors. Ecoforecasts may be used for both historical and near real-time *assessment* of (automated assignment of semantic *meaning* to) data. SMA of each time series are

assigned “fuzzy logic” semantic values, usually based on seasonal or situation-based numeric ranges. For example, in a cold-water mortality ecoforecasts for corals, a 3 h mean sea temperature of 16 °C during November-April could be assigned the semantic value of “conducive”, while a value of 14 °C was considered “severely conducive”, and 12 °C “drastically conducive” to coral mortality; during warmer months, such low sea temperatures might be assigned a value of “unbelievably low” and automatically ignored. A numeric score is assigned to the daily output of each ecoforecasts, known as a Stimulus/Response Index (S/RI), based on the count of matching rules, the set of fuzzy-logic semantic values that matched each rule, and their persistence (count of successive 3 h windows with the same fuzzy value).

#### *Principal Component Analysis*

Principal component analysis (PCA), also known as Empirical Orthogonal Function (EOF) analysis, is a statistical method for calculating the dominant statistical modes of variability in data (Mariano in prep.). The set of these “data vectors” defines a locus of points in a parameter space. PCA defines an orthogonal basis or coordinate system for this space, such that the center of the coordinate system is at the centroid mean of the locus of data points, and the first coordinate axis is in the direction of maximum variability of the data. The second coordinate axis is set orthogonal to the first axis and is maximized for explaining the remaining data variability, etc. The set of all orthonormal basis vectors of this coordinate system are the EOFs (e.g., Wilson-Diaz 2001), while the coefficients to express each data vector in the coordinate system defined by the EOFs are referred to as the principal components (PCs).

The choice of data vectors used in PCA varies depending on the aim of analysis. To characterize diurnal variability in sea temperature, for example, the 24 hourly values of each day may form the components of a single data vector: the first few EOFs (axes) of the PCA then represent dominant modes of diurnal variability. To construct the PCA results shown in the sections below, the following procedures were followed:

A complete set of data vectors was constructed using fixed-length time “frames” within time series. For discrete two-dimensional fields, e.g., satellite SST imagery, the field was ‘unraveled’ by index  $x_i$ ,  $y_i$ , into a one-dimensional vector.

The mean value was first removed. For time series, the choice of which mean to remove varied from a whole-record mean, daily mean, linear trend, or even a least-squares best fit (e.g., to a diurnal pattern of sea temperature). For spatial data, either a time-mean (for each pixel over time), a spatial mean (for each image as a whole), or a difference relative to one site within each image (e.g., to analyze gradients) is removed. The choice of mean to remove depended on the goals of the analysis (see below).

The covariance matrix between data vectors was calculated. For “extended” or “extended spatial” PCA (see below), coincident data vectors for disparate time series and/or images were concatenated into a single  $1 \times N$  vector. For variables having scales that were not easily compared with one another, e.g., because they are in different physical units or because their natural ranges of variability are very different, the correlation matrix was calculated instead. Extended PCA on correlation matrices is similar to the technique of canonical-correlation analysis (Knapp 1978).

From the covariance matrix (used in the present work for individual time series), or correlation matrix (used for multiple time series and spatial data), PCA determines

eigenvectors (Mariano in prep.; see Eq. 4-3 below). Care is taken in choosing the pivot axis for computability reasons. For example, in spatial PCA of a data set consisting of only 900 or so satellite images per year, each image was  $81 \times 81 = 6561$  pixels or more; in this case, time is a more convenient pivot axis than spatial coordinate(s), for computing eigenvectors. “Scores” (PCs) are then calculated for each data vector for each EOF.

The equations below (Eq. 4-3) summarize the construction of data vectors and analysis of principal components for variability in a time series of the sea temperature variability metric,  $\Theta$ , over successive 14 d (336 h) “frames”. The individual components of each data vector in this example are not hourly values for sea temperature itself,  $T_s$ , but rather hourly values of a 3 d SMA of 1 d standard deviation. In effect, this example finds the principle modes of variability of the variability itself (see Fig. 4-3, Fig. 4-11, Fig. 4-12). Similar formulae apply for the 24 h and 91 d analyses shown in succeeding sections.

$$\text{Observation data vectors : } A_{raw} = \begin{bmatrix} \Theta(h_1) & \dots & \Theta(h_{336}) \\ \Theta(h_{336+1}) & \dots & \Theta(h_{2 \times 336}) \\ \vdots & \vdots & \vdots \\ \vdots & \vdots & \vdots \end{bmatrix}$$

Remove linear trend (Least Squares fit) :

$$A_{raw}^{h_{(j/336)+1}, \dots, h_{(j/336)+336}} = B_j X_j + C_j + \varepsilon_j$$

$$A^{ij} = A_{raw}^{ij} - (B_j X_j + C_j) = \varepsilon_j$$

$$\text{Calculate covariance } C^{ij} = A^T A, \text{ where } i = 1 \dots 336, j = 1 \dots 336 \quad (4-3)$$

$$\text{Solve for eigenvectors } \forall \vec{E}_i \ni: (C - \lambda_i I) \vec{E}_i = 0 \quad \exists \lambda_i, i = 1 \dots 336$$

$$\text{Principal components } P = A[E_{1..336}]$$

$$P = \begin{bmatrix} eig_1[\Theta(h_1)] & \dots & eig_1[\Theta(h_{336})] \\ eig_2[\Theta(h_1)] & \dots & eig_2[\Theta(h_{336})] \\ \vdots & \vdots & \vdots \\ \vdots & \vdots & \vdots \\ eig_{336}[\Theta(h_1)] & \dots & eig_{336}[\Theta(h_{336})] \end{bmatrix}$$

Prior to PCA, time series were normalized by removal of a mean or trend. For diurnal analysis, a daily mean was subtracted; for variability analysis of 14 and 91 d frames, a simple parametric model based on mean annual climatology was removed. To characterize higher-frequency anomalous variability, linear trends for 14 and 91 d frames were removed. For co-variability analysis with other variables (i.e., “extended PCA”) a seasonal climatology was removed from both 14 and 91 d frames. Time series of images for spatial PCA were normalized by removing a mean. For extended and spatial PCA, correlation coefficients were used in place of covariance matrices, in order to avoid normalization of dispersions when cross-analyzing disparate types of data. Choice of dimension used to calculate the image mean varied: for co-variability analysis, the time-mean of each pixel across all years was the best choice; to characterize circulation patterns, the per-image spatial mean was selected. Mean or trend was added back to each EOF after analysis, to aid in the interpretation of the results.

### *Self-Organizing Maps*

A self-organizing map (SOM; Kohonen 1990; Kohonen 1998) is a type of artificial neural network, which is in effect a non-parametric algorithm for performing cluster analysis. A SOM is an array of potential patterns in data, called “units”: initially, each unit may be thought of as a null vector, having the same dimensions as the data to be analyzed. The units are arranged in a (usually) two-dimensional array or map: once “trained” (see below), units that adjoin one another in the topology of the array are similar to one another.

At the start of training, all units are initialized using, e.g., vectors of random numbers. The map is then presented with each data vector in random sequence. A best

matching unit (BMU) to most closely “match” each vector is selected by minimizing a similarity metric, e.g., simple Euclidean distance. Matching units are slightly “nudged” or trained so as to match that data vector more closely. Units surrounding the BMU in the map are also trained; training of neighbors depends on a neighborhood function, e.g., Gaussian distance-weighting, whose extent is reduced (i.e., the weighting function is narrowed) as training progresses.

Once training is complete: the result is a two-dimensional array, each unit of which is a non-linear statistical representation of one of the observed “patterns” of variability in the original data. The dominant (most frequently matched) patterns in a SOM may be assigned physical interpretations by the researcher. The distance metric also serves as one estimate of the “error” in the analysis. The map can then be used to pattern-match new data – the BMU for each new data vector describes what physical “pattern” that particular data best matches.

SOMs for this work were trained using the SOM Toolbox 2.0 (Alhoniemi, Himberg, Parviainen, and Vesanto; see Appendices) for MATLAB<sup>®</sup>. For all analyses in the present work, rectangular, “flat” maps (i.e., without wrap-around edge connections) were used, and units were initialized with EOFs, most dominant first. A Euclidean (component-wise) distance metric was chosen, using the “ep” inverse exponential neighborhood weighting function (Liu et al. 2006a) and “long” batch training – i.e., randomized sampling and relatively slow collapse of the neighborhood with time.

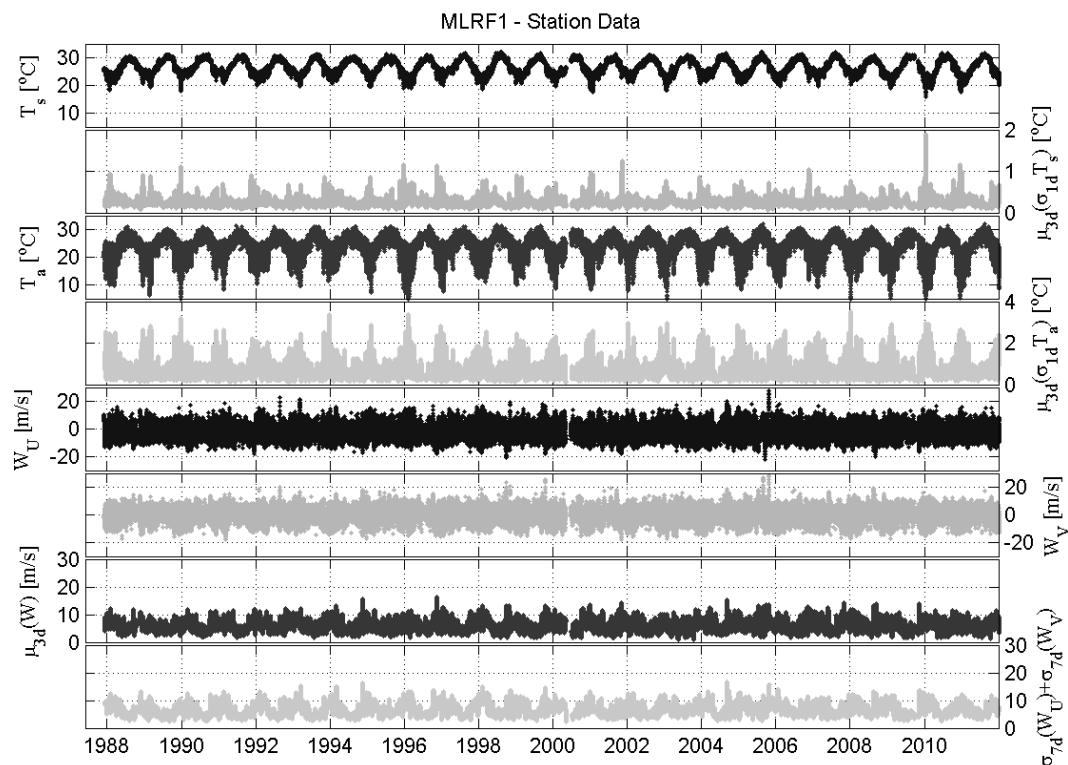
Time series for extended SOM and images for spatial SOM were normalized both by removing a mean or statistical model (see PCA, above), and also by dividing by a

maximum range. As in the normalization step for PCA, described above, the dimension or subset upon which to calculate model and maximum range were chosen to suit analysis (see Results). After training, SOM units were de-normalized for interpretation.

### **3. Results**

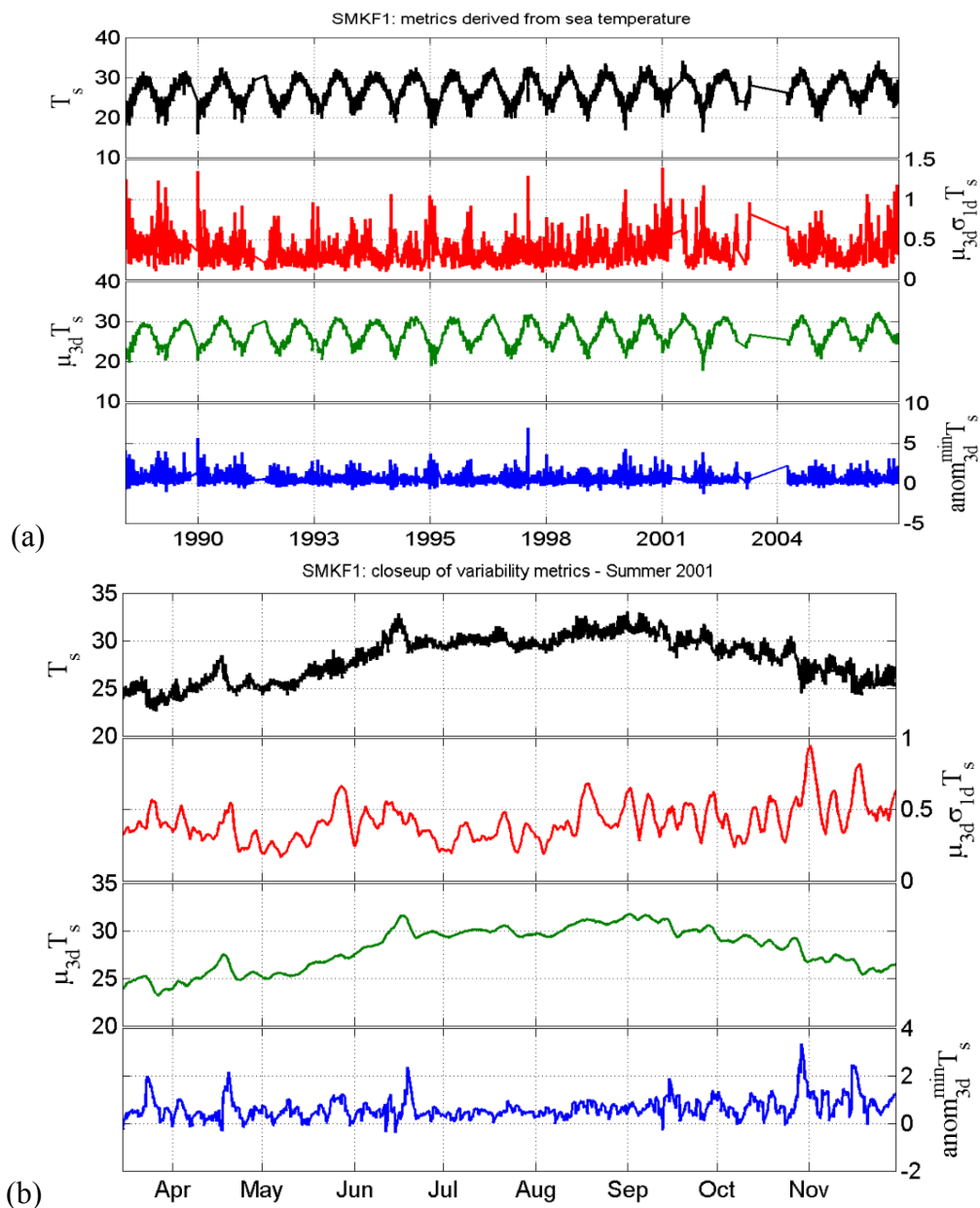
#### *Variability Metrics*

Fig. 4-3 shows whole records of quality-controlled sea and air temperature and wind speed at a particular SEAKEYS site, MLRF1, together with representative examples of variability metrics. Spanning over twenty years of data, this plot nonetheless makes apparent some features of interest. For example, the magnitude of air temperature variability is generally four times that of sea temperature variability, i.e., the smoothed standard deviations are approximately twice as large. Also, both wind speed and wind variability exhibit strong seasonal peaks, as do both the air and sea temperature variability metrics (e.g., the months of NDJFMA when stations often endure cold front passages, exhibit higher 3-day mean wind peaks, and have larger smoothed standard deviations of all variables, relative to the months MJJASO). There are also peaks in sea temperature variance at this site, and at all reef-crest sites analyzed, that do not coincide with any significant peaks in the atmospheric forcing variables of wind speed, wind variance, or air temperature variance.



**Figure 4-3: Complete time-series records of quality-controlled NDBC *in situ* data from the Molasses Reef SEAKEYS station, together with representative variability metrics calculated from those data, from top to bottom: sea temperature, sea temperature variability ( $\Theta$ ), air temperature, air temperature variability ( $\mu_{3d}\sigma_{1d}T_a$ ), wind vector components  $W_U$  and  $W_V$ , 3 d SMA wind speed ( $\mu_{3d}U_{10}$ ), and wind vector variability ( $\sigma_{7d}(W_U + \sigma_{7d}W_V)$ ).**

Fig. 4-4 shows various alternative views and variability metrics for *in situ* sea temperature at one SEAKEYS site in particular, Sombrero Key Reef, which exhibited distinctive interannual and higher-frequency variability over its twenty year record (Ch. 2). Fig. 4-4a shows the entire record at SMKF1; Fig. 4-4b shows data for the summer months of 2001, when coral reefs at Sombrero Key experienced a geographically isolated coral bleaching episode (Manzello et al. 2007a).



**Figure 4-4: Alternate variability metrics for *in situ* sea temperature from SMK1: (a) whole record and (b) detail of summer 2001. Hourly sea temperature (black), 3 d SMA of 1 d standard deviation  $\sigma_{3d} T_s$  (red), 3 d SMA  $\mu_{3d} T_s$  (green), and an alternative variability metric (see text), the anomaly between 3 d SMA and 1 d minimum hourly value  $anom_{3d}^{min} T_s$  (blue).**

The last metric shown in each panel of Fig. 4-4 is the anomaly of a 3 d SMA relative to a 1 d moving minimum (see Eq. 4-2). This metric seeks to tease out brief periods of rapid temperature *increase*, increasing temperature being more likely to impact

benthic ecology during warmer months. In August-September of 2001 for example (Fig. 4-4b, bottom plot) this metric showed frequent spikes. These spikes were relatively high for the year, although in the context to the total record (Fig. 4-4a, bottom), they were not significant. This is consistent with the analysis of Manzello et al. (2007a), that coral bleaching is more closely correlated with extremes in sea temperature relative to the annual cycle, rather than extremes in short-term variability per se.

#### *Context from Satellite Imagery*

Periods of anomalous sea temperature variability labeled as “non-wind events” (see below), were frequent in the reef-crest SEAKEYS sea temperature records. One such event can be seen in more detail in Fig. 1-3 and Fig. 4-5: high and variable winds occurred at site MLRF1 in mid-June 2006 (Fig. 4-5), but a period of anomalous sea temperature variability preceded the onset of that high wind variability by several days. Furthermore, a 3 d SMA of the total heat budget (Ch. 3) showed clear air-sea forcing for the second anomalously high  $\Theta$  event in mid-June, but no corresponding forcing (heat fluxes, wind vector variability, or air temperature variability) that would explain the earlier variability event beginning on June 4<sup>th</sup>, 2006. That event actually preceded any observable spikes in the air temperature or wind variability. However, the event did coincide with the passage of a counter-clockwise spiral (i.e., apparent cyclonic circulation) just offshore of the site, as shown by the satellite imagery (Fig. 1-3).

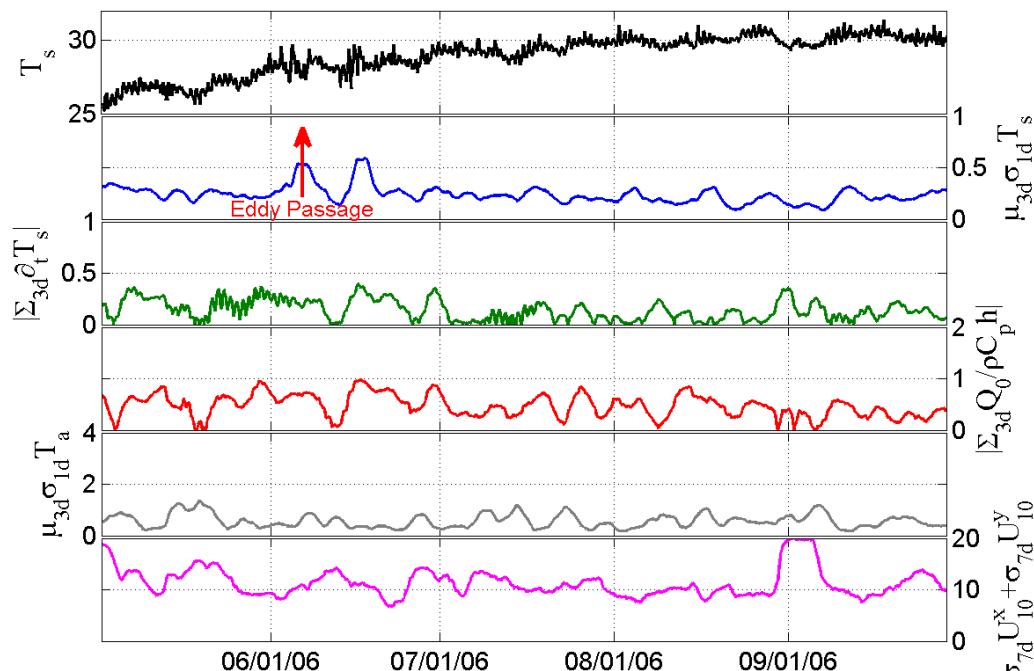


**Figure 4-5: Time series of (from top to bottom) sea temperature  $T_s$ , (black),  $T_s$  variability metric  $\Theta$  (blue), cumulative total (green) and net sea-surface (red) heat budgets, air temperature variability  $\mu_{3d}\sigma_{1d}T_a$  (gray), and wind variability  $\sigma_{7d}U_{10}^x + \sigma_{7d}U_{10}^y$  (magenta) for May-September 2006. Two anomalous sea temperature variability events occurred in June; the first, around June 4th (arrow), coincided with light winds, and passage of a vortex visible in satellite imagery offshore (Fig. 1-3).**

Gramer et al. (2009) analyzed periods of high sea temperature variability as indicated by the 3 d SMA of 1 d moving standard deviation of hourly sea temperature for the years 2005-2008 (total of 1185 d of complete sea temperature data). “Events” were identified when sea temperature variability at any of the three sites FWYF1, MLRF1, or SMK1 was greater than the 95<sup>th</sup> percentile for the entire hourly record; 3 d SMA of wind speed and 7 d SMA of wind vector variability were also analyzed. Synoptic 1 km-resolution satellite ocean color and SST imagery of the SF from USF were examined visually during each such period, for unambiguous indications of a recirculation (vortex) that immediately adjoined the reef tract at each site. For purposes of this analysis,

vortices were simply defined as ovoid features with apparent cyclonic or anti-cyclonic circulation, which appeared to extend to within two pixels (2 km) of each station site.

Results are summarized here by site and event type, and in Table 4-1 below. At Sombrero Key, 44 *events* were recognized, for a total of 273 d of high  $\Theta$ . The method classified 43% of these as *vortex/meander-driven*; 11% were classified as *wind-driven*, and 46% as possibly due to *mixed* forcing, i.e., these events required more analysis. After analysis of all available 1 km USF satellite imagery for the duration of these events, a total of 35 variability events at SMKFI were classified as *non-wind*. At Molasses Reef 28 events were recognized, including a total of 108 d of high  $\Theta$ . Classifications at MLRF1 were: vortex /meander – 39%, wind – 25%, “mixed” – 36%. Total *non-wind* events classified after further analysis were 19. At Fowey Rocks (FWYF1), 38 events were recognized for total 133 d of high  $\Theta$ . Classifications at FWYF1: Vortex/meander – 52%, wind – 2%, “mixed” – 46%. Total *non-wind* events there, after analysis, were 30.

**Table 4-1: Events of anomalous sea-temperature variability at three FRT sites for the years 2005-2008, summarized by probable forcing type (see text).**

<i>Station</i>	<i>Presumed forcing: Vortex/meander %</i>	<i>Wind-forced %</i>	<i>“Mixed” forcing %</i>	<i>Final “non- wind” events</i>	<i>Total events</i>	<i>Total days</i>
<i>SMKFI</i>	43%	11%	46%	35 (80%)	44	273 d
<i>MLRF1</i>	39%	25%	36%	19 (68%)	28	108 d
<i>FWYF1</i>	52%	2%	46%	30 (79%)	38	133 d
<i>Total:</i>		23%		49 (77%)	64	

Overall across the three sites during the 1185 d (approximately 39 month) record spanning the years 2005-2008, 64 total multiday single- or multi-station events were identified. Of these, 15 were identified on the basis of wind variability metrics as being likely results of wind or wind-wave forcing; all 15 of these wind events coincided with anomalously high sea-temperature variability at all three sites simultaneously. The

remaining 49 events were classified as *non-wind* events. Based on visual examination of satellite imagery, 41 non-wind events (84%) coincided in time (within 1 d) with presence of a *cyclonic* feature immediately offshore of at least one site involved in that event.

Fig. 4-6 shows the variability-metric time series  $\Theta$  and  $\mu_{3d}U_{10}$  at SMKF1 for one particular year, 2005. Red arrows highlight periods of anomalous sea temperature variability; darker red arrows annotated with the year-day correspond to chlorophyll *a* satellite imagery in the panels of Fig. 4-7. Based solely on wind metrics, all of these events shown with year-day were automatically described as non-wind related, except day 307. That is an example of an event where wind variability was somewhat high and may have been somewhat favorable for upwelling due to coastal Ekman divergence at the reef-crest. However, visual examination of images like this allowed the event on day 307 and several similar events at all three sites to nonetheless be ascribed as non-wind related.

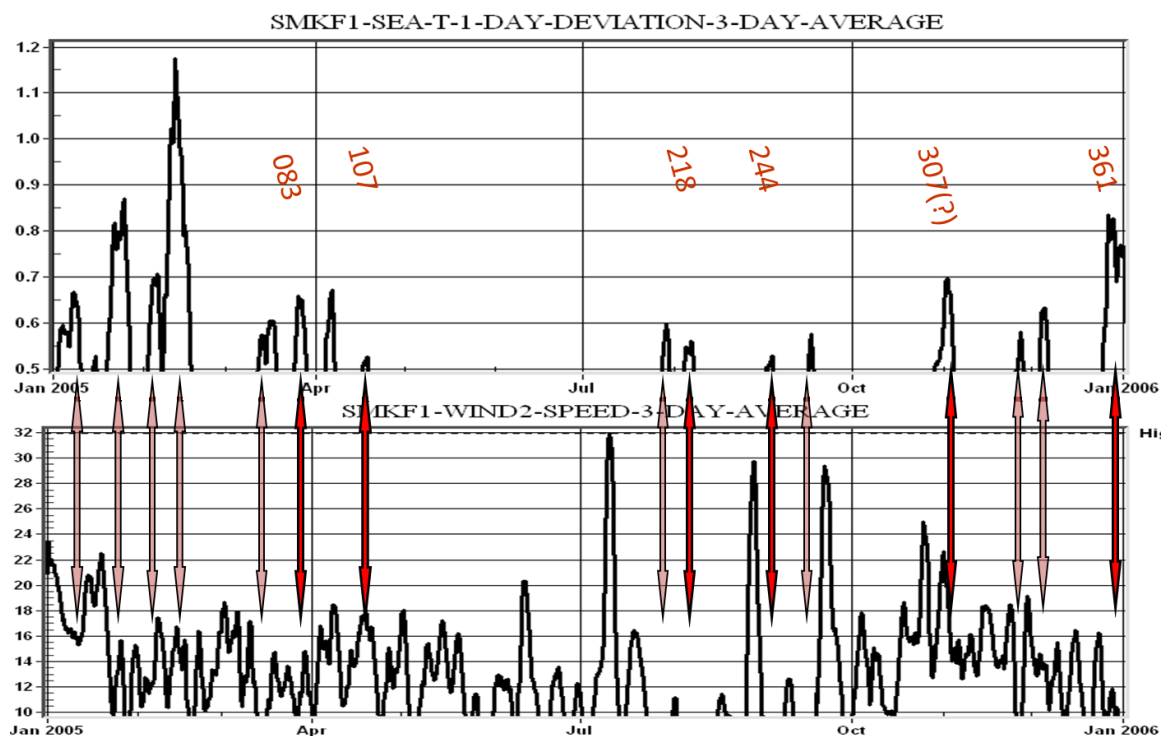


Figure 4-6: Sea temperature and wind variability metrics for SMKF1 during 2005. See text and Fig. 4-7 for further discussion.

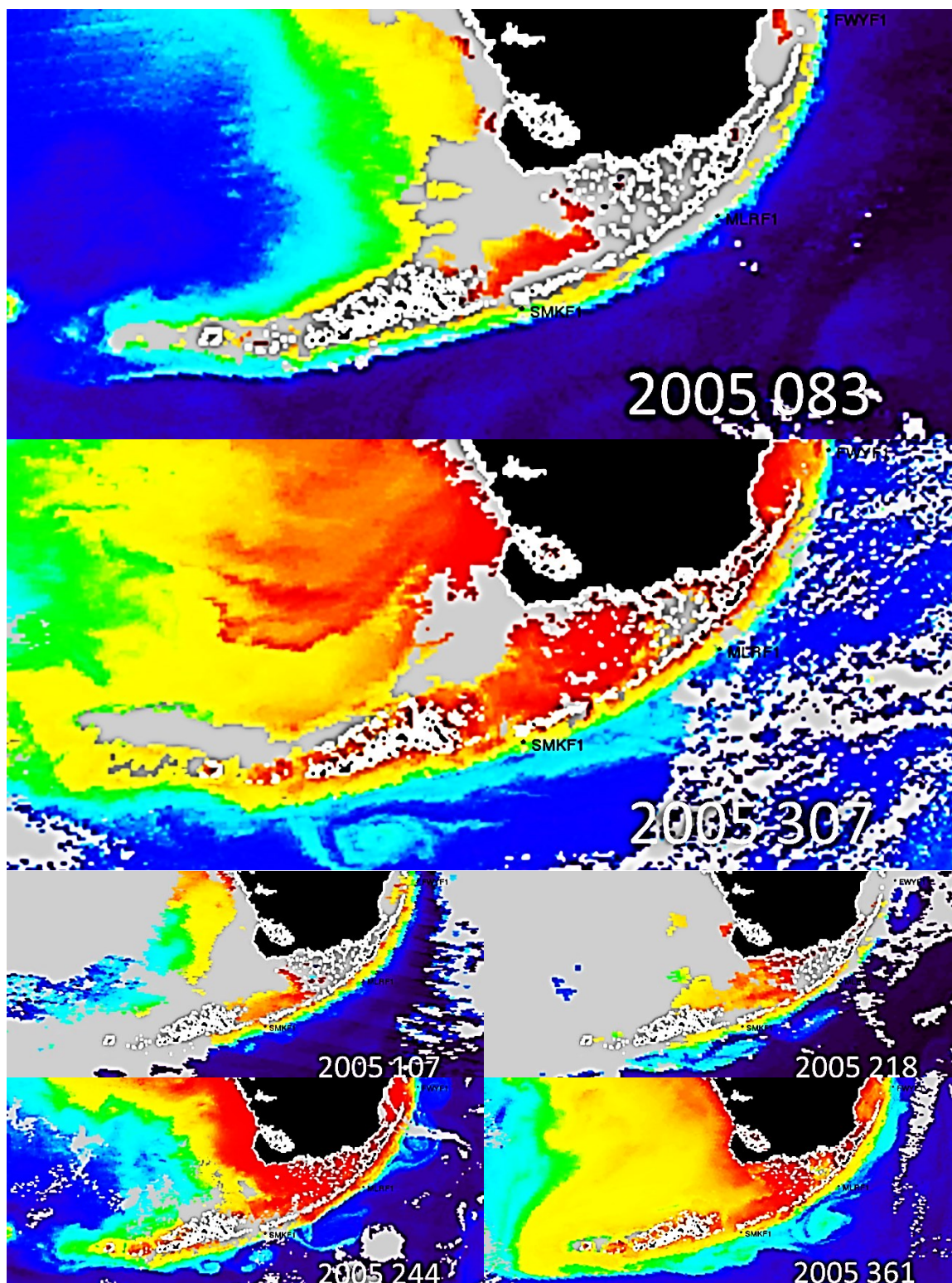
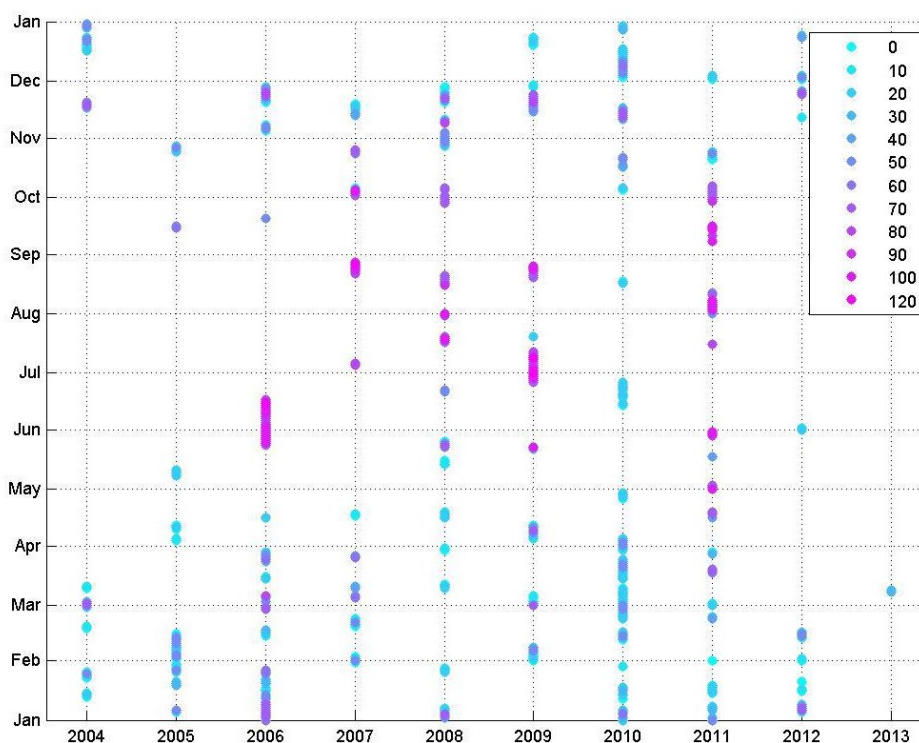


Figure 4-7: Chlorophyll *a* images of the Florida Keys, coincident with days of “non-wind related” anomalous sea temperature variability at SMKF1 in 2005. Images are from the USF IMA RS Web site, with contrast and sharpness enhanced to show subtle features: high chlorophyll *a* concentration estimates are denoted by red, while dark blue denotes very low concentration; clouds are shown in gray. Year-days 83 (March 24<sup>th</sup>) and 307 (November 3<sup>rd</sup>) are enlarged both to show the position of SMKF1 relative to the images, and to illustrate the detail available in the images.

### *Heuristic Ecological Forecasts*

An “onshore flux” ecoforecast (see above) has been implemented by the author as part of the CHAMP project at AOML. This ecoforecast monitors sea and air temperature and wind variability metrics at four of the SEAKEYS stations, along with satellite chlorophyll *a* time series for each site. It provides researchers and managers who have an interest in the FRT with automated email alerts daily, and with historical reports beginning in 2004. Seasonality and severity (S/RI, see above) of occurrences of “onshore flux” ecoforecasts for one site, MLRF1, are shown in Fig. 4-8.



**Figure 4-8: Stimulus/Response Index (S/RI) for the "onshore flux" ecoforecast, evaluated in near real-time based on variability metric criteria calculated from SEAKEYS data broadcast hourly. Alerts are frequently seen during cold-front passages (November-April) but produce low S/RI (<60, light color); alerts during warmer months are not as frequent, but show higher S/RI (60-120, darker color) due to higher observed sea-temperature variability according to the metrics, to coincident peaks in satellite-derived chlorophyll *a*, and to the *lack* of coincident atmospheric variability.**

For non-wind events in particular, the S/RI was increased relative to other events, either by anomalously high sea-temperature variability metric, or by coincidence of high USF satellite-derived chlorophyll *a* values at the site, or both. Thus, onshore flux events are more frequent or even ubiquitous during months of frequent cold-front passages over the FRT (NDJFMA). Yet during warmer months (MJJASO) in many years (2006, 2008, 2009, 2011), when wind variability is generally much less, the S/RI actually suggests less frequent but more intense variability events at these reef-crest sites. This, coupled with the results summarized above from Gramer et al. (2009), indicates a direct impact on the thermal environment of the FRT due to vortical and internal wave fields offshore.

#### *Principal Component Analysis*

PCA for individual *in situ* time series was performed both on total records, and on records selected from each of the four seasons, January-March (JFM), April-June (AMJ), July-September (JAS), and October-December (OND). PCA was also done for south Florida “dry season” NDJFMA, and “wet season” MJJASO – but all of the features gleaned from these analyses were also noted either in the annual PCA, or in one or more of the seasonal analyses; thus these “wet” and “dry” season results are not presented here.

“Realizations” or data vectors were constructed for input to PCA as follows: first, the total record for each variable was divided into individual 24 h, 14 d, or 91 d “frames”. The 24 h and 14 d frames were also analyzed by season. Furthermore, PCA was done on subsets of only those 24 h and 14 d frames during which a metric exceeded a cutoff value: for sea temperature variability, when the metric  $\Theta$  exceeded its whole-record 95<sup>th</sup> percentile; for heat fluxes, when the difference (error) between observed sea temperature and the heat budget exceeded its 95<sup>th</sup> percentile.

Prior to computation of covariance and correlation matrices for PCA of 14 d or 91 d frames, the least-squares trend-line of each frame was removed. In addition to PCA of detrended time series, an attempt was also made to compute EOFs for time series where the diurnal cycle was removed using harmonic analysis. However, both phase shifts and asymmetries in the observed diurnal cycle made this approach problematic. As a result, these time series with diurnal cycle removed were not analyzed further.

### EOFs of Measured Time Series

Initial analysis looked at 14 d “frames” of unfiltered hourly *in situ* sea temperature from all seasons (Fig. 4-9). The first or dominant EOF (#1) explains 37% of the total variability, and shows a pattern consistent with a week-long cooling trend. This result is consistent with the passage of mild cold-fronts, and is likely due to a relatively small subset of frames during cooling months. The second and third EOFs explain only 11% of variability each, and are likely consistent with diurnal cycle and lunar month tides (#2), and with the onset of somewhat shorter (3-7 d) weather events (#3). These EOFs represent important signals, particularly the first one. However, these PCA results are very sensitive to extreme events in the input signals, suggesting the value of first normalizing the data before PCA is performed – as was done for succeeding figures.

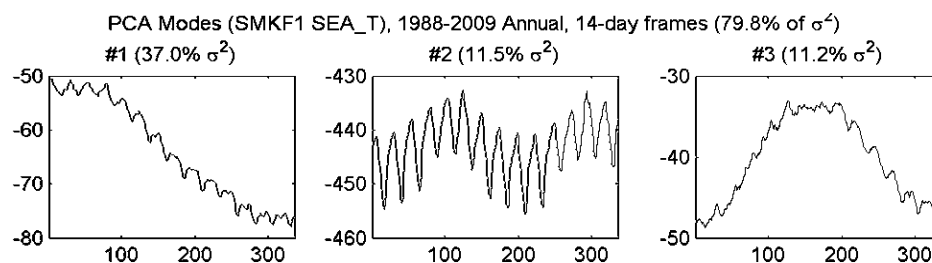


**Figure 4-9: Dominant EOFs for un-normalized hourly sea temperature at Sombrero Key SEAKEYS station, arranged arbitrarily into 14 d (336 h) "frames" for analysis. This figure illustrates the importance of first attempting to normalize data prior to PCA.**

When a linear trend-line and biweekly mean were removed, the EOFs showed new features (Fig. 4-10a). The pattern shown was replicated relatively closely at all sites analyzed: The first dominant mode explained 19% of variance in the 14 d frames, and was dominated by diurnal variability with a tidal overlay. A second mode was also significant, explaining 17% of variability: this pattern was again dominated by air-sea cooling as in Fig. 4-9, with the effect of the diurnal cycle hardly apparent at all. The lack of a diurnal signal in the second mode illustrates an issue commonly encountered with interpreting PCA results: the method enforces vector orthogonality between each of the modes identified, thereby forcing frequencies of variability that are strongly apparent in one mode to be muted in others. In analysis of variability using SOM (see below), this is not an issue. The third (below) and succeeding EOFs were not considered significant.

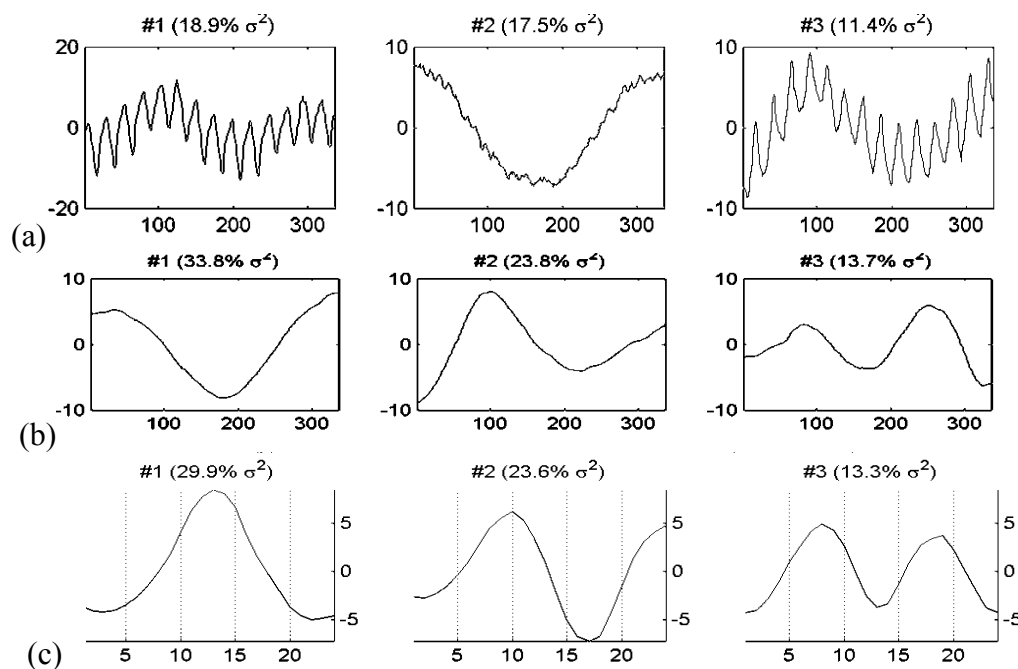


**Figure 4-10: Dominant EOFs of detrended SMKF1 sea temperature. (a) Hourly time series: the first two modes represent the dominant frequencies of variability less than 14 d period; similar results were seen at most other sites analyzed in the FRT. (b) Daily mean: the dominant modes each again represent a dominant frequency of variability between 1 and 14 d period; this result varied somewhat by site, however, depending on the importance of “weather-band” (synoptic atmospheric) variability at each site. (c) Hourly time series with 24 h frame, highlighting diurnal variability.**

PCA of daily mean sea temperature showed similar patterns: the first three modes (Fig. 4-10b) are all distinct frequencies of multi-day variability. In the case shown (SMKF1), as at most reef-crest sites, the longest period available in the frame (just under 14 d) was quite dominant explaining 33% of daily mean variability, with succeeding modes dominated by ever higher periods of variability. At reef flat sites, a somewhat different result can be seen (figures not shown), with variability at somewhat higher frequencies closer to the “weather band” dominating (see also Ch. 2, e.g., Fig. 2-3). The dominant mode of diurnal variability (Fig. 4-10c) was that of daily insolation; a secondary mode featured rapid cooling after mid-day, attributable to frequent development of afternoon thunderstorms over the FRT in warmer months (see PAR analysis, Appendices).

### **Variability Metric EOFs**

An initial attempt to characterize dominant forcing with PCA involved using vectors constructed from *variability metrics* (see above) for sea temperature and forcing variables,  $\Theta$ ,  $\mu_{3d}\sigma_{1d}T_a$ ,  $\sigma_{7d}U_{10}^x + \sigma_{7d}U_{10}^y$ ,  $\Sigma_{3d}(Q_0/\rho C_p h)$ , and  $\Sigma_{3d}\partial T_s$ . Frames of these individual time series comprising 14 d (336 h) were analyzed first (Fig. 4-11a-d, for SMKF1). The two first components were dominant in every case, explaining between 60 and 75% of variance between them. The dominant pattern for each of the metrics was that of rapid cooling with a highly variable wind vector, over a period of 3 to 4 d – consistent with the passage of a cold front and high pressure system. Use of 91 d frames for variability metrics provided little new information (figures not shown). When the

metrics were analyzed on 24 h frames, diurnal warming was seen to dominate in all cases (e.g., Fig. 4-11e, Fig. 4-11f).

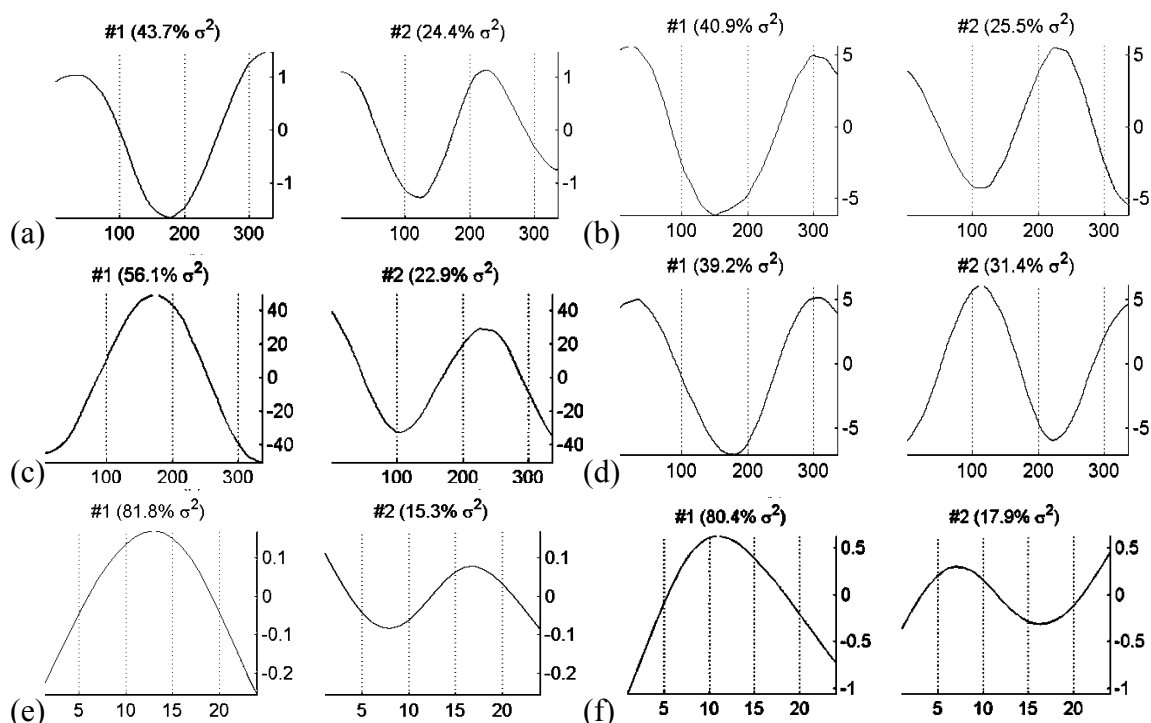


**Figure 4-11: Dominant EOFs of 14 d frames of variability metrics for: (a) sea temperature,  $\Theta$ ; (b) air temperature,  $\mu_{3d}\sigma_{1d}T_a$ ; (c) winds,  $\sigma_{7d}U_{10}^x + \sigma_{7d}U_{10}^y$ ; (d) net heat flux,  $\Sigma_{3d}(Q_0/\rho C_p h)$ . Dominant EOFs of 24 h (diurnal) frames for the variability metrics of (e) sea and (f) air temperature.**

Patterns of *covariability* between time-series were explored using the technique of simultaneous or “extended” PCA (see above) on 24 h and 14 d frames. Extended PCA of  $T_s$  or its variability metric,  $\mu_{3d}\sigma_{1d}T_s$ , were done vs. directly measured forcing variables  $U_{10}^x$ ,  $U_{10}^y$ ,  $T_a$  and against their variability metrics  $\sigma_{3d}U_{10}^x + \sigma_{3d}U_{10}^y$ ,  $\sigma_{3d}U_{10}^x + \sigma_{3d}U_{10}^y$ , and  $\mu_{3d}\sigma_{1d}T_a$ . Many combinations of sea temperature and these other variables produced dominant EOFs that were difficult to interpret physically. A result of interest, however, was from analysis of 14 d frames of sea- and air temperature metrics vs. the 3 d SMA and vector-variability metrics for wind (Fig. 4-12 shown for one reef-crest site). Wind speed

(SMA) and wind direction ( $\sigma_{3d}U_{10}^x + \sigma_{3d}U_{10}^y$ ) did not exhibit covariability in all cases:

The three dominant modes were consistent respectively with: #1, the passage of cold fronts (strong variability in all variables, explaining 22% of *total data vector variability*); #2, strong, steady winds but less variability in air temperature (16% of variability), and a pattern (12% of variability) of wind and air temperature variability followed 3-4 d later by sea temperature. The delayed pattern of the latter two modes suggests not so much direct air-sea cooling, as the effects of wind-driven circulation or wave breaking following the passage of cold-fronts in winter or tropical easterly waves in summer.

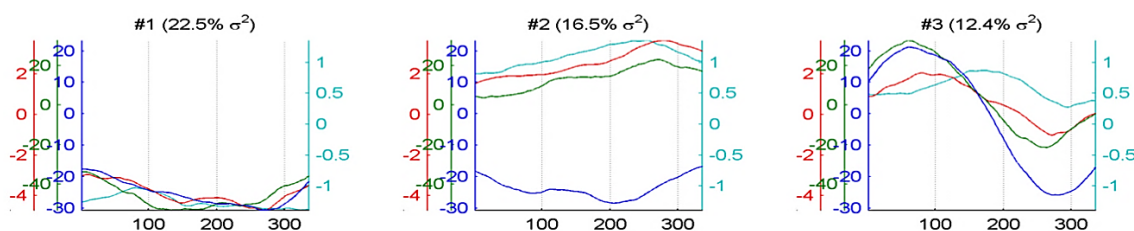


**Figure 4-12: Extended PCA at SMKF1, showing dominant patterns of covariability between variability metrics for sea temperature (light blue) and air temperature (red), wind vector variability (green), and 3 d SMA wind speed (dark blue). Note that the zero-line position is consistent across panels but varies by time series: the origin for sea temperature variability is at the plot center, while for the others it is slightly above center.**

PCA was then restricted to only those 14 d frames containing periods of anomalous sea temperature variability greater than the 95<sup>th</sup> percentile of either of residual vs. the total heat budget, or of the variability metric  $\mu_{3d}\sigma_{1d}T_s$  (Fig. 4-13). Again, two patterns were dominant – that of cold-front passage with rapid reef cooling, or that of strong, steady wind and lagged cooling. However, a third pattern (explaining just 12% of the total variability) also emerged, where sea temperature variability appears essentially uncorrelated in time with variability in any of the other metrics: this pattern was seen to

explain a similar percentage of combined variability in the results from doing extended PCA with the total heat budget ( $\sum_{3d} \partial_t T$ ) during periods of anomalous sea temperature variability (figures not shown). In analysis using self-organizing maps (see below), this pattern was found to actually be quite common. It is likely that its significance was suppressed in the present result, due to the constraint that all EOFs be orthogonal.

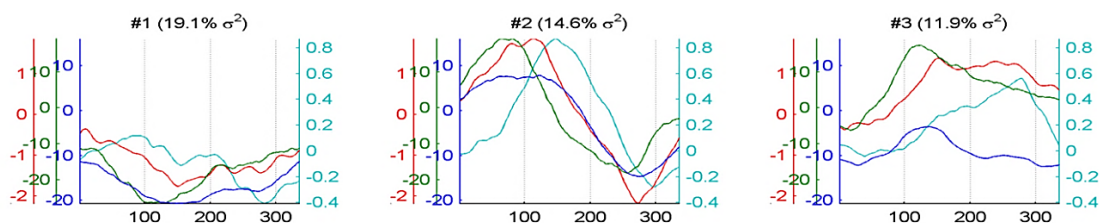


**Figure 4-13: Dominant extended EOFs as for Fig. 4-12, but only during those 14 d frames when anomalous sea temperature variability was observed. Note again the multiple origins in each plots.**

### Satellite Spatial PCA

Spatial PCA was also performed on synoptic SST anomaly from AVHRR (see Additional Data above), similar to that done on lower-resolution mean SST data from the WFS by Liu et al. (2006). Synoptic 1 km AVHRR SST and anomaly fields in 81x81 km boxes surrounding three of the SEAKEYS stations (SMKF1, MLRF1, and FWYF1) were extracted from the USF Web site for complete years 2005, 2006 and 2007. Synoptic boxes were discarded that had more than 50% of the pixels in the 16x16-pixel center box masked due to clouds, land, or unphysical values, resulting in the use of only 25% of all images. This subset comprised approximately 900 SST or anomaly fields per year per station, including data from all NOAA satellites in orbit with AVHRR onboard that year. A further feature of the methodology in Liu et al. that was replicated for this study was the calculation of per-image PCs for the most significant EOFs: the result is a set of

scalar time series, quantifying relative significance of each mode to the synoptic SST field around each SEAKEYS station, as a function of time. Again initial analysis showed the importance of removing a mean: these EOFs were dominated by seasonal changes in the cross-shore gradient that dominates the SST field in the FRT (figures not shown). The results shown in Fig. 4-14 were achieved by removing both a per-field spatial mean and a long-term time-mean for each pixel. The one significant EOF demonstrates larger SST variability in shallower regions, less variability in inter-island bridge channels than elsewhere, and greater variability in shallows of the Middle Keys vs. elsewhere. Even so, the usefulness of EOFs is greatly reduced by prevalence of cloud cover: both of the EOFs succeeding the one shown were strongly affected by cloud cover and were not significant.

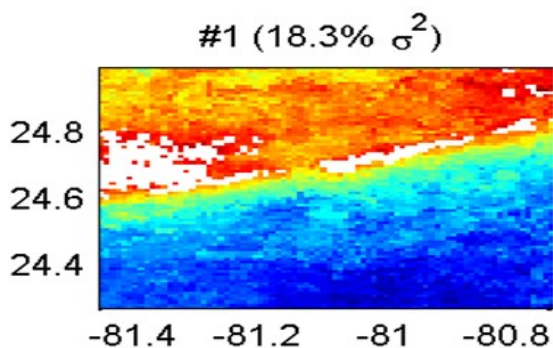


**Figure 4-14: Dominant EOF from spatial PCA of synoptic AVHRR SST anomaly, i.e., with the long-term field mean removed, for SMKF1 (all good images). Color scale is not shown, but the range in the image is from dark blue (-3 K) to dark red (+3 K).**

### **Extended Spatial PCA**

Periods of significant sea temperature variability that were poorly explained by the heat budget were examined relative to horizontal gradients in synoptic AVHRR SST, in an attempt to estimate corrections to the advective and mixing terms based on weekly composite SST in the heat budget. As described in Chapter 3, SST fields derived from AVHRR during daylight satellite passes are often nearly isothermal. Thus, the attempt to

estimate surface advection indirectly focused primarily on night hours. However, frequent cloud cover made it difficult to interpret dominant EOFs for data vectors constructed from both sea temperature anomaly and the synoptic AVHRR SST imagery. Improving this methodology is a goal of future work.

### *Self-Organizing Maps*

SOM analysis was performed on individual *in situ* and heat budget time series, using the same “frames” used in PCA (see above), consisting of either 24 h, 14 d, or 91 d: many of these results were similar to those found through PCA, and are not shown here. Extended SOM analysis (similar to extended PCA) of variability-metric time series is presented below, as is spatial SOM analysis on composite AVHRR SST anomaly fields from the USF data. Spatial SOM analysis was also done on USF’s synoptic AVHRR SST, but this gave little additional information. As with PCA, these data were analyzed both as complete records and by selecting frames and images that corresponded to periods of anomalously high sea-temperature variability. As for extended and spatial PCA, the goal was to find patterns in forcing time series and satellite imagery that can help the researcher to provide a physical interpretation for anomalous *in situ* sea temperature variability.

Fig. 4-15 shows extended SOM between variability metrics in 14 d frames, restricted to those frames containing periods of anomalously high sea temperature variability, similar to the PCA shown in Fig. 4-13 above. One of the importance differences between PCA and SOM emerges with this figure. That is, the “dominant” modes of variability in the SOM are not necessarily restricted to just the first two to three

units of the map. If the dimensions of the map are chosen carefully, each unit on the SOM may represent an actual pattern of variability that occurs within the data.

In other words, the statistical significance of SOM results is *not restricted* to those units matching, for example, greater than some given percentage of data vectors. Fig. 4-15 in particular shows several patterns that represent the effects of synoptic or convective weather variability. However, an array of units in the center of the map (labeled arbitrarily #4, #1, and #5) show a pattern of sea temperature variability lasting from 4 to 6 d, which is not coincident with peaks in any of the other variables. Together, these three patterns are BMUs (see above) for a total of 49 different frames.

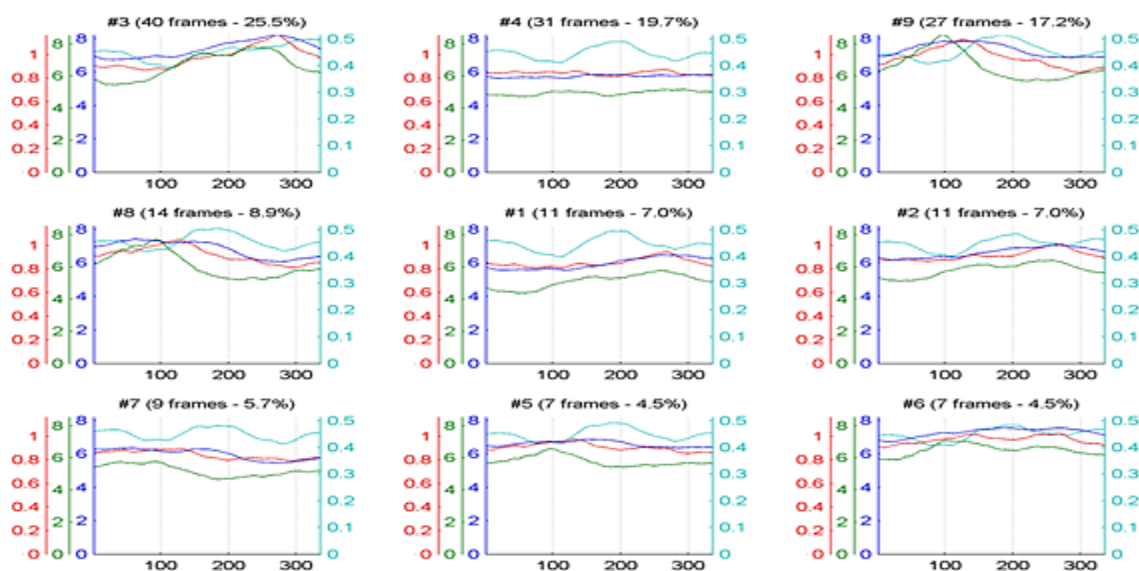


**Figure 4-15: Extended SOM performed on vectors that are the result of concatenating 14 d frames from time series of 3 d sea (light blue) and air temperature variability (red), 3 d SMA of wind speed (dark blue), and 3 d wind vector-component variability (green). Measurements from SMKF1, and frames are restricted to periods of anomalously high sea temperature variability (>95<sup>th</sup> percentile). Data were de-normalized following analysis: Note the varying scale of each of the individual plots within each panel.**

Fig. 4-16 shows an extended SOM analysis of all frames from SMKF1 regardless of sea temperature variability, but restricted to only those frames that lie within the

summer months of July-September (JAS). In this analysis, a large number of the frames (42) best match the pattern for sea temperature variability that is unaccompanied by atmospheric variability. This result suggests that during JAS at this site, sea temperature variability peaks may be largely attributable to forcing terms other than air-sea fluxes, including inertial surface motions, breaking of internal waves on the fore-reef slope, or passage of vortices and meanders offshore (Ch. 2 and Results summarized above). SOM units matching less than 14% of 14 d frames are not shown in Fig. 4-16 or Fig. 4-17.

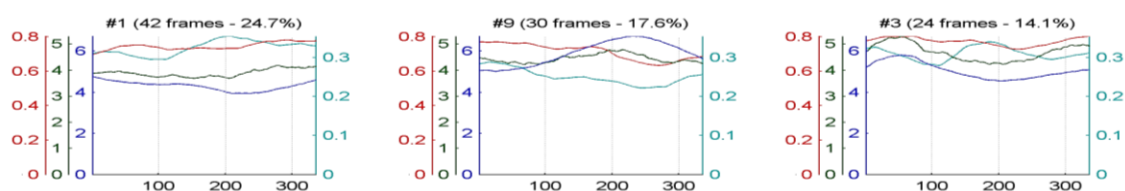


**Figure 4-16: Extended SOM of all 14 d frames lying in summer months (JAS) for variability metrics at SMKF1, regardless of sea temperature variability. Shown are sea (light blue) and air temperature variability (red), 3 d SMA wind speed (dark blue), and 3 d wind vector-variability (green). Note the varying scales of plots within each panel (see above).**

Finally, Fig. 4-17 shows the same analysis for summer frames but at a different reef-crest site further west than SMKF1, Sand Key lighthouse station (SANF1). At this site, sea temperature variability is still seen that is not coincident with atmospheric forcing (units labeled #9, #8). Other potential forcing mechanisms are suggested by this result, e.g., upwelling related to vortical instabilities in the FC front or IW breaking. In addition, however, there are more frequent summer patterns noted where sea temperature variability lags atmospheric forcing by several days (units labeled #3 and #1, and other less frequent units not shown). This suggests enhanced wind- and wave-driven transport at this site in the Lower Keys relative to other sites further east and north in the FRT.

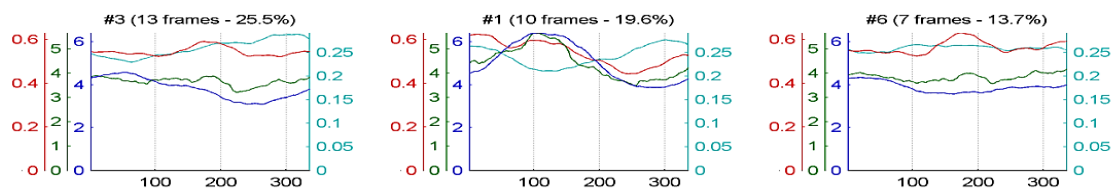
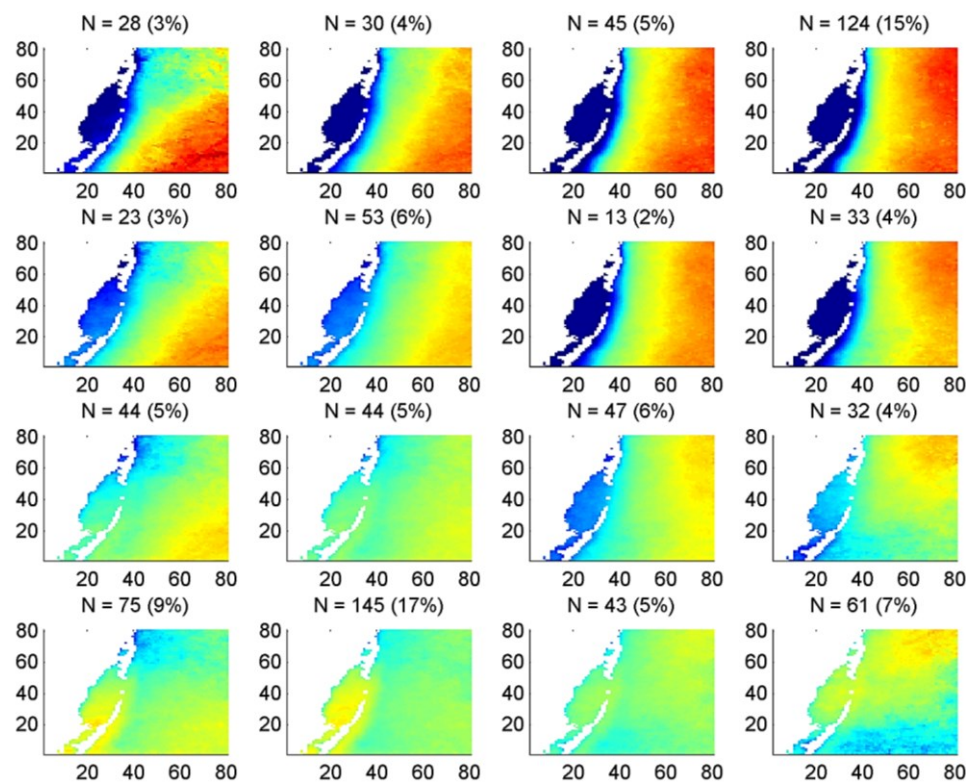


**Figure 4-17: Extended SOM for summer months like that in Fig. 4-16, but for the Sand Key SEAKEYS station (SANF1). Some features are more prevalent in this SOM than at other reef-crest sites, e.g., patterns where sea temperature variability lags atmospheric forcing by several days.**

### Spatial SOM Analysis

Fig. 4-18 is a 4x4 SOM classifying all NOAA AVHRR synoptic SST anomaly fields (840 SST images) for 2005 centered on Fowey Rocks SEAKEYS station FWYF1. Not used were approximately 3,000 SST images from 2005 where more than 50% of the 16x16 pixel area surrounding FWYF1 was cloudy or land-masked. Median SST for each image was subtracted from all its pixels prior to analysis, to reduce the effect of diurnal and annual cycles. SST anomaly across all 840 images ranges from -3.2 to +2.9 K.

As for succeeding figures, each of the 16 subplots in Fig. 4-18 represents a SOM unit, the mean state of a locus or “mode” of similar synoptic SST fields. The number “N” of synoptic SST images which best match each unit is shown above that unit, along with the percentage of all useable synoptic images for 2005 matching that unit. Note that during training, a SOM is automatically arranged so that nodes with similar geometric features (i.e., those that are similar) appear close to one another on the map. This is in contrast to figures where SOM units were instead arranged in order from those most-frequently matched by the data (upper left) to those with fewest matches (lower right), such as those for extended SOM analysis of time series (Fig. 4-15, Fig. 4-16, Fig. 4-17).



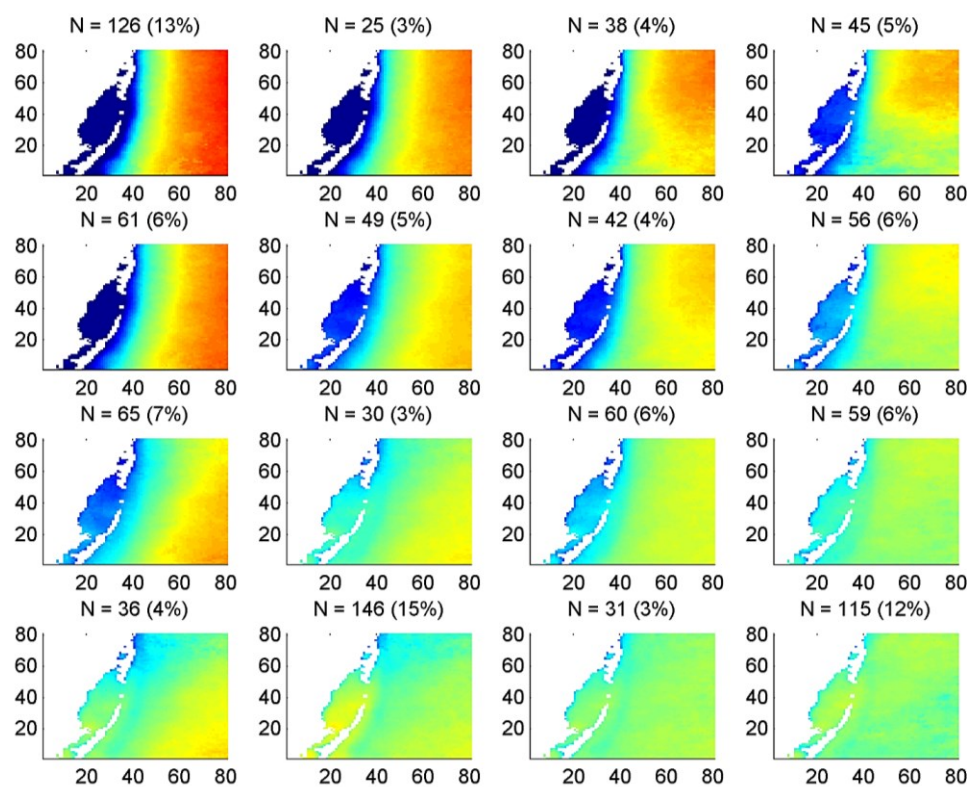
**Figure 4-18: Spatial SOM on all good AVHRR SST anomaly images, i.e., with the per-image mean removed, surrounding Fowey Rocks SEAKEYS station (FWYF1) for 2005. Biscayne Bay, just to the west of the center in each unit, is a potential source of cooler water in warm months (top units) and warmer water in winter (bottom). Color bar is not shown, but the SST anomaly values shown span a range from -3 (dark blue) to +3 K (dark red). The number “N” and percentage shown above each unit in the map refer to the number of useable synoptic images from 2005 that best matched that pattern. All axes show distance in km from the image origin at 25.22° N, 080.42° W.**

Fig. 4-19 shows the same analysis at FWYF1, but for all images in the year 2006.

Spatial patterns are very similar to those for 2005 (Fig. 4-18). Patterns arise in 2006 which are similar to those in 2005. (Note that both SOMs share very similar units, although their placement within each map may differ by reflection about either of the map axes.) In particular, water is apparently flowing from Biscayne Bay onto the FRT that is either cooler than the image mean (upper units) or warmer (lower units).

Some interesting differences between years also emerge, however. The presence of “lobes” of cooler water offshore of FWYF1 is somewhat greater in 2005 (units at right and upper left in Fig. 4-18): this may indicate that larger-scale eddies were either more

prevalent in 2005 or that they translated through the region more slowly on average in 2005. Units where Biscayne Bay shares a warm anomaly with the FRT are less common in 2006 than in 2005. Furthermore, the likelihood that such a Biscayne Bay warm anomaly would be carried southward along the FRT was correspondingly less, while the pattern where a warm anomaly was carried northeast and offshore was more frequent.



**Figure 4-19: Spatial SOM of FWYF1 similar to Fig. 4-18, but for the year 2006. The SST anomaly values shown in color range from -3 (dark blue) to +3 K (dark red). Number “N” and percentage refer to the number of useable synoptic images from 2006 that best matched that unit. All axes show distance in km from the image origin at 25.22° N, 080.42° W.**

Finally, the importance of cloud filtering for SOM is illustrated by Fig. 4-20.

Note that the periodic appearance of clouds in satellite imagery does not significantly reduce the usefulness of spatial SOM the way it is seen to do in spatial PCA (Fig. 4-14).

However, when cloud tops are misinterpreted as valid SST data, the resulting sea

temperature anomalies can significantly hamper SOM analysis, as can be seen in the units lying near the lower right corner of this map.

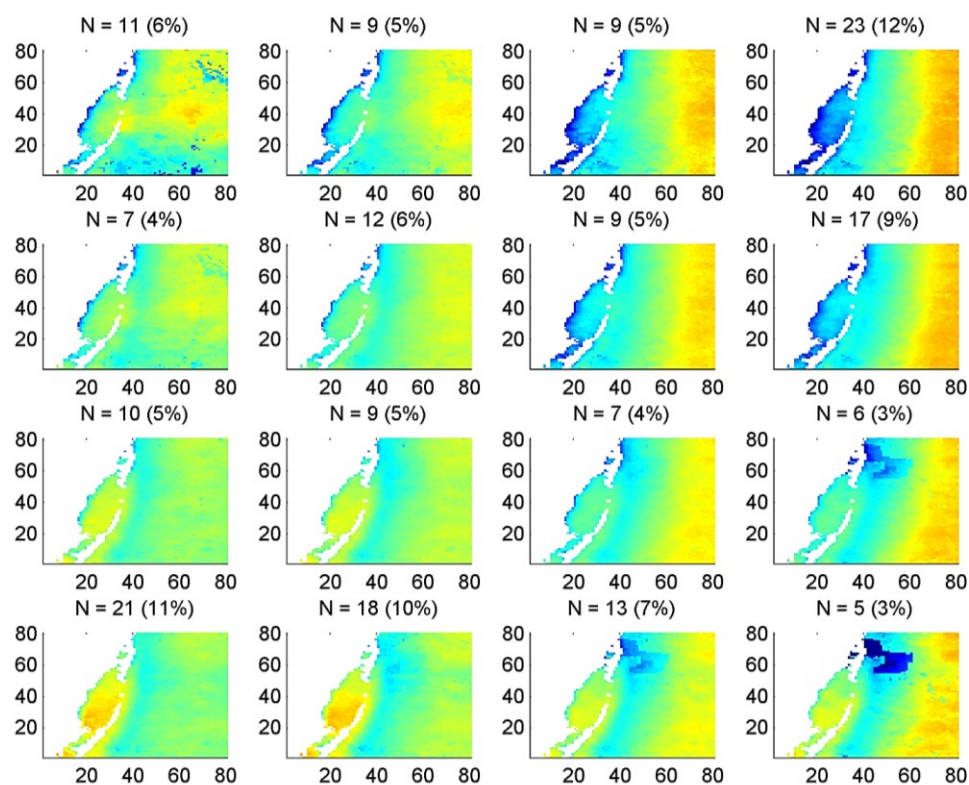


**Figure 4-20: SOM of SST anomaly surrounding FWYF1 during spring months (April-June) of 2005, totaling 186 useable SST images. Note the spurious feature in units at lower right of the map, highlighting the need for rigorous quality control of SST fields prior to SOM or PCA analysis. Manual removal of these features was necessary to produce the results shown in, e.g., Fig. 4-18.**

### **Anomaly Analyses of Extreme Events**

Long-term sea temperature records in the FRT cover several historical events which caused significant ecological impacts to corals. The winter of 2010, for example, produced mass coral mortality related to cold sea temperatures in the FRT (Lirman et al. 2010), centered on the dates January 10<sup>th</sup> to 15<sup>th</sup>, 2010. The summers of 1997, 1998, and 2005 also produced major coral bleaching events related to high sea temperatures (e.g., Manzello et al. 2007a). One site in particular, Sombrero Key Reef (SMKF1),

experienced severe bleaching in all three years, as well as milder bleaching in 2001 and 2004. However, the summers of 2004 and 2005 were unusual in that more severe bleaching was likely prevented in the FRT by the effects of tropical weather systems (Manzello et al. 2007b). In 2005, landfall of two storms in particular coincided with significant changes in both *in situ* sea temperatures and prevalence of coral bleaching in the FRT (op cit.): Hurricane Katrina on August 25<sup>th</sup> and Hurricane Wilma on October 24<sup>th</sup>, 2005.

A “mass-coral-stress” ecoforecast was constructed using published indices and methods (Hendee et al. 2001; Manzello et al. 2007a; Lirman et al. 2010). This ecoforecast attributes thermal stress to coral reef sites when 30 d SMA *in situ* sea temperature exceeds the peak climatological monthly mean at a site by 1 K or more, when hourly sea temperatures are low enough to cause coral mortality, or for certain other conditions of combined high sea-temperature and very light winds (*doldrums*, op. cit.). The mass-coral-stress S/RI predicts the likely severity of associated bleaching and mortality.

Fig. 4-21 shows complete time-series records of several variables discussed in the present Chapter. For years 1995-2007 at SMKF1, the figure shows *in situ* sea temperature; its variability metric,  $\Theta$ ; S/RI for the mass-coral-stress ecoforecast; PCs for the two most dominant EOFs from each of sea temperature 14 d PCA (“ $T_s$  PC”; see EOFs in Fig. 4-9) and 14 d extended PCA of covariability between  $\Theta$  and other metrics (“ $\Theta$  PC”; see Fig. 4-13); and Best Matching Unit from the 14 d extended SOM of variability metrics shown in Fig. 4-15 (“ $\Theta$  BMU”). Finally, for years 1995-2010 at MLRF1, PC1 and PC2 of the 14 d sea temperature PCA are shown (EOFs similar to those in Fig. 4-9).

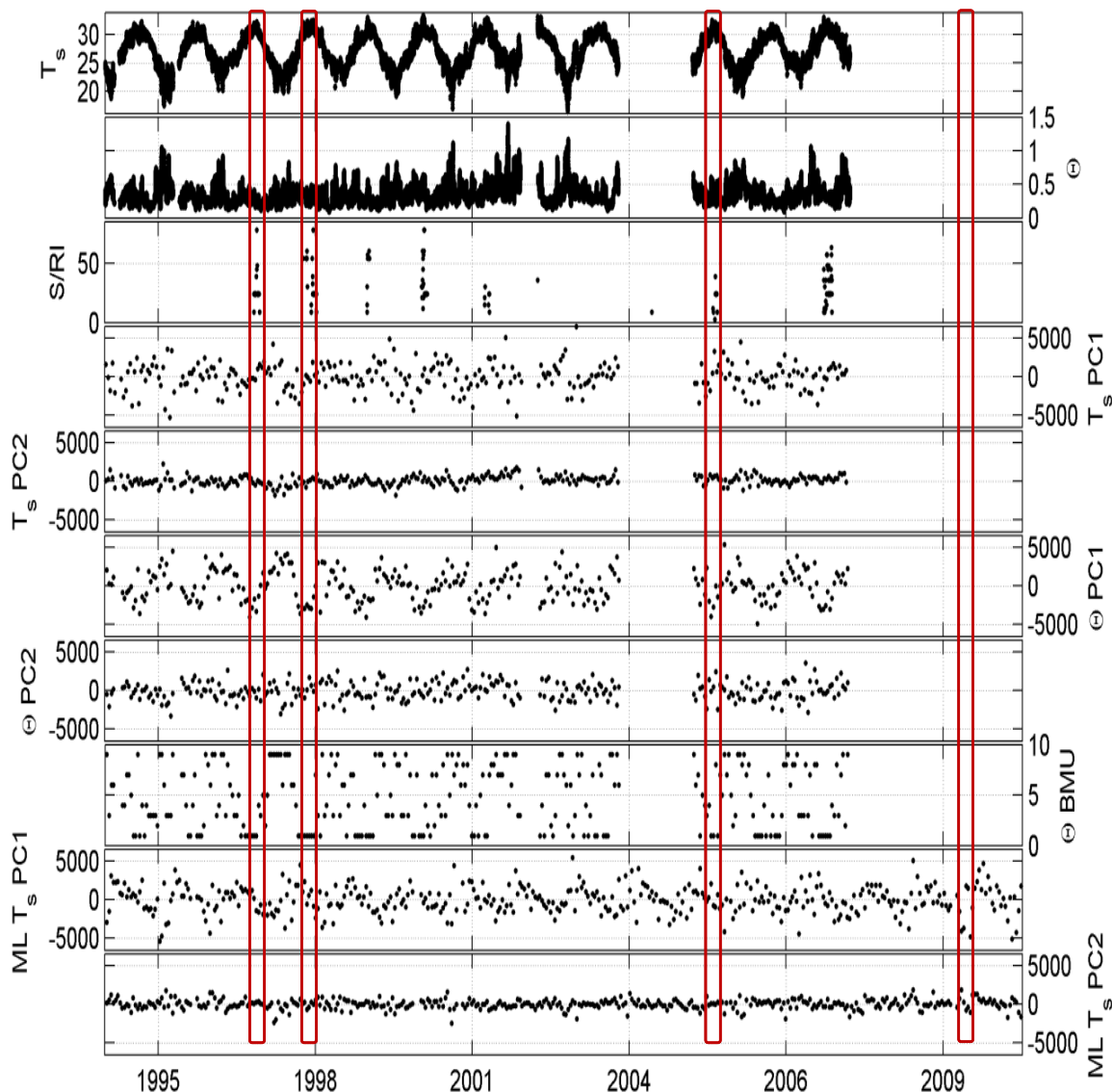


**Figure 4-21: Anomaly analyses for SMKF1: sea temperature,  $T_s$ ; its variability metric,  $\Theta$ ; S/RI for the “mass-coral-stress” ecoforecast (see text); the two dominant PCs from each of sea temperature PCA (Fig. 4-9) and extended PCA of  $\Theta$  and other variability metrics (Fig. 4-13); BMU from extended SOM of  $\Theta$  and other variability metrics (Fig. 4-15); and PC1 and PC2 of the equivalent  $T_s$  PCA on MLRF1. Highlighted periods are mass-bleaching summers of 1997 and 1998, a bleaching event in 2005 that was moderated by hurricanes, and severe cold-snap mortality event of January 2010.**

The “mass-coral-stress” S/RI highlights differences in the severity of coral bleaching in 1997 and 1998 vs. that in 2001 or 2005; however, bleaching is also indicated by the S/RI in years when it was not observed at SMKF1 (especially 1999, 2000, and 2007). The figure shows that warm months are generally dominated by  $\Theta$  BMU #1 (moderate, apparently uncorrelated variability in both sea temperature and meteorology),

especially during years when coral bleaching was *actually observed*. This is consistent with the result in Ch. 3, that diurnal insolation (balanced by horizontal convection) is the dominant forcing term during warming periods. A notable exception to this are the weeks of August 25<sup>th</sup> and October 21<sup>st</sup>, 2005, when the BMU switched to #8 and #9, consistent with stronger, variable winds.

During warming periods at both SMKF1 and MLRF1, and especially summers with coral bleaching, the  $T_s$  PC1 for rapid air-sea cooling is near zero, while the PC2 for diurnal insolation is simultaneously enhanced. The 14 d periods containing hurricane landfalls in 2005 are again an exception to this with high  $T_s$  PC1 scores, as are the non-bleaching summers of 1999, 2000, and 2007, despite their high ecoforecast S/RIs. A similar pattern is seen in extended PCA of variability metrics, with high  $\Theta$  PC1 during bleaching summers vs. enhanced  $\Theta$  PC2 for non-bleaching years.

During the 2010 cold-snap, sea temperature data were not available at SMKF1. For reef-crest sites like MLRF1 for which data were available, both the  $T_s$  PCA (bottom two panels of Fig. 4-21) and  $\Theta$  PCA (not shown) were dominated by the EOF associated with rapid air-sea cooling. The PCs for these EOFs were large, but not anomalously so in the context of the previous 20 years of winter extremes. However, a third PC was anomalously high during this period – that for an EOF associated with very large variability in both sea and *air* temperature; this EOF otherwise explained a negligible portion of the overall variability.

SOM showed a similar feature as well. Prior to and following the cold-snap, the  $\Theta$  BMU for MLRF1 (figure not shown) was generally that for rapid air-sea cooling, i.e., similar to unit #9 in Fig. 4-15. During the cold-snap itself, units similar to #9 remained

the BMUs. However, during this period the similarity metric which compares the current pattern with its BMU, known as the *quantization error* for the SOM (Kohonen 1998), was greater than at any other time in the record. This is due to the fact that conditions during January 2010 were sufficiently anomalous that extended PCA and SOM patterns based on the rest of the 25-year record of SEAKEYS data do not contain accurate representations of them. This in itself indicates the severity of the event.

#### **4. Summary**

Anomalous *in situ* sea temperature variability is observed in the FRT which is not consistent with air-sea forcing or the other terms described in the heat budget of Ch. 3. Such events may be related to mesoscale and sub-mesoscale oceanic variability in the Florida Current. Such processes drive both upwelling and cross-shore flows, and have been shown to affect sea temperature at the reef crest (Gramer et al. 2009). In order to identify distinct “events” of anomalous sea-temperature variability, metrics estimated from standard deviations of sliding “top-hat” time windows were developed.

Events were classified in terms of patterns of forcing and regional-scale variability, using principal component analysis (PCA) and self-organizing map (SOM) analysis. Extended PCA and SOM were used to analyze covariability between sea temperature and other coincident time series. Spatial PCA and SOM were used to analyze the covariability between sea temperature and satellite imagery or model fields.

Both PCA and SOM identified events of sea temperature variability that followed increases in wind variability by lags of from 3 to 5 d. PCA and SOM of 14 d frames identified sea-temperature variability events that were not correlated with coincident heat

budget forcing at all. For such events, PCA and SOM were also performed on coincident 1 km synoptic satellite SST imagery surrounding each monitoring site. Distinct patterns of SST associated with such events were identified that suggest anomalous regional-scale ocean circulation; further analysis of these patterns will be the subject of future work.

Periods of sea temperature variability associated with severe coral ecosystem impacts was also analyzed using variability metrics, ecoforecasts, PCA, and SOM. Variability metrics and ecoforecasts based on these metrics provide consistent alerts of sea temperature variability that may impact reef ecology. However, these techniques may also indicate impacts when none are observed, limiting their usefulness for decision-making about coral reef ecosystem management.

PCs for the EOFs and extended EOFs identified in this work provide additional insight into periods of extreme variability when impacts did occur, such as the mass summer coral-bleaching episodes of 1997, 1998, and 2005, and the severe cold-snap of 2010. If they can be calculated in near real-time, i.e., with delays of a few days or less, these PCs may therefore provide a means to improve ecoforecasts also. Automated pattern-matching against the extended SOMs identified above (e.g., Fig. 4-15) can certainly be done in near real-time.

The present chapter demonstrates that both SOM and PCA provide a means to distinguish events where ecological impacts are more likely, based not simply on cutoff criteria, but on multi-day patterns of atmospheric and sea-temperature covariability. Both of these techniques therefore hold promise for improving the accuracy and usefulness of information about the reef thermal environment for coral reef ecosystem management.

## Chapter 5. Conclusions and Recommendations

### 1. Conclusions

The Florida Reef Tract (FRT) is an ecosystem of coral reefs 3-8 km wide, fringing the south and east Florida Shelf. Managing impacts of thermal and other stressors on this large, fragile ecosystem requires reliable information on sea temperature variability. To this end, *in situ* sea temperature and meteorological data were gathered at reef sites in the FRT for over two decades. A heat budget (e.g., Wilson-Diaz et al. 2009) is developed to model near-bottom sea temperature using these data, and anomalous events in the record not well-explained by the heat budget are analyzed.

#### *Sea Temperature Variability and Covariability*

Sea temperature on the FRT varies strongly by site. Geography and topography are important factors. Over two decades of *in situ* hourly measurements for sea temperature, air temperature, and winds were analyzed at diverse sites in the FRT, together with shorter hourly records of barometric pressure, dew-point temperature, and light. To provide additional data germane to sea temperature variability, data were interpolated at each site from a long-term atmospheric reanalysis product, ERAI, for sea-surface downward short- and longwave radiative fluxes, atmospheric specific humidity, barometric pressure, significant wave height, and peak wave period and direction. Empirical adjustments were applied to correct systematic errors in ERAI-derived radiative fluxes and significant wave height, based on *in situ* data comparisons.

Long-term mean and variability in sea temperature and meteorology at these sites were analyzed. Whole-record average sea temperature ranged between 25.8 and 26.9 °C, with no obvious geographic pattern. Variability in hourly mean at very shallow sites near the outer reefs (SEAKEYS sites FWYF1, MLRF1, SMKF1, and SANF1) shows dominant diurnal and annual periods, with diurnal amplitude of order 0.5-1.4 K by season, and annual amplitude 7-8 K. Interannual between year-day variability at these sites is greater, at 10 K. The shorter record of sea temperatures at one deeper fore-reef slope site (LOOE1) show similar annual (8 K) cycles, but a much greater range of diurnal variability (0.8-3.0 K by season) likely due to upwelling processes. Sea temperature at very shallow, flat sites (SEAKEYS sites LONF1 and DRYF1) is also dominated by diurnal and annual cycles but with greater amplitudes in both, 1-2 and 10-12 K, respectively. Interannual between year-day variability at LONF1 is 14 K. Site-specific features include a strong response to winter cold-front passage in the “weather band” (3-42 d period) at LONF1, and variability at the local inertial ( $\approx 27$  h) period at SMKF1.

Finally, only one site analyzed shows a robust interannual trend in its annual mean sea temperature: SMKF1, a site that lies near both the reef crest, and near a large inter-island channel that connects the reef tract with Florida Bay. It is suggested that this long-term warming trend at SMKF1 may be a result of greater cross-shore transport of heat at this site relative to other sites near the reef crest. This may suggest that under climate warming scenarios, this area of the Middle Keys will be more susceptible to thermal stress than other areas of the FRT.

Covariability was evaluated between changes in daily mean sea temperature and other variables including insolation, longwave flux, air temperature change, winds, sea

state, and horizontal sea-temperature gradients. Insolation was generally found to dominate during warmer months; air-sea temperature and moisture content differences play a more significant role during cooler months, and particularly during extreme weather events, such as winter cold fronts, thunderstorms, or occasional easterly atmospheric waves. Cold front passages tend to dominate sea temperature variability in November-April.

However, analysis of covariability also suggests that other forcing mechanisms for sea temperature variability may be at work, mechanisms not directly related to the meteorological or radiative forcing analyzed above. A portion of this unexplained variability on the reef crest and fore-reef slope may be related to oceanic variability – internal waves, eddies, and meanders of the FC. Yet analysis also points out differences in sea temperature variability and covariability between otherwise similar sites, which do not appear to be consistent with these processes. Such differences suggest there is important forcing at smaller spatial scales, depending on details of geomorphology and seafloor topography.

#### *Reef Heat Budget*

To better understand the dynamics that drive the observed sea temperature variability, an ocean heat budget (e.g., Wilson-Diaz et al. 2009) was developed for the FRT, to model near-bottom sea temperature using *in situ* and ERAI reanalysis data. Corrected ERAI data for downward radiative fluxes, humidity, pressure, and sea state were used, together with upward radiative fluxes estimated from *in situ* sea temperature and ERAI sea-state using published empirical relationships. Turbulent fluxes were

estimated using the COARE 3.0a algorithms (Fairall et al. 2003). Surface flux estimates for sites near the deeper ocean compare well with published climatologies.

As expected from covariability analysis, turbulent air-sea fluxes dominate other forcing terms on the FRT at times, for example during doldrums when wind-forced circulation is at a minimum, or during extreme weather events such as winter cold fronts or energetic convective weather. Other forcing mechanisms dominate at times, however: a simple ocean heat budget based on surface fluxes significantly overestimates sea temperature variability at reef sites. Furthermore, these other mechanisms are seen to produce different sea temperature responses at different locations.

At many reef sites, diurnal warm layer evolution is important to lower-frequency sea temperature variability. In addition, water over shallow topography cannot absorb all the short-wave radiation entering the sea surface, and reflectivity and heat exchange at the seafloor at such sites is important for sea temperature evolution there as well. In the present work, a simple sub-model of benthic heat exchange provided important inputs to the overall heat budget at all sites, and especially the shallowest sites.

A satellite SST product with a 20-year record is evaluated together with empirical estimates of surface water transports based on wind and waves, to estimate horizontal advection and “pseudo-Fickian” mixing of heat. These estimates are not found to significantly improve predictability of sea temperature variability at most sites, although they allow successful modeling of some events of variability at 7 d and longer periodicities. In addition, analysis of residuals offers some hope that alternative parameterizations for heat mixing rates (Ch. 3) may provide better results for the heat budget in future, using these or other satellite products.

### *Horizontal Convection*

Ultimately, successful modeling of annual and other cycles in sea temperature at reef sites in the FRT in the present work was found to rely largely on a sub-kilometer scale ocean dynamical process called the *thermal siphon* (Monismith et al. 2006). This process can significantly moderate sea temperature variability for shallow reefs near sloping topography, by exchanging heat between the reef and deeper water nearby. This is especially the case for sites with steep topographic slope (rise/run  $\beta > 0.01$ ).

The importance of horizontal convection has not been previously reported in the coastal waters of the FRT. The present work provides new evidence for its operation on the reef-crest and fore-reef slope of the FRT, based on historical measurements of ocean currents and sea temperature from moorings. Furthermore, the parameterizations for the impact of horizontal convection on reef-crest thermal variability were shown to be consistent with estimates of cross-shore heat exchange from these same data.

The dynamics of sea temperature variability at shallow, high relief sites like coral reefs is a balance between air-sea fluxes, diurnal warming, benthic exchanges, "passive" heat advection, and lateral mixing processes (heat diffusion and horizontal convection). An accurate heat budget balance for reefs relies on site-specific features at small spatial and temporal scales, including horizontal convection, variability in light attenuation, and specific seafloor flux terms. Horizontal convection counteracts surface heating or cooling over sloping sea floor topography: Thermal and momentum balances determine the horizontal convection rate, and mixing of momentum and density gradients limits it.

### *Applications to Remote Sensing*

Remote monitoring of thermal stress on individual reefs can be greatly improved using the present heat budget model. Quantifying the effects of seafloor reflection, cross-reef advection and mixing, and horizontal convection requires detailed information on seafloor topography and bottom type. When high-resolution bathymetry is accounted for adequately, the reef heat budget accurately reproduces annual- and shorter-period sea-temperature variability on individual coral reefs. The resulting heat budget can successfully model summer warming, as well as extreme cold weather like that in early 2010 in the FRT.

This result is shown to be robust, even when *in situ* data are not used in the heat budget. Similar heat budget accuracy was demonstrated when input data consisted of only satellite and model data (MISST 9 km SST and ERAI). Examples of these results are shown in Fig. 3-10 and Fig. 3-11. For these results, it is worth noting again that no additional tuning or data corrections were performed beyond those applied to the original budget based on *in situ* data.

The satellite- and model-derived heat budget accuracy suggests that the scope of application for the heat budget model described in this work extends beyond sites where long-term records of *in situ* data have been gathered. In particular, at the many protected and other coral reef sites around the world where *in situ* sea temperature and other data are available only from infrequent process studies or shorter-term monitoring programs, the requirements are only that seafloor characteristics and regional oceanography are known, and that sufficient *in situ* data exist to tune the heat budget model and its inputs. Products based on this reef heat budget may ultimately provide researchers and resource

managers with “now-casts” and short-term forecasts of sea-temperature variability at infrequently visited reef sites elsewhere in the world. Expansion of this research to other geographic regions, both within and outside of the Florida Keys, is currently planned.

#### *Analysis of Anomalous Events*

Finally, after all terms in the present heat budget have been accounted for, there are still intermittent periods of unusual sea-temperature variability in these records that are not adequately explained by the heat budget. Some of these events appear to be attributable to extreme atmospheric forcing that is not well modeled by existing methods for estimating air-sea flux, e.g., tropical weather events like those in 2005. Some of these anomalous short-duration events may also be due to small-scale convective weather during the Florida rainy season, or to small-scale ocean heat advection and mixing, not adequately represented in the data used by this study. Future improvements in both atmospheric reanalysis and in high-resolution ocean modeling of this region would clearly be of benefit in examining these sources of variability.

Events of anomalous variability are observed in any case which are not coincident with any observed atmospheric extremes, and yet are more persistent than would be suggested by the operation of smaller-scale dynamical processes such as horizontal convection. A substantial portion of these events – approaching 80% in the analysis presented here - are related to mesoscale and sub-mesoscale oceanic variability, such as internal waves, strong frontal gradients, or eddies and other instabilities in the Florida Current. Such processes drive both upwelling and cross-shore flows over the reef crest, and have been shown to affect sea temperature at the reef crest (Gramer et al. 2009).

In order to identify distinct incidences or “events” of anomalous sea-temperature variability in the *in situ* time series, variability metrics estimated from standard deviations of sliding “top-hat” time windows were developed for sea and air temperature, as well as wind speed and direction (vector variability). In order to classify those events in terms of patterns of forcing and regional-scale variability, two methods for modal or cluster analysis were used. Principal component analysis (PCA) and self-organizing map analysis (SOM) were each applied to “data vectors” consisting of 1, 14, and 91 d “frames” in the hourly variability metrics.

PCA is widely used to analyze variability in oceanographic data, whether one-, two-, three-, or four-dimensional. SOM is now an increasingly accepted method of analyzing patterns of variability in oceanographic data as well. After appropriate normalization, both PCA and SOM identified events of sea temperature variability that followed increases in wind variability by lags of from 3 to 5 d. PCA of 14 d frames further identified sea-temperature variability events that were not correlated with coincident atmospheric variability at all; analysis of 14 d frames with SOM also confirmed both patterns. For events of anomalous variability uncorrelated with heat budget forcing, PCA and SOM were also performed on coincident 1 km synoptic satellite SST imagery surrounding each monitoring site. Distinct patterns of SST associated with such events were identified that suggest anomalous regional-scale ocean circulation; further analysis of these patterns will be the subject of future work.

## 2. Significance of the Research

The coral reefs of Florida represent a precious natural resource for their biodiversity and their contribution to local economies: income from reef-related tourism in Florida Keys National Marine Sanctuary (FKNMS) alone was conservatively estimated at \$1.2 Billion per annum in 2002 (Causey 2002), while annual reef-dependent revenues over the entire FRT were estimated at over \$6 Billion during the same period (Johns et al. 2001; Johns et al. 2004). However, many questions remain unanswered concerning the physical oceanography in the FRT and its impact on the FRT ecosystem (e.g., Porter and Porter 2002). Answers to these questions will be crucial, if government authorities and commercial interests are to exercise more informed, effective stewardship and use of this fragile ecosystem (Lee et al. 2002; Keller and Causey 2005). Identifying the patterns of thermal variability and its dominant forcing are both necessary in order to understand better the ecology of coral reefs (Keller et al. 2009), and to predict potential impacts on reefs from climate change and shorter-term anthropogenic influences.

### *Monitoring of Ecological Impacts on Corals and Fisheries*

Berkelmans et al. (2004), Manzello et al. (2007a; 2007b), Lirman et al. (2011), and others have found that episodes of anomalous, multiday sea temperature variability on or near the reef crest may play a significant role (either positive or negative) in modulating thermal stress on corals, their endosymbionts, and other reef organisms.

Manzello et al. (2007b) have shown that rapid cooling events associated with tropical cyclones appear to benefit corals in the FRT and elsewhere, by moderating warm-water thermal stress. The heat budget model provides a context for understanding

the physical processes underlying this effect. Such cooling events are readily identified in the *in situ* sea temperature records; their causes may be attributed to combined effects of reduced insolation, wind-driven transport or mixing, mixing or transport due to surface waves, and increased water depth. Improvements to the heat budget model, particularly with respect to surface waves, will allow these relative contributions to be quantified, and the impact of storm-related cooling to be estimated on reefs that are not directly monitored by *in situ* data.

Thermal extremes within the FRT characterized by the present study have also caused severe, widespread mortality of corals (e.g., Lirman et al. 2011) and other marine organisms there. More moderate variability in sea temperature also serves as a control on the growth rate of reef-building corals (e.g., Cantin et al. 2010). Limits on coral growth can be important for reef viability, for when corals are unable to grow and excrete carbonate structure at an adequate rate, reef systems will begin to degrade due to a variety of natural processes. Longer-term patterns of sea temperature variability on reefs also trigger spawning of corals and other organisms. Prevailing mean sea temperature conditions the settlement success of organisms after spawning as well – including corals and other invertebrates, and commercially important or protected reef fish species.

#### *Cross-shore Fluxes, Upwelling, and Land-Based Sources of Pollution*

Several processes are identified in this work as driving sea temperature variability on Florida reefs: cross-shore advection and mixing at multiple scales, horizontal convection, benthic water exchange, and upwelling. It should be noted that all of these processes may do more than merely condition the thermal environment of coral reefs. They can also change the availability of reproductive materials during spawning and

settlement (e.g., Sponaugle et al. 2005; Criales et al. 2007), of nutrients for photosynthesis and respiration (James and Barko 1991; Hitchcock et al. 2005), and of prey for filter feeding by corals and other reef organisms (Monismith et al. 2010). Just as the overall heat budget provides a better understanding of the reef thermal environment, quantifying these smaller-scale dynamic processes can also improve estimates of loading for nutrients and organic or inorganic particulates (e.g., Leichter et al. 2003).

Episodic sea temperature variability itself has also been found (Leichter et al. 1996; Leichter et al. 1998; Leichter and Miller 1999; Leichter et al. 2005; Davis et al. 2008; Gramer et al. 2009) to be an appropriate indicator of water flux across the reef slope and the reef crest. Larger variability can be coincident with passage of eddies offshore (Gramer et al. 2009), and with shoaling of internal waves (e.g., Davis et al. 2008). Allochthonous (i.e., far-field) water flowing across a reef system may also bring with it nutrient fluxes, either from inshore coastal waters or deeper waters offshore.

The value of having one readily measured physical variable, sea temperature variability, as an indicator for upwelling and cross-shore fluxes can be seen in the short-term biological productivity changes observed by Gramer et al. (2009) over several years to coincide with sea temperature variability at SEAKEYS reef-crest sites. Where sea temperature is measured with sufficient frequency, the heat budget allows variability due to atmospheric forcing to be accurately accounted for. Signals for upwelling and other processes then stand out in the sea temperature record. Furthermore, sea temperature at and below the thermocline in the Straits of Florida bears a linear relationship with concentrations of dissolved nutrients  $\text{NO}_2$ ,  $\text{NO}_3^-$ , and phosphates (e.g., Leichter et al. 2003; Hitchcock et al. 2005; T. P. Carsey pers. comm.).

Quantifying carbonate dynamics on reefs is similarly dependent on rates for advection and horizontal mixing of “baseline” offshore ocean waters. Furthermore, rates of exchange of CO<sub>2</sub> between the ocean and atmosphere depend on surface temperature and its variability (e.g., Manzello et al. 2012). Episodic near-surface cooling that cannot be related to surface forcing by a heat budget may therefore represent a proxy for estimating both nutrient and carbon fluxes onto Florida reefs and coastal areas, from upwelling, cross-shore circulation, and other processes.

Cross-shore flows in the FRT also transport reproductive material – eggs, larvae, planulae – to appropriate habitats on or near the reef (Yeung et al. 2001; Sponaugle et al. 2005). Such connectivity is a critical link in the long-term viability of reef ecosystems in Florida and elsewhere; identifying the frequency and spatial extent of cross-shore flows from sea temperature measurements and the heat budget model may be a significant aid in the biological monitoring of reef ecosystems.

Finally, cross-shore flows at the reef-crest may transport land-based sources of pollution from inshore, and river plumes, surface oil, or other contaminants from offshore. It is possible to identify many of these cross-shore transport events in the *in situ* and remotely sensed sea temperature records. However, in order to do so with accuracy, all other significant sources of ocean heating must be accounted for. The innovations in the heat budget model presented here may therefore ultimately have much broader significance for the management of coastal ecosystems and communities than solely in the monitoring of coral reef thermal stress.

### *Impacts of Climate Change*

Our current understanding of the global air-sea climate system comes from coupled numerical models at regional and larger scales, using predominantly remote-sensing products at kilometer scales and greater. To downscale from regional long-term or climate-scale forecasts to coral reef ecosystem impacts means accounting for physical processes at all scales – from global systems to individual coral communities. The spatial and time resolution of the best available models and remote sensing products for the coastal ocean are currently insufficient to achieve this level of downscaling (Fig. 5-1).

The heat budget model has been successful at reproducing sea temperature extremes at the seafloor in diverse sites in the FRT, using only remotely sensed and reanalysis data (Ch. 3). This suggests that it captures the essential air-sea and hydrodynamics that drive the physical relationship between larger-scale forcing and reef sea temperature. An important test of this conclusion will be to apply the heat budget model to historical 20<sup>th</sup> and early 21<sup>st</sup> Century runs of models at still larger scales – climate system models. A statistical comparison of the climate-forced heat budget model output with observed reef sea temperature would be done in the context of the errors in the climate-forcing models relative to observed sea-surface forcing.

This should provide needed context to better understand historical impacts of sea temperature variability within the FRT (e.g., Manzello et al. 2007a; Manzello et al. 2007b). It may also provide further insight into the causes of observed interannual temperature variability there. Ultimately, however, the result may also provide the climate, oceanographic, and management communities with some confidence that this heat budget model can in turn reproduce the potential impacts of *future* climate scenarios

on reef-scale thermal stress as well, both within the FRT and in other fragile reef and coastal environments.

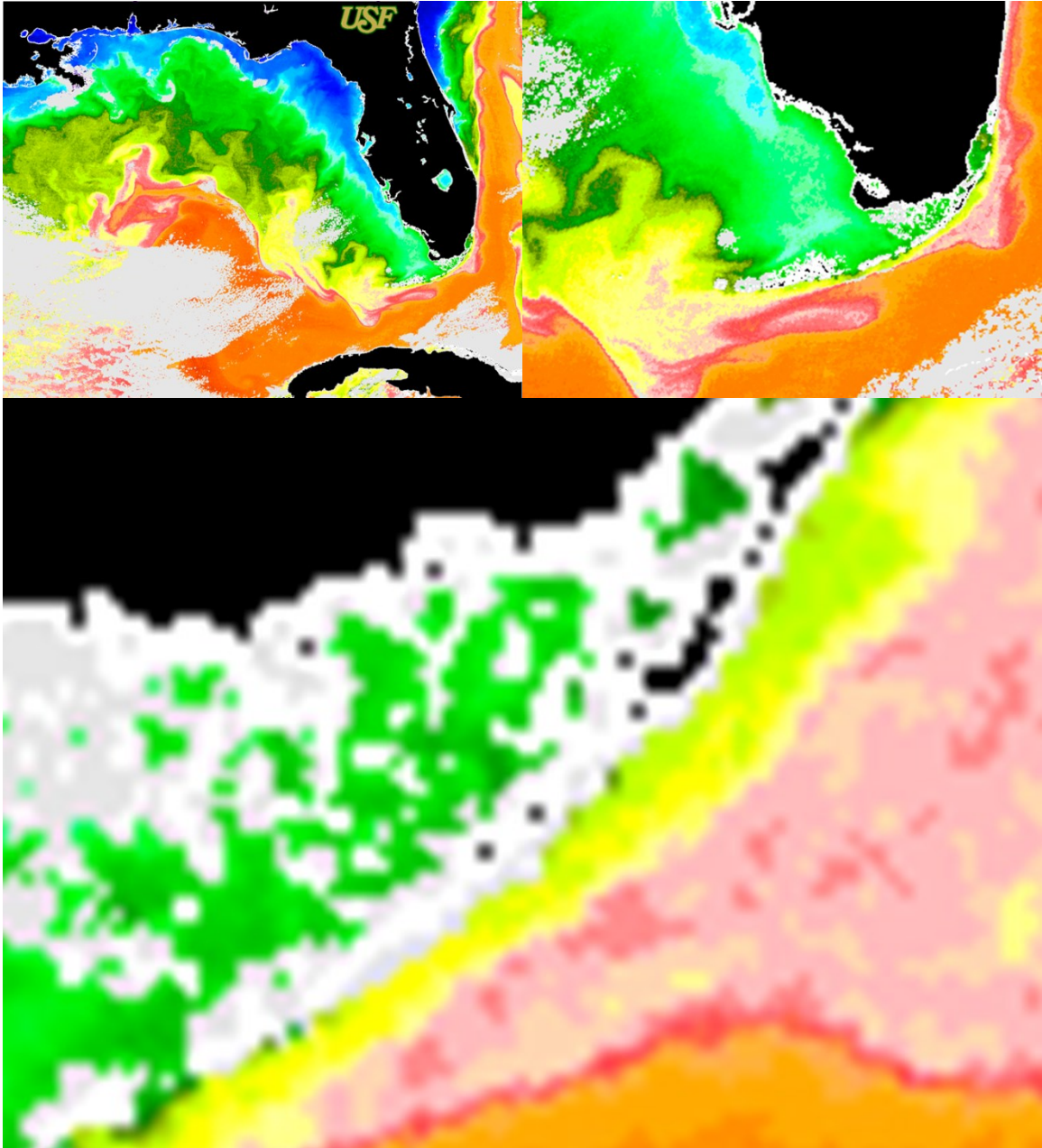


**Figure 5-1: Increasingly magnified satellite SST image of the Gulf of Mexico, south Florida waters, and the Upper Keys portion of the FRT, highlighting limitations of the best available larger-scale data sets, in understanding the complex environment of the FRT. These images are 1 km resolution and are available multiple times daily subject to cloud cover. Understanding the impact on coral reefs of climate-scale variability using models with horizontal resolutions  $\sim 10^2$  km and time resolutions  $\sim 10^1$  d represents a still greater challenge.**

*Connectivity and Other Implications for Management*

The rigorous analysis of sea temperature and forcing on the reef-crest in the present work has led to a better understanding of air-sea and ocean dynamics there – and these complex dynamics are themselves of more than just physical interest. For the reef crest is not only subject to a wide range of dynamical processes, but is also in many ways the most *ecologically* dynamic – and sensitive – area of the FRT reef ecosystem. First, the reef crest lies at the “front line” of the continental shelf. At the crest have historically been found the greatest concentration of massive and branching reef-building corals anywhere in the FRT, maintained in a high-light environment thanks to the shallowness of the crest topography and offshore promontories.

More recently, the reef crest in the FRT has experienced some of the most precipitous losses of live coral cover. Furthermore, coral communities here are most likely to receive episodic natural pulses of nutrients from deeper waters offshore (together with corals on the shelf-break or reef slope, zone (iv) above), and to exchange genetic materials with the waters of the chain of Western Boundary Currents (Loop, Yucatan, and Caribbean Currents, Mesoamerican gyre, and Caribbean Inflow) that lie upstream of the FRT.

With respect to genetic diversity, there is strong evidence linking vortex-topography interaction and other features of circulation with the settlement and survival of larvae from reef fishes, corals and other invertebrates in the FRT (Yeung et al. 2001; Sponaugle et al. 2002; Sponaugle et al. 2005; Fiechter et al. 2008; Grorud-Colvert and Sponaugle 2009). These relationships between oceanography and reef ecology in turn may have strong impact on the design and management of protected areas in and around

the FRT. Clearly, the dynamics at the FRT reef crest are worthy of study for many reasons.

One of the primary aims of this research project has been to construct and validate automated information systems to recognize likely *impacts on reefs and related ecosystems*, using the near real-time observations of sea temperature, chlorophyll *a*, and ocean currents available within the FRT. The results of this physical oceanographic research will improve the accuracy and timeliness of products produced by CHAMP and related projects, e.g., NOAA Coral Reef Watch. Among the primary aims of both CHAMP and Coral Reef Watch is to provide timely, actionable information, such as ecoforecasts, to managers of protected resources, and to other stakeholders among the research community, commercial interests, and the public. Many ecoforecasts are already provided by CHAMP to scientists and managers for the FKNMS, based primarily on point data (both *in situ* and remotely sensed). The broader spatial perspectives provided by high resolution SST, chlorophyll *a* and other satellite data, together with a better understanding of the relative magnitude of forcing terms for sea temperature and thermal stress at disparate sites in the FRT, are expected to improve significantly the sophistication and predictive power of these ecoforecasts.

#### *Improved Regional Modeling*

The results described in the present work will contribute to the more effective management of fragile coral reefs and their associated fisheries, in the context of anthropogenic and other near- and far-field influences. However, the occasional events not well explained by the heat budget also show that further study is warranted. Analysis in this work of higher-frequency sea temperature variability, not well described by the

heat budget, has sought to characterize the likely forcing mechanisms associated with that variability. Additional application of the methods described in Ch. 4 holds some promise in furthering the understanding of reef sea temperature variability.

Ultimately, a better understanding of the physical stressors on reefs will require a quantitative characterization of circulation and heat exchanges there. This quantitative picture may be achieved for the FRT in future if the available remote sensing data can be combined with ocean surface current observations, e.g., the University of Miami's High-Frequency Wellen Radar (Shay et al. 2007), and with targeted *in situ* oceanographic observations from moorings or shipboard surveys. These ongoing direct measurements at diverse sites must be assimilated into numerical models of the coupled air-sea dynamics over reefs. Importantly, such modeling will need to be done at temporal and spatial resolutions sufficient to model those features of coastal ocean circulation and heat exchange that are likely to affect the reef and fisheries ecology.

The current research provides validation for high-resolution numerical ocean models already developed for the FRT (Fiechter and Mooers 2003; Fiechter et al. 2008; Kourafalou et al. 2009). The analysis of historical records presented here also provides a point of comparison for other historical direct ocean measurements of the region. This work improves the current understanding of the inherent time and spatial scales of variability and forcing for sea temperature that are significant to corals and other reef organisms. These results will be of use in determining the sufficiency and statistical coherency of existing and planned monitoring programs, as well as efforts to preserve and enhance the resilience of these ecosystems. Recommendations are made below for future observations, analysis, and modeling efforts in the region.

### 3. Recommendations for Future Research

#### *Reef Heat Budgets*

One proposed direction for future research into reef heat budgets is to analyze *in situ* data with higher sampling frequencies (10 min or less), and at fixed sites along a cross-shore section including the reef crest. This can provide an estimate of errors introduced into turbulent flux calculations by the use of hourly means, and into the advection and mixing terms by the use of km-scale SST data (see discussion in Ch. 3). The aim of such error estimates would be to improve the modeling of higher-frequency sea temperature variability near the reef-crest.

There are multiple years of 10 min-average wind speed and direction measurements available from the SEAKEYS archive, as well as limited 10 min-average tide height data. However, these archives do not include higher-frequency measurements of sea or air temperature or specific humidity. Similarly, there is relatively little hourly or higher-frequency *in situ* data for sea temperature at sites spanning the reef-crest.

Targeted field studies in the FRT could be necessary for this purpose. However, there are similar studies currently ongoing in the Great Barrier Reef in Australia. In addition, the reef-monitoring stations of the NOAA AOML ICON network in the Caribbean and Pacific may provide observations averaged at 10 min or higher intervals, for use in estimating of turbulent flux errors due to higher-frequency variability.

#### *Region-wide Applications*

Geographic expansion of the heat budget to all coral reef areas of the FKNMS is another important direction for future work. In addition to the SEAKEYS monitoring stations, the FKNMS (see Fig. 1-1) has for years had a program to deploy self-contained

benthic sea temperature sensors in those parts of the FRT that lie within the FKNMS. The principal investigator for this program was Dr. J. Harold Hudson, and a statistical analysis of the time series data from these thermistors was published by Moulin (2005).

Many of the FKNMS benthic thermistors were deployed in the back-reef and Bridge Channels, rather than at the reef crest. Comparing these data with heat budget model outputs for these sites should allow for the calibration of the heat budget model parameters to conditions within different regions of the FKNMS, including those areas where SEAKEYS data are limited, such as back-reefs.

These data may also be compared statistically to collocated satellite SST (see Ch. 3 and Ch.4). This will characterize geographic differences in the correlation between SST and *in situ* sea temperature, and differences in modes of high-frequency (2-72 hour period) sea temperature variability, between the back-reef and the reef crest. Such analysis would be useful to refine the representation of cross-shore advection between these distinct zones, particularly during periods of high sea temperature variability.

Finally, expanding the heat budget model to deeper reef systems, such as those within the Flower Garden Banks National Marine Sanctuary or the Hawaiian Islands, will necessitate incorporating an additional term for mixed-layer deepening. In reef regions where seafloor topography is less complex than that in the FRT, hydrodynamic models may provide useful estimates of mixed-layer depth and sub-thermocline temperature needed in this term. A new operational HYCOM model for the Gulf of Mexico, for example, features a 2 km horizontal resolution and data assimilation of atmospheric and sea-surface temperature fields. Similar ocean modeling efforts are now underway for other regions with deeper reefs.

### *Improving Ecological Forecasts*

The results presented above are expected to provide considerable benefit to managers, by enhancing the remote monitoring of the FRT for ecological impacts. The ocean and air-sea dynamics encapsulated in the heat budget model are expected to apply to other regions within and outside of the FRT as well. This can ultimately help to improve the monitoring of impacts from thermal extremes in more remote coral reef ecosystems of the world.

One way to achieve this goal is to apply the heat budget for the improvement of ecological forecasts. NOAA AOML's ICON project utilizes expert systems such as the "onshore flux" ecoforecast described in Ch. 4. These rule-based systems process, integrate, and analyze multiple environmental data sources, in order to automatically assess extremes or potentiating patterns in those data. The primary purpose of ecoforecasts is to alert managers, field researchers, and other interested parties in near real-time, of possible ecological impacts in the environment.

The reef heat budget will be used to improve "thermal stress" and "coral bleaching" alerts and products for coral reef managers and the public. Providing such analysis and assessment to managers in "near real-time" requires outputs from the heat budget daily, and thus ongoing daily processing of meteorology and sea temperature. This will require use of operational data sources in place of the reanalysis and weekly composite data used in this research.

CFSR is the NOAA NCEP Climate Forecast System Version 2 (CFSV2), a global, reliable, complete atmospheric data set (Fig. 5-2). In addition to daily updated outputs, the CFSR provides a long record of historical data. Such long records of forcing variables are important in evaluating the contribution of bias and RMSE in CFSR to the

heat budget error. Analysis may also suggest empirical adjustments to CFSR forcing to improve comparison of heat budget outputs with historical data. For advection and mixing, synoptic satellite and regional-scale ocean modeling outputs are available in near real-time. However, issues identified by the present work with existing SST and model datasets suggest that further research may be needed to provide reliable, near real-time estimates of sea temperature gradients and Laplacians for an operational heat budget.

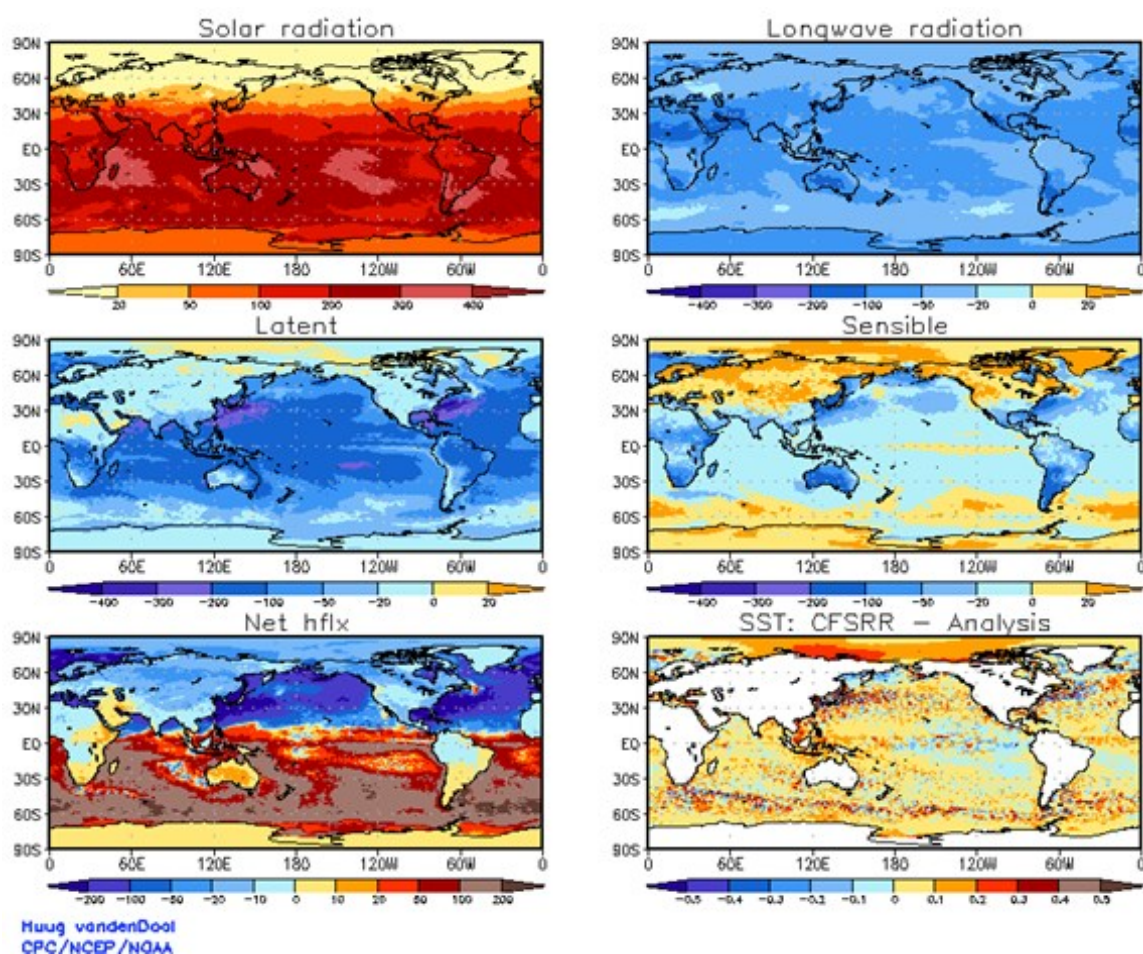


**Figure 5-2: Monthly mean sea/land-surface fields from the NOAA Climate Forecast System Reanalysis and Reforecast project (CFSRR) for December 2010. Panels include: insolation and longwave radiation, latent and sensible heat flux, net surface heat flux, and forecast SST. The Climate Forecast System and its reanalysis may provide near real-time forcing data necessary for operational daily heat budget models utilizing the methods of the present research.**

### *Ocean Modeling*

Another potential next step utilizing the present work is the improvement of hydrodynamic ocean models, e.g., in the modeling of upwelling, Bay- and river-water intrusions through tidal channels, and other sub-regional scale events within the FRT. Current ocean hydrodynamic models do not take sufficient account of the complex topography of the FRT's barrier reef system. As a result, they tend to overestimate the importance of larger-scale cross-shore advection of heat (Fig. 2-2). A suggested next step in ocean modeling for linear reef systems like the FRT would be to evaluate high-resolution bathymetry for these areas using metrics other than the areal average. For example, water depth might be assigned to each model grid-point based on the minimum or the 25<sup>th</sup> percentile of depth for that rectangle within the higher-resolution bathymetry.

Current gridded models are not of sufficient horizontal resolution to effectively model the horizontal convection process, and may not effectively model the importance of seafloor reflectivity, nor of time-varying light attenuation in the water column. A further contribution of the present work to improved modeling should be to develop parameterizations for horizontal convection which are computationally efficient. Additionally, for many coastal areas, it may be useful to assimilate satellite ocean color or other data to improve the modeling of radiative transfer within these shallow waters.

### *Offshore Processes*

Evidence in the present work and many cited references has suggested that vortical instability (i.e., meanders of the FC, eddies, sub-mesoscale vortices) plays a role in forcing environmental variability on reefs in the FRT. A significant question raised by this is whether direct observations of sea temperature, ocean currents, and other water

properties offshore of the FRT can help to explain reef thermal variability that is not well represented by the heat budget of Ch. 3 or by the other techniques described in Ch. 4. Data on velocity, vorticity, and deformation fields derived from the WERA dataset, for example, may be analyzed to gain insight into prevailing circulation offshore of the FRT. One approach would use methods described in Ch. 4, “extended spatial” PCA and SOM, on WERA data to analyze these remotely sensed currents in the context of *in situ* sea temperature variability events.

This approach has been applied to the WERA surface currents and SEAKEYS data for April-September (AMJJAS) of 2009 and AMJJAS of 2010 already. These quality-controlled hourly ocean surface currents (Fig. 5-3a) provide what is in effect “unfiltered” information on circulation patterns associated with sea temperature variability anomalies. PCA and SOM modes associated with these information-rich fields are difficult to interpret. Derived fields such as horizontal divergence, relative vorticity (Fig. 5-3b) or the Okubo-Weiss parameter (Fig. 5-3c; see Parks 2008 for a description) extract information from these hourly fields that is likely to be more useful in characterizing cross-shore heat exchanges and upwelling.

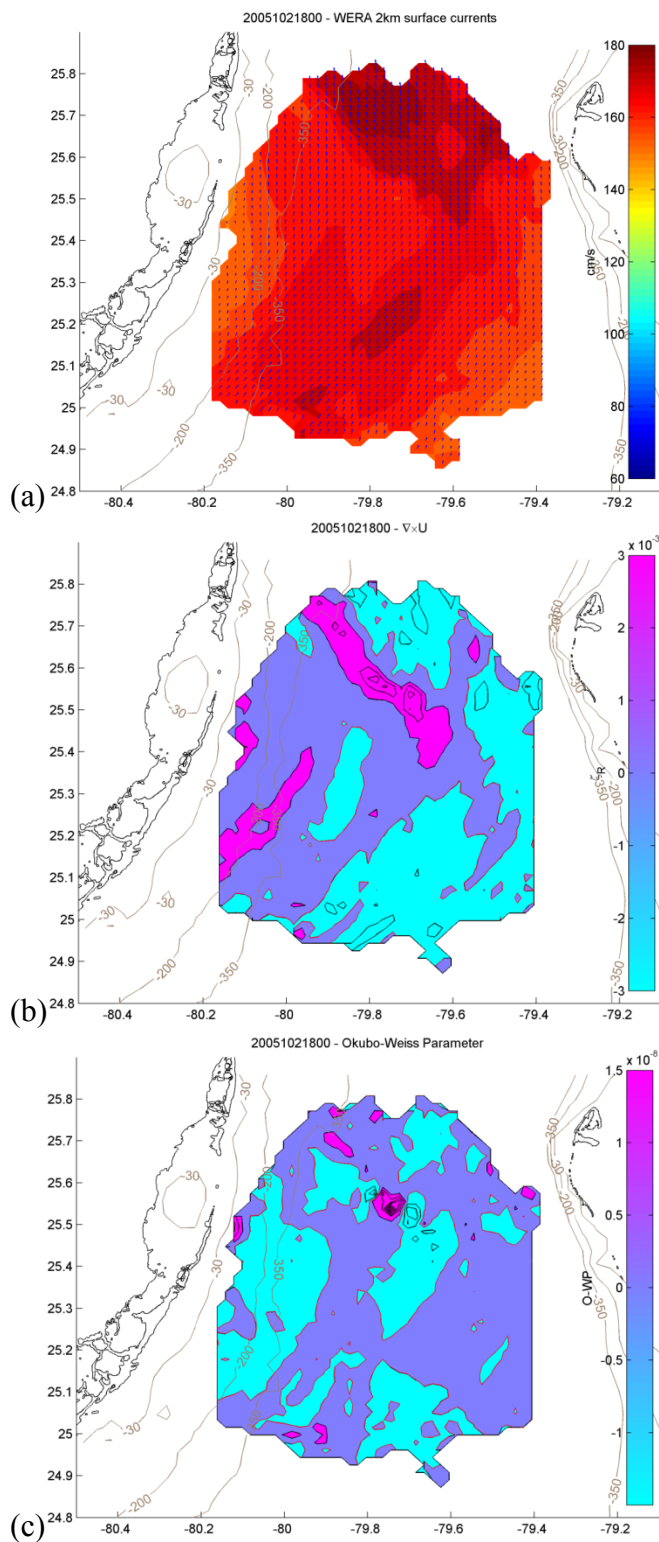


**Figure 5-3: RSMAS HF WERA data field for the Straits of Florida offshore of FWYF1 (black star), April 12<sup>th</sup> 2005 18:00 local time: (a) quality-controlled surface current speed (color) and direction (arrows); (b) curl of this velocity field; (c) Okubo-Weiss Parameter (Parks, 2008) for this field.**

The complexity of patterns in these fields may be reduced still further, to straightforward time series of coefficients, using wavelet analysis (see e.g., Fig. 2-11 above; Grinsted et al. 2004) in wavenumber or frequency space. Extended PCA or SOM is applied to vectors containing, e.g., sea temperature and the most significant wavelet coefficients. Temporal aliasing arose in the extended PCA and SOM of time series described in Ch. 4 due to the delimiting of time "frames" for analysis. To eliminate this aliasing analysis should focus on periods of extreme variability. Such events can be characterized based on their persistence and likely lag time with respect to suspected forcing. Frames are chosen of sufficient length to accommodate major events and their likely precursors, with each frame centered on the time of peak variability.

This line of research may lead to conclusions regarding vortical forcing offshore of the current WERA sites in the northern FRT. An important further consideration would then be whether these conclusions could also provide information on thermal variability elsewhere in the FRT, such as the reef-crest of the Middle or Lower Keys. Several methods have been suggested to describe the incidence and scale of vortices and similar disturbances near the reef crest of the Keys, and how they may relate to observed circulation further north. These methods include time-dependent wavenumber power spectra based on satellite imagery; analysis of historical direct ocean current observations (by other HF radar installations and other methods) over other areas of the FRT; additional targeted *in situ* observations of ocean currents in the Florida Keys; or the derivation of dynamical fields over the whole FRT using sequential satellite imagery (maximum cross-correlation, for example). Such methods might allow statistical

comparisons to be made between patterns of circulation in the WERA footprint and those in other areas of the FRT.

Techniques for identifying meanders of the frontal zone of the FC, in particular, are another area of research that may provide useful information for the management of ecosystems and fisheries in the FRT. As suggested above, the proximity of the FC front to the FRT plays a role in forcing variability on the fore-reef slope and reef-crest – including fluxes of heat, reproductive materials, nutrients and carbonates, and anthropogenic pollutants such as oil. Improved information on that proximity in different areas of the FRT could also have other applications as well – for fishing interests, research and monitoring efforts, and public safety.

Frontal analysis of synoptic satellite imagery is one approach to detecting FC meanders, e.g., by calculating intensity gradient fields. Such analysis could be confirmed by “process studies” using additional space- or ground-based radar observations of surface ocean currents, or by the use of geostrophic currents derived from satellite Sea Surface Height anomaly (SSHA). Another approach might involve statistical analysis of indirect indices for FC state, such as the Florida Current transport time series at 26.5°N (Di Nezio et al. 2009), and the latitude and longitude of the greatest northern extent of the LC in the eastern Gulf of Mexico (EM Johns pers. comm.; DB Olson pers. comm.).

The techniques of GHSOM and ESOM may prove useful to explore patterns in such spatial data. The number of units or “modes” in a standard SOM is arbitrarily selected by the researcher. A GHSOM (Dittenbach et al. 2002) on the other hand uses metrics of data variance within and across units, called geometric quantization errors, to

expand SOM maps adaptively in three dimensions during training. At each stage of training, the GHSOM may either add a row or column to the current map layer, may add a new layer of units to “break out” modes of variability within a single existing unit, or may do neither and simply continue to train the units of the existing layer with the new data. A GHSOM was profitably employed by Liu et al. (2006) to analyze modes of spatial variability in multi-day mean SST fields on the WFS. This technique has already been applied to a combined cluster analysis of raw data from both *in situ* sea temperature and forcing terms for several SEAKEYS stations, and will be repeated with anomaly data based on the climatological heat budget results for these stations.

An Emergent SOM (ESOM; Ultsch and Roske 2002) by contrast, uses fixed but very large SOM maps – generally containing more units than there are data vectors to be analyzed. Training an ESOM map against all available data allows patterns to emerge in a natural way, in effect doing a non-linear two-dimensional cluster analysis with no explicit constraints on the number of clusters. This method has been successfully applied to predict sea level at a coastal station based on observed atmospheric forcing (*ibid.*), and more broadly in complex problems of medical diagnosis and related fields. As part of ongoing work, beyond the scope of the present study, an ESOM has been constructed to do characteristic analysis of anomalies in the heat budget for station MLRF1.

Quantifying the impact of circulation patterns on the biogeochemical environment throughout the FRT will ultimately require data on the properties of watermasses associated with those different patterns. Waters carried over the reef from Florida Bay or from the WFS, or autochthonous waters of the FRT mid-shelf itself each have their own

characteristic seasonal thermal and chemical properties. The same is true of waters carried into the FRT from offshore – continental slope water, surface FC water, and sub-thermocline water in the Straits of Florida.

Field measurements are needed to properly characterize watermass properties. However, dissolved nutrient and CO<sub>2</sub> concentrations measured in far-field and near-field waters during different seasons may be used as end-members for mixing within the FRT. Methods for tracking the surface expressions of inherent water properties using satellite imagery exist in the literature, and their improvement is the subject of active research. Combining such techniques with the analysis of circulation patterns described above may provide a wealth of biogeochemical information helpful for the management of coral reefs, seagrass fields, and the inshore communities served by these natural resources.

## Appendices

### Appendix I. Online Data and Codes

All data and algorithms used in the preparation of this work are publicly available.

Listed below are online sources for all data and code, verified as of March 2012:

**Table A-1: Online sources for data and codes used in this work.**

Air Sea Tools for MATLAB <sup>®</sup> .	<a href="http://woodshole.er.usgs.gov/operations/sea-mat/air_sea-html/">http://woodshole.er.usgs.gov/operations/sea-mat/air_sea-html/</a>
AOML CHAMP/ICON <i>in situ</i> and integrated data (2001-2013).	<a href="http://www.coral.noaa.gov/data">http://www.coral.noaa.gov/data</a>
AVHRR, USF AVHRR weekly SST (1993-2012)	<a href="http://www.imars.usf.edu/">http://www.imars.usf.edu/</a>
CORE.2 Global Air-Sea Fluxes (1949-2006)	<a href="http://dss.ucar.edu/datasets/ds260.2/">http://dss.ucar.edu/datasets/ds260.2/</a>
AOML CHAMP/ICON Ecoforecasts Toolkit, and Reef Heat Budget codes	<a href="http://www.coral.noaa.gov/research/">http://www.coral.noaa.gov/research/</a>
ERA-Interim, ECMWF Reanalysis – Interim (1979-2013)	<a href="http://dss.ucar.edu/datasets/ds627.0/">http://dss.ucar.edu/datasets/ds627.0/</a>
FKEYS and GoM HYCOM (2003-2013).	<a href="http://www.hycom.org/">http://www.hycom.org/</a>
NARR, NOAA NCEP North American Regional Reanalysis (1979-2013)	<a href="http://dss.ucar.edu/datasets/ds608.0/">http://dss.ucar.edu/datasets/ds608.0/</a>
NDBC, C-MAN/SEAKEYS quality-controlled station data (1987-2013)	<a href="http://www.ndbc.noaa.gov">http://www.ndbc.noaa.gov</a>
NGDC 3" CRM, NOAA NGDC 3 arc sec. Coastal Relief Model bathymetry	<a href="http://www.ngdc.noaa.gov/mgg/coastal/crm.html">http://www.ngdc.noaa.gov/mgg/coastal/crm.html</a>
NOCS Surface Fluxes v2.0 (1973-2009)	<a href="http://www.noc.soton.ac.uk/noc_flux/noc2.php">http://www.noc.soton.ac.uk/noc_flux/noc2.php</a>
OAFflux v3 (1985-2011), ISCCP (1983-2009)	<a href="http://oafux.whoi.edu/data.html">http://oafux.whoi.edu/data.html</a>
Seawater Library for MATLAB <sup>®</sup>	<a href="http://www.cmar.csiro.au/datacentre/ext_docs/seawater.htm">http://www.cmar.csiro.au/datacentre/ext_docs/seawater.htm</a>
SOM Toolbox for MATLAB <sup>®</sup>	<a href="http://www.cis.hut.fi/somtoolbox">http://www.cis.hut.fi/somtoolbox</a>
TMD, Tide Model Driver MATLAB <sup>®</sup> toolbox	<a href="http://www.esr.org/ptm_index.html">http://www.esr.org/ptm_index.html</a>
TOGA COARE 3.0a air-sea flux algorithms	<a href="ftp://ftp.etl.noaa.gov/users/cfairall/bulkalg/cor3_0/matlab3_0">ftp://ftp.etl.noaa.gov/users/cfairall/bulkalg/cor3_0/matlab3_0</a>
WW3, NCEP WaveWatch III.	<a href="http://polar.ncep.noaa.gov/waves/wavewatch/wavewatch.shtml">http://polar.ncep.noaa.gov/waves/wavewatch/wavewatch.shtml</a>

## Appendix II. Ground-truth Comparisons and Seasonal Statistics

**Table A-2: Results of robust linear regressions between data products used in the heat budget and *in situ* comparison data (see Chs. 2 and 3). Numbers shown are, in order, *bias, slope, RMSE*. ERAI for RSMAS radiative comparisons was interpolated to FWYF1, 1 km weekly composite AVHRR data for  $T_s$  gradient comparisons were interpolated to MLRF1, all other data are for station indicated.**

<i>Statistical Comparison</i>	<i>Winter (JFM)</i>	<i>Spring (AMJ)</i>	<i>Summer (JAS)</i>	<i>Autumn (OND)</i>	<i>Overall</i>
RSMAS vs. ERAI $Q_{SW}^I$	7.6, 0.64, 2.8	19, 0.27, 2.1	13, 0.42, 2.6	8.8, 0.46, 2.0	7.6, 0.68, 3.2 MJ/m <sup>2</sup> /d
RSMAS vs. adj. $Q_{SW}^I$	7.0, 0.58, 2.5	17, 0.24, 1.9	12, 0.38, 2.3	8.0, 0.42, 1.9	7.0, 0.62, 2.9
RSMAS vs. NARR $Q_{SW}^I$	8.0, 0.67, 3.9	18, 0.32, 4.2	15, 0.35, 4.3	11, 0.30, 3.9	8.6, 0.64, 4.7
MLRF1 vs. ERAI $Q_{SW}^I$	-0.2, 0.89, 2.1	0.4, 0.86, 3.0	1.2, 0.89, 3.2	-1.2, 1.00, 2.1	0.4, 0.89, 2.7
MLRF1 vs. adj. $Q_{SW}^I$	-3.2, 0.98, 2.1	0.3, 0.95, 3.0	1.1, 0.98, 3.2	-1.3, 1.10, 2.1	0.3, 0.98, 2.7
RSMAS vs. ERAI $Q_{LW}^I$	22, 0.31, 2.1	4.9, 0.86, 0.6	19, 0.47, 0.38	12, 0.65, 1.3	4.9, 0.85, 0.8
RSMAS vs. adj. $Q_{LW}^I$	21, 0.32, 2.1	7.1, 0.79, 0.6	23, 0.35, 0.29	9.7, 0.71, 1.4	4.0, 0.88, 0.8
RSMAS vs. NARR $Q_{LW}^I$	22, 0.30, 2.5	2.3, 0.94, 1.2	31, 0.16, 0.87	15, 0.62, 2.1	11, 0.70, 2.0
RSMAS vs. ERAI $w_h$	--	0.5, 0.47, 0.2	--	--	0.5, 0.47, 0.2 m
RSMAS vs. adjusted $w_h$	--	0.3, 0.47, 0.1	--	--	0.3, 0.47, 0.1
RSMAS vs. WW3 $w_h$	--	0.1, 0.89, 0.2	--	--	0.1, 0.89, 0.2
MLRF1 vs. ERAI $T_a$	3.1, 0.85, 1.6	1.9, 0.93, 1.4	4.3, 0.84, 1.3	2.9, 0.86, 1.4	1.9, 0.92, 1.4 °C
SMKF1 vs. ERAI $q_a$	0.0017, 0.85, 0.0010	0.0031, 0.80, 0.0011	0.0140, 0.25, 0.0008	0.0022, 0.85, 0.0012	0.0018, 0.88, 0.0012 kg/kg
MLRF1 vs. AVHRR $T_s$	7.4, 0.68, 0.6	2.0, 0.92, 0.6	9.2, 0.67, 0.6	4.4, 0.82, 0.6	2.3, 0.9, 0.6 °C
LONF1 vs. AVHRR $T_s$	8.7, 0.60, 1.1	6.2, 0.76, 1.0	16, 0.46, 0.8	4.9, 0.79, 1.0	3.7, 0.85, 1.1
TSG vs. AVHRR $\partial_x T_s$	( <i>p</i> -statistic > 0.25)	$-9.2 \times 10^{-5}$ , 0.9, $1.1 \times 10^{-4}$	( <i>p</i> -statistic > 0.25)	$11 \times 10^{-5}$ , 1.1, $1.6 \times 10^{-4}$	$3.1 \times 10^{-5}$ , 1.3, $1.5 \times 10^{-4}$ K/m
AVHRR vs. GoM $\partial_x T_s$	$0.2 \times 10^{-5}$ , 0.72, $1.5 \times 10^{-4}$	$-9.9 \times 10^{-5}$ , 0.71, $1.4 \times 10^{-4}$	$-12 \times 10^{-5}$ , 0.03, $1.0 \times 10^{-4}$	$1.3 \times 10^{-5}$ , 0.53, $1.4 \times 10^{-4}$	$-5.6 \times 10^{-5}$ , 0.77, $1.4 \times 10^{-4}$
AVHRR vs. FKEYS $\partial_x T_s$	$9.9 \times 10^{-5}$ , -0.04, $1.6 \times 10^{-4}$	$3.3 \times 10^{-5}$ , 0.049, $0.9 \times 10^{-4}$	$2.7 \times 10^{-5}$ , 0.19, $0.8 \times 10^{-4}$	$9.3 \times 10^{-5}$ , 0.09, $1.5 \times 10^{-4}$	$4.3 \times 10^{-5}$ , 0.19, $1.2 \times 10^{-4}$
LOOE1 vs. GoM $u_{xs}$	-0.01, 0.07, 0.05	0.00, 0.12, 0.05	0.02, -0.09, 0.05	-0.00, 0.08, 0.04	0.00, 0.06, 0.05 m/s
LOOE1 vs. GoM $u_{ls}$	0.03, 0.49, 0.23	-0.01, 0.55, 0.18	-0.03, 0.16, 0.15	-0.06, 0.25, 0.18	-0.02, 0.35, 0.19
LOOE1 vs. FKEYS $u_{xs}$	-0.01, 0.20, 0.06	-0.01, 0.20, 0.06	-0.01, 0.28, 0.06	-0.01, -0.05, 0.05	-0.01, 0.12, 0.05
LOOE1 vs. FKEYS $u_{ls}$	0.11, 0.66, 0.33	0.22, 0.65, 0.34	0.18, 0.59, 0.37	0.10, 0.45, 0.32	0.15, 0.58, 0.34

**Table A-3: Long-term seasonal and overall *median* (first value in each cell) and *interquartile range* (second value) for data products used in heat budget, interpolated to individual stations as indicated. Statistics for *in situ* depth-averaged currents from Looe Key ADCP are shown in bold; statistics for other *in situ* data not shown here are described in detail in Ch. 2.**

<i>Station and Product</i>	<i>Winter (JFM)</i>	<i>Spring (AMJ)</i>	<i>Summer (JAS)</i>	<i>Autumn (OND)</i>	<i>Overall</i>
MLRF1 adj. ERAI $Q_{SW}^1$	15.7, 5.2	22.8, 3.3	20.0, 3.9	13.6, 3.4	18.0, 7.5 MJ/m <sup>2</sup> /d
MLRF1 adj. ERAI $Q_{LW}^1$	31.7, 2.8	34.1, 2.3	36.0, 0.5	33.1, 2.8	33.8, 3.7
MLRF1 adj. ERAI $w_h$	0.7, 0.5	0.4, 0.4	0.3, 0.3	0.7, 0.5	0.5, 0.5 m
MLRF1 ERAI $T_a$	22.3, 3.8	26.2, 3.0	27.9, 2.1	24.4, 3.8	25.6, 4.6 °C
MLRF1 ERAI $U_{10}$	9.5, 5.4	7.6, 5.4	6.3, 4.0	9.3, 5.5	8.1, 5.5 kts
SMKF1 ERAI $q_a$	0.01, 0.005	0.02, 0.004	0.02, 0.001	0.01, 0.005	0.01, 0.005 kg/kg
MLRF1 AVHRR $T_s$	23.4, 1.3	26.7, 2.6	29.2, 1.0	25.7, 2.3	26.2, 4.1 °C
LONF1 AVHRR $T_s$	22.1, 3.0	27.4, 3.3	29.8, 1.4	24.0, 3.7	25.9, 6.3
MLRF1 AVHRR $\partial_{xs}T_s$	$9.3 \times 10^{-5}$ , $1.5 \times 10^{-4}$	$-1.2 \times 10^{-5}$ , $1.2 \times 10^{-4}$	$-2.1 \times 10^{-5}$ , $1.2 \times 10^{-4}$	$11.9 \times 10^{-5}$ , $1.8 \times 10^{-4}$	$3.8 \times 10^{-5}$ , $1.7 \times 10^{-4}$ K/m
MLRF1 AVHRR $\partial_{ls}T_s$	$-1.6 \times 10^{-5}$ , $0.7 \times 10^{-4}$	$-0.8 \times 10^{-5}$ , $0.8 \times 10^{-4}$	$-0.9 \times 10^{-5}$ , $1.1 \times 10^{-4}$	$-1.6 \times 10^{-5}$ , $1.0 \times 10^{-4}$	$-1.2 \times 10^{-5}$ , $0.9 \times 10^{-4}$
MLRF1 AVHRR $\nabla^2 T_s$	$-0.2 \times 10^{-8}$ , $2.2 \times 10^{-7}$	$4.2 \times 10^{-8}$ , $2.1 \times 10^{-7}$	$4.1 \times 10^{-8}$ , $2.6 \times 10^{-7}$	$-2.5 \times 10^{-8}$ , $2.8 \times 10^{-7}$	$1.4 \times 10^{-8}$ , $2.5 \times 10^{-7}$ K/m <sup>2</sup>
MLRF1 GoM $\partial_{xs}T_s$	$6.7 \times 10^{-5}$ , $2.1 \times 10^{-4}$	$-10.7 \times 10^{-5}$ , $1.9 \times 10^{-4}$	$-11.3 \times 10^{-5}$ , $1.3 \times 10^{-4}$	$7.7 \times 10^{-5}$ , $2.0 \times 10^{-4}$	$-2.3 \times 10^{-5}$ , $2.2 \times 10^{-4}$ K/m
MLRF1 GoM $\partial_{ls}T_s$	$-0.7 \times 10^{-5}$ , $0.4 \times 10^{-4}$	$-1.9 \times 10^{-5}$ , $0.5 \times 10^{-4}$	$0.3 \times 10^{-5}$ , $0.4 \times 10^{-4}$	$-0.9 \times 10^{-5}$ , $0.4 \times 10^{-4}$	$-0.8 \times 10^{-5}$ , $0.4 \times 10^{-4}$
MLRF1 GoM $\nabla^2 T_s$	$-0.9 \times 10^{-8}$ , $0.7 \times 10^{-7}$	$4.8 \times 10^{-8}$ , $0.7 \times 10^{-7}$	$5.3 \times 10^{-8}$ , $0.5 \times 10^{-7}$	$-2.1 \times 10^{-8}$ , $0.6 \times 10^{-7}$	$1.6 \times 10^{-8}$ , $0.8 \times 10^{-7}$ K/m <sup>2</sup>
MLRF1 FKEYS $\partial_{xs}T_s$	$7.3 \times 10^{-5}$ , $2.2 \times 10^{-4}$	$2.9 \times 10^{-5}$ , $1.2 \times 10^{-4}$	$1.4 \times 10^{-5}$ , $1.0 \times 10^{-4}$	$8.3 \times 10^{-5}$ , $2.1 \times 10^{-4}$	$4.3 \times 10^{-5}$ , $1.5 \times 10^{-4}$ K/m
MLRF1 FKEYS $\partial_{ls}T_s$	$0.0 \times 10^{-5}$ , $0.3 \times 10^{-4}$	$-0.3 \times 10^{-5}$ , $0.2 \times 10^{-4}$	$-0.1 \times 10^{-5}$ , $0.1 \times 10^{-4}$	$-0.1 \times 10^{-5}$ , $0.2 \times 10^{-4}$	$-0.1 \times 10^{-5}$ , $0.2 \times 10^{-4}$
MLRF1 FKEYS $\nabla^2 T_s$	$0.1 \times 10^{-8}$ , $1.5 \times 10^{-7}$	$-0.7 \times 10^{-8}$ , $1.0 \times 10^{-7}$	$-1.6 \times 10^{-8}$ , $0.9 \times 10^{-7}$	$-0.8 \times 10^{-8}$ , $1.2 \times 10^{-7}$	$-0.8 \times 10^{-8}$ , $1.1 \times 10^{-7}$ K/m <sup>2</sup>
LONF1 AVHRR $\partial_{xs}T_s$	$-0.6 \times 10^{-5}$ , $1.3 \times 10^{-4}$	$0.5 \times 10^{-5}$ , $1.4 \times 10^{-4}$	$-0.7 \times 10^{-5}$ , $1.6 \times 10^{-4}$	$0.1 \times 10^{-5}$ , $1.4 \times 10^{-4}$	$-0.07 \times 10^{-5}$ , $1.4 \times 10^{-4}$ K/m
LONF1 AVHRR $\partial_{ls}T_s$	$-3.4 \times 10^{-5}$ , $1.4 \times 10^{-4}$	$-0.9 \times 10^{-5}$ , $1.6 \times 10^{-4}$	$-0.6 \times 10^{-5}$ , $1.5 \times 10^{-4}$	$-0.7 \times 10^{-5}$ , $1.3 \times 10^{-4}$	$-1.35 \times 10^{-5}$ , $1.5 \times 10^{-4}$
<b>LOOE1 ADCP <math>u_{xs}</math></b>	<b>0.01, 0.03</b>	<b>0.01, 0.03</b>	<b>0.01, 0.03</b>	<b>0.00, 0.03</b>	<b>0.00, 0.03 m/s</b>
<b>LOOE1 ADCP <math>u_{ls}</math></b>	<b>0.01, 0.28</b>	<b>0.01, 0.26</b>	<b>-0.01, 0.28</b>	<b>-0.05, 0.30</b>	<b>-0.01, 0.28</b>
LOOE1 GoM $u_{xs}$	-0.01, 0.06	0.00, 0.06	0.02, 0.06	0.00, 0.06	-0.01, 0.28
LOOE1 GoM $u_{ls}$	0.03, 0.36	-0.01, 0.26	-0.05, 0.20	-0.08, 0.21	-0.04, 0.26
LOOE1 FKEYS $u_{xs}$	-0.01, 0.08	-0.01, 0.08	-0.01, 0.07	-0.01, 0.06	-0.01, 0.07
LOOE1 FKEYS $u_{ls}$	0.13, 0.47	0.14, 0.50	0.21, 0.48	0.08, 0.42	0.14, 0.47

### Appendix III. Propagation of Errors

Measurement error estimates for all directly measured, remotely sensed, and reanalysis quantities are given in Ch. 2 and Ch. 3. The propagation of errors for individual heat budget components may be summarized as follows. Analytical equations are written for explicit propagation of instrument and representation errors,  $\sigma$ . Error covariance COV and correlation  $\rho$  are calculated directly from data time series, except where noted. The representation error for the total heat budget is expressed as:

$$\begin{aligned} \sigma^2[\partial_t T] &= \sigma^2\left[\frac{Q_0}{\rho C_p h}\right] + \sigma^2[\vec{u}_{hc} \cdot \nabla_h T_{hc}] + \sigma^2[\vec{u}_{km} \cdot \nabla_h T_{km} + K_{h\theta, km} \nabla^2 T_{km}] + \sigma^2[\vec{u}_{qe} \cdot \nabla_h T_{sfc}] + 2COV_{\partial_t T} \\ COV_{\partial_t T} &= COV_{\frac{Q_0}{\rho C_p h} \vec{u}_{km} \cdot \nabla_h T_{km} + K_{h\theta, km} \nabla^2 T_{km}} + COV_{\frac{Q_0}{\rho C_p h} \vec{u}_{qe} \cdot \nabla_h T_{sfc}} + COV_{\frac{Q_0}{\rho C_p h} \vec{u}_{hc} \cdot \nabla_h T_{hc}} + COV_{\vec{u}_{hc} \cdot \nabla_h T_{hc} \vec{u}_{km} \cdot \nabla_h T_{km} + K_{h\theta, km} \nabla^2 T_{km}} \\ &+ COV_{\vec{u}_{hc} \cdot \nabla_h T_{hc} \vec{u}_{qe} \cdot \nabla_h T_{sfc}} + COV_{\vec{u}_{km} \cdot \nabla_h T_{km} + K_{h\theta, km} \nabla^2 T_{km} \vec{u}_{qe} \cdot \nabla_h T_{sfc}} \end{aligned} \quad (A-1)$$

Errors for model and reanalysis terms are described below. Water density and water depth are treated as time-varying, uncertain variables in the heat budget. However, the correlation between seawater depth and net sea surface heat flux, as might be expected, is found to be negligible for all sites ( $|\rho| < 0.06$ ,  $p < 0.0001$ ), even taking into account water-column absorption, so that the correlation between errors in their estimates may be ignored. Error covariance between the terms in the net heat flux however was

significant, in particular covariance of the turbulent flux errors,  $\sigma[Q_{LH}]$  and  $\sigma[Q_{SH}]$  – see below for definitions of these terms. Thus:

$$\begin{aligned}\sigma^2\left[\frac{Q_0}{\rho C_p h}\right] &= \frac{Q_0^2}{\rho^4 C_p^4 h^2} \left[ \frac{\sigma_{Q_0}^2}{Q_0^2} + \frac{\sigma_h^2}{h^2} - 2 \frac{\sigma_{Q_0} \sigma_h}{Q_0 h} \rho_{\sigma_{Q_0}, \sigma_h} \right] \\ \sigma_{Q_0}^2 &= \sigma^2[\gamma Q_{SW} + Q_{LW} + Q_{LH} + Q_{SH}] = \sigma^2[\gamma Q_{SW}] + \sigma^2_{Q_{LW}} + \sigma^2_{Q_{LH}} + \sigma^2_{Q_{SH}} + 2COV_{\sigma_{Q_0}} \\ COV_{\sigma_{Q_0}} &= COV_{\gamma Q_{SW}, Q_{LW}} + COV_{\gamma Q_{SW}, Q_{LH}} + COV_{\gamma Q_{SW}, Q_{SH}} + COV_{Q_{LW}, Q_{LH}} + COV_{Q_{LW}, Q_{SH}} + COV_{Q_{LH}, Q_{SH}}\end{aligned}\quad (A-2)$$

As described in Ch. 3, outgoing shortwave radiation  $Q_{SW}^0$  is simply modeled by an albedo  $A$ ,  $Q_{SW} = (1-A) \cdot Q_{SW}^1$ . Albedo will vary with time, but in the error propagation formula, the constant error assumed for this time series is assumed known with certainty.

The correlation  $\rho[\gamma, Q_{SW}]$  is certainly significant, as both terms depend explicitly on solar zenith angle, and therefore on diurnal and seasonal cycles. Therefore, correlation in their error is calculated directly.

$$\sigma^2[\gamma Q_{SW}] = \gamma^2 (1-A)^2 \sigma^2[Q_{SW}^1] + Q_{SW}^2 \sigma_\gamma^2 + 2\gamma Q_{SW} (1-A)^2 \sigma_\gamma \sigma[Q_{SW}^1] \rho[\sigma_\gamma, \sigma_{Q_{SW}^1}] \quad (A-3)$$

Representation errors for turbulent heat fluxes were estimated using the methods of Fairall et al. (2003), summarized as follows. Reynolds fluxes of momentum,  $\tau$ , and of sensible and latent heat,  $Q_{SH}$  and  $Q_{LH}$ , respectively, at the sea surface may be approximated from variables directly measured at a given reference height ‘ $r$ ’, together with estimates for near the sea-surface labeled ‘ $s$ ’, using bulk formulae (Clayson et al. 1996; Fairall et al. 1996; Fairall et al. 2003):

$$\bar{\tau} = \overline{w'u'} = c_D^{1/2} c_D^{1/2} (U_r^2 + V_r^2 + U_g^2)^{1/2} (\bar{U}_r - \bar{u}_s), \quad (A-4)$$

$$Q_{SH} = \overline{w'\theta'} = c_D^{1/2} c_\theta^{1/2} (U_r^2 + V_r^2 + U_g^2)^{1/2} (\theta_r - \theta_s), \quad (A-5)$$

$$Q_{LH} = \overline{w'q'} = c_D^{1/2} c_q^{1/2} (U_r^2 + V_r^2 + U_g^2)^{1/2} (q_r - q_s). \quad (A-6)$$

Here  $\mathbf{U}_r$  is the hourly mean wind velocity vector and  $U_r$  and  $V_r$  its scalar components,  $\mathbf{u}_s$  is an hourly mean estimate of the ocean surface-current vector,  $w'$  and  $u'$  are horizontal and vertical components of rapidly varying (Reynolds) velocity,  $\theta$  is potential temperature,  $q$  is specific humidity, and  $U_g$  is a “gustiness” parameter which is designed to model fluxes which can still occur even when (hourly mean) winds are zero. Primed variables indicate a rapidly varying quantity, while over-bars (as well as unprimed variables) refer to hourly averages. Each of the bulk parameters  $c_D$ ,  $c_\theta$ , and  $c_q$  – referring to the momentum drag coefficient, temperature bulk coefficient, and specific humidity bulk coefficient, respectively – may depend on local wind speed, and on surface roughness due to sea state (including wave age).

The TOGA-COARE empirical formulae estimate both the above parameters and the resulting fluxes, based solely on measured or estimated bulk quantities. Propagation of errors from each of these quantities and their covariance are then calculated using the error estimation codes described in Fairall et al. (2003). This methodology has the advantage of having been verified by thousands of hours of direct Reynolds flux and bulk-variable measurements over the tropical ocean. Furthermore, the appropriateness of these bulk flux and error estimation methods for subtropical coastal environments like the FRT has been studied previously (e.g., Sopkin et al. 2007).

For calculating estimation errors in the turbulent flux terms, it is assumed that air density and heat of vaporization are both constant. Bulk coefficients are calculated directly at each time step by the COARE 3.0a algorithm, so that these coefficient time series are used directly in the error formulae below. Define the value  $\theta = T_s - T_a$ , so that

$\sigma_\theta^2 = \sigma_{T_s}^2 + \sigma_{T_a}^2 - 2T_s T_a \text{COV}[\sigma_{T_s}, \sigma_{T_a}]$ . Nominal measurement errors in sea and air temperature are each assumed constant, so that their covariance is zero.

$$\sigma^2[Q_{SH}] = \rho_a^2 C_{p_a}^2 C_D C_\theta \bullet \sigma^2[\theta \sqrt{U_{10}^2 + V_{10}^2 + U_g^2}] \quad (\text{A-7})$$

Defining  $W = (U_{10}^2 + V_{10}^2 + U_g^2)^{1/2}$ , the error covariance values between wind speed and air-sea temperature difference are as follows (**Eq. A-8a and Eq. A-8b**):

$$\sigma^2[\theta W] = U_{10}^2(\theta^2 \sigma_{U_{10}}^2 + \sigma_\theta^2) + V_{10}^2(\theta^2 \sigma_{V_{10}}^2 + \sigma_\theta^2) + U_g^2(\theta^2 \sigma_{U_g}^2 + \sigma_\theta^2) + 2\theta W \sigma_\theta \sigma_W \rho_{\sigma_\theta, \sigma_W}$$

$$\sigma_W = \sigma[\sqrt{U_{10}^2 + V_{10}^2 + U_g^2}] = \frac{1}{W} [2U_{10}^2 \sigma_{U_{10}}^2 + 2V_{10}^2 \sigma_{V_{10}}^2 + 2U_g^2 \sigma_{U_g}^2 + \text{COV}_{U^2, V^2} + \text{COV}_{U^2, U_g^2} + \text{COV}_{V^2, U_g^2}]^{1/2}$$

In addition to a nominal measurement error of 0.55 [ $\text{ms}^{-1}$ ] in the components of wind velocity (NDBC 2009), a consistent error of 0.03 is also noted in regression slopes between redundant wind sensors at multiple sites (SMKF1, MLRF1, FWYF1). Thus measurement error in wind velocity components is calculated to be, respectively,  $\sigma_{U_{10}} = 0.55 + (0.03U_{10})$  and  $\sigma_{V_{10}} = 0.55 + (0.03V_{10})$ . Both wind speed and the wind vector components at these sites exhibit a strong seasonal cycle (Peng et al. 1999). It is also noted that while the U and V vector components of wind speed are generally uncorrelated, the covariance between their squares need not be. Furthermore,  $U_g$  may be approximated as a function of air temperature (above), while recognizing that the error covariance between  $U_g^2$  and the square of seasonally variable wind components may be non-negligible. These correlations and covariance values are therefore estimated from available hourly data, and the results themselves investigated for seasonal variability.

For latent heat flux, again define a value  $q = q_s - q_a$ , the difference between specific humidity and saturation (sea-surface) specific humidity, so that  $\sigma_q^2 = \sigma_{q_s}^2 + \sigma_{q_a}^2$

–  $2q_s q_a \text{COV}[\sigma_{q_s}, \sigma_{q_a}]$ . If not derived from reanalysis,  $q_a$  is estimated from a formula based on Relative Humidity, which in turn is calculated from measured air and dew-point temperatures (see below). Estimation errors  $\sigma_{q_a}$  and  $\sigma_{q_s}$ , may potentially have significant covariance, and this covariance is calculated directly in the error budget.

$$\sigma^2[Q_{LH}] = \rho_a^2 L_e^2 C_D C_q \bullet \sigma^2[q \sqrt{U_{10}^2 + V_{10}^2 + U_g^2}] \quad (\text{A-9})$$

Writing  $W = (U_{10}^2 + V_{10}^2 + U_g^2)^{1/2}$  and  $\sigma_W$  as above, error covariance between wind and air-sea-surface specific humidity difference is written as (**Eq. A-10**):

$$\sigma^2[qW] = U_{10}^2 (q^2 \sigma_{U_{10}}^2 + \sigma_q^2) + V_{10}^2 (q^2 \sigma_{V_{10}}^2 + \sigma_q^2) + U_g^2 (q^2 \sigma_{U_g}^2 + \sigma_q^2) + 2qW \sigma_q \sigma_W \rho_{\sigma_q, \sigma_W}$$

Correlation between specific humidity and wind speed varies in both sign and magnitude by season, and may differ significantly across sites. A site-specific seasonal climatology of the error correlation  $\rho_{\sigma_q, \sigma_W}$  is thus used to estimate latent flux error.

When simultaneous *in situ* measurements of air and dew-point temperature are available in the SEAKEYS record, time series for Relative and specific humidity have been calculated from these measurements. The estimation errors for the calculated value of Relative Humidity take the form:

$$\begin{aligned} \sigma_{RH}^2 &= (100 e^{c\theta_d - c\theta_a})^2 \left( \frac{\sigma_{e^{c\theta_d}}^2}{e^{2c\theta_d}} + \frac{\sigma_{e^{-c\theta_a}}^2}{e^{-2c\theta_a}} + 2 \frac{\sigma_{e^{c\theta_d}} \sigma_{e^{-c\theta_a}}}{e^{c\theta_d - c\theta_a}} \rho[\sigma_{e^{c\theta_d}}, \sigma_{e^{-c\theta_a}}] \right) \\ &= 10^4 (e^{-2c\theta_a} \sigma_{e^{c\theta_d}}^2 + e^{2c\theta_d} \sigma_{e^{-c\theta_a}}^2 + 2e^{c\theta_d - c\theta_a} \sigma_{e^{c\theta_d}} \sigma_{e^{-c\theta_a}} \rho[\sigma_{e^{c\theta_d}}, \sigma_{e^{-c\theta_a}}]) \end{aligned} \quad (\text{A-11})$$

Where:

$$\sigma_{e^{c\theta_d}} = c e^{c\theta_d} \sigma_{\theta_d}, \sigma_{e^{-c\theta_a}} = c e^{-c\theta_a} \sigma_{\theta_a}, \rho[\sigma_{e^{c\theta_d}}, \sigma_{e^{-c\theta_a}}] = c^2 \sigma_{\theta_d} \sigma_{\theta_a} \rho[e^{c\theta_d}, e^{-c\theta_a}] \quad (\text{A-12})$$

Specific humidity is then calculated from Relative Humidity and air temperature with the following error (**Eq. A-13**):

$$\begin{aligned}\sigma_{q_a}^2 &= (0.42 \times 10^{-4} R H e^{0.06\theta_a})^2 \left( \frac{\sigma_{RH}^2}{e^{0.12\theta_a}} + \frac{\sigma_{e^{0.06\theta_a}}^2}{e^{0.12\theta_a}} + 2 \frac{\sigma_{RH} \sigma_{e^{0.06\theta_a}}}{R H e^{0.06\theta_a}} \rho[\sigma_{RH}, \sigma_{e^{0.06\theta_a}}] \right) \\ &= 1.8 \times 10^{-9} (e^{0.12\theta_a} \sigma_{RH}^2 + 0.0036 R H^2 e^{0.12\theta_a} \sigma_{\theta_a}^2 + 0.12 R H e^{0.12\theta_a} \sigma_{RH} \sigma_{\theta_a} \rho[\sigma_{RH}, \sigma_{e^{0.06\theta_a}}])\end{aligned}$$

Since Relative Humidity error depends explicitly on  $\theta_a$ , the correlation in this expression is calculated as:

$$\rho[\sigma_{RH}, \sigma_{e^{0.06\theta_a}}] = 0.0036 \sigma_{\theta_a} \rho[\sigma_{RH}, e^{0.06\theta_a}]$$

Similarly, saturated (sea-surface) specific humidity is estimated from sea temperature, resulting in an error formula of:

$$\sigma_{q_s}^2 = (1.8 \times 10^{-5}) (0.98)^2 (0.06)^2 e^{0.12\theta_s} \sigma_{\theta_s}^2 = 6.2234 \times 10^{-8} e^{0.12\theta_s} \sigma_{\theta_s}^2$$

## Bibliography

Achberger C, and 377 other authors (2012) State of the Climate in 2011 Special Supplement to the Bulletin of the American Meteorological Society Vol. 93, No. 7, July 2012. Bulletin of the American Meteorological Society 93:S1-+

Alpers W (1985) Theory of radar imaging of internal waves. *Nature* 314:245-247

Ardhuin F, Marie L, Rasclé N, Forget P, Roland A (2009) Observation and estimation of Lagrangian, Stokes, and Eulerian currents induced by wind and waves at the sea surface. *Journal of Physical Oceanography* 39:2820-2838

Ardhuin F, Rogers E, Babanin AV, Filipot JF, Magne R, Roland A, van der Westhuysen A, Queffelec P, Lefevre JM, Aouf L, Collard F (2010) Semiempirical dissipation source functions for ocean waves. Part I: Definition, calibration, and validation. *Journal of Physical Oceanography* 40:1917-1941

Baker AC, Glynn PW, Riegl B (2008) Climate change and coral reef bleaching: An ecological assessment of long-term impacts, recovery trends and future outlook. *Estuarine Coastal and Shelf Science* 80:435-471

Barnes BB, Hu C, Schaeffer BA, Lee Z, Palandro DA, Lehrter JC (2013) MODIS-derived spatiotemporal water clarity patterns in optically shallow Florida Keys waters: A new approach to remove bottom contamination. *Remote Sensing of Environment* 134:377-391

Barron MG, Vivian DN, Yee SH, Santavy DL (2009) Methods to estimate solar radiation dosimetry in coral reefs using remote sensed, modeled, and in situ data. *Environmental Monitoring and Assessment* 151:445-455

Baskett ML, Nisbet RM, Kappel CV, Mumby PJ, Gaines SD (2010) Conservation management approaches to protecting the capacity for corals to respond to climate change: a theoretical comparison. *Global Change Biology* 16:1229-1246

Bednarz TP, Lei CW, Patterson JC (2008) An experimental study of unsteady natural convection in a reservoir model cooled from the water surface. *Experimental Thermal and Fluid Science* 32:844-856

Bednarz TP, Lei CW, Patterson JC (2009) Unsteady natural convection induced by diurnal temperature changes in a reservoir with slowly varying bottom topography. *International Journal of Thermal Sciences* 48:1932-1942

Berkelmans R, De'ath G, Kininmonth S, Skirving WJ (2004) A comparison of the 1998 and 2002 coral bleaching events on the Great Barrier Reef: spatial correlation, patterns, and predictions. *Coral Reefs* 23:74-83

- Berrisford P, Dee D, Fielding K, Fuentes M, Kallberg P, Kobayashi S, Uppala S (2009) The ERA-Interim archive ERA Report Series. ECMWF, Shinfield Park, Reading, UK 16pp
- Berry DI, Kent EC (2009) A new air-sea interaction gridded dataset from ICOADS with uncertainty estimates. *Bulletin of the American Meteorological Society* 90:645-+
- Bertelsen RD, Butler MJ, Herrnkind WF, Hunt JH (2009) Regional characterisation of hard-bottom nursery habitat for juvenile Caribbean spiny lobster (*Panulirus argus*) using rapid assessment techniques. *New Zealand Journal of Marine and Freshwater Research* 43:299-312
- Betts AK, Kohler M, Zhang YC (2009) Comparison of river basin hydrometeorology in ERA-Interim and ERA-40 reanalyses with observations. *Journal of Geophysical Research-Atmospheres* 114:D02101
- Bourassa MA, Vincent DG, Wood WL (2001) A sea state parameterization with nonarbitrary wave age applicable to low and moderate wind speeds. *Journal of Physical Oceanography* 31:2840-2851
- Brock JC, Palaseanu-Lovejoy M, Wright CW, Nayegandhi A (2008) Patch-reef morphology as a proxy for Holocene sea-level variability, Northern Florida Keys, USA. *Coral Reefs* 27:555-568
- Burpee R (1979) Peninsula-scale convergence in the south Florida sea breeze. *Monthly Weather Review* 107:852-860
- Caccia VG, Boyer JN (2007) A nutrient loading budget for Biscayne Bay, Florida. *Marine Pollution Bulletin* 54:994-1008
- Cannizzaro JP, Carder KL (2006) Estimating chlorophyll a concentrations from remote-sensing reflectance in optically shallow waters. *Remote Sensing of Environment* 101:13-24
- Cantin NE, Cohen AL, Karnauskas KB, Tarrant AM, McCorkle DC (2010) Ocean warming slows coral growth in the central Red Sea. *Science* 329:322-325
- Cardenas MB, Wilson JL (2007) Effects of current-bed form induced fluid flow on the thermal regime of sediments. *Water Resources Research* 43:12
- Castellari S, Pinardi N, Leaman K (1998) A model study of air-sea interactions in the Mediterranean Sea. *Journal of Marine Systems* 18:89-114
- Castillo KD, Lima FP (2010) Comparison of in situ and satellite-derived (MODIS-Aqua/Terra) methods for assessing temperatures on coral reefs. *Limnology and Oceanography-Methods* 8:107-117

- Causey B (2002) The role of the Keys National Marine Sanctuary in the South Florida Ecosystem Restoration initiative. In: Porter J, Porter K (eds) *The Everglades, Florida Bay, and Coral Reefs of the Keys: An Ecosystem Sourcebook*. CRC Press, Boca Raton, pp883-894
- Chassignet EP, Hurlburt HE, Metzger EJ, Smedstad OM, Cummings JA, Halliwell GR, Bleck R, Baraille R, Wallcraft AJ, Lozano C, Tolman HL, Srinivasan A, Hankin S, Cornillon P, Weisberg R, Barth A, He R, Werner F, Wilkin J (2009) US GODAE Global Ocean Prediction with the HYbrid Coordinate Ocean Model (HYCOM). *Oceanography* 22:64-75
- Chave AD, Thomson DJ, Ander ME (1987) On the robust estimation of power spectra, coherences, and transfer-functions. *Journal of Geophysical Research-Solid Earth and Planets* 92:633-648
- Chen ZQ, Muller-Karger FE, Hu CM (2007) Remote sensing of water clarity in Tampa Bay. *Remote Sensing of Environment* 109:249-259
- Chollett I, Mueller-Karger FE, Heron SF, Skirving W, Mumby PJ (2012) Seasonal and spatial heterogeneity of recent sea surface temperature trends in the Caribbean Sea and southeast Gulf of Mexico. *Marine Pollution Bulletin* 64
- Chubarenko IP (2010) Horizontal convective water exchange above a sloping bottom: The mechanism of its formation and an analysis of its development. *Oceanology* 50:166-174
- Clayson CA, Fairall CW, Curry JA (1996) Evaluation of turbulent fluxes at the ocean surface using surface renewal theory. *Journal of Geophysical Research-Oceans* 101:28503-28513
- Comer LE, Grenney WJ (1977) Heat-transfer processes in bed of a small stream. *Water Research* 11:743-744
- Criales MM, Browder JA, Mooers CNK, Robblee MB, Cardenas H, Jackson TL (2007) Cross-shelf transport of pink shrimp larvae: interactions of tidal currents, larval vertical migrations and internal tides. *Marine Ecology-Progress Series* 345:167-184
- Cummings JA (2005) Operational multivariate ocean data assimilation. *Quarterly Journal of the Royal Meteorological Society* 131:3583-3604
- Davis KA, Leichter JJ, Hench JL, Monismith SG (2008) Effects of western boundary current dynamics on the internal wave field of the Southeast Florida shelf. *Journal of Geophysical Research-Oceans* 113:C09010
- Davis KA, Monismith SG (2011) The modification of bottom boundary layer turbulence and mixing by internal waves shoaling on a barrier reef. *Journal of Physical Oceanography* 41:2223-2241

- Dee DP, Uppala S (2009) Variational bias correction of satellite radiance data in the ERA-Interim reanalysis. *Quarterly Journal of the Royal Meteorological Society* 135:1830-1841
- Dee DP, Uppala SM, Simmons AJ, Berrisford P, Poli P, Kobayashi S, Andrae U, Balmaseda MA, Balsamo G, Bauer P, Bechtold P, Beljaars ACM, van de Berg L, Bidlot J, Bormann N, Delsol C, Dragani R, Fuentes M, Geer AJ, Haimberger L, Healy SB, Hersbach H, Hólm EV, Isaksen L, Kållberg P, Köhler M, Matricardi M, McNally AP, Monge-Sanz BM, Morcrette JJ, Park BK, Peubey C, de Rosnay P, Tavolato C, Thépaut JN, Vitart F (2011) The ERA-Interim reanalysis: configuration and performance of the data assimilation system. *Quarterly Journal of the Royal Meteorological Society* 137:553-597
- Derber JC, Wu WS (1998) The use of TOVS cloud-cleared radiances in the NCEP SSI analysis system. *Monthly Weather Review* 126:2287-2299
- DiNezio P, Gramer L, Johns W, Meinen C, Baringer M (2009) Observed interannual variability of the Florida Current: Wind forcing and the North Atlantic Oscillation. *Journal of Physical Oceanography* 39:721-736
- Dittenbach M, Rauber A, Merkl D (2002) Uncovering hierarchical structure in data using the growing hierarchical self-organizing map. *Neural Networks* 6:199-216
- Divins DL, Metzger D (2008) NGDC 3-arcsecond Coastal Relief Model. <http://www.ngdc.noaa.gov/mgg/coastal/crm.html>
- Dunckley JF, Koseff JR, Steinbuck JV, Monismith SG, Genin A (2012) Comparison of mixing efficiency and vertical diffusivity models from temperature microstructure. *Journal of Geophysical Research-Oceans* 117:12
- Dye DG, Shibasaki R (1995) Intercomparison of global PAR data sets. *Geophysical Research Letters* 22:2013-2016
- Dye DG (2004) Spectral composition and quanta-to-energy ratio of diffuse photosynthetically active radiation under diverse cloud conditions. *Journal of Geophysical Research-Atmospheres* 109:12
- Egbert GD, Erofeeva SY (2002) Efficient inverse modeling of barotropic ocean tides. *Journal of Atmospheric and Oceanic Technology* 19:183-204
- Egbert GD, Erofeeva SY, Ray RD (2010) Assimilation of altimetry data for nonlinear shallow-water tides: Quarter-diurnal tides of the Northwest European Shelf. *Continental Shelf Research* 30:668-679
- Emery WJ, Thomson RE (2001) *Data Analysis Methods in Physical Oceanography*. Elsevier Science Inc., Amsterdam, The Netherlands
- ESA (2009) European Space Agency Earth Observations Portal Web site, accessed January 2009. <http://catalogues.eoportal.org/eoli.html>

- Evans EC, McGregor GR, Petts GE (1998) River energy budgets with special reference to river bed processes. *Hydrological Processes* 12:575-595
- Fairall CW, Bradley EF, Rogers DP, Edson JB, Young GS (1996) Bulk parameterization of air-sea fluxes for Tropical Ocean Global Atmosphere Coupled Ocean Atmosphere Response Experiment. *Journal of Geophysical Research-Oceans* 101:3747-3764
- Fairall CW, Bradley EF, Godfrey JS, Wick GA, Edson JB, Young GS (1996) Cool-skin and warm-layer effects on sea surface temperature. *Journal of Geophysical Research-Oceans* 101:1295-1308
- Fairall CW, Bradley EF, Hare JE, Grachev AA, Edson JB (2003) Bulk parameterization of air-sea fluxes: Updates and verification for the COARE algorithm. *Journal of Climate* 16:571-591
- Farrow DE, Patterson JC (1993) On the response of a reservoir sidearm to diurnal heating and cooling. *Journal of Fluid Mechanics* 246:143-161
- Fiechter J, Mooers CNK (2003) Simulation of frontal eddies on the East Florida Shelf. *Geophysical Research Letters* 30(22):
- Fiechter J, Haus BK, Melo N, Mooers CNK (2008) Physical processes impacting passive particle dispersal in the Upper Florida Keys. *Continental Shelf Research* 28:1261-1272
- Finkl CW, Andrews JL (2008) Shelf geomorphology along the southeast Florida Atlantic continental platform: Barrier coral reefs, nearshore bedrock, and morphosedimentary features. *Journal of Coastal Research* 24:823-849
- Fofonoff NP, Millard RC, Jr. (1983) Algorithms for computation of fundamental properties of seawater UNESCO Technical Papers in Marine Science. Endorsed by UNESCO/SCOR/ICES/IAPSO Joint Panel on Oceanographic Tables and Standards and SCOR Working Group 51 58 pp.
- Fratantoni PS, Lee TN, Podesta GP, Muller-Karger F (1998) The influence of Loop Current perturbations on the formation and evolution of Tortugas eddies in the southern Straits of Florida. *Journal of Geophysical Research-Oceans* 103:24759-24779
- Gentemann CL, Minnett PJ, Sienkiewicz J, DeMaria M, Cummings J, Jin Y, Doyle JD, Gramer L, Barron CN, Casey KS, Donlon CJ (2009) MISST The Multi-Sensor Improved Sea Surface Temperature Project. *Oceanography* 22:76-87
- Gierach MM, Subrahmanyam B, Thoppil PG (2009) Physical and biological responses to Hurricane Katrina (2005) in a 1/25 degrees nested Gulf of Mexico HYCOM. *Journal of Marine Systems* 78:168-179
- Gilbert PS, Lee TN, Podesta GP (1996) Transport of anomalous low-salinity waters from the Mississippi River flood of 1993 to the Straits of Florida. *Continental Shelf Research* 16:1065-&

- Gilhousen DB (1988) Quality control of meteorological data from automated marine stations. Fourth International Conference on Interactive Information and Processing Systems for Meteorology, Oceanography, and Hydrology:113-117
- Gilhousen DB (1998) Improved real-time quality control of NDBC measurements. 10th Symposium on Meteorological Observations and Instrumentation:363-366
- Godfrey J, Lindstrom E, Nunez M, Bradley E, Coppin P (1991) On the net surface heat flux into the western equatorial Pacific. *Journal of Geophysical Research* 96:3391-3400
- Graber HC, Haus BK, Chapman RD, Shay LK (1997) HF radar comparisons with moored estimates of current speed and direction: Expected differences and implications. *Journal of Geophysical Research-Oceans* 102:18749-18766
- Graham NAJ, McClanahan TR, MacNeil MA, Wilson SK, Polunin NVC, Jennings S, Chabanet P, Clark S, Spalding MD, Letourneur Y, Bigot L, Galzin R, Ohman MC, Garpe KC, Edwards AJ, Sheppard CRC (2008) Climate warming, Marine Protected Areas and the ocean-scale integrity of coral reef ecosystems. *PLoS ONE* 3:e3039
- Gramer LJ, Johns EM, Hendee JC, Hu C (2009) Characterization of biologically significant hydrodynamic anomalies on the Florida Reef Tract. In: Dodge R (ed) Proc 11<sup>th</sup> Int Coral Reef Sym, 7-11 July 2008, Ft. Lauderdale, FL 470-474
- Gramer LJ, Mariano AJ, Hendee JC (2012) Heat budget for Florida reefs: Reef-scale thermal stress via satellite. In: Yellowlees D, Hughes TP (eds) Proc 12th Int Coral Reef Sym, 9-13 July 2012, Cairns, Australia ICRS2012\_2014A\_2012
- Gramer LJ, Mariano AJ (in review) The dynamics of sea temperature variability on Florida's reef tract: Part I. Analysis of variability and covariability. *Journal of Marine Research*
- Gramer LJ, Mariano AJ (in prep.) The dynamics of sea temperature variability on Florida's reef tract: Part II. Ocean heat budget. *Journal of Marine Research*
- Grinsted A, Moore JC, Jevrejeva S, Bt (2004) Application of the cross wavelet transform and wavelet coherence to geophysical time series. *Nonlinear Processes in Geophysics* 11:561-566
- Grorud-Colvert K, Sponaugle S (2009) Larval supply and juvenile recruitment of coral reef fishes to marine reserves and non-reserves of the upper Florida Keys, USA. *Marine Biology* 156:277-288
- Guimaraes G, Peter JH, Penzel T, Ultsch A (2001) A method for automated temporal knowledge acquisition applied to sleep-related breathing disorders. *Artificial Intelligence in Medicine* 23:211-237
- Haus BK, Wang JD, Rivera J, Martinez-Pedraja J, Smith N (2000) Remote radar measurement of shelf currents off Key Largo, Florida, USA. *Estuarine Coastal and Shelf Science* 51:553-569

- Haus BK, Wang JD, Martinez-Pedraja J, Smith N (2004) Southeast Florida Shelf circulation and volume exchange, observations of km-scale variability. *Estuarine Coastal and Shelf Science* 59:277-294
- Haus BK, Shay LK, Work PA, Voulgaris G, Ramos RJ, Martinez-Pedraja J (2010) Wind speed dependence of single-site wave-height retrievals from High-Frequency radars. *Journal of Atmospheric and Oceanic Technology* 27:1381-1394
- Hearn CJ (2008) *The dynamics of coastal models*. Cambridge Univ Pr, New York
- Hench JL, Leichter JJ, Monismith SG (2008) Episodic circulation and exchange in a wave-driven coral reef and lagoon system. *Limnology and Oceanography* 53:2681-2694
- Hendee JC, Mueller E, Humphrey C, Moore T (2001) A data-driven expert system for producing coral bleaching alerts at Sombrero Reef in the Florida Keys, USA. *Bulletin of Marine Science* 69:673-684
- Hendee J, Gramer L, Kleypas J, Manzello D, Jankulak M, Langdon C (2007) The Integrated Coral Observing Network: Sensor solutions for sensitive sites. ISSNIP: The Third International Conference on Intelligent Sensors, Sensor Networks and Information Processing:669-673
- Hendee JC, Gramer LJ, Manzello D, Jankulak M (2009) Ecological forecasting for coral reef ecosystems. In: Dodge R (ed) *Proc 11th Int Coral Reef Sym, Ft. Lauderdale, FL* 534-538
- Heron M, Heron S, Skirving W (2008) Mitigation of Coral Bleaching on the Reef Front by Wave Mixing. *Western Pacific Geophysics Meeting* 89(23)
- Hewitson BC, Crane RG (2002) Self-organizing maps: applications to synoptic climatology. *Climate Research* 22:13-26
- Hitchcock GL, Lee TN, Ortner PB, Cummings S, Kelble C, Williams E (2005) Property fields in a Tortugas Eddy in the southern straits of Florida. *Deep-Sea Research Part I-Oceanographic Research Papers* 52:2195-2213
- Hochberg EJ, Atkinson MJ, Andrefouet S (2003) Spectral reflectance of coral reef bottom-types worldwide and implications for coral reef remote sensing. *Remote Sensing of Environment* 85:159-173
- Hochberg EJ, Atkinson MJ, Apprill A, Andrefouet S (2004) Spectral reflectance of coral. *Coral Reefs* 23:84-95
- Hoegh-Guldberg O, Fine M, Skirving W, Johnstone R, Dove S, Strong A (2005) Coral bleaching following wintry weather. *Limnology and Oceanography* 50:265-271
- Holland PW, Welsch RE (1977) Robust regression using iteratively re-weighted least-squares. *Communications in Statistics Part a-Theory and Methods* 6:813-827

- Hu CM, Nelson JR, Johns E, Chen ZQ, Weisberg RH, Muller-Karger FE (2005a) Mississippi River water in the Florida Straits and in the Gulf Stream off Georgia in summer 2004. *Geophysical Research Letters* 32:5
- Hu CM, Muller-Karger FE, Taylor C, Carder KL, Kelble C, Johns E, Heil CA (2005b) Red tide detection and tracing using MODIS fluorescence data: A regional example in SW Florida coastal waters. *Remote Sensing of Environment* 97:311-321
- Hu CM, Muller-Karger F, Murch B, Myhre D, Taylor J, Luerssen R, Moses C, Zhang CY, Gramer L, Hendee J (2009) Building an Automated Integrated Observing System to Detect Sea Surface Temperature Anomaly Events in the Florida Keys. *Ieee Transactions on Geoscience and Remote Sensing* 47:2071-2084
- Hughes GO, Griffiths RW (2008) Horizontal convection. *Annual Review of Fluid Mechanics* 40:185-208
- ICON (2012) NOAA Integrated Coral Observing Network (ICON) Web site, accessed June 2012. <http://ecoforecast.coral.noaa.gov>
- Ishizaki H, Yamanaka G (2010) Impact of explicit sun altitude in solar radiation on an ocean model simulation. *Ocean Modelling* 33:52-69
- Jacovides CP, Tymvios FS, Asimakopoulos DN, Theofilou KM, Pashiardes S (2003) Global photosynthetically active radiation and its relationship with global solar radiation in the Eastern Mediterranean basin. *Theoretical and Applied Climatology* 74:227-233
- Jago OK, Kench PS, Brander RW (2007) Field observations of wave-driven water-level gradients across a coral reef flat. *Journal of Geophysical Research-Oceans* 112:14
- James WF, Barko JW (1991) Estimation of phosphorus exchange between littoral and pelagic zones during nighttime convective circulation. *Limnology and Oceanography* 36:179-187
- Jin Z, Qiao Y, Wang Y, Fang Y, Yi W (2011) A new parameterization of spectral and broadband ocean surface albedo. *Optics Express* 19:26429-26443
- Johns GM, Leeworthy VR, Bell FW, Bonn MA (2001) Socioeconomic study of reefs in Southeast Florida. Final Report. Hazen and Sawyer Environmental Engineers & Scientists 348pp
- Johns GM, Milon JW, D. S (2004) Socioeconomic study of reefs in Martin County, FL. Final Report. Hazen and Sawyer Environmental Engineers & Scientists 120pp
- Jones NL, Lowe RJ, Pawlak G, Fong DA, Monismith SG (2008) Plume dispersion on a fringing coral reef system. *Limnology and Oceanography* 53:2273-2286
- Katsaros KB, Soloviev AV (2004) Vanishing horizontal sea surface temperature gradients at low wind speeds. *Boundary-Layer Meteorology* 112:381-396

- Katsaros KB, Soloviev AV, Weisberg RH, Luther ME (2005) Reduced horizontal sea surface temperature gradients under conditions of clear skies and weak winds. *Boundary-Layer Meteorology* 116:175-185
- Keller BD, Causey BD (2005) Linkages between the Florida Keys National Marine Sanctuary and the South Florida Ecosystem Restoration Initiative. *Ocean & Coastal Management* 48:869-900
- Keller BD, Gleason DF, McLeod E, Woodley CM, Airame S, Causey BD, Friedlander AM, Grober-Dunsmore R, Johnson JE, Miller SL, Steneck RS (2009) Climate change, coral reef ecosystems, and management options for Marine Protected Areas. *Environmental Management* 44:1069-1088
- Kiranmayi L, Bhat GS (2009) Quasi-periodic, global oscillations in sea level pressure on intraseasonal timescales. *Climate Dynamics* 32:925-934
- Kirk JTO (1994) *Light and Photosynthesis in Aquatic Ecosystems*. Cambridge Univ. Press, New York
- Knapp TR (1978) Canonical correlation analysis: A general parametric significance-testing system. *Psychological Bulletin* 85(2): 410–416
- Kohonen T (1990) The self-organizing map. *Proceedings of the IEEE* 78:1464-1480
- Kohonen T (1998) The self-organizing map. *Neurocomputing* 21(1-3): 1-6
- Kourafalou VH, Peng G, Kang H, Hogan PJ, Smedstad OM, Weisberg RH (2009) Evaluation of Global Ocean Data Assimilation Experiment products on South Florida nested simulations with the Hybrid Coordinate Ocean Model. *Ocean Dynamics* 59:47-66
- Kraus E, Businger J (1994) *Atmosphere-ocean interaction*. Oxford University Press, USA
- Large WG, Yeager SG (2009) The global climatology of an interannually varying air-sea flux data set. *Climate Dynamics* 33:341-364
- Leal SS, Tiba C, Piacentini R (2011) Daily UV radiation modeling with the usage of statistical correlations and artificial neural networks. *Renewable Energy* 36:3337-3344
- Lee BC, Fan YM, Chuang LZH, Kao CC (2009) Parametric sensitivity analysis of the WAVEWATCH III Model. *Terrestrial Atmospheric and Oceanic Sciences* 20:425-432
- Lee TN (1975) Florida Current spin-off eddies. *Deep-Sea Research* 22:753-763
- Lee TN, Rooth C, Williams E, McGowan M, Szmant AF, Clarke ME (1992) Influence of Florida Current, gyres and wind-driven circulation on transport of larvae and recruitment in the Florida Keys coral reefs. *Continental Shelf Research* 12:971-1002
- Lee TN, Clarke ME, Williams E, Szmant AF, Berger T (1994) Evolution of the Tortugas Gyre and its influence on recruitment in the Florida-Keys. *Bulletin of Marine Science* 54:621-646

- Lee TN, Leaman K, Williams E, Berger T, Atkinson L (1995) Florida Current meanders and gyre formation in the southern Straits of Florida. *Journal of Geophysical Research-Oceans* 100:8607-8620
- Lee TN, Williams E (1999) Mean distribution and seasonal variability of coastal currents and temperature in the Florida Keys with implications for larval recruitment. *Bulletin of Marine Science* 64:35-56
- Lee TN, Smith N (2002) Volume transport variability through the Florida Keys tidal channels. *Continental Shelf Research* 22:1361-1377
- Lee TN, Williams E, Johns E, Wilson D, Smith N (2002) Transport processes linking south Florida coastal ecosystems. In: Porter J, Porter K (eds) *The Everglades, Florida Bay, and Coral Reefs of the Florida Keys: An Ecosystem Sourcebook*. CRC Press, Inc., Boca Raton, FL, pp309-342
- Legg S (2004) Internal tides generated on a corrugated continental slope. Part II: Along-slope barotropic forcing. *Journal of Physical Oceanography* 34:1824-1838
- Lei CW, Patterson JC (2005) Unsteady natural convection in a triangular enclosure induced by surface cooling. *International Journal of Heat and Fluid Flow* 26:307-321
- Lei C, Patterson JC (2006) Natural convection induced by diurnal heating and cooling in a reservoir with slowly varying topography. *Jsme International Journal Series B-Fluids and Thermal Engineering* 49:605-615
- Leichter JJ, Wing SR, Miller SL, Denny MW (1996) Pulsed delivery of subthermocline water to Conch Reef (Florida Keys) by internal tidal bores. *Limnology and Oceanography* 41:1490-1501
- Leichter JJ, Shellenbarger G, Genovese SJ, Wing SR (1998) Breaking internal waves on a Florida (USA) coral reef: a plankton pump at work? *Marine Ecology-Progress Series* 166:83-97
- Leichter JJ, Miller SL (1999) Predicting high-frequency upwelling: Spatial and temporal patterns of temperature anomalies on a Florida coral reef. *Continental Shelf Research* 19:911-928
- Leichter JJ, Stewart HL, Miller SL (2003) Episodic nutrient transport to Florida coral reefs. *Limnology and Oceanography* 48:1394-1407
- Leichter JJ, Deane GB, Stokes MD (2005) Spatial and temporal variability of internal wave forcing on a coral reef. *Journal of Physical Oceanography* 35:1945-1962
- Leichter JJ, Helmuth B, Fischer AM (2006) Variation beneath the surface: Quantifying complex thermal environments on coral reefs in the Caribbean, Bahamas and Florida. *Journal of Marine Research* 64:563-588
- Leloup JA, Lachkar Z, Boulanger JP, Thiria S (2007) Detecting decadal changes in ENSO using neural networks. *Climate Dynamics* 28:147-162

Lesser MP, Mazel C, Phinney D, Yentsch CS (2000) Light absorption and utilization by colonies of the congeneric hermatypic corals *Montastraea faveolata* and *Montastraea cavernosa*. *Limnology and Oceanography* 45:76-86

Lewis MR, Wei JW, Van Dommelen R, Voss KJ (2011) Quantitative estimation of the underwater radiance distribution. *Journal of Geophysical Research-Oceans* 116:14

Lidz BH, Reich CD, Peterson RL, Shinn EA (2006) New maps, new information: Coral Reefs of the Florida Keys. *Journal of Coastal Research* 22:260-282

Lirman D, Deangelo G, Serafy J, Hazra A, Hazra DS, Herlan J, Luo J, Bellmund S, Wang J, Clausing R (2008) Seasonal changes in the abundance and distribution of submerged aquatic vegetation in a highly managed coastal lagoon. *Hydrobiologia* 596:105-120

Lirman D, Schopmeyer S, Manzello D, Gramer LJ, Precht WF, Muller-Karger F, Banks K, Barnes B, Bartels E, Bourque A, Byrne J, Donahue S, Duquesnel J, Fisher L, Gilliam D, Hendee J, Johnson M, Maxwell K, McDevitt E, Monty J, Rueda D, Ruzicka R, Thanner S (2011) Severe 2010 Cold-water event caused unprecedented mortality to corals of the Florida reef tract and reversed previous survivorship patterns. *Plos One* 6:e23047

Liu YG, Weisberg RH (2005) Patterns of ocean current variability on the West Florida Shelf using the self-organizing map. *Journal of Geophysical Research-Oceans* 110:12

Liu YG, Weisberg RH, Mooers CNK (2006a) Performance evaluation of the self-organizing map for feature extraction. *Journal of Geophysical Research-Oceans* 111

Liu YG, Weisberg RH, He RY (2006b) Sea surface temperature patterns on the West Florida Shelf using growing hierarchical self-organizing maps. *Journal of Atmospheric and Oceanic Technology* 23:325-338

MacCready P, Pawlak G (2001) Stratified flow along a corrugated slope: Separation drag and wave drag. *Journal of Physical Oceanography* 31:2824-2839

MacKellar MC, McGowan HA, Phinn SR (2012) Spatial heterogeneity of air-sea energy fluxes over a coral reef-Heron Reef, Australia. *Journal of Applied Meteorology and Climatology* 51:1353-1370

Manzello DP (2004) A decade of SEAKEYS data: SST trends and patterns. In: Hendee JC (ed) *The effects of combined sea temperature, light, and carbon dioxide on coral bleaching, settlement, and growth*. U.S. Department of Commerce, National Oceanic and Atmospheric Administration, Ocean and Atmospheric Research pp35-36

Manzello DP, Berkelmans R, Hendee JC (2007a) Coral bleaching indices and thresholds for the Florida Reef Tract, Bahamas, and St. Croix, US Virgin Islands. *Marine Pollution Bulletin* 54:1923-1931

Manzello DP, Brandt M, Smith TB, Lirman D, Hendee JC, Nemeth RS (2007b) Hurricanes benefit bleached corals. *Proceedings of the National Academy of Sciences of the United States of America* 104:12035-12039

- Manzello DP, Enochs IC, Melo N, Gledhill DK, Johns EM (2012) Ocean acidification refugia of the Florida Reef Tract. *Plos One* 7:10
- Mao YD, Heron ML (2008) The influence of fetch on the response of surface currents to wind studied by HF ocean surface radar. *Journal of Physical Oceanography* 38:1107-1121
- Mao YD, Lei CW, Patterson JC (2009) Unsteady natural convection in a triangular enclosure induced by absorption of radiation - a revisit by improved scaling analysis. *Journal of Fluid Mechanics* 622:75-102
- Mao Y, Lei C, Patterson JC (2010a) Characteristics of instability of radiation-induced natural convection in shallow littoral waters. *International Journal of Thermal Sciences* 49:170-181
- Mao YD, Lei CW, Patterson JC (2010b) Unsteady near-shore natural convection induced by surface cooling. *Journal of Fluid Mechanics* 642:213-233
- Mariano AJ (in prep.) An introduction to the analysis, interpolation, and assimilation of space-time data. Cambridge University Press
- Markovic M, Jones CG, Winger K, Paquin D (2009) The surface radiation budget over North America: gridded data assessment and evaluation of regional climate models. *International Journal of Climatology* 29:2226-2240
- Maynard JA, Marshall PA, Johnson JE, Harman S (2010) Building resilience into practical conservation: identifying local management responses to global climate change in the southern Great Barrier Reef. *Coral Reefs* 29:381-391
- McGillicuddy DJ, Robinson AR, Siegel DA, Jannasch HW, Johnson R, Dickey T, McNeil J, Michaels AF, Knap AH (1998) Influence of mesoscale eddies on new production in the Sargasso Sea. *Nature* 394:263-266
- McNally AP, Derber JC, Wu W, Katz BB (2000) The use of TOVS level-1b radiances in the NCEP SSI analysis system. *Quarterly Journal of the Royal Meteorological Society* 126:689-724
- Mesinger F, DiMego G, Kalnay E, Mitchell K, Shafran PC, Ebisuzaki W, Jovic D, Woollen J, Rogers E, Berbery EH, Ek MB, Fan Y, Grumbine R, Higgins W, Li H, Lin Y, Manikin G, Parrish D, Shi W (2006) North American Regional Reanalysis. *Bulletin of the American Meteorological Society* 87:343-360
- Monismith SG, Imberger J, Morison ML (1990) Convective motions in the sidearm of a small reservoir. *Limnology and Oceanography* 35:1676-1702
- Monismith SG, Genin A, Reidenbach MA, Yahel G, Koseff JR (2006) Thermally driven exchanges between a coral reef and the adjoining ocean. *Journal of Physical Oceanography* 36:1332-1347

- Monismith SG, Hench JL, Fong DA, Nidzieko NJ, Fleenor WE, Doyle LP, Schladow SG (2009) Thermal variability in a tidal river. *Estuaries and Coasts* 32:100-110
- Monismith SG, Davis KA, Shellenbarger GG, Hench JL, Nidzieko NJ, Santoro AE, Reidenbach MA, Rosman JH, Holtzman R, Martens CS, Lindquist NL, Southwell MW, Genin A (2010) Flow effects on benthic grazing on phytoplankton by a Caribbean reef. *Limnology and Oceanography* 55:1881-1892
- Morel A, Antoine D (1994) Heating rate within the upper ocean in relation to its biooptical state. *Journal of Physical Oceanography* 24:1652-1665
- Morel A, Smith RC (1974) Relation between total quanta and total energy for aquatic photosynthesis. *Limnology and Oceanography* 19:591-600
- Morgan PP (1994) SEAWATER: A library of MATLAB(R) computational routines for the properties of sea water. Version 1.2. Report CSIRO Marine Laboratories
- Moses CS, Andrefouet S, Kranenburg CJ, Muller-Karger FE (2009) Regional estimates of reef carbonate dynamics and productivity using Landsat 7 ETM+, and potential impacts from ocean acidification. *Marine Ecology-Progress Series* 380:103-115
- Moulin A (2005) Spatio-Temporal Variability of Florida Reef Tract Bottom Temperature: 1988 – 2003. Florida Institute of Technology, Thesis, 129pp (177pp with figures and Appendices)
- Murawski SA, Matlock GC (2006) Ecosystem science capabilities required to support NOAA's Mission in the year 2020. US Department of Commerce, National Oceanic and Atmospheric Administration, National Marine Fisheries Service, National Ocean Service
- Nadaoka K, Nihei Y, Kumano R, Yokobori T, Omija T, Wakaki K (2001) A field observation on hydrodynamic and thermal environments of a fringing reef at Ishigaki Island under typhoon and normal atmospheric conditions. *Coral Reefs* 20:387-398
- NDBC (2009) Handbook of automated data quality control checks and procedures, accessed May 2013. <http://www.ndbc.noaa.gov/qc.shtml> 78 pp.
- NDBC (2012) NOAA National Data Buoy Center (NDBC) Web site, accessed June 2012. <http://www.ndbc.noaa.gov>
- Nihei Y, Nadaoka K, Tsunashima Y, Aoki Y, Wakaki K (2002) Field-observation analysis of sea-bottom effects on thermal environments in a coral reef. In: Chung JS, Matsui T, Chen J, Kyojuka Y (eds) *Proceedings of the Twelfth. International Society Offshore& Polar Engineers*, Cupertino, pp362-367
- Nobes DC, Villinger H, Davis EE, Law LK (1986) Estimation of marine sediment bulk physical-properties at depth from sea-floor geophysical measurements. *Journal of Geophysical Research-Solid Earth and Planets* 91:14033-14043
- Nof D (1988) Eddy-wall interactions. *Journal of Marine Research* 46:527-555

- Nof D (1999) Strange encounters of eddies with walls. *Journal of Marine Research* 57:739-761
- Ogden JC, Porter JW, Smith NP, Szmant AM, Jaap WC, Forcucci D (1994) A long-term interdisciplinary study of the Florida-Keys seascape. *Bulletin of Marine Science* 54:1059-1071
- Onn R, Steinhardt AO (1993) Multiwindow spectrum estimation - A linear algebraic approach. *International Journal of Adaptive Control and Signal Processing* 7:103-116
- Ortner PB, Lee TN, Milne PJ, Zika RG, Clarke ME, Podesta GP, Swart PK, Tester PA, Atkinson LP, Johnson WR (1995) Mississippi River flood waters that reached the Gulf-Stream. *Journal of Geophysical Research-Oceans* 100:13595-13601
- Palandro D, Hu C, Andrefouet S, Muller-Karger FE (2004) Synoptic water clarity assessment in the Florida Keys using diffuse attenuation coefficient estimated from Landsat imagery:489-493
- Palandro DA, Andrefouet S, Hu C, Hallock P, Muller-Karger FE, Dustan P, Callahan MK, Kranenburg C, Beaver CR (2008) Quantification of two decades of shallow-water coral reef habitat decline in the Florida Keys National Marine Sanctuary using Landsat data (1984-2002). *Remote Sensing of Environment* 112:3388-3399
- Papaioannou G, Papanikolaou N, Retalis D (1993) Relationships of photosynthetically active radiation and shortwave irradiance. *Theoretical and Applied Climatology* 48:23-27
- Park J, Lindberg CR, Thomson DJ (1987) Multiple-taper spectral-analysis of terrestrial free oscillations .1. *Geophysical Journal of the Royal Astronomical Society* 91:755-794
- Park S, Chu PC (2008) Thermal fronts and cross-frontal heat flux in the southern Huanghai Sea and the East China Sea. *Acta Oceanologica Sinica* 27:1-20
- Parks AB (2008) Observing eddy variability using HF radar in the Straits of Florida. University of Miami, Thesis, 123pp
- Payne RE (1972) Albedo of sea-surface. *Journal of the Atmospheric Sciences* 29:959-&
- Peltier WR, Caulfield CP (2003) Mixing efficiency in stratified shear flows. *Annual Review of Fluid Mechanics* 35:135-167
- Peng G, Mooers CNK, Graber HC (1999) Coastal winds in south Florida. *Journal of Applied Meteorology* 38:1740-1757
- Peters H, Shay LK, Mariano AJ, Cook TM (2002) Current variability on a narrow shelf with large ambient vorticity. *Journal of Geophysical Research-Oceans* 107:15
- Pitts PA (1997) An investigation of tidal and nontidal current patterns in Western Hawk Channel, Florida Keys. *Continental Shelf Research* 17:1679-1687
- Pitts PA (2002) Near-shore circulation in the lower Florida Keys. *Journal of Coastal Research* 18:662-673

- Porter J, Porter K (2002) The Everglades, Florida Bay, and coral reefs of the Florida Keys: an ecosystem sourcebook. CRC Press, Boca Raton, FL
- Prasad TG, Hogan PJ (2007) Upper-ocean response to Hurricane Ivan in a 1/25 degrees nested Gulf of Mexico HYCOM. *Journal of Geophysical Research-Oceans* 112:C04013
- Prastowo T, Griffiths RW, Hughes GO, Hogg AM (2009) Effects of topography on the cumulative mixing efficiency in exchange flows. *Journal of Geophysical Research-Oceans* 114:12
- Price JF, Weller RA, Pinkel R (1986) Diurnal cycling - Observations and models of the upper ocean response to diurnal heating, cooling, and wind mixing. *Journal of Geophysical Research-Oceans* 91:8411-8427
- Raschle N, Arduin F (2009) Drift and mixing under the ocean surface revisited: Stratified conditions and model-data comparisons. *Journal of Geophysical Research-Oceans* 114:17
- Reed RK (1976) Estimation of net long-wave radiation from oceans. *Journal of Geophysical Research-Oceans and Atmospheres* 81:5793-5794
- Reed RK, Halpern D (1975) Heat content of upper ocean during coastal upwelling - Oregon, August 1973. *Journal of Physical Oceanography* 5:379-383
- Richardson DE (2007) Physical and Biological Characteristics of Billfish Spawning Habitat in the Straits of Florida. University of Miami, p206
- Riedel KS, Sidorenko A (1995) Minimum bias multiple taper spectral estimation. *Ieee Transactions on Signal Processing* 43:188-195
- Riegl B, Bruckner A, Coles SL, Renaud P, Dodge RE (2009) Coral reefs threats and conservation in an era of global change. *Year in Ecology and Conservation Biology 2009*. Blackwell Publishing, Oxford, pp136-186
- Rosmond TE, Teixeira J, Peng M, Hogan TF, Pauley R (2002) Navy Operational Global Atmospheric Prediction System (NOGAPS). *Oceanography* 15:99-108
- Schmitz WJ (1996) On the world ocean circulation: Volume I - Some global features / North Atlantic Circulation. Woods Hole Oceanographic Institution 148
- Semedo A, Suselj K, Rutgersson A, Sterl A (2011) A global view on the wind sea and swell climate and variability from ERA-40. *Journal of Climate* 24:1461-1479
- Shapiro GI, Huthnance JM, Ivanov VV (2003) Dense water cascading off the continental shelf. *Journal of Geophysical Research-Oceans* 108:19
- Shay LK, Lee TN, Williams EJ, Graber HC, Rooth CGH (1998) Effects of low-frequency current variability on near-inertial submesoscale vortices. *Journal of Geophysical Research-Oceans* 103:18691-18714

- Shay LK, Cook TM, An PE (2003) Submesoscale coastal ocean flows detected by very high frequency radar and autonomous underwater vehicles. *Journal of Atmospheric and Oceanic Technology* 20:1583-1599
- Shay LK, Martinez-Pedraja J, Cook TM, Haus BK, Weisberg RH (2007) High-frequency radar mapping of surface currents using WERA. *Journal of Atmospheric and Oceanic Technology* 24:484-503
- Skirving W, Heron S, Steinberg C, Strong A, McLean C, Heron M, Choukroun S, Arzayus F, Bauman A (2004) Palau Modeling Final Report. National Oceanic and Atmospheric Administration/Australian Institute of Marine Science, Townsville:46 pp.
- Smith NP (1983) Temporal and spatial characteristics of summer upwelling along Florida's Atlantic shelf. *Journal of Physical Oceanography* 13:1709-1715
- Smith NP (1998) Tidal and long-term exchanges through channels in the Middle and Upper Florida Keys. *Bulletin of Marine Science* 62:199-211
- Smith NP (2002) Tidal, low-frequency and long-term mean transport through two channels in the Florida Keys. *Continental Shelf Research* 22:1643-1650
- Smith NP, Lee TN (2003) Volume transport through tidal channels in the middle Florida Keys. *Journal of Coastal Research* 19:254-260
- Smith SG, Swanson DW, Chiappone M, Miller SL, Ault JS (2011) Probability sampling of stony coral populations in the Florida Keys. *Environmental Monitoring and Assessment* 183:121-138
- Soloviev AV, Luther ME, Weisberg RH (2003) Energetic baroclinic super-tidal oscillations on the southeast Florida shelf. *Geophysical Research Letters* 30
- Sopkin K, Mizak C, Gilberta S, Subramanian V, Luther M, Poor N (2007) Modeling air/sea flux parameters in a coastal area: A comparative study of results from the TOGA COARE model and the NOAA Buoy model. *Atmospheric Environment* 41:4291-4303
- Spigel RH, Imberger J, Rayner KN (1986) Modeling the diurnal mixed layer. *Limnology and Oceanography* 31:533-556
- Sponaugle S, Cowen RK, Shanks A, Morgan SG, Leis JM, Pineda JS, Boehlert GW, Kingsford MJ, Lindeman KC, Grimes C, Munro JL (2002) Predicting self-recruitment in marine populations: Biophysical correlates and mechanisms. *Bulletin of Marine Science* 70:341-375
- Sponaugle S, Fortuna J, Grorud K, Lee T (2003) Dynamics of larval fish assemblages over a shallow coral reef in the Florida Keys. *Marine Biology* 143:175-189
- Sponaugle S, Lee T, Kourafalou V, Pinkard D (2005) Florida current frontal eddies and the settlement of coral reef fishes. *Limnology and Oceanography* 50:1033-1048

- Stalker JC, Price RM, Swart PK (2009) Determining spatial and temporal inputs of freshwater, including submarine groundwater discharge, to a subtropical estuary Using Geochemical Tracers, Biscayne Bay, South Florida. *Estuaries and Coasts* 32:694-708
- Sturges W, Leben R (2000) Frequency of ring separations from the loop current in the Gulf of Mexico: A revised estimate. *Journal of Physical Oceanography* 30:1814-1819
- Sturman JJ, Oldham CE, Ivey GN (1999) Steady convective exchange flows down slopes. *Aquatic Sciences* 61:260-278
- Thomas J, Frost RR, Harvey RD (1973) Thermal-conductivity of carbonate rocks. *Engineering Geology* 7:3-12
- Thomson DJ (1990) Time-series analysis of Holocene climate data. *Philosophical Transactions of the Royal Society of London Series a-Mathematical Physical and Engineering Sciences* 330:601-616
- Tolman HL (2008) A mosaic approach to wind wave modeling. *Ocean Modelling* 25:35-47
- Ullsch A, Roske F (2002) Self-organizing feature maps predicting sea levels. *Information Sciences* 144:91-125
- Uncles RJ, Stephens JA (2001) The annual cycle of temperature in a temperate estuary and associated heat fluxes to the coastal zone. *Journal of Sea Research* 46:143-159
- USF (2009) University of South Florida Institute for Marine Remote Sensing Web site containing MODIS and SEAWiFS chl\_a, and MODIS and AVHRR SST, accessed November 2009: <http://imars.usf.edu/sst>
- Vickers D, Mahrt L (2006) Evaluation of the air-sea bulk formula and sea-surface temperature variability from observations. *Journal of Geophysical Research-Oceans* 111:14
- Virmani JJ, Weisberg RH (2005) Relative humidity over the west Florida Continental Shelf. *Monthly Weather Review* 133:1671-1686
- Walker BK, Riegl B, Dodge RE (2008) Mapping coral reef habitats in southeast Florida using a combined technique approach. *Journal of Coastal Research* 24:1138-1150
- Wang JD, Vandekreeke J (1986) Tidal circulation in north Biscayne Bay. *Journal of Waterway Port Coastal and Ocean Engineering-Asce* 112:615-631
- Wang JD, Luo JG, Ault JS (2003) Flows, salinity, and some implications for larval transport in South Biscayne Bay, Florida. *Bulletin of Marine Science* 72:695-723
- Wang M (2008) Comparison of Wave Parameters and Spectra between WERA HF Radars and Tri-Axys Buoys. University of Miami, p70
- Webb BW, Zhang Y (1997) Spatial and seasonal variability in the components of the river heat budget. *Hydrological Processes* 11:79-101

- Wells JR, Fram JP, Pawlak G (2012) Solar warming of near bottom water over a fringing reef. *Journal of Marine Research* 70:641-660
- Wilson-Diaz D, Mariano AJ, Evans RH (2009) On the heat budget of the Arabian Sea. *Deep-Sea Research Part I-Oceanographic Research Papers* 56:141-165
- Wilson-Diaz D, Mariano AJ, Evans RH, Luther ME (2001) A principal component analysis of sea-surface temperature in the Arabian Sea. *Deep-Sea Research Part II-Topical Studies in Oceanography* 48:1097-1114
- Wolanski E (1986) Observations of wind-driven surface gravity-waves offshore from the Great-Barrier-Reef. *Coral Reefs* 4:213-219
- Wolanski E, Spagnol S (2000) Sticky waters in the Great Barrier Reef. *Estuarine Coastal and Shelf Science* 50:27-32
- Xu Q, Zheng QA, Lin H, Liu YG, Song YT, Yuan YL (2008) Dynamical analysis of mesoscale eddy-induced ocean internal waves using linear theories. *Acta Oceanologica Sinica* 27:60-69
- Yee SH, Santavy DL, Barron MG (2008) Comparing environmental influences on coral bleaching across and within species using clustered binomial regression. *Ecological Modelling* 218:162-174
- Yeung C, Jones DL, Criales MM, Jackson TL, Richards WJ (2001) Influence of coastal eddies and counter-currents on the influx of spiny lobster, *Panulirus argus*, postlarvae into Florida Bay:1217-1232
- Yu LS, Weller RA (2007) Objectively analyzed air-sea heat fluxes for the global ice-free oceans (1981-2005). *Bulletin of the American Meteorological Society* 88:527-+
- Zamudio L, Hogan PJ (2008) Nesting the gulf of Mexico in Atlantic HYCOM: Oceanographic processes generated by Hurricane Ivan. *Ocean Modelling* 21:106-125
- Zepp RG, Shank GC, Stabenau E, Patterson KW, Cyterski M, Fisher W, Bartels E, Anderson SL (2008) Spatial and temporal variability of solar ultraviolet exposure of coral assemblages in the Florida Keys: Importance of colored dissolved organic matter. *Limnology and Oceanography* 53:1909-1922
- Zhang YC, Rossow WB, Lacis AA, Oinas V, Mishchenko MI (2004) Calculation of radiative fluxes from the surface to top of atmosphere based on ISCCP and other global data sets: Refinements of the radiative transfer model and the input data. *Journal of Geophysical Research-Atmospheres* 109:27, D19105
- Zhao J, Barnes B, Melo N, English D, Lapointe B, Muller-Karger F, Schaeffer B, Hu C (2013) Assessment of satellite-derived diffuse attenuation coefficients and euphotic depths in south Florida coastal waters. *Remote Sensing of Environment* 131:38-50

## VITA

Lewis James Gramer was born in Norwalk, Ohio, on October 4, 1966, and became a Florida resident ten days later, on October 14, 1966. His mother was Ms. Mary Ann Gramer née Lewis. He received his early education at Naranja Head Start, Naranja Elementary School, and Redland Junior High School in south Florida. He was graduated from South Dade Senior High School in Homestead, Florida as Valedictorian in June 1983, participating in the Summer Science Scholar program at University of Florida in 1982 and as a Community Lab research assistant at the University of Miami in 1982-1983. In September 1983 he entered the Massachusetts Institute of Technology, from which he was graduated with the S.B. degree in Mathematics (Course XVIII-A) with a Minor in Literature in June 1990. While at M. I. T. he completed courses at Harvard University in comparative literature. He worked as a principal software engineer and vice president of technology in the software and financial services industries from 1988 to 2004. He began his second career as an oceanographic researcher at the Cooperative Institute for Marine and Atmospheric Studies (CIMAS) in May 2005. In August 2006 he was admitted as a degree-seeking student to the Graduate Program of the Rosenstiel School of Marine and Atmospheric Science of University of Miami, where he was granted a Ph.D. degree in August 2013.

Permanent Address: 442 SE 22<sup>nd</sup> Dr., Homestead, Florida 33033